UNIVERSITY OF LONDON THESIS

Degree PhD Year 2008 Name of Author SAMARASINGHE, SUREN RAVINDRA

Deposition of noble metals by electrohydrodynamic atomisation

A dissertation submitted for the degree of

Doctor of Philosophy

August, 2008

Suren R. Samarasinghe

Department of Mechanical Engineering

University College London

Torrington Place

London WC1E 7JE

ProQuest LLC
789 East Eisenhower Parkway
P.O. Box 1346
Ann Arbor, MI 48106-1346

DECLARATION

I, Suren Ravindra Samarasinghe, confirm that the work presented in this thesis is my own. Where information has been derived from other sources, I confirm that this has been indicated in the thesis.

ABSTRACT

There is an expanding interest in rapid prototyping capabilities of direct write technologies. Due to this, a number of candidate deposition systems have been used for fabricating microscale structures for electronics and biomedical applications such as fabricating conducting tracks for next generation electronic devices, bone replacement parts, flat screen displays and polymeric light emitting diodes...etc. In response to this growing interest in direct write technologies, an experimental investigation was carried out in order to find out whether electrohydrodynamic atomisation can be used as a competing direct write technology.

In this research, initially, gold and silver alcosols were subjected to electrohydrodynamic atomisation. Different modes of atomisation and their parameters such as flow rate and voltage were recorded and a mode selection map was constructed for further studies. The main objective was to investigate the feasibility of electrohydrodynamic atomisation to fabricate films of thickness ranging between 100 nm – 1 μm to be used as substrates for e.g in surface enhanced Raman spectroscopy, cell biology and bio-engineering.

The gold alcosol was subjected to atomisation and the droplets resulting from jet break-up were collected on a substrate in order to produce dense gold films. Different flow rates and voltages were used and the optimum conditions such as flow rate, applied voltage and distance between the substrate and the capillary exit, for film fabrication were obtained. The deposition time was varied from 60 –

900 s and the variation of film thickness and surface morphology was observed with increasing deposition time. Dense film thicknesses ranging from ~0.5 – ~2 μm were fabricated by electrohydrodynamic deposition technique.

In order to pattern microscale structures on a substrate, gold and silver alcosols were subjected electrohydrodynamic atomisation printing. The main objective was to investigate whether using a low concentrated metal particle solution in conjunction with electrohydrodynamic atomisation printing technique can be utilised to produce conducting tracks in the range of 20 – 200 μms in diameter to be used in next generation electronic devices. Tracks containing metal particles were deposited at various flow rates. With increasing flow rate, the track width increased and the finest track width of ~110 μm was achieved. Templates were used to fabricate finer tracks in conjunction with electrospraying and in this case gold tracks of ~20 μm were patterned on silicon wafer. Due to low metal particle concentration conductive tracks were not possible to produce by these methods. Layer-by-layer deposition method was used with electrohydrodynamic printing to fabricate conducting tracks. The electrical resistivity of the printed gold track in this study was measured to be 1.8×10^{-7} Ωm.

The gold hydrosol containing spherical shaped nanoparticles and a silver suspension containing micro size particles were subjected to co-axial electrohydrodynamic atomisation to study the encapsulation of these metals with polyethylene glycol (PEG) : polyethylene oxide (PEO) fibres. The main objective was to investigate feasibility of encapsulating metal particles in polymeric fibres. PEG and PEO was used as a model system to encapsulate silver and gold particles

and this technique can be further developed to produce composite fibres to be used in optical, electrical and sensing devices. The relationships between the jet speed and particle arrangement in the encapsulation sheaths were also characterised using advance analytical techniques.

PUBLICATIONS

- ✓ S.R. Samarasinghe, I. Pastoriza-Santos, M.J. Edirisinghe, M.J. Reece and Luis M. Liz-Marzán, Printing Gold Nanoparticles with an Electrohydrodynamic Direct-Write Device, *Gold Bulletin*, 2006, **39**, 48 – 53.

- ✓ S. R. Samarasinghe, K. Balasubramanian and M. J. Edirisinghe, Encapsulation of silver particles using co-axial jetting, *Journal of Materials Science: Materials in Electronics*, 2008, **19**, 33 – 38.

- ✓ S.R. Samarasinghe, I. Pastoriza-Santos, M.J. Edirisinghe and L.M. Liz-Marzán, Fabrication of nano-structured gold films by electrohydrodynamic atomisation, *Applied Physics A: Materials and Processing*, 2008, **91**, 141 – 147.

- ✓ Stride E, Pancholi K, Edirisinghe MJ, Samarasinghe S, Increasing the nonlinear character of microbubble oscillations at low acoustic pressures, *Journal of Royal Society Interface*, DOI: 10.1098/rsif.2008.0005.

- ✓ S.R. Samarasinghe and M.J. Edirisinghe, Synthesis, processing & forming gold structures from a 0.1 wt. % concentration solution, Gold Bulletin, *in press*.

ACKNOWLEDGMENTS

- I would like to express my deepest gratitude to my supervisor Prof. Mohan Edirisinghe for providing me this opportunity and financial assistance and his wonderful guidance and support he gave me through out this study.
- I would also like to thank Dr. M. Reece from QM for his assistance and guidance.
- I would also like to thank Dr. Isabel Pastoriza Santos and Prof. Lis Marzan for preparing the sending the gold and silver nanoparticle solutions.
- I would also like to thank Kevin Reeves for assistance with scanning electron microscopy and my colleagues in the bio and functional research group for their support and for making the research environment more interesting.
- Finally I would like to thank my parents for their encouragement and constant support throughout my study.

TABLE OF CONTENTS

LIST OF TABLES AND FIGURES

Tables

Figures

Chapter 1

Introduction

1.1 Electrohydrodynamic atomisation and printing

Over the last two decades, integrated circuit feature dimensions have reduced in size dramatically. Recently, there has been a lot of interest in the rapid prototyping capabilities of direct write technologies, propelling the development of micro-electronic components and devices. In response to these growing direct write technologies, a feasibility study was carried out using electrohydrodynamic atomisation in conjunction with nanoparticle suspension technology as a means to fabricate metal films / fine line interconnects and metal encapsulated fibres for electronic components and devices. The main advantage of using nanoparticles for production of microelectronic devices is their low melting point. The melting point of the particles dramatically decreases when the particle size decreases to nanoscale [Szczech *et al.*, 2002].

Electrohydrodynamic atomisation (EHDA), also known as electrospraying or electrostatic atomisation can be explained as 'tiny droplets obtained from the electrically forced (electro) break-up of a moving (dynamic) liquid (hydro)' [Grace and Marijnissen, 1994]. In this process a liquid is forced through a metal capillary which is connected to a power supply. Another electrode (counter electrode) which is normally grounded is kept below the capillary exit. Due to the

external electric field created between the capillary and the ground electrode, the liquid at the exit of the capillary produces a liquid jet that later disintegrates into droplets.

This phenomenon was systematically studied by Zeleny (1914, 1915 and 1917) with subsequent analysis made by Taylor (1964 and 1969). Electrohydrodynamic atomisation has been extensively explored by many scientists over the last two decades after its importance was discovered in mass spectrometry [Fenn *et al.*, 1989]. Compared with other atomisation techniques, electrohydrodynamic atomisation offers easy generation of droplets, due to its electrical charge of the same polarity it avoids coalescence of droplets and achieves a narrow size distribution of droplets by the cone-jet mode [Watanabe *et al.*, 2003].

Electrohydrodynamic atomisation can occur in different modes, for example stable cone-jet mode, where a single jet forms from the cone apex which later disintegrates into droplets and spindle mode, where spindle-like fragments detach from the unstable cone. The stable cone-jet mode is the most studied and is great interest to this research, as it can generate near-monodisperse droplets of a few micrometers to sub-micrometer in size [Cloupeau and Prunetfoch, 1989, Cloupeau and Prunetfoch, 1990].

In the cone-jet mode, a liquid is forced through a capillary at a low flow rate which is exposed to an external electric field. Due to the electric field, a surface charge is induced on the growing droplet at the exit of the capillary. Due to the surface charge and the external electric field, an electric stress is created in the

liquid surface. For a given flow rate and applied voltage regime this electrical stress overcomes the surface tension stress. During this process the electrical stresses transform the droplet at the exit of the capillary into a conical shape and later, a thin jet (when compared with capillary diameter) evolves from the apex of the cone which later disintegrates into a number of primary droplets with a narrow size distribution and a number of smaller secondary droplets and satellites. But the total volume of these secondary droplets is much smaller than the volume of the primary droplets [Hartman *et al.*, 1999b, Hartman *et al.*, 2000].

The droplet size in the stable cone-jet mode depends mainly on the liquid flow rate, applied voltage and the liquid properties such as density, viscosity, electrical conductivity and surface tension. Depending on the flow rate of the liquid, applied voltage and the properties of the liquid, the main droplet size can range from hundreds of micrometers to nanometers. The primary droplet size in the stable cone-jet mode is independent of the applied voltage but depends mainly on the flow rate of the liquid, while the secondary droplets depend on the viscosity, surface tension of the liquid and the applied voltage in addition to the liquid flow rate. There exists an optimum flow rate between the minimum flow rate and maximum flow rate for stable cone-jet mode, which results in a minimum standard deviation in droplet size distribution [Cloupeau and Prunetfoch, 1989].

In addition to liquid flow rate, applied voltage and the liquid properties, the shape of the ground electrode plays a very important role in the jet break up process in cone-jet mode. When a ring or a plate shaped ground electrode is used, it was found that the larger droplets were in the central regions of the spray while the

smaller droplets were at the extremities of the spray [Hartman *et al.*, 1999a, Hartman *et al.*, 1999b]. Jayasinghe and Edirisinghe (2004) reported that using a point shaped ground electrode can help to focus the conical spray onto the point head of the ground electrode. By using a point-shaped ground electrode to focus the droplets. Jayasinghe and co-workers (2002) innovated the electrohydrodynamic atomisation printing device, to deposit ceramic droplets onto a substrate according to a pre-designed structure.

1.2 Aims and objectives

The primary aim of this research is to understand the electrohydrodynamic atomisation processing technique and whether it can be utilised as a deposition technique to deposit metal micro- and nanoparticles suspended in a liquid. A thorough literature review should be carried out on electrohydrodynamic atomisation and the parameters that affect this process should be understood. A detailed study should be carried out on other techniques which have been used to deposit metal particles should be carefully analysed.

The first objective of this research is to electrohydrodynamically atomise a solution containing metal particles and to observe its ability to atomise in stable cone-jet mode. The droplets produced from atomisation should be collected on a substrate to form metal films in the range of 100 nm – 1 μm. Furthermore, the parameters should be varied to find out the effect this has on the films by characterising with scanning electron microscopy.

The second objective of this research is to pattern different geometries containing metal particles, by electrohydrodynamic atomisation printing technique and to produce conducting tracks. The track width should be in the range of 20 – 200 μm and the final resistivitity of the track should be close to its bulk material.

The final objective of this research is to use co-axial needle (one needle inside the other) configuration to encapsulate metal particles within a fibre by electrospinning technique. The composite fibre diameter should be in the range of 1 – 100 μm. The processing parameters such as the flow rate and applied voltage should be varied and the particle distribution along the fibre should be carefully analysed and understood.

1.3 Content of thesis

Chapter **1** introduces the electrohydrodynamic atomisation processing route and electrohydrodynamic atomisation printing method. This chapter briefly introduces the most important spraying mode of electrohydrodynamic atomisation used in this research, namely the stable cone-jet mode. It also contains an overview of the thesis contents. The aims and objectives of the research are clearly stated and the scope of this research is also explained.

Chapter **2** presents a detailed literature review study of the investigations that have been carried out previously by other researchers in the area of electrohydrodynamic atomisation. Various modes of electrohydrodynamic atomisation and the factors influencing atomisation are discussed in more detail, as

well as the different metal deposition techniques used to fabricate metal films and tracks, together with their advantages and disadvantages are also reviewed.

Chapter **3** gives a detailed description of the experimental procedures. This chapter discusses the solutions used for experiments and their preparation details, characterisation techniques and the equipments used in this research. This chapter also contains details of the design and motion of two-dimensional (2D) electrohydrodynamic atomisation print-patterning equipment and other devices used in conjunction with the patterning device.

Chapter **4** contains the results obtained from this research. Firstly, it introduces the fabrication of gold films by electrohydrodynamic atomisation. Secondly, the gold and the silver alcosols were subjected to electrohydrodynamic atomisation and with the help of the printing device, gold and silver 2D microstructures were patterned on silicon wafer. In order to reduce the track size, templates were used in conjunction with electrohydrodynamic atomisation. Lastly, silver microparticles and gold nanoparticles were encapsulated in fibres by co-axial electrospinning.

Chapter **5** contains the discussion of the results obtained in the experiments carried out in Chapter **4**. Gold films were fabricated using electrohydrodynamic atomisation. The main processing parameters, namely deposition time and sintering temperature were varied and the resulting films were characterized by scanning electron microscopy. Furthermore the particle movement and the landing of particles on the films were analysed in more detail. In the second set of

experiments gold and silver solutions were atomised in the stable cone-jet mode and tracks containing metal particles were deposited on silicon wafer (substrate) by electrohydrodynamic atomisation printing technique. The main parameters such as the flow rate, the distance between the nozzle and substrate and its effect on the printed track are analysed. The particle movement within the track during solvent evaporation are analysed in more detail. In order to produce conductive tracks, a layer-by-layer deposition technique was employed. The main processing parameters were discussed and the electrical resistivity of the deposited tracks are also measured. By using co-axial electrospinning technique metal micro- and nanoparticles were encapsulated in polymeric fibres. The distribution of silver and gold particles along the fibre are discussed in more detail.

Chapter **6** concludes with summarising the key results that were obtained from this research. A suggestion to the future work that could be carried out using this process is also explained.

Chapter 2

Literature Review

2.1 Electrohydrodynamic atomisation

The electrohydrodynamic atomisation of liquids was first noted and reported by Gilbert in 1600. He reported that a droplet of water on a smooth surface could be extended into a shape of a cone if a piece of rubbed amber was held at a certain distance from the water droplet. Later, in 1745, Bose was the first to describe the electrohydrodynamic atomisation of fluids [Ganan-Calvo, 1999]. Due to its physical richness, small dimensions and surprising reproducibility etc., for centuries it has attracted lot of interest by many physicists.

Many years later, Rayleigh (1878, 1879a, 1897b and 1882) observed the instabilities of a pendant drop or jet and suggested conditions when the pendant drop or jet become unstable when exposed to an external electric field. Rayleigh stated that the stability of the pendant drop or jet is dependent upon the balance of forces between the outward electrical stress that disrupt the drop or jet and the counteracting surface tension forces which try to hold the drop or jet together. Based on Rayleigh's analysis many researchers have tried to understand this natural phenomenon theoretically and experimentally, but fundamental problems of electrohydrodynamic atomisation spraying remains still unsolved.

After Rayleigh's findings, Zeleny (1914 and 1915) carried out the first systematic study on electrohydrodynamic atomisation. He studied the break-up of a pendant drop which was produced at the tip of a glass capillary which was exposed to an external electric field. By applying an electric field he observed the oscillations in the liquid at the exit of the capillary. Three modes of spraying at the exit of the capillary were discussed in the parametrical space (Q,V) where Q and V are the liquid flow rate at the exit of the glass capillary and applied voltage, suggesting the first mode classification criterion. He was able to give qualitative description of the process and in 1917 was able to obtain photographs of drops at the tip of the glass capillary which was exposed to an electric field [Zeleny, 1917]. The apparatus used by him in his experiments contained the essential features that are used even now by researchers. Furthermore in 1935, measurements of voltage and spray current were also reported by Zeleny (1935) after which there was little progress for more than a decade.

Vannegut and co-workers (1952) obtained highly charged droplets with a 0.1 mm diameter by varying the applied voltage between 5 – 10 kV, using a similar experimental set-up to that of Zeleny. They used a simple apparatus for electrohydrodynamic atomisation consisting of a glass tube that was drawn down to a capillary (having a diameter of few tenth's of a millimetre) which was filled with water or any liquid. One end of a conducting wire was also inserted into the glass capillary and the other end was connected to a high voltage power supply. They reported a detailed description of their observations, explaining different stages in the development of the pendant drop when exposed to an electric field.

Drozin (1955) carried out similar experiments and observed the different stages of a pendant drop at the exit of the capillary with increasing applied voltage. An interesting finding was that he was able to relate the physical properties of a liquid to the electrostatic atomisation process. He discovered that a liquid with a very low dielectric constant could not be atomised and a liquid could only be atomised if the conductivity of the liquid was below a certain upper limit. But quantitative measurements regarding the limits of the conductivity were not explained in detail.

Thereafter the attention was focused on the liquid properties, the droplet size and the electric field configurations. During this time, the most significant work was carried out by Taylor (1964), who studied the break-up of glycerine and glycerine-water drops, when the electric field was applied to the capillary tube carrying the liquid. His experimental set-up differed from the basic experimental set-up used by his predecessors. The capillary tube was held vertically upwards and interestingly the gravitational and electrical forces on the spray acted in opposite directions. In his experiments, he measured the potential difference between the liquid and the plate shaped ground electrode when the jet appeared from the drop. Taylor observed that the liquid was first drawn out into some fine filaments before breaking into fine droplets mainly due to the high viscosity of the glycerine and glycerine-water mixture used. He also reported that some of the filaments issued from the viscose liquid were as much as 5 cm long and 20 μm wide. He also compared the voltage required to initiate the instabilities with those suggested by Zeleny and successfully obtained the conditions of a liquid breakdown in a more qualitative way.

Taylor also reported that when a conducting fluid was used and the jet had a high viscosity, the liquid would not vibrate before break-up but would adopt a conical shape with a sharp apex. The semi-vertical angle of the conical meniscus was found to be close to 49.3°. This is the angle at which a conical meniscus of a conducting liquid can exist in equilibrium under an applied electric field. The threshold values for applied potential for which the liquid starts to issue a jet were also measured by him and compared with the predictions made earlier [Taylor, 1964]. He predicted that the threshold applied voltage of a liquid would be related to the surface tension of the liquid and the geometry of the liquid [Taylor, 1969], which was found to be an inaccurate prediction according to later studies. They also found out that other liquid properties also affect this process [Michelson, 1990]

Instead of using the glass capillary, Carson and Hendrick (1965) used a metallic capillary and obtained the current in pulse form. They successfully obtained very similar photographs to that of Taylor using glycerine and octoil. They also found that there was a lower limit for the applied voltage above which the pulsation occurs. During this time an important finding was made by Hogan and Hendrick (1965). They measured the charge to mass ratios and considered the key factors that would influence this. Nagornyi and Bezrukov (1980) investigated the decreasing droplet size with increasing applied potential, thereby suggesting the conditions necessary to produce smaller droplets by electrostatic atomisation.

Since 1980, electrostatic atomisation has been extensively studied by many researchers because of its application potential. Smith (1986) published a general

discussion on electrostatic atomisation with some quantitative descriptions of the effect of liquid properties had on the experimental results, while some other researchers tried to characterize the process through an energy approach or attempted a joule-heating mechanism. Hayati and co-workers (1986, 1987a and 1987b) investigated in detail the mechanisms that were present in the atomisation process.

The most contributing work after Zeleny and Taylor was the classification of the functional modes of spraying carried out by Cloupeau and Prunet-Foch (1990 and 1994). The modes were classified into two groups based on the continuity of the generation of sprayed droplets. Each individual mode was described in more detail based on the geometrical configuration of the meniscus at the exit of the capillary. The effect of the liquid flow rate and the applied voltage and its effect on each mode and the importance of corona discharge were also investigated [Cloupeau, 1994]. Jaworek and Krupa (1999) reported a concluding investigation on mode classification (explained in **Section 2.1.1**) with the addition of precession and oscillating modes.

In recent years, the stable cone-jet mode of atomisation has attracted lot of interest from researchers due to its greater application potential mainly due to its ability to produce near-monodisperse droplets. Researchers have used high flow rate ($>10^{-5}$ ml/s) and low flow rate regimes ($<10^{-5}$ ml/s). Meesters and co-workers (1992) investigated the cone-jet mode of atomisation at high flow rates. They observed that so-called space charge controlled regime of the Taylor cone in which very high droplet production was achieved. Loscertales and Fernandez were able to

produce nanometer scale droplets at very low flow rate (10^{-7} ml/s) [Grace and Marijnissen, 1994].

Delamora and Loscertales (1994) presented a numerical method for estimating the current through the liquid cone and the resulting droplet diameter. These relations are often refereed to as the scaling laws of electrostatic atomisation in the cone-jet mode [Ganan-Calvo *et al.*, 1997]. These relations were modified by Ganan-Calvo (1997) who did comprehensive work suggesting modifications for the scaling law, both for the electrostatic sprayed droplets and the flowing current due to application of potential difference based on their experimental investigations. They proposed that there might be three possible factors governing the electrostatic atomisation process by setting up the mathematical model, being surface tension, inertia and the viscous force. He ended up with a scaling theory considering six fundamental equations, two for each of the factors mentioned above. However, among these equations, the most important two are those relating to the current and the droplet size, with different governing factor combinations. The equations were derived and summarized recently by Ganan-Calvo (2004).

2.1.1 Different modes of atomisation

In the electrohydrodynamic atomisation, the shear stress acting on the liquid surface due to the electric field causes the liquid at the exit of the capillary to elongate and to form a cone and/or a jet, which later disintegrate into droplet due to the mechanical and electrical forces. A few papers have been published classifying the known modes of atomisation [Hayati *et al.*, 1987a, Hayati *et al.*, 1987b, Cloupeau and Prunetfoch, 1990, Grace and Marijnissen, 1994, Grigorev and

Shiryaeva, 1994, Shiryaeva and Grigorev, 1995] however, criteria on which they were based was not always consistent. The formation of the jet and later its disintegration into droplets and the characteristics of each spraying mode was not described systematically in detail. However, in this review, modes are discussed based on mainly two characteristics criteria, following the work done by Jaworek and Krupa (1999):

- The geometrical form of the liquid at the exit of the capillary.
- The type of the jet behaviour in the disintegration into droplets.

In general, spraying modes can be classified into two groups according to the above mentioned criteria. The first group includes the spraying modes in which only fragments of liquid are ejected from the capillary exit. Dripping, micro-dripping and spindle mode are a few modes of atomisation which belong to the first category. The second group consists of the modes which are characteristic in that the liquid issues a capillary in the form of a long continuous jet which later disintegrates into droplets only at some distance, usually few millimetres, from the exit of the capillary. The meniscus and the jet in this group can be stable, can vibrate, rotate spirally around the axis or whip irregularly [Jaworek and Krupa, 1999].

2.1.1.1 Dripping mode

In the dripping mode, regular sphere shaped drops are formed and then detached from the exit of the capillary when the gravitational force and electrical force together overcome the surface tension forces. After the droplet detachment from the exit of the capillary, the meniscus contracts back, forming a

hemispherical-like meniscus before the same process takes place again. The drop formation time is much longer than that of the fall of the former drop, so the drop formation is not effected by the charges carried by the previous drops (**Figure 2.1**).

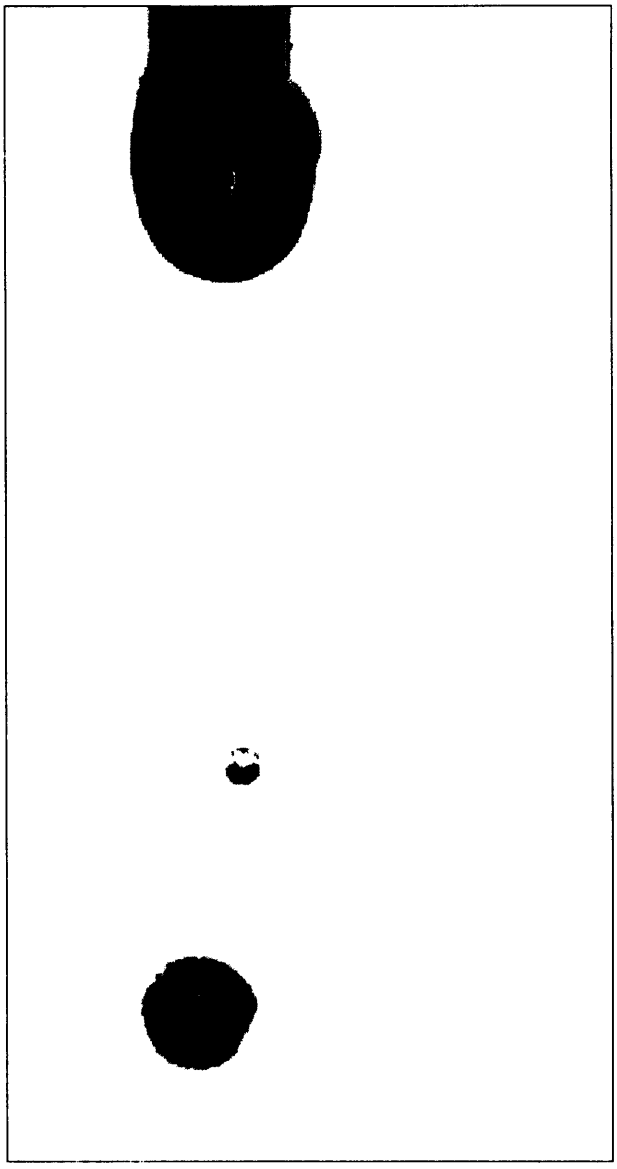

Figure 2.1 Dripping mode [Jaworek and Krupa, 1999]

With increasing voltage, the meniscus elongates due to the electrostatic forces causing smaller droplets to detach from the meniscus. When the voltage is further increased, for a short time the drop can be connected with the capillary by a

liquid thread, which breaks off next as the drop falls down and a sibling (secondary) is generated from the thread. The sibling is usually perpendicular to the capillary axis. When compared with other spraying modes, the production frequency of droplets in dripping mode is usually very low [Jaworek and Krupa, 1999].

2.1.1.2 Micro-dripping mode

In the micro-dripping mode, the liquid at the exit of the capillary forms a stable meniscus at the end of which a small (much smaller than the capillary diameter) droplet is formed. As shown in **Figure 2.2**, the droplet is detached from the meniscus and does not undergo further disruption. This mode of atomisation occurs at low liquid flow rates. The main difference between the micro-dripping and dripping modes is that the meniscus does not retract after the droplet detachment.

The droplet production frequency is usually two orders of magnitude higher than that of the dripping mode. The size of the droplets can range from a few micrometers up to hundreds of micrometers in diameter and the droplet size distribution is usually monodisperse. The frequency of the droplets produced ranges from a few droplets up to a few thousand droplets per second. The space charge formed by the previously generated droplets is too weak to affect the generation process because the droplets are quickly removed by the electric filed as well as the size of the droplet not being sufficiently big enough [Jaworek and Krupa, 1999].

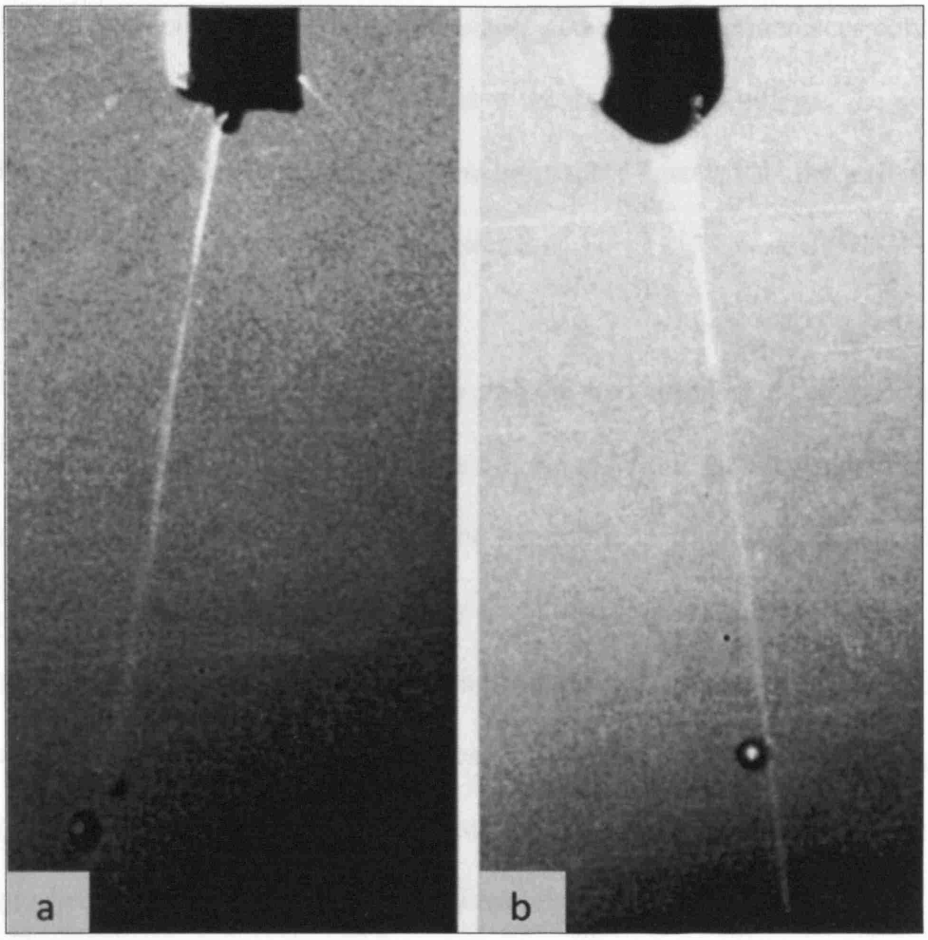

Figure 2.2 Micro-dripping mode showing forms of the meniscus. a) Flat liquid ethylene glycole and b) cone like liquid ethylene glycole [Jaworek and Krupa, 1999]

2.1.1.3 Spindle mode

The dripping and micro-dripping modes can be generated only in limited ranges of voltage and flow rate. If the flow rate is sufficiently high and with an increasing electric field, the liquid elongates towards the direction of the electric field and a thick jet detaches as a spindle like fragment of liquid as shown in **Figure 2.3**. Because of the shape of the jet produced, this mode of atomisation is referred as spindle mode [Cloupeau and Prunetfoch, 1990]. After detachment of the spindle it can break up into several smaller droplets of different sizes which

2.1.1.4 Multi-spindle mode

In this mode of atomisation, the droplet generation is similar to spindle mode, but the spindle like jets only emit periodically from some distinct points at the circumference of the capillary. The jet takes the form of short spindles. The droplet generation process is caused by the electric field between the electrodes and is also affected by the space charge. If the liquid exits the capillary quicker than the jet formation with the aid of the sufficiently high electric field that liquid exits faster from the capillary and as a result fragments of liquid form (**Figure 2.4**). After detachment from the capillary the quantity of liquid can disintegrate into a few smaller droplets. The jet emission sites are believed to have uniform distribution on the capillary rim with the number of the sites increasing with increasing applied voltage. The droplets generated from this type of atomisation are therefore smaller in size than in the spindle mode [Jaworek and Krupa, 1999].

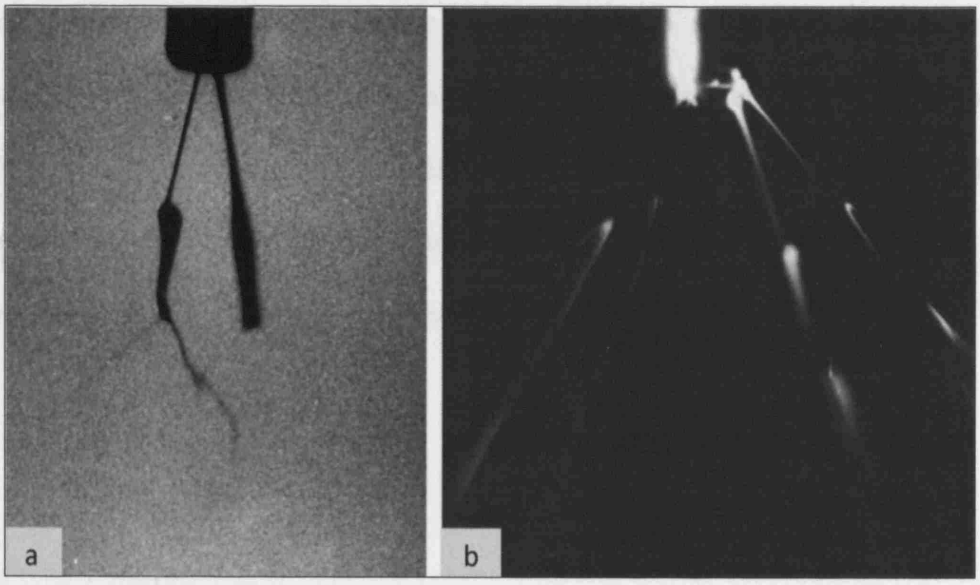

Figure 2.4 Multi-spindle mode. a) Jet formation b) Spatial distribution of the generated aerosol [Jaworek and Krupa, 1999]

2.1.1.5 Cone-jet mode

Cone-jet mode is the most widely used atomisation mode due to its ability to produce near-monodisperse droplets at a relatively reasonable frequency. In the cone-jet mode the liquid at the exit of the capillary forms a cone with a thin jet at the cone apex, stretching along the capillary axis. In this mode the jet diameter is less than 100 μm's. According to past literature three different forms of the cone are possible: linear sides, convex or concave [Cloupeau and Prunetfoch, 1990].

The end of the jet undergoes two types of instabilities (varicose and kink) due to the electrical stress created on the liquid and solution properties, which later disintegrates into droplets (**Figure 2.5**). In the case of varicose instabilities, the waves are generated on the surface of the jet but the jet does not change its linear position. In the nodes of the wave the liquid contracts and the jet disintegrates into equal droplets, which further flow close to the capillary axis. In the case of kink instabilities the jet moves irregularly and breaks up into the droplets due to electrical and inertial forces. The space charge in the cone-jet mode is much more stable than in other spraying modes because the droplets are smaller and less mobile. The jet diameter becomes lower and it's length becomes shorter with the increasing voltage [Cloupeau and Prunetfoch, 1990].

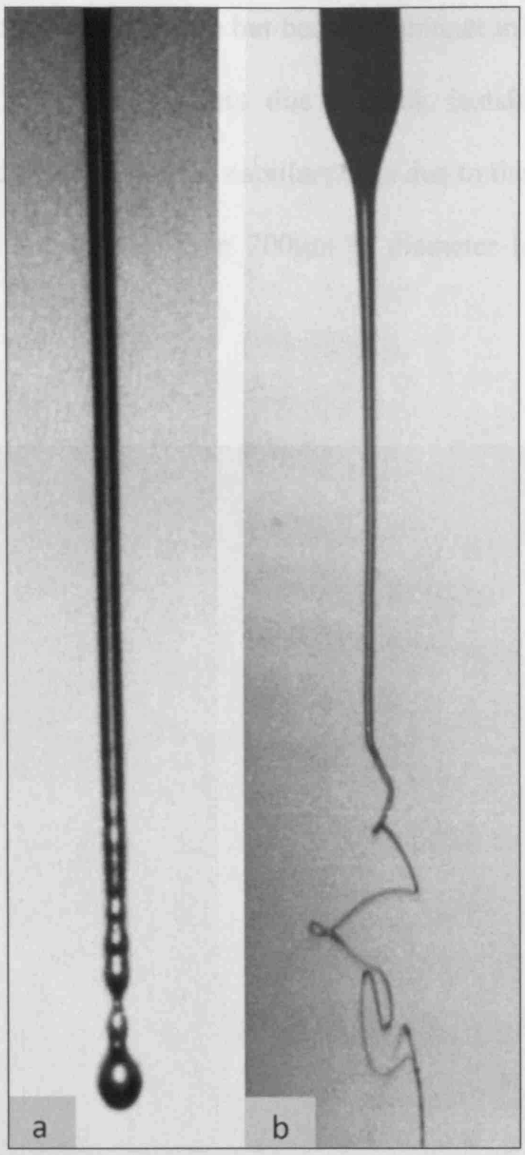

Figure 2.5 Cone-jet mode showing two types of jet instabilities. a) varicose instabilities and b) kink instabilities [Jaworek and Krupa, 1999]

2.1.1.6 Oscillating-jet mode

Oscillating-jet mode occurs at high liquid flow rates, which allow the jet to become continuous and steadily connected with the capillary. The intermitant drop generation no longer exists, but replaced by a continuous jet issues from the tip of the capillary and changes its position (oscillates) in one plane with the capillary axis as a result of the space charge of the formerly formed droplets as well as the

gas ions. The jet is not usually smooth but becomes thinner in a few places. The jet later disintegrates into small droplets due to kink instabilities (**Figure 2.6**). Furthermore, the jet deviates from the capillary axis due to the space charge effect. Usually the droplets are smaller than 200μm in diameter [Jaworek and Krupa, 1999].

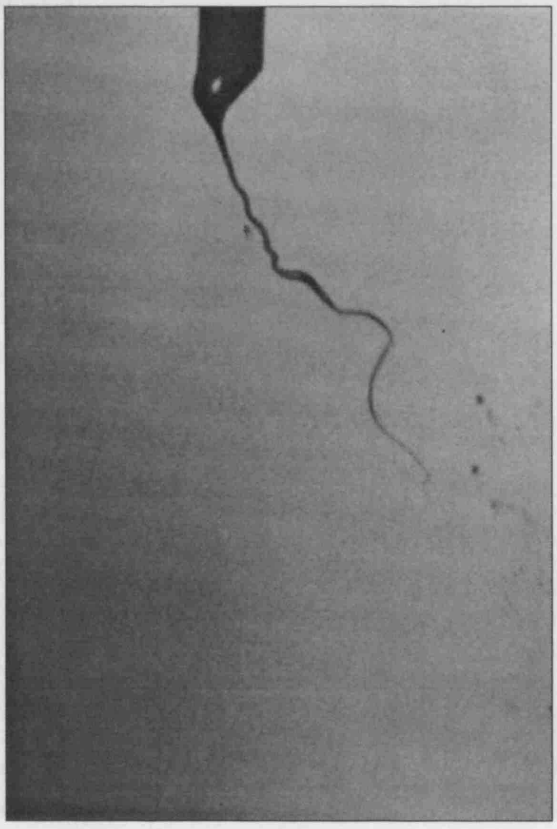

Figure 2.6 Oscillating mode [Jaworek and Krupa, 1999]

2.1.1.7 Precision mode

In this mode of atomisation [Jaworek and Krupa, 1996] the liquid escapes the capillary in the form of a skewed cone which smoothly changes into a thin jet. Both cone and the jet rotate regularly round the capillary axis. The diameter of the jet is smaller than 100 μm but becomes thinner at its end (**Figure 2.7**). The jet disintegrates into small droplets at the distance of about 5 – 10 mm from the tip of

the capillary. With increasing voltage the jet length becomes longer. This mode of atomisation allows for the generation of fine aerosol forming uniform spatial dispersion. The size distribution does not change significantly with increasing voltage [Jaworek and Krupa, 1999].

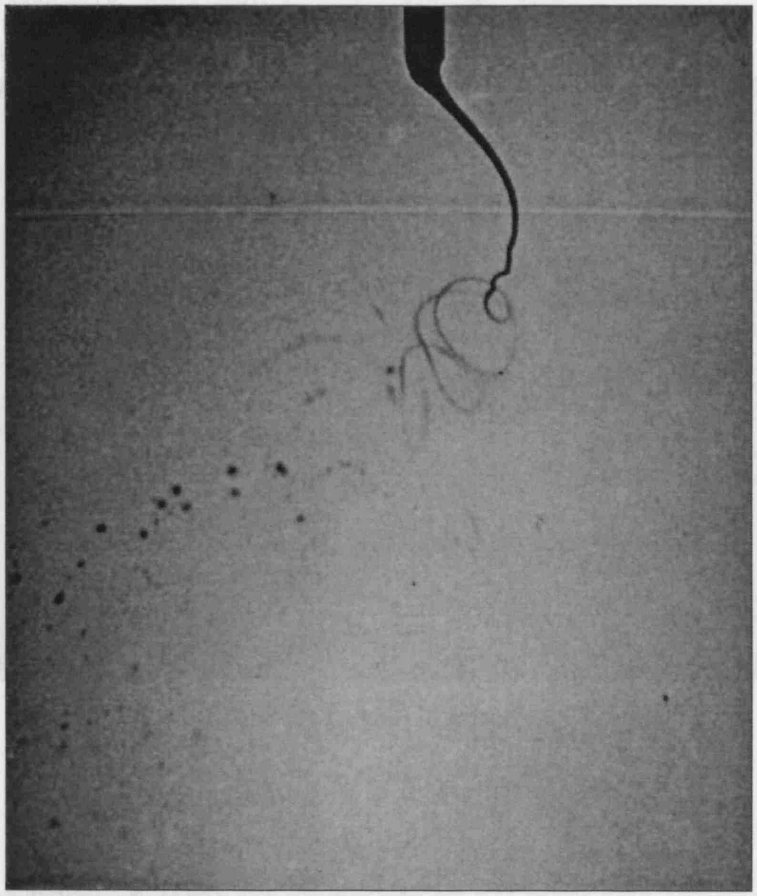

Figure 2.7 Precision mode [Jaworek and Krupa, 1999]

2.1.1.8 Multi jetting mode

Multi jetting mode can occur from the cone-jet mode by increasing the applied voltage and liquid flow rate. At first, the cone usually becomes skewed, leading to a single jet at the rim of the capillary. However this situation is unstable and therefore two opposite jets or three symmetrically distributed jets are formed. The meniscus becomes flat with only short cones at the emission points

(**Figure 2.8**). The diameter of the jets is usually less than a few tens of micrometers. The jet later disintegrates into small droplets due to kink instabilities forming a fine mist around the capillary axis. With increasing applied voltage and liquid flow rate, 2 – 8 may be ejected from the capillary. When multiple jets are formed, each jet is formed faster and becomes thinner [Jaworek and Krupa, 1996].

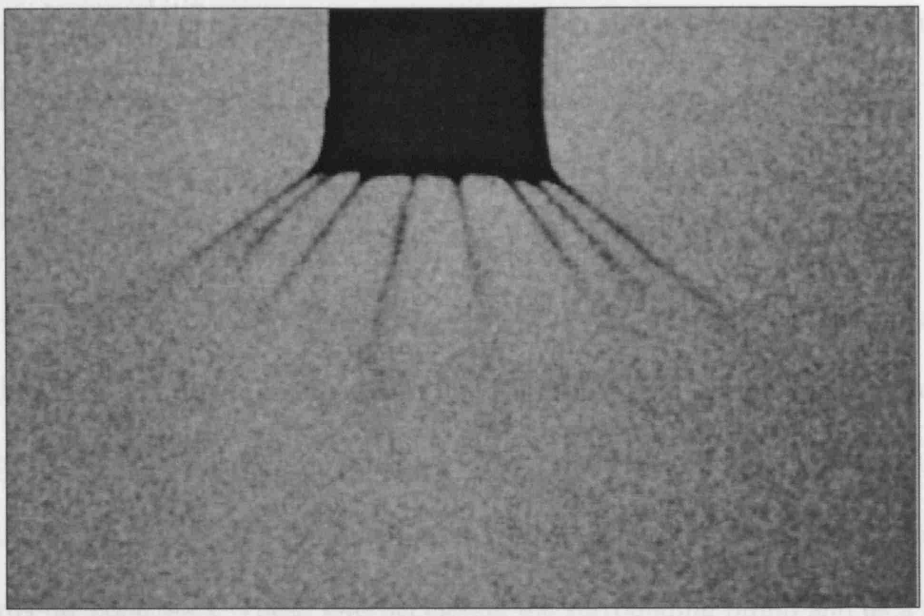

Figure 2.8 Multi-jet mode [Jaworek and Krupa, 1999]

2.1.2 Mechanism of stable cone-jet mode

The stable cone-jet mode is the most widely studied mode of atomisation due to its ability to produce near-monodisperse droplets over a wide size range, from submicron to hundred's of micron. There are three stages of electrohydrodynamic processing in the cone-jet mode. These stages are discussed in more detail below.

2.1.2.1 Acceleration of the liquid in the liquid cone

In the stable cone-jet mode, the shape of the cone is a result of the balance of liquid pressure, liquid surface tension, gravity and electric stresses in the liquid surface, the liquid inertia and the liquid viscosity. Taylor calculated analytically the conical shape, later referred to as the 'Taylor cone', which balanced the surface tension and the electrical stress [Taylor, 1964]. A Taylor cone forms when the outward stress due to an applied electric field balances the inward stress due to the liquid surface tension. **Figure 2.9** shows the various forces acting on the Taylor cone which was later modified by Hartman and co-workers (1999).

In a liquid, charge is mainly transported by ions and the free chargers at the liquid surface also mainly consist of ions. Due to this surface charge, the normal electric field inside the liquid is small compared to the normal electric field outside the liquid. The tangential electric field accelerates the ions at the liquid surface towards the cone apex. These ions accelerate the surrounding liquid and as a result a thin jet emerges at the cone apex. This acceleration process and the shape of the liquid cone are a result of the balance of the liquid pressure, liquid surface tension, gravity and electric stresses in the liquid surface and the inertia and viscosity of the liquid. Furthermore, the droplet size also depends on the forces acting on the liquid.

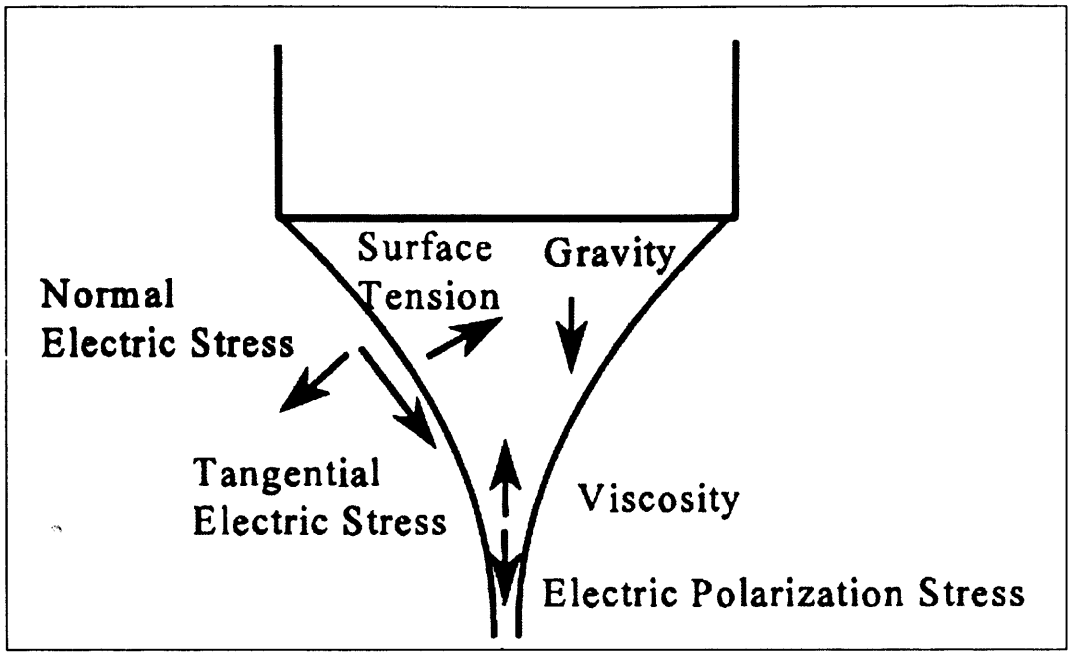

Figure 2.9 Forces acting in the liquid cone [Hartman *et al.*, 1999]

2.1.2.2 Break-up of the jet into droplets

The droplet size range after electrohydrodynamic atomisation in the cone-jet mode depends on the diameter of the jet, and on the break-up of this jet into droplets. For any given liquid there exists a minimum flow rate below which a stable cone-jet mode cannot exist. At the minimum flow rate, the jet break-up is due to axisymmertric instabilities also called 'varicose instabilities'. At higher flow rates, the current through the liquid cone increases. With increasing current, the surface charge on the jet increases. Above a certain surface charge the jet break-up will also be influenced by lateral or azimuth instabilities of the jet. These instabilities are also referred to as 'kink instabilities'. When the influence of these kink instabilities increases, the size distribution of main droplets becomes wider. These kink instabilities are sometimes also described to as a whipping motion of the jet [Cloupeau and Prunetfoch, 1989]. **Figure 2.10** shows the jet break-up modes under the effect of various instabilities where jet break-up changes from

axisymmetric to one which resembles whipping (kink instabilities). **Figure 2.11** also shows the real time images of this transition from the varicose break-up of the jet and the effect of this transition.

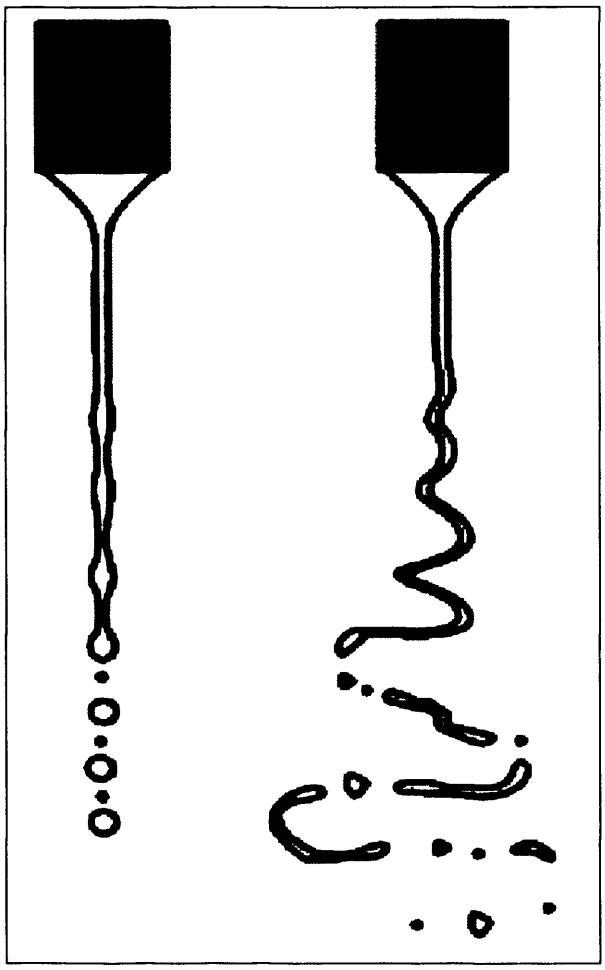

(a) (b)

Figure 2.10 Jet break-up modes. (a) the axisymmetric varicose break-up and (b) the lateral kink break-up [Hartman *et al.*, 2000]

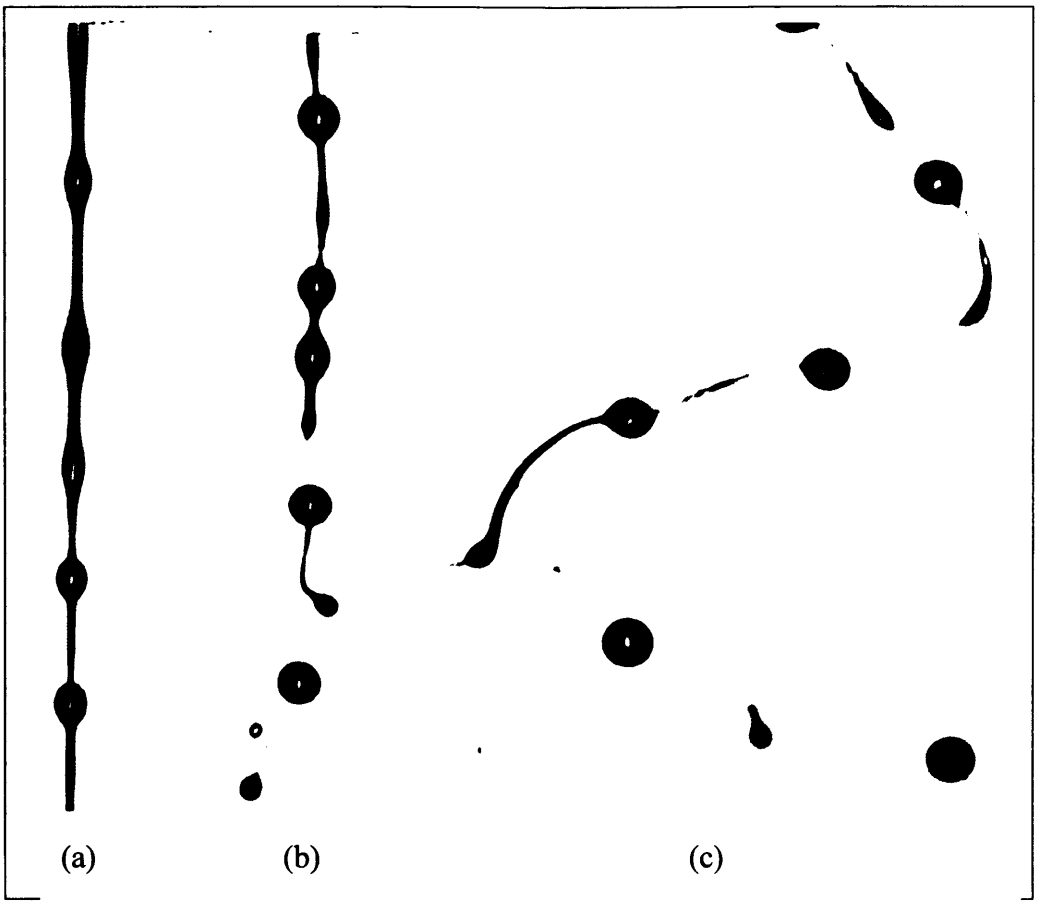

Figure 2.11 (a-c) The transition from varicose break-up toward whipping break-up [Hartman *et al.*, 2000]

2.1.2.3 Evolution of spray after droplet production

A liquid jet is unstable to surface deformations and will eventually disintegrate into droplets. Electrical interactions between the highly charged droplets with different sizes cause a 'size segregation effect' due to high mobility. Smaller droplets are found at the edge of the spray and the larger droplets in the centre of the spray [Ganan-Calvo *et al.*, 1994, Hartman *et al.*, 2000].

2.1.3 Factors influencing electrohydrodynamic atomisation

The main factors influencing the atomisation process are flow rate, applied voltage and the properties of the liquid such as its electrical conductivity, viscosity, surface tension and density. Furthermore it has been reported that the electrode configuration also effect the atomisation process.

2.1.3.1 Effect of applied voltage

The applied voltage plays an important role in electrohydrodynamic atomisation. An electric field is applied between the capillary and the ground electrode. The strength of electric field can be controlled by varying the applied voltage to the capillary. Furthermore, it has been reported in past literature that inter-electrode spacing [Sung and Lee, 2004] and the configuration of the ground electrode [Kim and Lee, 2004] can also effect the atomisation process in a relatively weaker way.

Tang and Gomez (1996) observed that the applied voltage is a key parameter in establishing the cone-jet mode. The atomisation of the liquid takes place mainly due to electrical forces produced by this field, therefore a higher applied voltage leads to a stronger atomisation effect on the liquid. Different modes of atomisation can be observed when the applied voltage is gradually increased. At lower applied voltages dripping and micro-dripping modes can be observed. When the applied voltage is further increased cone-jet and multi-jet modes can be observed [Cloupeau and Prunetfoch, 1990].

The applied voltage can also effect the production of droplets in this process. With varying applied voltages, the shape of the cone and mode of atomisation vary accordingly. Therefore the droplets produced from the liquid cone will be of different sizes. A higher applied voltage induces higher electrical field strength and stronger electric forces can cause a stronger atomisation effect. This in turn will have higher droplet production frequency with smaller droplet sizes. The shape of the cone-jet with varying applied voltages of a ceramic suspension was investigated by Jayasinghe and Edirisinghe (2004). They observed that with increasing applied voltage, the shape of the cone changes (**Figure 2.12**) and the effect this had on the droplets which were collected from the corresponding jet break up. Higher applied voltage generates smaller droplets and reduces the cone depth and the jet diameter.

Due to these reasons the applied voltage plays a very important role in investigations that are based on droplet sizes. But for different experiments, the voltage range that is required for the formation of the stable cone-jet mode will not necessarily be the same. For a given liquid and a corresponding flow rate there could be lower and upper voltage boundaries for which the cone-jet regime could be obtained. By plotting these voltage boundaries at different liquid flow rates, two limiting voltage curves can be obtained, which sets the boundary of a cone jet domain in the voltage-flow rate curve. But a quantitative description to predict the voltage required for the formation of a cone-jet mode for a given set of liquids becomes difficult and has not been published [Tang and Gomez, 1996].

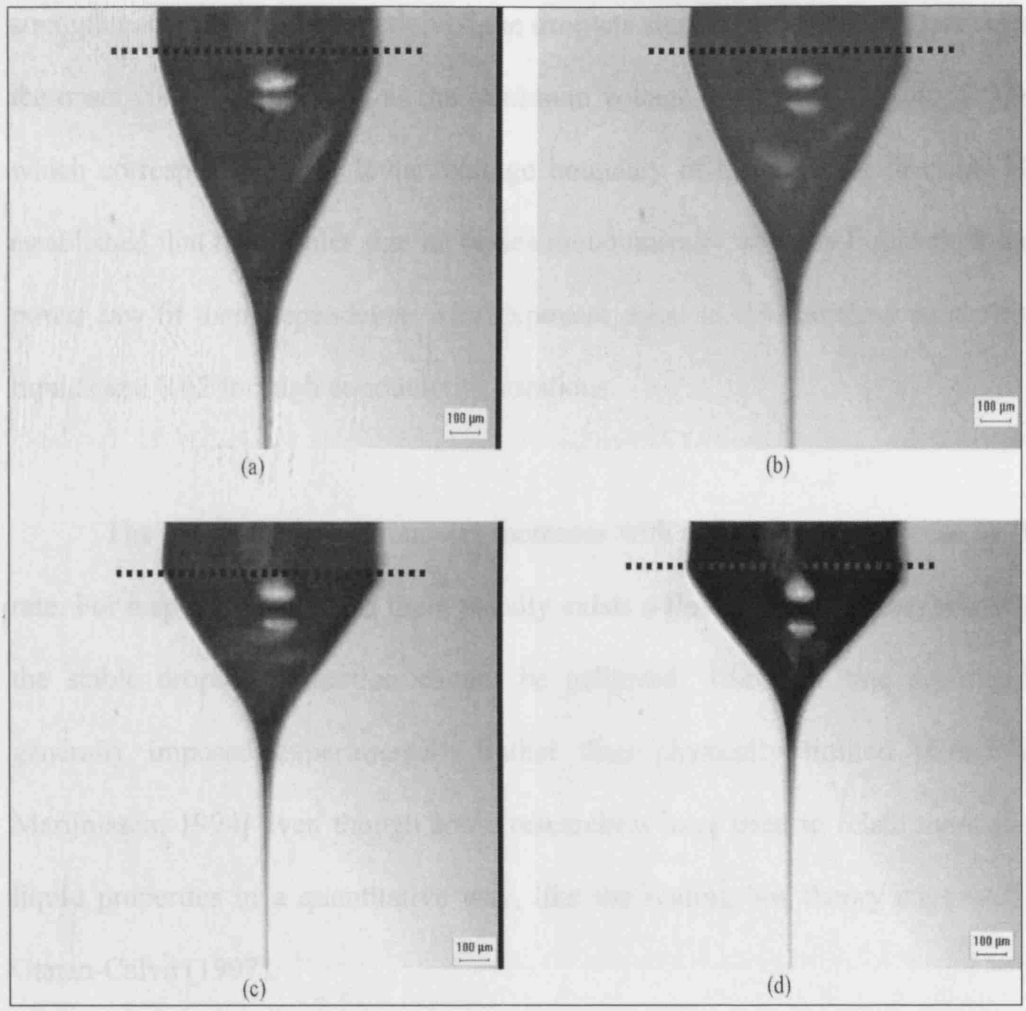

Figure 2.12 Variation in cone shape with increasing applied voltage (kV): (a) 8, (b) 9, (c) 10 and (d) 11 at a constant flow rate of 1.67 x 10^{-9} m^3s^{-1}. The dotted line represents the exit of the needle [Jayasinghe and Edirisinghe, 2004]

2.1.3.2 Effect of liquid flow rate

The flow rate is the dominant parameter controlling the droplet size of the electrospray. Droplet sizes spanning two orders of magnitude can be easily generated from the cone-jet electrospray by varying the liquid flow rate. The flow rate in the electrostatic atomisation process can be changed by changing the cross-sectional area of the capillary transporting the liquid or by changing the output of the prefusor pump [Tang and Gomez, 1996]. The flow rate and the electrical field

strength can affect the production of the droplets significantly. The authors defined the onset voltage conditions, as the minimum voltage required for a cone jet spray, which corresponds to the lower voltage boundary of the cone jet domain. They established that the droplet size increases monotonically with the liquid flow and a power law fit their dependence with exponent equal to 0.68 for low conductivity liquids and 0.62 for high conductivity solutions.

The average droplet diameter increases with simultaneous increase in flow rate. For a specific condition there usually exists a flow rate regime beyond which the stable droplet production cannot be achieved. The flow rate regimes are generally imposed experimentally rather than physically limited [Grace and Marijnissen, 1994] even though some researchers have tried to relate them to the liquid properties in a quantitative way, like the scaling law theory suggested by Ganan-Calvo (1997).

Within a stable flow rate range, electrostatic atomisation at relatively low flow rates produces finer droplets. This could be utilized for nanoparticle fabrication and mass spectrometry [Grace and Marijnissen, 1994]. With higher flow rates, the particles may become bigger, mainly due to a higher production frequency. Furthermore, the increase in flow rate can lead to an increase in polydispersity of the droplets [Higuera, 2003]. Jayasinghe and Edirisinghe (2004) investigated the effect on flow rate with respect to cone depth and jet diameter of a ceramic suspension. **Figure 2.13** shows the ceramic suspension undergoing electrohydrodynamic atomisation in the cone-jet mode at different flow rates. They

observed that the depth of the cone and the jet diameter increase with the increasing flow rate.

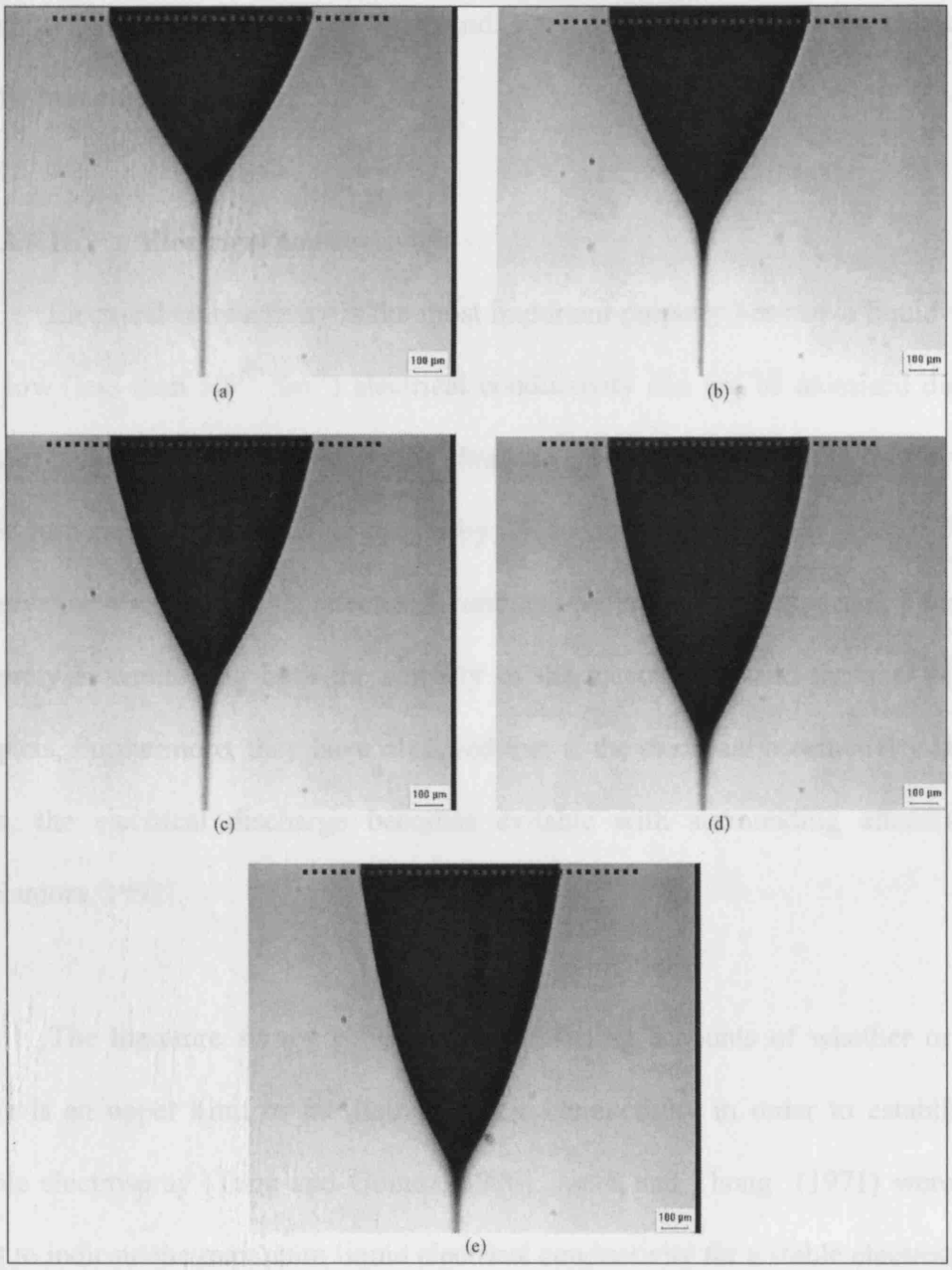

Figure 2.13 Variation in cone shape with increasing flow rate (x 10^{-9} m^3s^{-1}). (a) 2, (b) 4, (c) 6, (d) 8 and (e) 10 at a constant applied voltage of 8 kV. The dotted line represents the exit of the needle [Jayasinghe and Edirisinghe, 2004]

2.1.3.3 Influence of liquid physical properties

The main liquid properties influencing the electrohydrodynamic atomisation process are electrical conductivity, viscosity, surface tension, relative perimittivity and the density of the liquid. Each of these properties are discussed below in more detail.

2.1.3.3.1 Electrical conductivity

Electrical conductivity is the most important property because a liquid with too low (less than 10^{-10} Sm^{-1}) electrical conductivity can not be atomised due to lack of tangential stress caused by the charges. This was established as the driving force responsible for producing the jet by Cloupeau and Prunetfoch (1989). Their observation showed that the electrical conductivity is the most important physical property in controlling both the stability of the electrospray and the size of the droplets. Furthermore, they have observed that if the electrical conductivity is too high, the electrical discharge becomes evitable with surrounding atmosphere [Delamora, 1992].

The literature survey offers some conflicting accounts of whether or not there is an upper limit to the liquid electric conductivity in order to establish a stable electrospray [Tang and Gomez, 1996]. Jones and Thong (1971) were the first to indicate the maximum liquid electrical conductivity for a stable electrospray was 10^{-5} $\Omega^{-1}cm^{-1}$. Mutoh and co-workers (1979) claimed that it is impossible to establish a stable cone-jet mode for a liquid where its electrical conductivity is higher than 10^{-7} $\Omega^{-1}cm^{-1}$. A similar conclusion was also reached by Hayati and co-workers (1987a and 1987b) who reported that a stable electrospray

could be established only for semiconducting liquids, although no specific upper conductivity limit was mentioned. On the other hand Smith (1986) was the first to point out that there is no such limit exists. His opinion is supported by the fact that even stable liquid metal sprays can be established under vacuum conditions for the direct production of metal particles [Mahoney *et al.*, 1969]. Fernandez de la Mora and Loscertales (1994) showed that stable electrosprays can be established for liquid conductivities spanning a five order of magnitude range from 10^{-2} to 10^{-7} $\Omega^{-1}cm^{-1}$, with the resulting sprays producing droplets in the submicron range.

2.1.3.3.2 Viscosity

Viscosity of the liquid, which is a measure of the ease of the flowing motion of the liquid, can effect the jet formation as well as the droplet production [Ganan-Calvo, 1995]. Investigation carried out by Smith (1986) showed that increasing viscosity of the liquid, the droplet size increases dramatically. Rosell-Llompart and Fernandez de la Mora (1994) suggested that in the cone-jet mode, the effect of viscosity on droplet size is dependent on the dimensionless parameter π_η given by,

$$\pi_\eta = \frac{\sqrt[3]{\frac{\gamma^2 \rho \beta \varepsilon_0}{K}}}{\eta}$$

Where ρ is the density, ε_0 is the permittivity of vacuum, γ is the surface tension, β is the relative permittivity, K is the conductivity and η is the viscosity of the liquid. For liquids having $\pi_\eta >> 1$, viscosity has no effect but if $\pi_\eta << 1$, then

the droplet size increases with increasing viscosity and moreover, a broader size distribution of droplets occur.

Jayasinghe and Edirisinghe (2002) varied the viscosity of the liquids from 1 – 1350 mPaS and investigated the effect of viscosity on the mode of electrohydrodynamic atomisation and droplet size. From their experiments they showed that increasing viscosity helped to produce stable cone-jet mode with a smaller jet diameter. The droplets generated from the cone-jet mode increased in size with increasing viscosity and produced a wider size distribution of droplets.

2.1.3.3.3 Surface tension

Droplet production in electrohydrodynamic atomisation occurs when the electrical forces overcome the surface tension of the liquid. Surface tension of the liquid is the dragging action in the atomisation process, and it needs to overcome the electrical forces or no stable cone-jet mode will be formed. According to the experimental results obtained from Smith (1986) he concluded that the onset voltage for stable cone-jet mode spray will increase with the surface tension of the liquid. A liquid with high surface tension needs to be balanced by a high electric field, but this high electric field in turn can also result in higher polydispersity of droplets. As a result if the liquid surface tension is large enough a stable electrospray may not be established because the field requirement exceeds that of the electric breakdown in the gas surrounding the cone [Tang and Gomez, 1996].

2.1.3.3.4 Density

Density is another liquid property that influences the electrohydrodynamic process. Density of the liquid may affect the droplet production and the flow rate range for stable configuration. Density plays an important role in the acceleration processes of the liquid near the cone apex. It has been reported that the increase of the density of the liquid can reduce the minimum flow rate required for the cone-jet mode and droplet size [Hartman *et al.*, 2000].

2.1.3.4 Electrode configuration

Besides the applied voltage, liquid flow rate and liquid properties, configuration of the capillary and the ground electrodes will also influence the stability of modes undergoing electrohydrodynamic atomisation. The shape and the wettability of the capillary and the geometry of the ground electrode also play an important role which helps to enhance the stability of cone-jet mode and other modes of atomisation.

2.1.3.4.1 Effect of capillary diameter

The investigation carried out by Tang and Gomez (1996) showed the droplet diameter to be independent of the capillary diameter. They plotted a graph (**Figure 2.14**) of droplet diameter against various capillary diameters and obtained a single curve that co-related to the droplet sizes that were obtained from different capillaries. But it has been reported that the capillary size can affect the cone-jet domain of the electrospray [Cloupeau and Prunetfoch, 1989]. The maximum liquid flow rate for the cone-jet electrospray decreases dramatically as the capillary diameter increases, which means that the voltage flow rate graph for stable cone-jet

domain of the electrospray becomes smaller as the capillary size increases. Therefore, when the capillary size increases, the operational domain of the cone-jet electrospray becomes narrower.

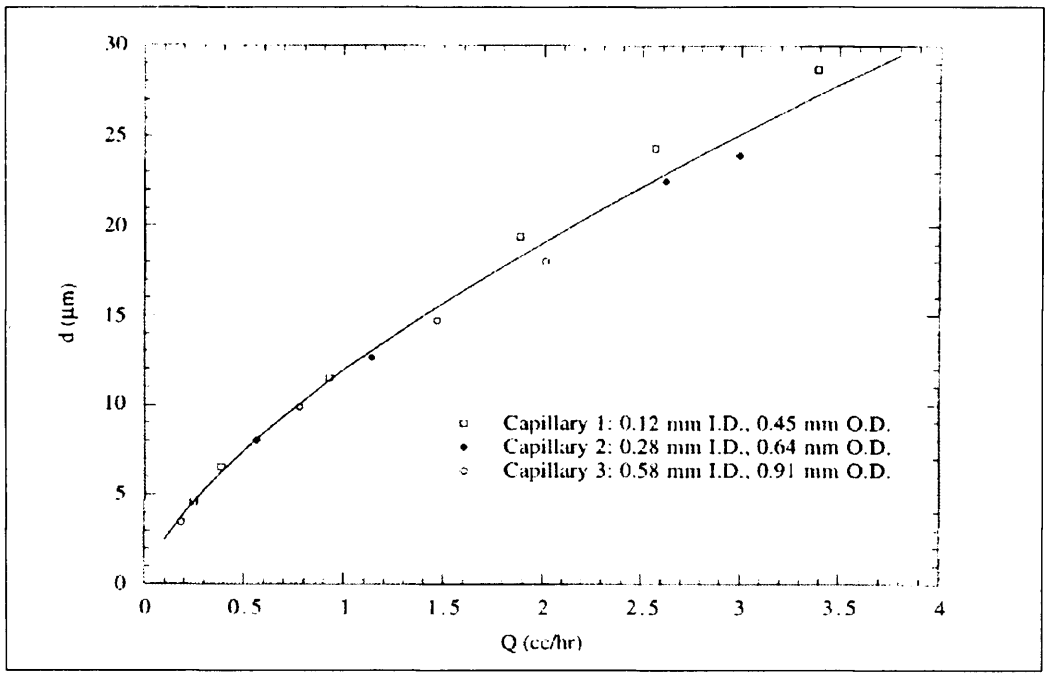

Figure 2.14 Droplet mean diameter vs liquid flow rate at the onset voltage condition for different capillary sizes [Tang and Gomez, 1996]

2.1.3.4.2 Effect of ground electrode configuration

The geometry of the ground electrode could decide the trajectory of the droplets produced from the jet disintegration. When a ring shaped ground electrode was used it produced a conical spray with large droplets segregated in the central regions and the finest droplets re-circulated above the ring [Ganan-Calvo, 1997]. **Figure 2.15** shows an electrospray set-up employing a ring shaped ground electrode that depicts the trajectory of the primary and satellite droplets ejecting from the jet break-up. The primary droplets are at the centre of the spray whereas the satellite droplets are found on the edges.

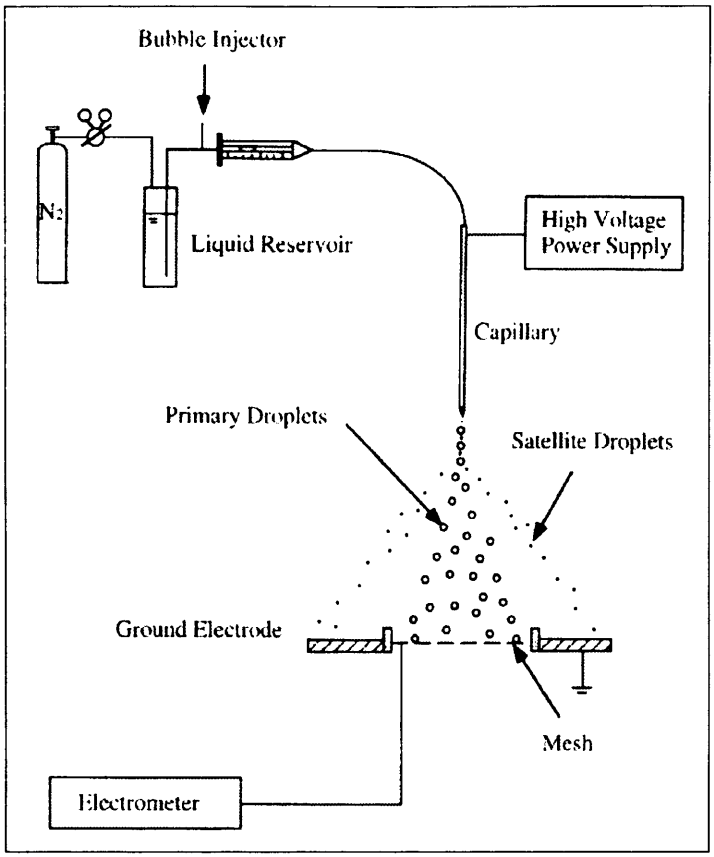

Figure 2.15 Configuration of the electrospray atomization system

Jayasinghe and Edirisinghe (2004) experimented with a point shaped ground electrode and found that most of the particles could be focused on a certain point. **Figure 2.16** shows the droplet trajectory of the droplets moving towards the point shaped electrode. This electrode configuration was used for electrostatic atomisation printing (EAP) [Jayasinghe *et al.*, 2002].

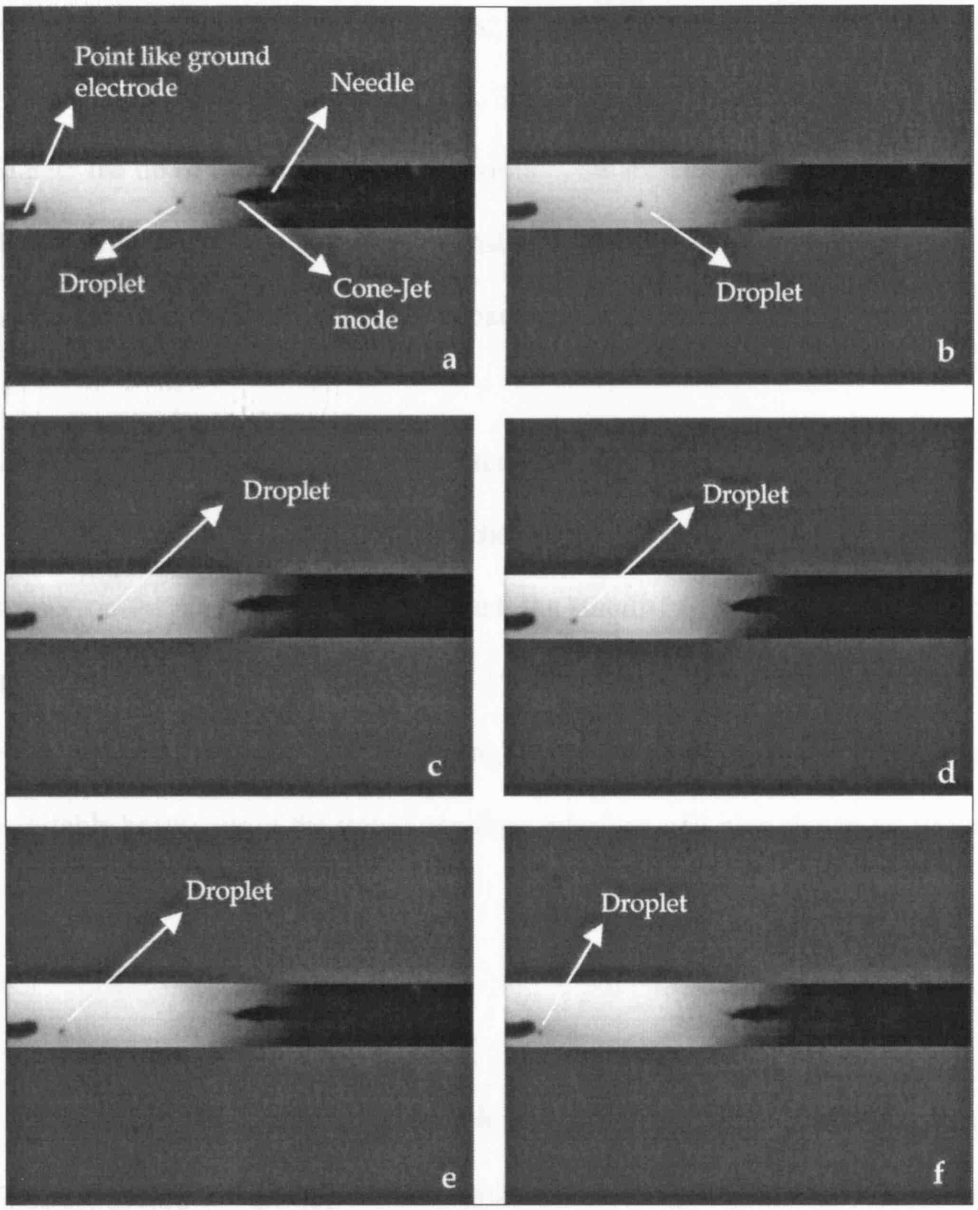

Figure 2.16 Sequence a–f shows a droplet of the suspension moving from the exit of the needle and towards the point-like ground electrode [Jayasinghe and Edirisinghe, 2004]

2.1.3.4.3 Distance between the capillary and ground electrode

The voltage limits for the various stability regimes are higher when the distance between the capillary and ground electrode spacing is larger. This is due to the strength of the electric field governed by the ratio of the applied voltage to the spacing between the electrodes. Noymer and Garel (2000) stated that the

relationship is not linear; in other words, the voltage limit does not double as the tip–to–ground electrode spacing doubles. This is due to the intensity of the electric field near the tip of the capillary which controls the nature of the liquid discharged, and the dominant dimension for the intensity of the field near the tip is the capillary diameter rather than the tip–to–ground spacing.

2.1.3.4.4 Capillary shape and material wettability

The shape of the capillary and the wettability of the material has a large influence on the shape of the cone formed, the stability of the jet and the mode of atomisation [Cloupeau and Prunetfoch, 1994]. At the base of the cone near the capillary exit, the shape of the cone strongly depends on the shape of the capillary. An unstable behaviour at the liquid capillary interface will give rise to an unstable jet.

2.1.4 Electrospinning

Electrospinning provides a simple and versatile method for generation of ultra thin fibres from a high viscous polymeric solution. One-dimensional (1D) nanostructures have been studied extensively by many researchers due to their unique properties and exciting applications in many areas [Xia *et al.*, 2003]. 1D nanostructures in the form of fibres, wires, rods, belts, tubes, spirals and rings from various materials have been explored and demonstrated using large numbers of synthetic and fabrication methods [Hu *et al.*, 1999]. Among these methods, electrospinning, which is based on electrostatic interactions, provides the simplest approach for fabrication of nano fibres with both solid and hollow interiors that are uniform in diameter, diversified in composition and exceptionally long in length

[Reneker and Chun, 1996, Huang *et al.*, 2003]. In electrospinning the formation of ultra thin fibres is based on the uniaxial stretching of a viscoelastic jet derived from a polymer solution or melt. The electrospinning technique may be considered as a variation of the electrospraying process [Hull *et al.*, 1997, Loscertales *et al.*, 2002]. Both electrospinning and electrospraying techniques use an electric field to induce the formation of a liquid jet. In electrospraying, small droplets or particles are formed due to varicose instabilities of the electrified jet which are often present in a solution of low viscosity. But in electrospinning, a solid fibre is generated as the electrified jet which is composed of a highly viscous polymer solution is continuously stretched due to the electrostatic repulsions between the surface charges and the evaporation of the solvent.

The first patent that described the electrospinning process was published in 1934, when Formalas revealed an apparatus for producing polymer filaments by taking advantage of the electrostatic repulsions between surface charges [Li and Xia, 2004]. From 1934 – 1944, Formalas published a series of patents describing the experimental setup for the production of polymeric fibres using an electrostatic force. In his experiments, cellulose acetate was introduced into the electric field. The polymer fibres were formed, from the solution, between the electrodes bearing electrical charges of opposite polarity. The potential difference depended on the properties of the spinning solution, such as molecular weight and viscosity. When the distance between the capillary and the collecting device was short, spun fibres tended to stick to the collecting device as well as to each other, due to incomplete solvent evaporation [Huang *et al.*, 2003].

In 1966, Simons patented an apparatus for the production of a non-woven fabric ultra thin and light in weight with different patterns, with the help of fibres produced by electrospinning. In his experiments, the positive electrode was immersed into the polymeric solution and the negative electrode was connected to a belt where the non-woven fabric was collected. Furthermore, he reported that the fibres from low viscosity solutions tended to be shorter and finer, whereas those from more viscous solutions were relatively continuous [Huang *et al.*, 2003].

Baumgarten (1971) made an apparatus to electrospin acrylic fibres with diameters in the range of 0.05 – 1.1 μm. The polymeric solution was forced through a metallic capillary at a controlled rate. A high voltage DC current was connected to the metallic capillary. When the applied voltage was raised, fibres were produced at the exit of the capillary and collected on a grounded metal screen.

Up until 1993, this technique was known as "electrostatic spinning", and there were only a few publications dealing with its use in the fabrication of thin fibres [Baumgarten, 1971, Larrondo and Manley, 1981a, Larrondo and Manley, 1981b, Larrondo and Manley, 1981c]. In the 1990s, several research groups particularly Reneker group at the University of Akron, revived interest in this technique by demonstrating the fabrication of thin fibres from a broad range of organic polymers. At this time the term "electrospinning" was introduced and is now widely used in literature [Huang *et al.*, 2003, Reneker and Chun, 1996, Doshi and Reneker, 1995]. The electrospinning process, especially in recent years has attracted a great deal of interest in nanotechnology, as ultra fine fibres or fibrous

structures of various polymers with diameters down to a few ten's of nanometers can be easily fabricated with this process.

2.1.4.1 Basic setup for electrospinning

Figure 2.17 shows a schematic illustration of the basic set-up for electrospinning. It consists of the main components such as a high voltage power supply, a metallic capillary (spinneret) and a collector (a grounded conductor). In the electrospinning process, direct current power supplies (DC) are used widely although the use of alternating current (AC) potential is also feasible [Kessick *et al.*, 2004]. The metal capillary or the spinneret is connected to a syringe which holds the polymer solution or melt. With the use of a syringe pump, the solution can be fed through the metal capillary at a controlled rate. When the voltage (usually in the range of 1 – 30 kV) is applied, the pendent drop of polymer solution at the exit of the capillary will become highly electrified and the induced charges are evenly distributed over the surface. As a result, the droplet at the exit of the capillary will experience two major types of electrostatic forces: the electrostatic repulsion between the surface charges; and the columbic force exerted by the external electric field. Due to these electrostatic interactions the liquid drop will be distorted into a conical object commonly known as the Taylor cone [Reneker and Chun, 1996, Huang *et al.*, 2003]. Once the electric field strength has exceeded the threshold value, the electrostatic forces can overcome the surface tension of the polymer solution and thus force the ejection of a liquid jet from the nozzle. This electrified jet then undergoes a stretching and whipping process leading to the formation of a long and thin thread. As the liquid jet is continuously elongated and the solvent is evaporated, its diameter can be greatly reduced from hundreds of

micrometers to as small as tens of nanometers. These charged threads / fibres can be collected on the grounded collector placed under the capillary which lay randomly along the collector.

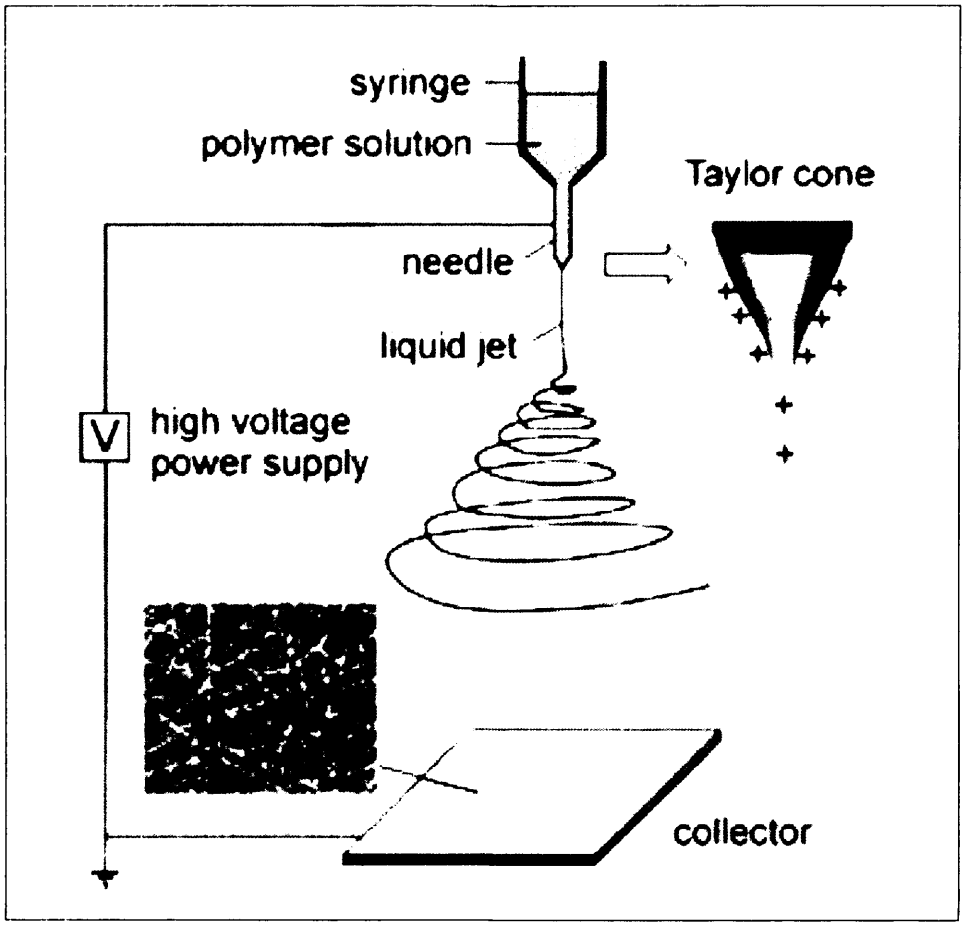

Figure 2.17 Schematic illustration of the basic setup for electrospinning. The insert show a drawing of the electrified Taylor cone and a typical SEM image of the non-woven mat of PVP nanofibres deposited on the collector [Li and Xia, 2004]

2.1.4.2 How electrospinning works

Although the set-up for electrospinning is extremely simple, the spinning mechanism is rather complicated. As in electrospraying, electrospinning also involves complex electro-fluid mechanical issues. Before 1999, the formation of fibres by electrospinning was ascribed to the splitting or splaying of the electrified jet as a result of repulsion between surface charges [Reneker and Chun, 1996]. Recently experimental observations have demonstrated that the thinning of a jet during the electrospinning process is mainly due to the bending instabilities associated with the electrified jet [Yarin *et al.*, 2001]. **Figure 2.18** shows the photograph of a spinning jet [Shin *et al.*, 2001]. From the image, it is very obvious that the jet was initially a straight line and then it becomes unstable. It appears that the cone shaped instability region is composed of multiple jets. However, closer examination using high-speed photography (**Figure 2.18b**) shows that the conical envelope contains only a single, rapidly bending or whipping thread. In some cases splaying of the electrified jet might also be observed though it was never a dominant process during spinning. Due to the frequency of the whipping process being so high conventional photography cannot properly resolve it, giving the impression that the original liquid jet splits into multiple branches as it moves towards the collector.

Based on the experimental observations and electrohydrodynamic theories, mathematical models have been developed by several groups to investigate the electrospinning process. Reneker and co-workers (2000) treated the charged liquid jet as a system of connected, viscoelastic dumbbells and provided a good analysis for the formation of bending instabilities [Yarin *et al.*, 2001]. They also calculated

the three-dimensional trajectory for the jet and the computed results were in agreement with the experimental data. Fridrikh and co-workers (2003) considered the jet as a long, slender object and thereby developed a different model to account for the electrospinning phenomenon. Their theoretical and experimental studies clearly showed that the spinning process only involves whipping of a liquid jet. The whipping instabilities are mainly caused by the electrostatic interactions between the external electric field and the surface charges on the jet. The formation of fibres with fine diameters is mainly achieved by the stretching and acceleration of the fluid filament in the instability region. Feng (2002 and 2003) proposed another model to describe the motion of a highly charged liquid jet in an electric field and the role of non-linear rheology in the stretching of an electrified jet was also examined. All these studies provide a better understanding of the mechanism responsible for electrostatic spinning process.

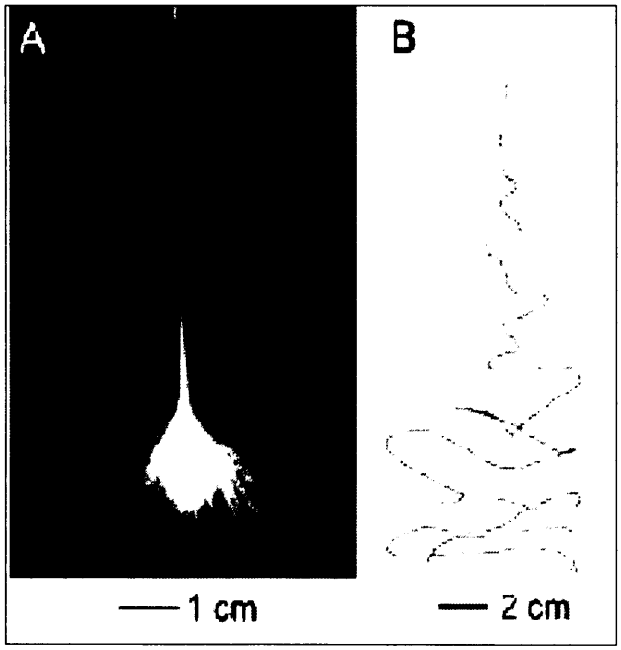

Figure 2.18 High-speed photograph illustrating the instability region of a liquid jet. a) 1/250s and b) 24ns [Shin *et al.*, 2001]

2.1.4.3 Some remarkable features in fibres

Electrospun fibres exhibit a range of unique properties and features that distinguish themselves from 1D nanostructures fabricated using different techniques. For example, electrospun fibres are highly charged and therefore it is possible to control its trajectory electrostatically by applying an electric field.

2.1.4.3.1 Extreme long length

Electrospun fibres are extremely long in length when compared with other 1D nanostructures synthesized or fabricated using other chemical or physical methods. Because electrospinning is a continuous process the fibres could be as long as several kilometres. In the electrospinning process, these fibres can be assembled into a three-dimensional, non woven mat as a result of bending instability of the spinning jet. Such a porous mat can be immediately used for various applications. The position and special orientation of an individual fibre can be easily controlled by moving around the collector. Since the collector is a macroscopic object, the manipulation of individual fibres could be done even without the use of a microscope. Powlowski and co-workers (2003) demonstrated that lightweight wing skins for micro-air vehicle could be directly formed by electrospinning polymer fibres on a wing frame. Li and co-workers (2004b) demonstrated that individual fibres with several millimetres to centimetres long could be manipulated individually using a collector containing a void gap (e.g., metallic tweezers).

2.1.4.3.2 High surface area and complex pore structure

When compared with the fibres produced from conventional mechanical extrusion or spinning process, electrospun fibres are much thinner in diameter and thus higher in surface-to-volume ratio. A high density of pores can also be formed as a result of entanglement of fibres. Although the specific surface area of electrospun fibres is lower than in mesoporous materials the pores in an electrospun, non-woven mat are relatively large in size and all pores are interconnected to form a three-dimensional network. Hence, the entire surface is fully accessible to chemical species. In addition, surface areas of fibres could be further increased through the formation of much smaller pores in the surface of each individual fibre by controlling the solutions physical properties and parameters for electrospinning [Li and Xia, 2004].

2.1.4.4 Factors influencing electrospinning

Many parameters can affect the electrospinning process which transforms the polymer solution into fibres under the influence of an electric field. These parameters include (a) solution properties such as viscosity, electrical conductivity, surface tension and elasticity, (b) governing variables such as hydrostatic pressure in the capillary tube, electric potential at the tip of capillary and the distance between the capillary exit and ground electrode, and (c) ambient parameters such as solution temperature, humidity and air velocity in the electrospinning chamber [Doshi and Reneker, 1995].

Several researchers have investigated the spinnibility of different polymers. For example, Fong and co-workers (1999) found out that electrospinning of

aqueous poly(ethylene oxide) (PEO) dissolved in ethanol-to-water solutions that viscosities in the range of 1 – 20 poise and surface tension between 35 to 55 dynes/cm were suitable for fibre formation. At viscosities above 20 poise, electrospinning was not possible because of the instability of flow caused by the high cohesiveness of the solution. When the viscosity was less than 1 poises, the liquid jet breaks into droplets. Haiqing Lui and Hsieh (2002) used cellulose acetate (CA) solution and identified that viscosities between 1.2 and 10.2 poise were suitable for the production of fibres. Outside this range, the CA solution could not be electrospun. When the viscosity is increased further few fibres could be obtained and when the viscosity is less, the jet breaks into droplets. From these experimental investigations, the viscosity range of a given polymer solution which is spinnable is different. As long as the polymer solution can be electrospun into fibres the ideal targets would be in that: (1) the diameters of the fibre to be consistent and controllable, (2) the fibre surface to be defect free and (3) continuous single fibres be collectable [Huang *et al.*, 2003].

One of the most important qualities related to fibres produced by electrospinning is the fibre diameter. Since the fibres are the result from evaporation of solvent or solidification of polymer fluid jets, the fibre diameter mainly depends on the jet size and the concentration of polymer contents in the jet. A higher viscosity results in a larger fibre diameter. Another parameter which affects the fibre diameter is applied voltage. Experiments carried out by Demir and co-workers (2002) showed that, in electrospinning of polyurethane, with increasing applied voltage the diameter of the jet increased and hence the resulting fibre

diameters were also increased. In general, a higher applied voltage ejects more fluid in a jet, resulting in a larger fibre diameter.

Defects such as beads and pores formation in fibres is another common problem in electrospinning. It has been found out that concentration of the polymer also affect the formation of beads. Experiments carried out by Fong and co-workers (1999) found out that when the concentration of the polymer is higher fewer beads were present on the fibres. Furthermore it has been reported in the past literature that addition of some filler materials into a polymer solution can also result in fibres free from beads or pores. Experiments carried out by Zong and co-workers (2002) reported that by adding 1 wt.% of salt to a biodegradable PLDA polymer solution will result in bead-free fibres.

2.1.4.5 Co-axial electrospinning

Recently, with the emergence of co-axial jets for encapsulating liquids, electrospinning has found an alternate route to design new functionalized composite fibres with core-shell structures or hollow interiors. With co-axial electrospinning, two components can be co-axially and simultaneously electrospun through different feeding capillaries to generate composite fibres in the form of core-shell structure shown in **Figure 2.19**. The conventional method of producing fibres by electrospinning consists of a metallic capillary (spinneret), a syringe pump, a high voltage power supply and a grounded collector. By replacing the single capillary with a co-axial spinneret core-sheath and hallow fibres can be fabricated.

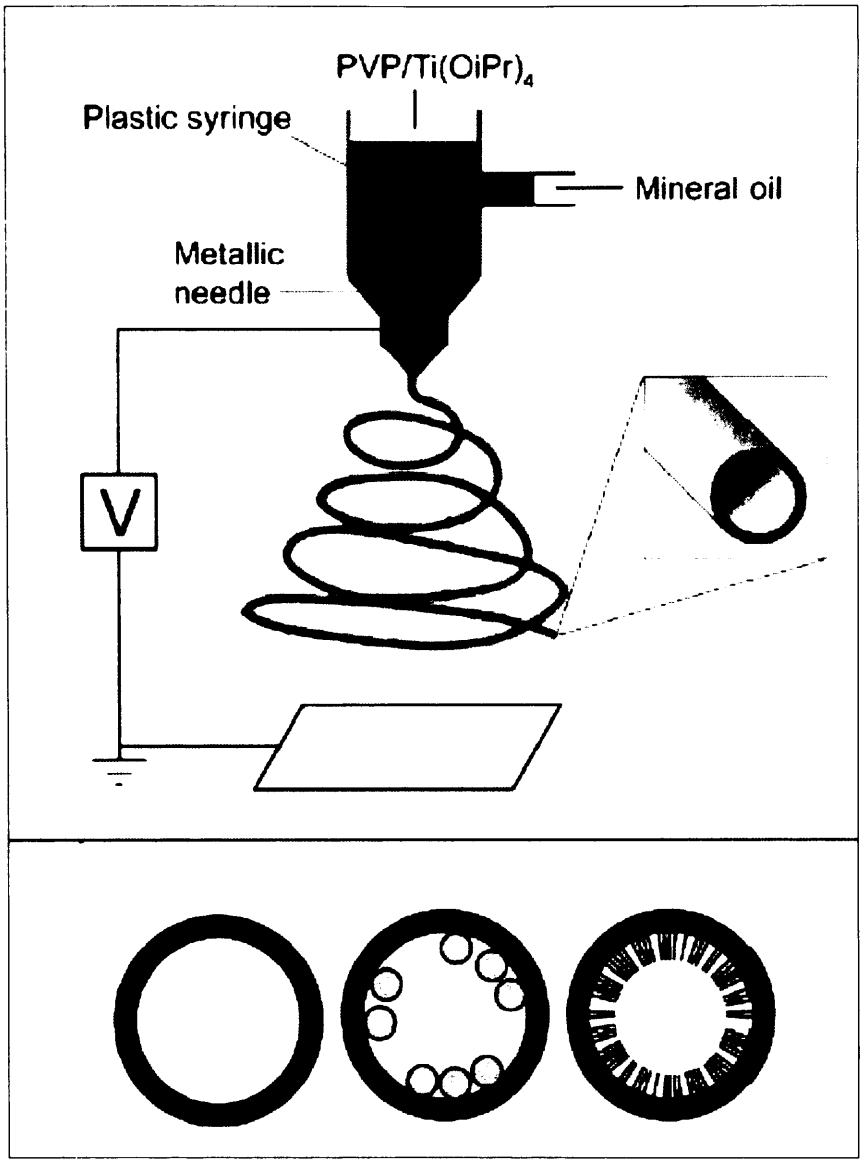

Figure 2.19 Schematic diagram for fabrication of core-sheath fibres with co-axial spinneret. The mineral oil is fed through the capillary and outer sheath contain sol gel precursor. After removal of oil core hollow fibres are generated [McCann *et al.*, 2005]

2.1.4.5.1 Encapsulation of metal particles

Metal structures having diverse geometries such as spheres, wires and hollow architectures have received extensive attention owing to their innumerable applications [Li *et al.*, 2004a], especially in the development of biological sensors and optoelectronic devices [Hickman *et al.*, 1991, Gomez-Romero, 2001, Willner

and Willner, 2001]. Recently considerable research interest has developed in the area of synthesis and organic functionalization of different sizes and shapes of metal particles [Kamat, 2002]. In particular, wires consisting of metal particles have been the focus of many recent investigations due to their potential use as active components for interconnects. These interconnects are utilized in fabricating electronic, photonic, and sensing devices but on the other hand it has also been demonstrated that these metallic wires are very sensitive to air and moisture and can result in the degradation in performance of devices they are incorporated in [Chen *et al.*, 2005].

A polymer could also be used to act as an envelope and this would protect metal wires from oxidation and corrosion which in turn could improve the performance over a long period of time. Materials arranged in the core of a sheath are considered as a new type of one-dimensional structure and have been observed to improve their functions [Xia *et al.*, 2003], e.g. co-axial cables. There are different methods to obtain a metal-polymer composite and these could be classified broadly as two different approaches [Corbierre *et al.*, 2001]. The first consists of an in-situ preparation of the particles in the matrix. This is effected either by the reduction of metal salts dissolved in the polymer matrix [Mayer, 1998] or by the evaporation of metals on the heated polymer surface. The second involves polymerizing the matrix around the metal particles [Lee *et al.*, 2000]. Although these methods lead to uniform metal encapsulation and coatings, they do not yield dense packing of metal particles [Corbierre *et al.*, 2001].

In recent years metal nanoparticles, particularly gold and silver have attracted a lot of interest from the scientific community due to their unique properties at nanoscale. The control organisation of these metal nanoparticles into ordered structures have been explored in recent years. Obtaining a structured organisation of a metal particle in the core and polymer as a coat has increased application potential in the areas of electronics, photonics and magnetics [Zhang *et al.*, 2006]. The advantages of encapsulating a metal in core shell assemblies are as follows.

- A metal coated with a polymer or dielectric layer prevents it external physical damage or chemical changes.
- The outer layer could prevent the metal particles from coming in contact with each other thereby resulting in optical losses.
- The contrast in properties between the core and polymer layer could help produce new properties.

2.2 Nanoparticle history and background

Nanotechnology, nanoscience, nanostructures, nanoparticles...etc are some of the most widely used terms in material science literature. Nanotechnology can be defined as the engineering of functional systems at the molecular scale. From the point of view of general public, the term nanotechnology appears to be the fabrication of miniature machines, which are able to travel through the human body to repair damage tissues or supercomputers small enough to fit into a shirt pocket. However, nanostructured materials have potential applications, such as biological detection in drug delivery, low threshold lasers, optical filters, and sensors, among others [Liz-Marzan, 2004].

The use of nanoparticles have been used in the decorative pigments since the time of Romans, such as those contained in the glass of the famous Lycurgus Cup (4th Century AD). The cup still can be seen at the British Museum and possesses the unique feature of changing colour depending on the light which it is viewed with. It appears red when the light is shone from inside and transmitted through the glass and looks green when viewed in reflected light. Investigations carried out on the glass later revealed that it contains very small amounts of metal crystals (~70 nm) containing gold and silver in an approximate molar ration of 14:1, hence it gives the Lycurgus Cup its special colour display [Liz-Marzan, 2004].

Faraday (1857) made an important break through in this field by reporting a systematic study of the synthesis and colour variations of colloidal gold. He reported the formation of deep-red solutions of colloidal gold by reduction of an aqueous solution of chloroaurate ($AuCl_4^-$) using phosphorus in CS_2. Thin films were prepared from the dried colloidal solution and he investigated the optical properties of the films. He observed the reversible colour changes of the films when subjected to mechanical compression [Daniel and Astruc, 2004]. Since then, thousands of scientific papers have been published on the synthesis, modifications, properties and assembly of metal nanoparticles using a wide variety of solvents and other substrates.

2.2.1 Some remarkable properties

Nanoparticles have attracted a lot of interest from the scientific community, as they effectively form a bridge between bulk materials and atomic or molecular

structures. A bulk material will have constant physical properties regardless of its size or shape. But with nanoparticles this is often not the case. The transition from bulk material to nanoparticles can lead to a number of changes in the physical properties. The main factors in this transition are the increase in surface area to volume ratio and the size of the particle into the realm where quantum effects predominate. The increase in the surface area to volume in a gradual process as the particles gets smaller. When the particle size gets smaller it leads to an increasing dominance of the behaviour of the atoms on the surface of a particle over that of those in the interior of the particle. This affects the properties of the particle in isolation and its interaction with other materials. High surface area is an important factor in the performance of catalysis and structures such as electrodes, allowing improvement in performance of such technologies as fuel cells and batteries. Due to the large surface area of nanoparticles, interactions between intermixed materials in nanocomposites leads to special properties such as increased strength and/or increased chemical / heat resistance. For example, silicon nanospheres, with diameters of 40 nm and 100 nm were not only harder than bulk silicon but are among the hardest materials known, falling between sapphire and diamond [National Science Foundation (2003, March 21)].

Nanoparticles have dimensions below the critical wavelength of light making them transparent, a property which makes them very useful for applications in packaging, cosmetics and coatings. One of the most important aspects of metal nanoparticles is that their optical properties. The optical properties depend mainly on the particle size and shape. For example, bulk gold looks yellowish in reflected light, but thin gold films looks blue in transmission light. But this blue colour

steadily changes into orange as the particle size is reduced to ~3 nm [Liz-Marzan, 2004].

Another important property of metal nanoparticles are their ability to merge into a solid without melting (a process called sintering) at lower temperatures than for larger particles. This leads to improved and easier to create coatings, particularly in electronic applications such as conducting wires and capacitors. For example, bulk gold melts at 1064 °C whereas a 5 nm diameter gold particle would be molten at about 830 °C and particles of about 2 nm diameter would liquefy at 350 °C [Cortie, 2004]. Like metallic nanoparticles, ceramic nanoparticles can also be formed into coatings and bulk materials at low temperatures reducing manufacturing costs. Superconducting wires have also been fabricated using ceramic nanoparticles, creating a material that is relatively flexible where traditional ceramic materials are far too brittle.

2.3 Different techniques used for fabricating gold films

2.3.1 Surface vertical deposition

Surface vertical deposition (SVD) is a relatively new fabricating technique which was reported by Diao and co-workers (2003). The gold nanoparticles in the solid-liquid-gas junction of the suspension grow on the substrate by the interface force between the substrate and metal suspension when the suspension surface descends. In this technique the density of the gold film mainly depends on the surface property of the substrate, the solvent of suspension, velocity of surface's descent and the concentration of the metal suspension.

Figure 2.20 shows a schematic diagram of the SVD process. The solid-liquid-gas junction in region A mainly depends on the surface tension of the suspension. The surface tension plays an important role in SVD process because the metal nanoparticles localized in region A to form the thin film. The main advantage of this process is the simplicity in making films and does not require expensive equipment. The disadvantages are the film fabrication process mainly depends on the substrates wettability, the solvent used in the suspension and the metal concentration of the solution.

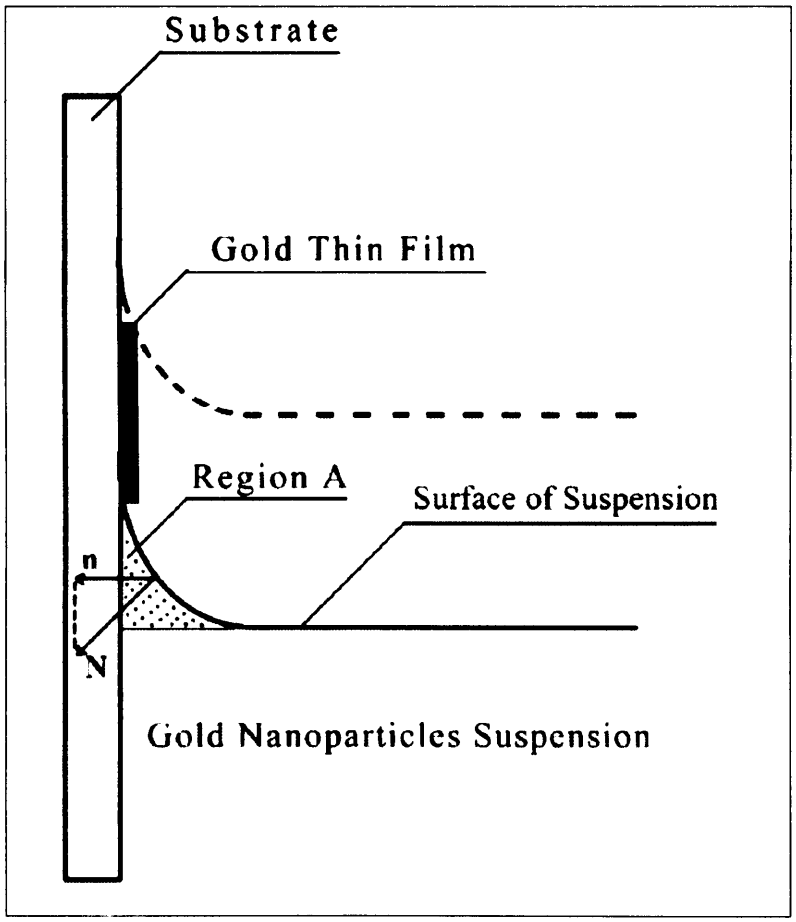

Figure 2.20 Schematic diagram of SVD process [Diao *et al.*, 2003]

2.3.2 Colloidal crystal templating method

Tessier and co-workers (2001) reported two new methods for forming thin porous metallic films by directly coating a substrate with a mixture of metallic and latex particles. In their experiments they used gold nanoparticles to demonstrate these methods. When the substrate is coated with the mixture and left for drying, it forms an ordered gold structure templated by latex particles. **Figure 2.21** shows a schematic diagram of these methods.

The first step in the assembling process is the arranging of latex particles into 2D crystals. They introduced two methods for forming such structures. In the first method, gold and latex mixture was dispersed in the angle between the two glass slides (**Figure 2.21a**). A mechanical device was used in order to move the glass slide at a controlled speed. The meniscus was dragged along the bottom plate and the deposited thin film of gold and latex particles dried at ambient conditions.

In the second method (**Figure 2.21b**), a static cell was used to fabricate the gold and latex film. When the gold and latex particles were placed in the circular cell chamber, a concave meniscus formed. The crystal nucleated in the centre of the chamber and grew radically outward completely filling the chamber after evaporation of the solvent at ambient conditions.

Figure 2.21c demonstrates the likely course of development of the film during evaporation of the solvent. In both methods, the latex particles are arranged into a multilayer 2D crystal by a combination of an increase in the particle volume fraction in the film and due to convective assembly. With evaporation, the

concentration of the latex particles increase, hence it produces an order structure first due to higher volume fraction. As the evaporation continues, the gold nanoparticles are concentrated around the latex particles forming a solid network. After evaporation the dried structures were immersed in toluene to fabricate gold porous films. In this technique the thickness of the deposited film and the resulting gold structure were controlled by the concentration of the latex and the speed of deposition. Colloidal crystal templating method is a simple technique which does not require any expensive equipment to fabricate metal films. The main disadvantage of this technique is the quality of the films mainly depends on the concentration of latex and metal particles in the solution and the evaporation of the solvent.

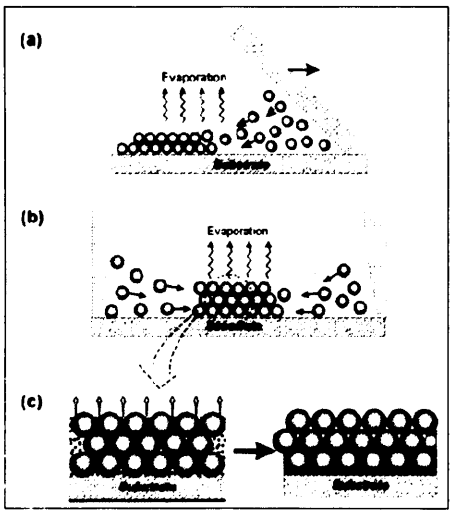

Figure 2.21 Schematic diagrams of the formation of structured gold films by the template-directed assembly of gold particles by colloidal crystals. a) Directional deposition of a latex/gold crystal at the trailing edge of a moving meniscus. b) Radial growth of a latex/gold crystal in an enclosed cell. c) Enlarged view of the crystallizing region in (a) and (b) where the gold particles are concentrated at the drying front and consequently compacted due to solvent evaporation [Tessier *et al.*, 2001]

2.3.3 Thermal evaporation technique

The thermal evaporation technique is another method of fabricating gold thin films. The deposition of materials are carried out in a vacuum chamber. In this process the material to be deposited is heated until evaporation. The material vapour finally condenses in a form of a thin film on the cold substrate surface and on the vacuum chamber walls. Normally the film fabrication process is carried out in relatively low pressures (10^{-6} – 10^{-5} Torr) to avoid any reactions between the vapour and the atmosphere. At these low pressures, the mean free path of vapour atoms are in the same order as the vacuum chamber dimensions, so these particles travel in straight lines from the evaporation source towards the substrate. In thermal evaporation techniques, different methods can be used to apply heat to the material. The material can be heated using either resistance heating (Joule effect) or bombardment with high energy electron beam, usually several KeV, from an electron gun (electron beam heating). **Figure 2.22** shows schematic diagrams of both methods of thermal evaporation techniques.

George and Glaunsinger (1994) fabricated gold thin films using ultra high vacuum (UHV) electron-beam evaporation. Films of controlled thickness were produced using a quartz crystal oscillator. Film thicknesses were varied from 40 – 180 nm with a deposition rate of 5 $Å s^{-1}$. They used different substrates such as alumina, silica and mica to deposit thin films and were examined as a function of film thickness, substrate, structure and mercury adsorption.

Varguez and co-workers (2008) fabricated gold films and tested the mechanical properties deposited on a polymer. Gold films in the range of

50 – 300 nm were deposited on polypropylene substrates using thermal evaporation inside a vacuum chamber at 3 x 10^{-5} Torr. They used high purity gold pieces to fabricate gold films at a deposition rate of 0.5 nm / s.

The initial setup cost is very high when compared with other film deposition methods. The main advantage of this process is the ability to control the evaporation rate thus fabricating fine films on substrate. Apart from the high set-up cost this technique is lot easier to use and there are only few precautions to be taken to avoid contamination when the system is opened or serviced.

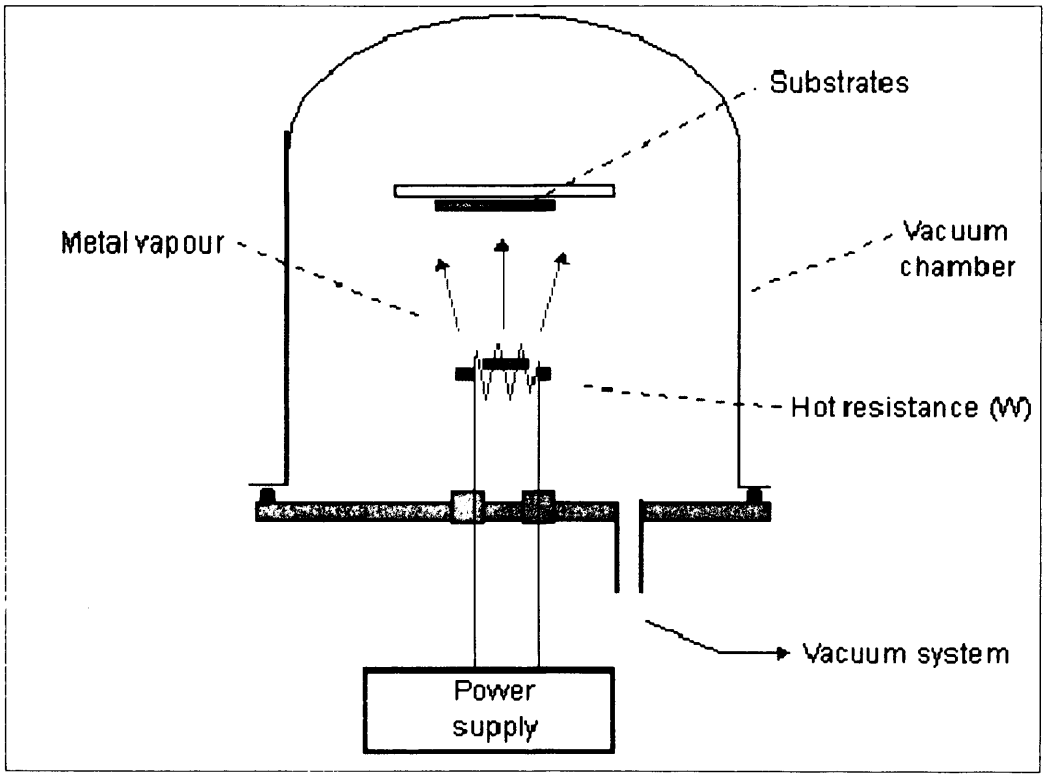

(a)

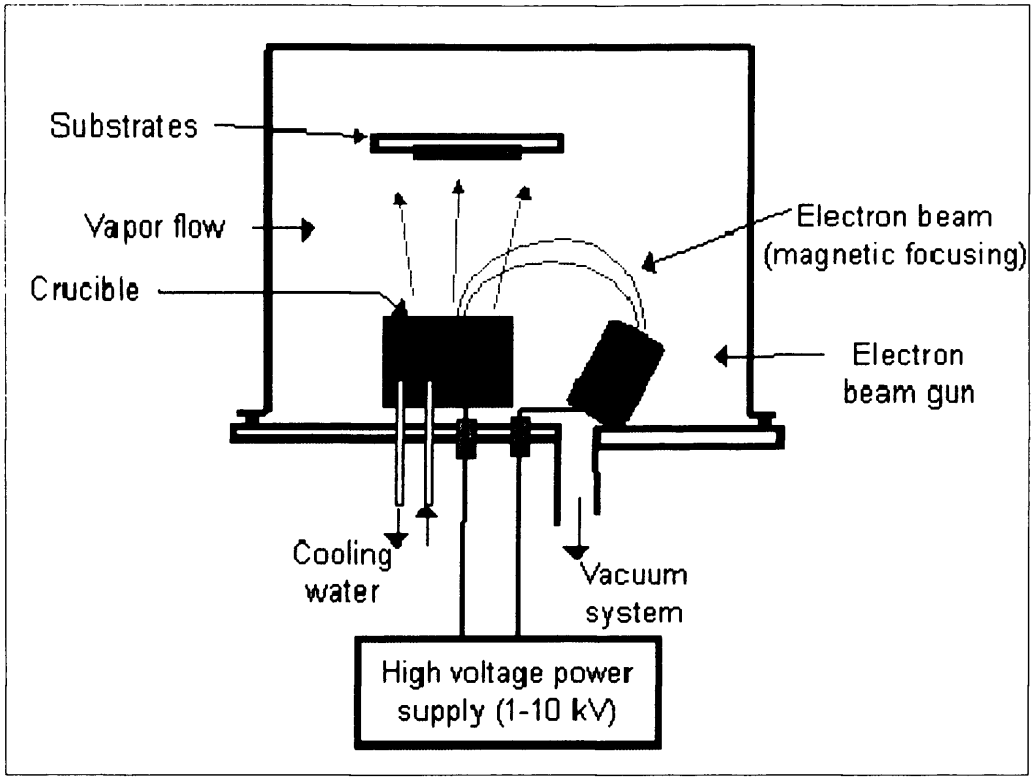

(b)

Figure 2.22 Schematic diagrams of a) resistance heating b) electron gun evaporators

2.3.4 Electrophoretic deposition

The electrophoretic deposition (EPD) technique with a wide range of novel application in processing of materials and coatings, has recently gained tremendous interest because of the high versatility of its use with different materials and their combinations but also of its cost-effectiveness requiring simple apparatus. In EPD, charged powder particles, dispersed or suspended in a liquid medium are attracted and deposited onto a conducting substrate of opposite charge on application of a DC electric field. There can be two types of EPD depending on which electrode the deposition occurs. When the particles are positively charged, the deposition happens on the cathode and the process is called cathodic electrophoretic deposition. The deposition of negatively charged particles on positive electrode

(anode) is termed as anodic electrophoretic deposition. By suitable modification of the surface charge on the particles, any of the two mode of deposition is possible. **Figure 2.23** presents a schematic diagram of the two electrophoretic deposition process [Besra *et al.*, 2007].

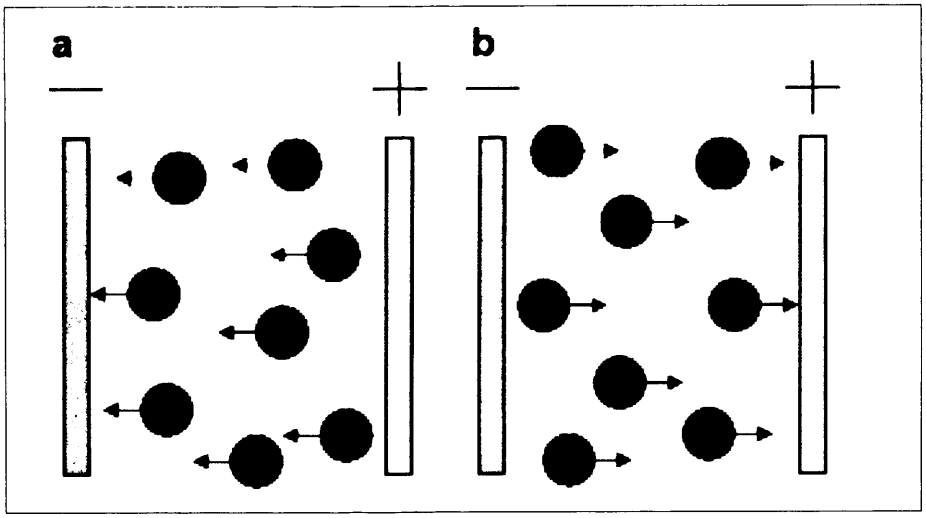

Figure 2.23 Schematic diagram of EPD process. a) Cathodic EPD and b) anodic EPD [Besra *et al.*, 2007]

EPD of silver particles has been investigated as a process to form electrode layer for electroceramic applications. Silver particles having an average diameter of 10 nms were dispersed in non-aqueous suspensions and deposited with excellent control of both surface roughness and particle packing. These deposits were then sintered to obtaining dense homogeneous films [Ogata *et al.*, 2001]. In a more recent publication, the same group demonstrated that electrically conducting layers can be formed by EPD of metallic nanoparticles at an average thickness of only two times the diameter of the starting powder [van Tassel and Randall, 2004]. Subramanian and co-workers (2001) used this technique produce metal composite nanostructures by depositing various metals such as Au, Pt and Ir on

nanostrucutred TiO_2 films. Iwata and co-workers (2007) used EPD technique to deposit small Au islands on silicon wafer using 10 nm diameter gold nanoparticles. They reported that the height profile of the island increased with increase deposition time.

2.3.5 Other methods

The formation of a silicon oxide layer and the micro structural changes in thick sputter deposited gold films on Si subtrates were studied using advanced analytical techniques by Popovic and co-workers (1990). The gold films were deposited by diode sputtering onto Si substrates and the thickness of gold films was 1μm after deposition. The films were later sintered in air at temperatures between 200 and 250 °C for a time ranging from 0.3 to 3h. The films were analysed using scanning electron microscopy to observe the micro structural changes in as-deposited and in sintered structures.

Maaroof and co-workers (2005) fabricated gold thin films on glass substrates by sputtering of $AuAl_2$ precursor films followed by a de-alloying etch. Alloy films of $AuAl_2$ were prepared by co-depositing the elements using high vacuum dc magnetron sputtering onto glass substrates. After co-depositing of $AuAl_2$ on glass substrate, aluminium was removed from the compound by immersing the films in NaOH solution. The residual film consists of mesoporous gold on glass. Nishino and Ikai (2006) also used dc magnetron sputtering at room temperature fabricating gold films with thickness ranging from 0.2 to 1.0μm on silicon substrates.

Recently Hu and co-workers (2008) reported a simple and environmentally friendly electroless plating solution of chloroauric acid ($HAuCl_4$) and hydrogen peroxide (H_2O_2) for depositing films onto (3-aminopropyl)-trimethoxysilane (APTMS) coated glass surfaces. In their experiments they used H_2O_2 as the reducing agent, reducing $AuCl_4^-$ to Au nanoparticles, and those nanoparticles were immobilised onto the glass surface by using the APTMS adhesive layer of the glass slide to fabricate thin gold films.

Zhao and co-workers (2006) proposed a straightforward, rapid and "green" approach for the fabrication of gold nano-structured films. In their experiments a gold electrode was firstly oxidised under a high potential and a non toxic reducing agent ß-D-glucose was used to reduce the gold oxide. Gold films having a thickness of 200 nm were produced by this method.

2.4 Different methods of patterning metal nanoparticles

2.4.1 Ink-jet printing

Ink-jet printing (IJP) is a well established direct write deposition technique which was developed by Heinzl and Hertz (1985). IJP has been used for reprographic applications over the years for home and office printing and have also penetrated the emerging markets of rapid prototyping and medical imaging [Kuhn and Myers, 1979], spectrometry sampling [Onnerfjord *et al.*, 1998], high speed titration [Litborn *et al.*, 1999], mass and tissue engineering [Klebe, 1988]. IJP has been also used in printing of hybrid microcircuits [Teng and Vest, 1987], deposition of patterned luminescent doped polymer films [Hebner *et al.*, 1998] and metallization of grid patterns of solar cells [Teng and Vest, 1988]. Ceramic sol-gel

inks have been used to decorate ceramic articles [Atkinson *et al.*, 1997] and patterns of ceramic [Kim and McKean, 1998] and carbon nanotubes [Huang *et al.*, 2004] have been similarly printed.

There are two types of IJP, namely continuous and drop-on-demand. A continuous IJP forms a stream of droplets even though there is no print demand (**Figure 2.24**). These droplets exiting the printer head are then charged and deflected to their destination by the help of an electric field and the droplets which are not required are collected or recycled. In continuous IJP process, a piezoelectric actuator was used to superimpose a modulated pressure and, on leaving the nozzle, the stream breaks up at a matching frequency into a continuous series of equidistant, equal size droplets. A charging electrode is placed where the droplets separate from the liquid stream and this voltage determines the landing destination of the droplet in the substrate. The applied voltage is limited to few hundred volts and if the voltage is too high the droplets undergo secondary atomisation. After leaving the charging electrode the droplets pass between two deflector plates at a constant potential of 3 – 18 kV. The droplets are deflected with respect to their charge and uncharged droplets are collected by a gutter and recycled into the ink reservoir where adjustments are made for solvent loss before recirculation to the printhead [Tay *et al.*, 2003].

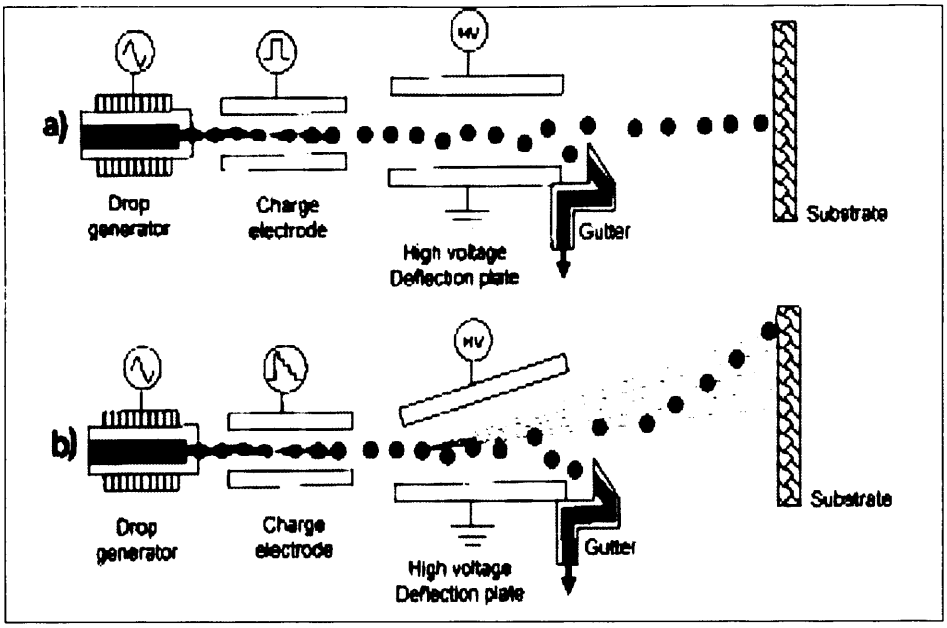

Figure 2.24 Schematic diagrams of continuous ink-jet printers (a) using binary deflection and (b) using multiple or analogue deflection [Tay *et al.*, 2003]

The continuous IJP can be a binary or multiple deflection system as shown in **Figure 2.24a**. In a binary deflection system, the droplets are either charged or uncharged. The charged droplets are transferred to the substrate and the uncharged droplets are collected into the gutter for recirculation. In multiple deflection system (**Figure 2.24b**) charged droplets are deflected by different amounts and uncharged droplets are collected and recirculated. Continuous IJP have superior printing speed and can be used at a printhead-to-paper distance of 25 – 50 mm but tend to have a higher capital cost [Tay *et al.*, 2003].

The drop-on-demand (DoD) IJP is the most common reprographic jet printing technique which was developed to overcome the limitations of continuous jet printing technology such was start-up and shut-down requirements, complex charging and need for ink recirculation. In the DoD printing technique, a drop of

ink is forced through the printer head by means of electricity or heat. There are two main type of DoD printers commonly used, namely thermal and piezoelectric [Tay *et al.*, 2003].

The thermal DoD ink jet method uses a disposable print head which contains ink, electrical heating elements and nozzle plates. A drop of ink is forced through the printer head and propelled from the nozzle. Due to electrical heating a bubble of vapour is formed by incipient boiling of the ink. The bubble collapses and capillary forces draw ink from the reservoir for the process to begin again. In the piezoelectric DoD ink jet method part of the chamber consists of a piezoelectric element which propagates an acoustic pressure wave towards the nozzle when excited by an electrical signal. By overcoming the inertial and viscous pressure loss and the pressure associated with the surface tension in the ink meniscus an ink droplet is formed at the nozzle and expelled. In both these types droplets are ejected only when needed for printing and no ink circulation devices are needed [Tay *et al.*, 2003].

Ink-jet printing has been used in metal deposition over the years. Gold and silver have been used to pattern microstructures by ink-jet printing. **Table 2.1** summarise the previous works on metallic nanoparticles carried-out by other researchers. The resistivity of bulk silver and gold is 1.62×10^{-8} Ωm and 2.44×10^{-8} Ωm, respectively.

Table 2.1 Deposition of metals by IJP

Metal	Particle Size (nm)	Width (μm)	Conc. (wt.%)	Curing Condition	Resistivity (Ωm)	Ref.
Ag	10 – 20	60	34.5	Electrical	2.7×10^{-8}	[Allen *et al.*, 2008]
Ag	5 – 7	1500	10	320 °C	1.1×10^{-6}	[Kamyshny *et al.*, 2005]
Ag	-	100	16	150 °C	4.8×10^{-8}	[Dearden *et al.*, 2005]
Ag	1 – 10	125	30	300 °C	3.5×10^{-7}	[Szczech *et al.*, 2002]
Ag	20	65	20	300 °C	3.5×10^{-8}	[Kim *et al.*, 2006]
Ag	10 – 50	130	25	260 °C	1.6×10^{-7}	[Lee *et al.*, 2005]
Ag	5 – 10	160	60	Microwave	1.6×10^{-7}	[Perelaer *et al.*, 2006]
Au	2 – 4	17	30	Laser	1.4×10^{-7}	[Bieri *et al.*, 2003]
Au	2 – 5	20	30	Laser	1.4×10^{-7}	[Bieri *et al.*, 2004]
Au	-	360	31	500 °C	2.7×10^{-7}	[Nur *et al.*, 2002]
Au	2 – 4	125	34	Laser	6.2×10^{-8}	[Chung *et al.*, 2004]

In in-jet printing, the droplet size mainly depends on the orifice inner diameter. It is well known that the droplet size is two times that of the orifice diameter. That is if the orifice diameter is 60 μm then the droplet size would range from 100 – 140 μm. Smaller droplets could be generated by using a very fine diameter orifice in printing. But another disadvantage of ink-jet printing is when fine needles are used the needle tends to get blocked when using very concentrated solutions. Therefore in order to reduce the metal track size more complex laser systems in conjunction with ink-jet printing have been used.

2.4.2 Electrohydrodynamic atomisation printing

Electrohydrodynamic atomisation printing (EHDAP), also known as electrostatic atomisation printing (EAP) is an emerging technology which uses the droplets produced from atomisation of a solution by an electric field. The most widely used mode of atomisation is known as the cone-jet mode which produces a near-monodispersion of droplets. Jayasinghe and co-workers (2002) used ceramic droplets generated from a stable cone-jet to deposit microstructures on a computer controlled moving substrate.

In this process, a suspension was forced through a needle at a controlled flow rate which is subjected to an electric field. A point shaped ground electrode was used underneath the substrate in order to focus the charged droplets into one area. At a given flow rate and electric field, the liquid or suspension undergoes atomisation in the cone-jet mode. Then with the help of a computer controlled device the substrate is moved at a pre-design pattern thus creating microstructures on a given substrate. **Figure 2.25** shows a schematic diagram of this process.

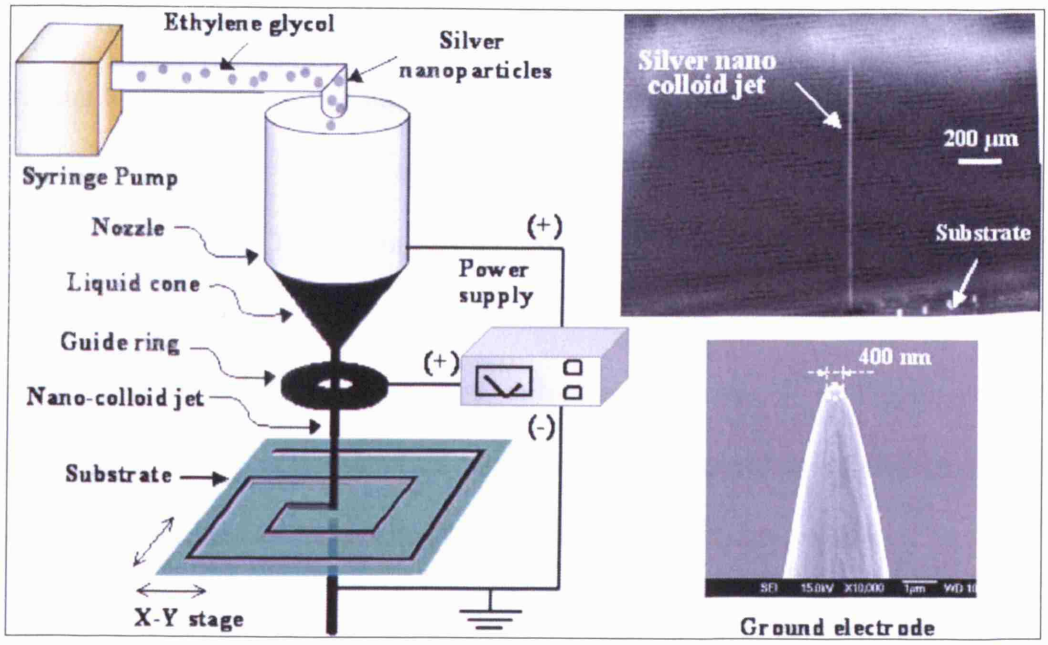

Figure 2.25 Schematic diagram of electrohydrodynamic atomisation process [Lee *et al.*, 2006].

Recently Lee and co-workers (2006) used electrohydrodynamic atomisation printing technique to deposit silver nanoparticles. In their experiments they used silver nanoparticles having a diameter of 3 – 7 nm suspended in toluene. The suspension consisted of 30 wt. % of silver with a very small amount of surfactants to prevent the agglomeration of silver nanoparticles. Silver tracks were printed on Kapton polyimide films and a minimum line of 32 μm in width and 0.3 μm in thickness was obtained. Furthermore, they used the same technique to pattern a spiral type inductor. In these experiments they used < 20 nm diameter silver nanoparticles suspended in ethylene glycol. The concentration of the silver particles in the solution was 20 wt. % and the finest silver track produced was ~100 μm in width and the average resistivity of track was 3.2×10^{-8} Ωm [Lee *et al.*, 2007].

When compared with ink-jet printing, electrohydrodynamic atomisation printing technique has a few advantages. It is well known that in ink-jet printing the droplets generated are approximately twice the nozzle diameter [Wang *et al.*, 2005]. Thus even if a 60 μm internal diameter nozzle was used, the relics are > 100 μm but in contrast, the electrohydrodynamic process allows much coarser nozzles, yet the droplet and relic diameters are << 100 μm. Another advantage of this processing route is the ability to process much higher volume loading without any blockages due to the usage of much coarser nozzles.

2.4.3 Microcontact printing

Microcontact printing (μCP) is a surface patterning technique which has attracted great interest from the surface science community, engineers and biologist. μCP can be classified as a soft lithography technique capable of creating micro- and nanoscale structures on a given substrate [Quist *et al.*, 2005]. Soft lithography was developed in order to control specific properties of surfaces at micro- and nanoscale levels through the use of a parallel fabrication process for surface patterning. Pioneering work in soft lithography was carried out by G.M. Whitesides and co-workers followed by many others resulting in both application development and studies of the parameters involved in the process [Xia and Whitesides, 1998, Whitesides *et al.*, 2001]. In this process (**Figure 2.26**), a patterned soft polymer stamp was used to transfer chemical, biological or functional material inks onto a solid substrate. The most commonly used elastometric material is poly(dimethylsiloxane) (PDMS), an inert material that is compatible with many chemical and biological inks [Quist *et al.*, 2005].

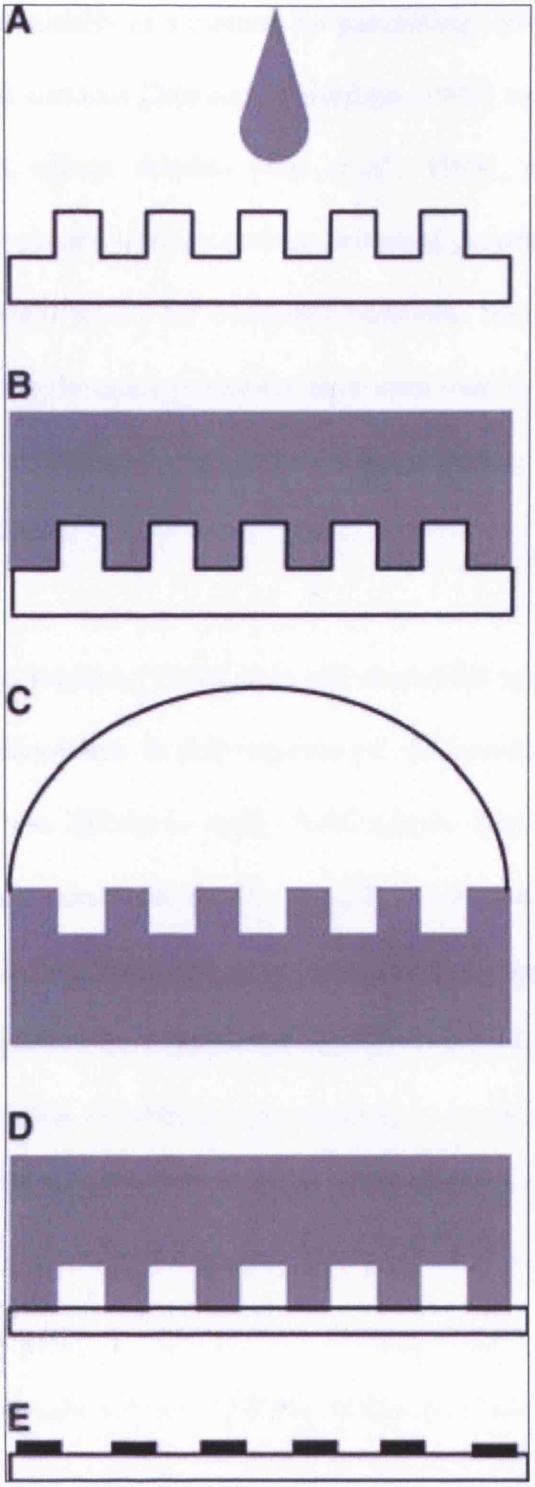

Figure 2.26 Schematic representation of the microcontact printing process. PDMS is applied to a masterdesign a) and allowed to cure (b), forming a mold/stamp. After peeling the stamp from the master, ''ink'' is applied (c), and the ink is transferred to a substrate (d) by stamping. After removal of the stamp, the ink is patterned on the substrate (e) [Quist *et al.*, 2005]

μCP was used initially as a method for patterining self-assembled alkylthiol monolayers onto gold surfaces [Xia and Whitesides, 1995] and later was extended to alkylsiloxanes on silicon dioxide [Xia *et al.*, 1995], and this resulted in numerous biotechnology applications such as patterned growth of a variety of cells and fabrication of micro-arrays for biosensor purposes. Subsequently, numerous techniques derived from the same principles have been used to produce patterns not only by transferring various molecules onto various surfaces, but also transferring metals [Quist *et al.*, 2005].

Wilbur and co-workers (1996) used self assembled monolayers formed by μCP to pattern gold nanowires. In their experiments the minimum feature size they were able to achieve was 200 nm in width. Wolfe and co-workers (2002) fabricated a palladium based microelectronic device by μCP. They used μCP to pattern thin films of metallic palladium into serpentine wires which functioned as a hydrogen sensor. μCP was employed by Delamarche and co-workers (2003) in conjunction with electroless deposition to fabricate copper patterns on glass substrates. Geissler and co-workers (2003) used μCP to pattern gold, silver, copper, palladium and aluminium nanowires. In their experiments they used μCP for patterning and later the substrate was subjected to wet chemical etching process in order to produce nanowires having a feature size of ~200 nm in diameter. Recently Allen and co-workers (2007) used μCP for patterning indium metal onto silicon substrate using an isotropic etching rather than using wet chemical etching.

As simple and efficient as it is, μCP does present some problems. The main disadvantage of this technique is the use of soft polymer. Swelling of the stamp

during inking often results in the pattern increasing its size. Deformation of the soft polymer stamps due to their elastomeric nature, such as pairing, buckling or roof collapse of structures during contact with the surface is a problem that results in distorted patterns [Rogers *et al.*, 1998]. Such deformations increase when the size of the corrugations reaches the submicron- or nanoscale. Another major drawback of soft lithography is the contamination of the patterns with unpolymerized low molecular weight siloxane from the stamp. Peeling the stamp from the master is also a concern in stamp fabrication in general and with nanometer-scale corrugations in particular. These problems have limited the size of the patterns to micro scale. In recent years, efforts have been made by many researchers to reduce the size of the patterns to the nano scale [Quist *et al.*, 2005].

2.4.4 Nanolithography

Lithography is a method of printing onto surfaces and has been used for centuries. Lithography techniques are used in many modern-day microfabrication, nanotechnology and molecular electronics. These methods often rely on patterning of a resistive film, followed by a chemical etch of the substrate. The prefix 'nano' denotes nanometer scale quality and resolution.

Electron beam lithography (EBL) uses an electron bream for patterning. The electron beam is focused onto a substrate coated with beam-sensitive materials and the beam is directed to produce a specific pattern. Because the diffraction limit of electrons is much smaller, the spatial resolution of EBL is greater than techniques using other beam sources (e.g. UV and X-ray photons). Ueno and co-workers (2005) used EBL process to create arrays of gold rods. A 2 nm Cr and

60 nm Au bilayer was deposited onto a mask prepared by EBL. Arrays of gold rods having dimensions of 40 nm (w) x 360 nm (l) x 60 nm (h) were patterned on substrate.

A rather different type of nanolithography is possible if the beam is comprised of ions or atoms instead of electrons. There are three main ion-beam lithography (IBL) techniques, focused ion beam (FIB), proton beam writing (p-beam writing) and ion projection lithography (IPL) [Watt *et al.*, 2005].

Focused ion beam (FIB), involves a focused heavy-ion beam rastered over a surface creating a pattern through modification of the substrate structure either by physically or chemically and deposition of atoms or removal of atoms from the surface through sputtering. Ga or Ar ions are normally used in this process [Reyntjens and Puers, 2001, Watt *et al.*, 2005]. Hanarp and co-workers (2003) used FIB lithography to create arrays of gold disks on substrates with controllable size, shape and interparticle spacing that can be used for optical applications. Proton beam writing and ion beam projection lithography are related IBL techniques although no reports of precious metal structures have been forthcoming to date [Stokes *et al.*, 2007].

Optical lithography has been used to pattern structures on a substrate with a sub-100 nm feature size with the use of very short wavelengths. Guo and co-workers (2005) used interference lithography to create gold gratings that can be used for optical applications. Gold nanowire structures with line widths ranging between 115 nm to 200 nm were prepared. Another recently developed optical

lithography technique is zone-plate-array lithography (ZAPAL). ZAPAL is a maskless optical technology that employs an array of optical lenses that focus incident light onto the substrate. Minimum line width reported todate are ~ 115 nm [Chao *et al.*, 2005].

Nanoimprint lithograpy (NIL) is another lithography technique for fabricating nanometer scale patterns on a substrate. NIL is a pattern transfer process and relies on other lithography techniques to generate templates. Li and co-workers (2000) used NIL technique to fabricate optically-functional structures on a substrate. Line widths reported in their experiments were about 20 nm.

There are several different Scanned Probe Lithography (SPL) techniques, including AFM and STM atom manipulation and Dip Pen Nanolithography (DPN). AFM and STM use a cantilever tip to push atoms around on surfaces to create patterns. DPN is a SPL technique in which a microscopic "pen" is coated with a chemical compound and brought into contact with a substrate to "write" on the substrate with the compound. DPN was used to fabricate and functionalise Au nanostructures on a semiconductor substrate. An AFM tip was used to pattern line widths as small as 10-15 nm and with ~5 nm spatial resolution [Stokes *et al.*, 2007].

2.4.5 Laser based particle deposition

Photo-lithography and electron-beam lithography are the most widely used patterning techniques which are at the heart of the modern-day microfabrication, nanotechnology and molecular electronics. Both of these methods require a

resistive film and harsh chemical etching, which makes them unsuitable for patterning nanoparticles or molecules with organic or biological functionalities, since it causes destruction of organic molecules and biological entities. Furthermore particles are strongly localized within the laser beam and the deposition accuracy can be below one micrometer. Other newly developed techniques, such as 'dip-pen lithography', allow direct transport and patterning of particles and molecules onto a substrate from the atomic force microscope (AFM) tip on a nanometer scale. However, such techniques can usually convey only a small amount of materials, since their transfer efficiency is relatively low. Another common technique which is called as 'microcontact printing', which uses an elastometer stamp, can fabricate heterogeneous structures of micro-size and larger dimensions, but it has a limited potential for a mixed functionality surface fabrication. Additional limitations of these and many other techniques are their incapability to produce structures and patterns of various compositions. As a complement to many existing micro- and nano-patterning techniques, Xu and co-workers (2004) developed laser-based particle deposition (LBPD) technique, which relies on guidance and deposition of particles by a laser beam.

The basic apparatus (**Figure 2.27**) consist of mist, source, process chambers and laser system. An ultrasonic nebulizer in the mist chamber which produces a mist of submicron-sized liquid droplets from colloidal suspensions or precursors. A laser beam, directed along the axis of the aperture guides and transports the droplets from the source to the process chamber. If desired, reactions in the precursor droplets can be initiated by the laser beam in-flight or on the deposit, producing new material. The aperture orifice diameter is significantly larger than

the transported droplets, and the strong focusing effect of the diffracted beam allows the controllable patterning of micron-sized lines [Xu *et al.*, 2004].

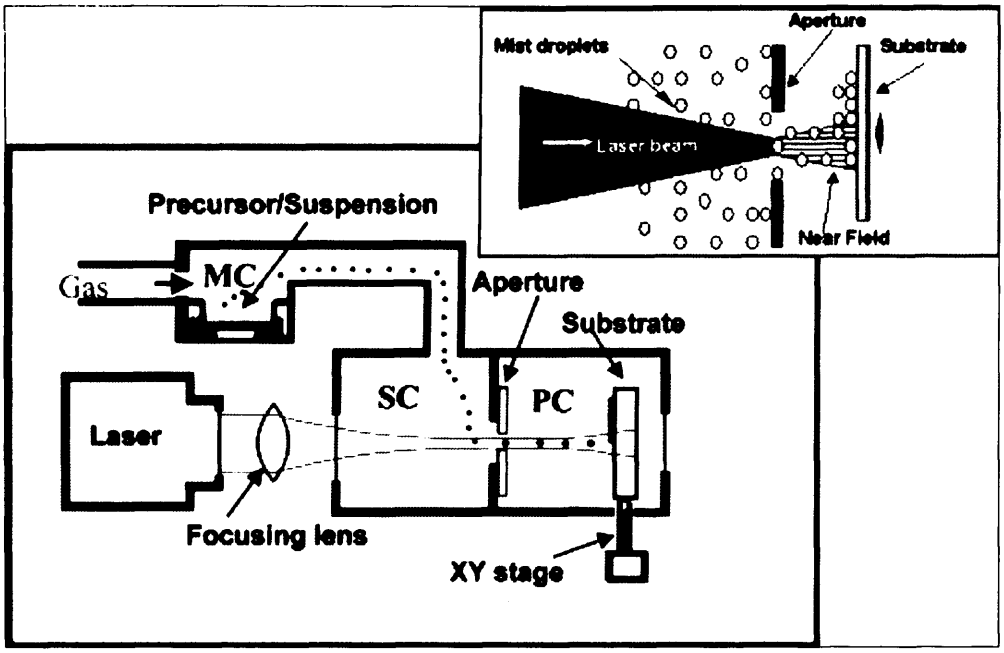

Figure 2.27 Schematic of the laser-based particle deposition (LBPD) apparatus: source of droplets/particles (nebulizer, carrier gas supply, and the mist chamber MC); supply (SC) and process (PC) chambers linked by a high-power laser aperture (details shown in the offset); laser system (532-nm YAG laser and focusing lenses); movable substrate on an XY stage [Xu *et al.*, 2004]

Chapter 3

Experimental details

This chapter gives a detailed explanation of the experimental details that were followed in this research. The materials that were used, corresponding suppliers and the product details are also given. The methods followed for the preparation of different solutions and the characterization techniques implemented are also discussed in detail. Initial experiments were repeated many times and it was found out that by repeating the experiments for ten times would be enough to get an accurate result. Thereafter, all experiments carried out in this research were repeated ten times and checked for reproducibility. All the equipment was calibrated and measurements were checked against known values quoted by the supplier or in the literature.

3.1 Materials

3.1.1 Preparation of sphere shaped gold hydrosol

The gold hydrosol was prepared and supplied by the University of Vigo, Spain. The gold hydrosol was used as received. The preparation of gold hydrosol is as follows.

Tetrachloroauric acid ($HAuCl_4.3H_2O$) and trisodium citrate were purchased from Aldrich (Poole, UK). All chemicals were used as received. Milli-Q water was

used to make up all solutions (R > 18.2 Ω mm). Small gold colloids with an average diameter of 15 nm and 10% polydispersity were synthesized according to the sodium citrate reduction method. This method consists of boiling 95 mL of 5 x 10^{-4} M $HAuCl_4$, and adding 5mL of a warm sodium citrate solution (1 wt.%) to the stirred solution [Enustun and Turkevich, 1963]. **Figure 3.1** shows a TEM image of the 15 nm diameter sphere shaped gold nanoparticles.

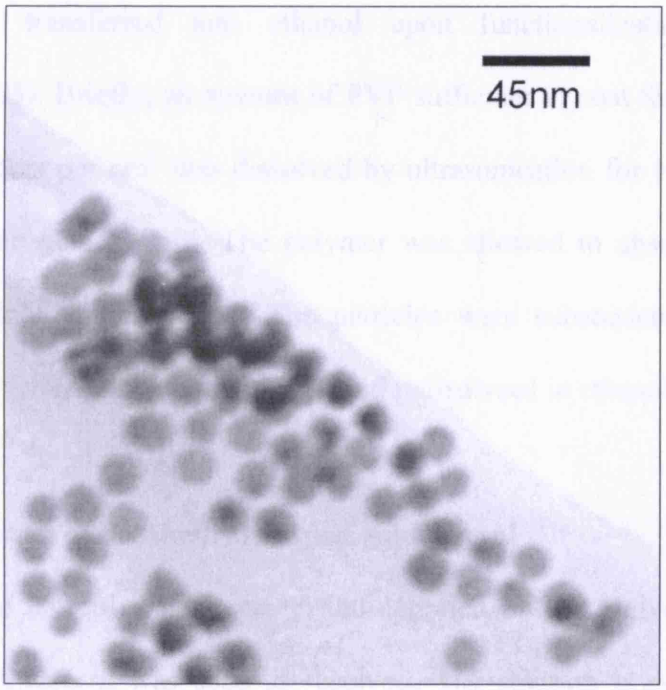

Figure 3.1 TEM image of gold sphere shaped particles

3.1.2 Preparation of sphere shaped gold alcosol

The gold alcosol was prepared and supplied by the University of Vigo, Spain. The gold alcosol was used as received. The preparation of gold alcosol is as follows. Tetrachloroauric acid ($HAuCl_4.3H_2O$) and trisodium citrate were purchased from Aldrich. Poly(vinylpyrrolidone) (PVP, MW 10,000) was supplied

by Fluka. All chemicals were used as received. Milli-Q water was used to make up all solutions (R > 18.2 MΩ cm).

Gold nanoparticles with an average diameter of 15 nm and 10% polydispersity were synthesized according to the standard sodium citrate reduction method [Enustun and Turkevich, 1963] by boiling 5 x 10^{-4} M $HAuCl_4$ in the presence of 1.6 x 10^{-3} M sodium citrate for 15 min. After cooling down, the particles were transferred into ethanol upon functionalization with PVP [Graf *et al.*, 2003]. Briefly, an amount of PVP sufficient to coat the particles with 60 PVP monomers per nm^2 was dissolved by ultrasonication for 15 min in water and added to the gold colloid. The polymer was allowed to absorb to the gold particles overnight while stirring. The particles were subsequently centrifuged (3500 r.p.m.) to remove the unbound PVP and redispersed in ethanol.

3.1.3 Preparation of decahedral shaped gold alcosol

The gold alcosol was prepared and supplied by the University of Vigo, Spain. The gold alcosol was used as received. The solution is constituted by a mixture of Au decahedral nanoparticles (70%) and Au prisms (30%). These particles have been used by the supplier due to their unique optical properties [Sánchez-Iglesias *et. al.*, 2006]. Gold spherical nanoparticles (2 – 3 nm in diameter) were prepared as was reported before [Teranishi *et al.*, 1998]. Briefly, 22 μL of an aqueous solution of 0.1136 M $HAuCl_4$ was added to 47.5 mL of a PVP solution in DMF / H_2O mixture (18:1; v/v) which contains 0.017g of PVP (M.W. 10000). Next, 2.5 mL of a freshly prepared 10 mM $NaBH_4$ solution was injected quickly into the solution under vigorous stirring. The gold sol was stirred for 2 h at

room temperature. (The seed was not used until 24 hrs after its preparation for the complete decomposition of $NaBH_4$). Before adding the preformed seed solution, 0.825mL of 0.1136M $HAuCl_4$ aqueous solution was added to 15mL of a PVP (M.W. 40 000) solution in DMF ([PVP]=2.5mM.) in a 50 mL vessel and the mixture was ultrasonically irradiated until the complete Au^{3+} reduction. In that moment, 1.7 mL of the preformed seed solution (5×10^{-5} M in gold) was added and further ultrasonic irradiation was allowed until the process finished. The ultrasonic irradiation was performed on a Sonopuls HD2200 ultrasonic homogenizer operating at the frequency of 20 kHz and at 30% of the maximum power (200 W). During the reaction the DMF solution achieved around 100 °C and later re-disperse in ethanol. The side length of the decahedral particle was 36.54±4.65nm and the side length of the prisms particles was 81.63±8.88nm. **Figure 3.2** shows the TEM images of the particles.

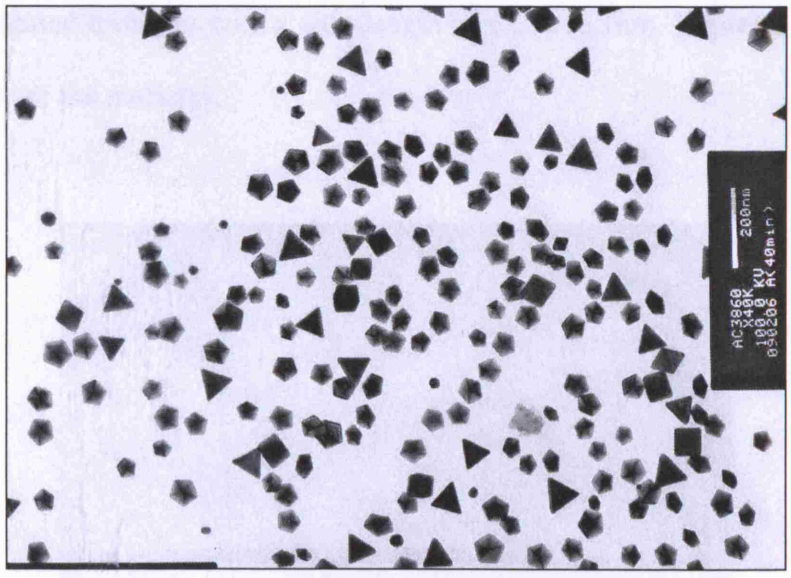

Figure 3.2 TEM images of the mix solution containing Au decahedral nanoparticles (70%) and Au prisms (30%)

3.1.4 Preparation of silver prism shaped alcosol

The gold alcosol was prepared and supplied by the University of Vigo, Spain. The gold alcosol was used as received. These particles have been used by the supplier due to their unique optical properties [Rodríguez-González *et. al.*, 2006]. Silver nanoplates were synthesized by reducing $AgNO_3$ with DMF in the presence of PVP. In a typical synthesis, 20 mL of $AgNO_3$ solution (3.75 mM, in DMF) was added dropwise to a 20 mL PVP (MW 40000) solution (0.005 M, in DMF). The mixture solution was exposed to high-intensity ultrasound irradiation under ambient conditions for 130 min. The ultrasonic irradiation was performed on a Sonopuls HD2200 ultrasonic homogenizer operating at the frequency of 20 kHz and at 30% of the maximum power (200 W). The product was purified by centrifugation. In this case, the reaction mixture was diluted with water and centrifuged at 4000 rpm for 30 min and redispersed in ethanol. The solution is constituted by 45% truncated triangles with a side length of 54.3±12.1nm and 55% of non-truncated triangles with a side length of 62.5±16.1nm. **Figure 3.3** shows a TEM image of the particles.

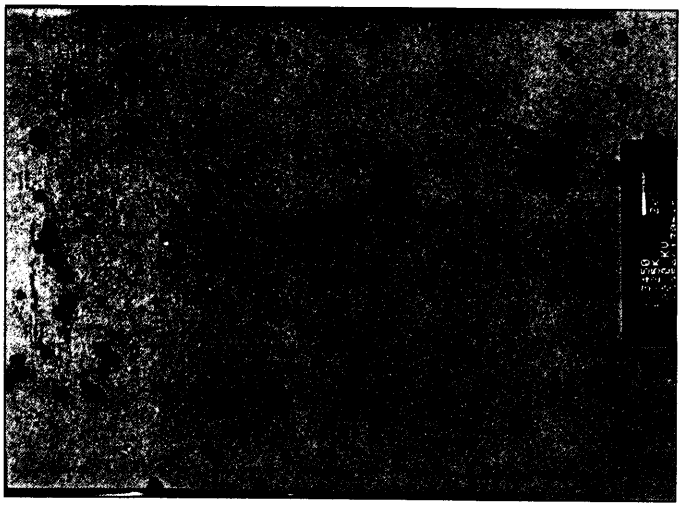

Figure 3.3 TEM image of the Ag nanoprism particles

3.1.5 Preparation of polymer solution

Polyethylene oxide (PEO) (98.5% purity) and polyethylene glycol (PEG) (99% purity) supplied from Sigma-Aldrich (Poole, UK) having an average molecular weight of 2,000,000 and 8000, respectively, was used for the preparation of polymer solution. PEO and PEG, both solids were mixed at a weight ratio of 1:2. Tetrahydrofuran (THF, 99.5% purity) solution supplied from Sigma-Aldrich (Poole, UK) was mixed at 4:3 weight ratio with respect to the PEO and PEG mixture. De-ionized water was added to the polymer mixture at a weight ratio of 10:1 and the resulting solution was stirred for 24 hrs before spraying. The polymer mixture was used as a model system to encapsulate conducting silver and gold particles by electrospinning and to investigate the particle distribution along the fibre.

3.1.6 Silver suspension

Achesan electrodrag 1415 Ag suspension (supplied by Agar Scientific, Stansted, UK) was used as received. According to the supplier, the suspension contained 52 wt. % of Ag flakes having a size of < 20μm with 50% < 9μm and 10% < 3.5μm. The Ag particles were suspended in a mixture of methylethyl ketone and diacetone alcohol (2:1) and the suspension also contained a thermoplastic binder.

3.1.7 Substrates

Silicon wafer was used as received as the substrate for all patterning work carried out in this research. The wafers were supplied by Silicon Materials, Germany. Each wafer was ~500 μm in thickness and the resistivity was ~0.1 Ωm.

The silicon wafers were polished and used as received without any modification to the surface. For template assisted electrohydrodynamic deposition studies Cu templates were used. The grids were provided by Gilder Grids, Lincolnshire, UK. Grids having a hole width from 22 – 80 μm were used in these experiments.

3.2 Characterisation

3.2.1 Loss on ignition

Loss on ignition method is a widely used method for finding out the weight content of the suspension or colloids. The weight loss was measured by weighing the samples before and after heating. Samples of the colloids were heated up to 300 °C in static air to calculate the actual weight loading of metal and subsequently the samples were cooled down in the furnace. Oxidation of Ag may occur during loss on ignition tests.

3.2.2 Density

The densities of the solutions were estimated using the standard density bottle. The volume of the density bottle provided by VWR International, UK was 10 ml. Both the weight of the empty bottle and that filled with solution were measured on the balance AND GR300-EC (A&D Intrucments Ltd., Japan) which was capable of giving precise value up to four decimals. The density bottle was calibrated using glycerol and distilled water and the values were validated with the reference data.

3.2.3 Surface tension

Surface tension of the suspensions were measured using Kruss Tensiometer K9 (Du Novy's ring method). The ring was hung from the hook by an eyelet. The liquid is raised until contact with the surface is registered. The sample is then lowered again so that the liquid film produced beneath the ring is stretched. As the film is stretched a maximum forced is experienced and this is recorded in the measurement and used to calculate the surface tension [www.kruss.info, 20th Aug 2008]. The mean value from a set of 10 recordings was taken, which normally had a negligible variation. The Tensiometer was calibrated using glycerol before measuring the suspensions and at every single instance it was thoroughly cleaned and dried before the next measurement.

3.2.4 Electrical conductivity

The electrical conductivity of the solutions was measured using HACH SensION^{TM} 156 dip-probe (Camlab Ltd., Cambridge, UK). The electrode was always cleaned with distilled water and dried before measurements. The electrode was placed in the sample for 30s to dislodge any air bubbles trapped inside the cell before recoding the values. The mean values from a set of 10 recordings were taken.

3.2.5 Viscosity

Kinematic viscosity, υ of the solutions was calculated by measuring the time, **t** taken by the solution to travel between two etched rings, using a U-tube viscometer (BS/U type). The time, **t** was measured manually by using a stop watch with millisecond accuracy. Once the average time was obtained it was then

multiplied with the viscometer constant, **C** to obtain the kinematic viscosity. For all the measurements the U-tube was immersed in a water bath maintained at 20 °C. De-ionised water and glycerol was used respectively to calibrate the viscometers. The dynamic viscosity, η of the solutions was then calculated by multiplying the kinematic viscosity with the relative density of the solution. All experiments were repeated 10 times and the mean value was taken.

3.3 Equipment used for electrohydrodynamic atomisation

The schematic diagram illustrating the electrohydrodynamic atomisation setup for single and co-axial jetting is shown in **Figure 3.4** and **Figure 3.5**, respectively. The equipment consists of a single or co-axial needle arrangement which is connected by a silicone rubber tube to a syringe pump or pumps, respectively. The needle setup was connected to a high voltage power supply supplied by Glassman Europe Ltd., Tadley, UK, which was capable of supplying up to 30kV. The jet behaviour was observed and recorded using a high speed camera in conjunction with microscopic lenses and a fibre optic light source was used for illumination near the needle exit.

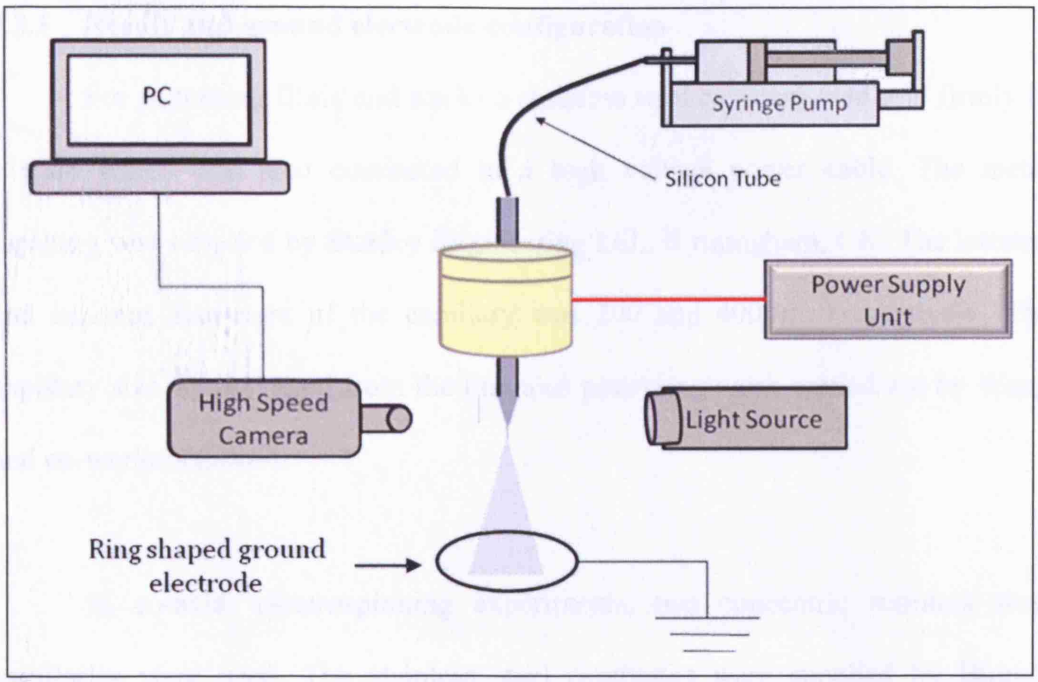

Figure 3.4 Schematic diagram for single needle jetting

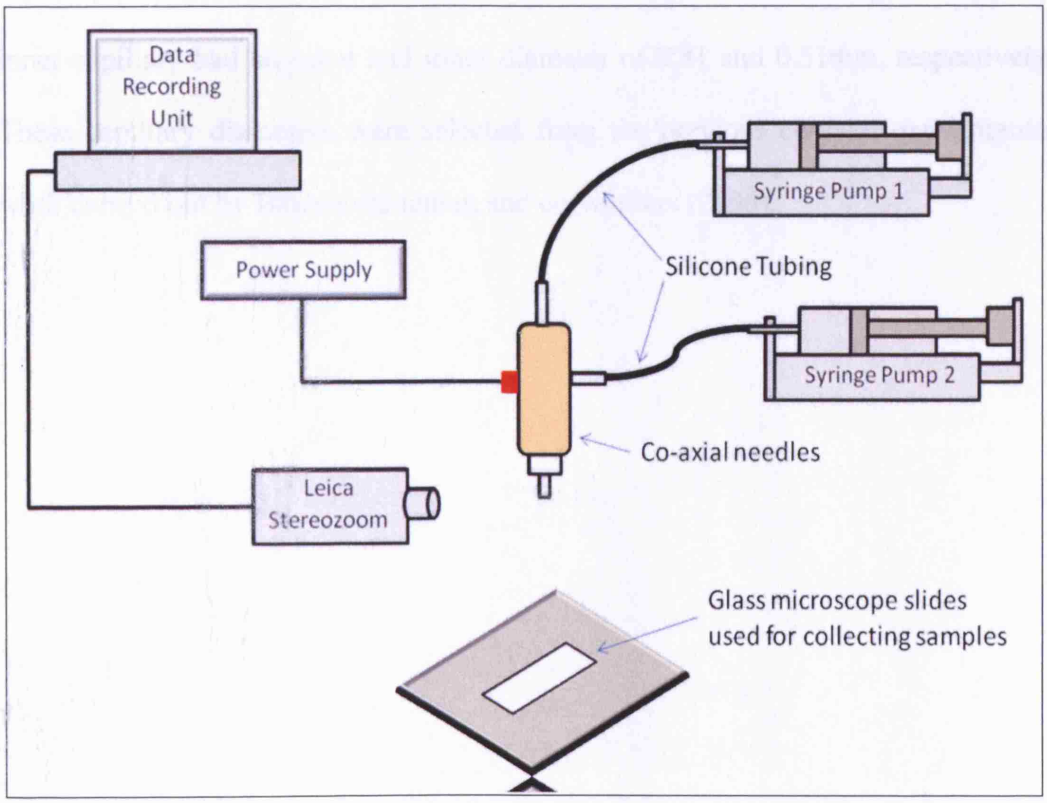

Figure 3.5 Schematic diagram of co-axial jetting

3.3.1 Needle and ground electrode configuration

For patterning films and tracks a stainless steel capillary was held firmly in a resin which was also connected to a high voltage power cable. The metal capillary was supplied by Stanley Engineering Ltd., Birmingham, UK. The internal and external diameters of the capillary was 200 and 400μm, respectively. The capillary size was selected from the previous patterning work carried out by Wang and co-workers (2005).

In co-axial electrospinning experiments, two concentric stainless steel capillaries were used. The stainless steel capillaries were supplied by Bignell Surgical Instruments Ltd., West Sussex, UK. The co-axial capillary device is shown in **Figure 3.6** and co-axial capillaries are shown in **Figure 3.7**. The outer capillary had an outer and inner diameter of 1.25 and 0.85mm, respectively. The inner capillary had an outer and inner diameter of 0.81 and 0.51mm, respectively. These capillary diameters were selected from the previous co-axial experimental work carried out by Balasubramanian and co-workers (2006).

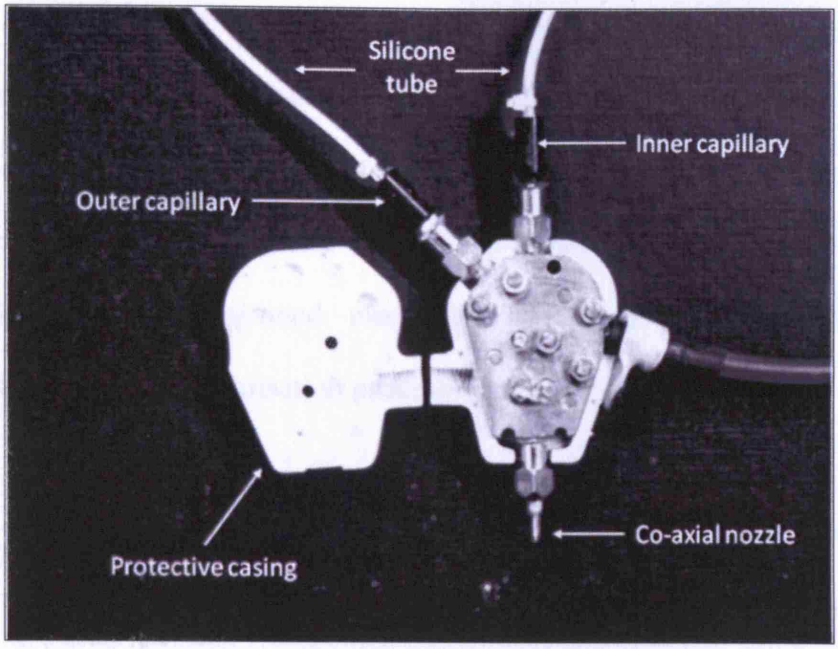

Figure 3.6 The capillary device used for co-axial electrospinning

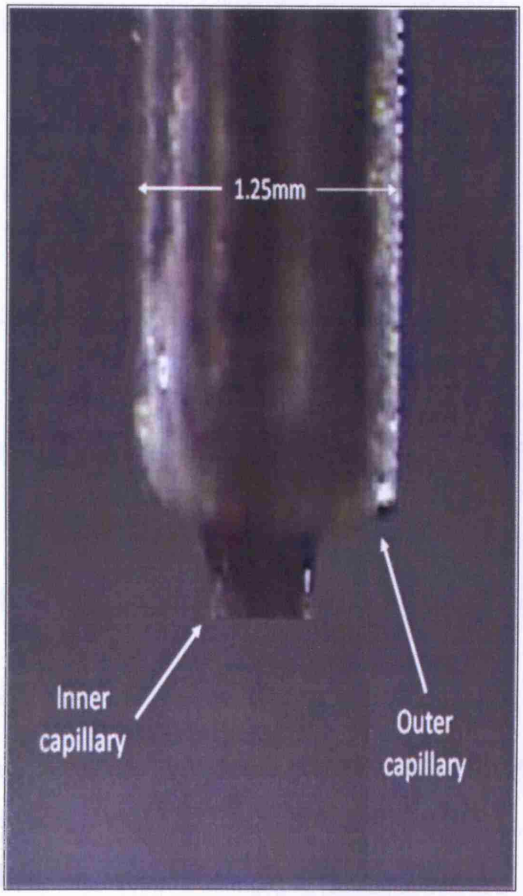

Figure 3.7 Digital picture of co-axial capillaries

A point shape ground electrode was used in electrohydrodynamic atomisation printing experiments. The point like ground electrode was held firmly in resin and connected to the ground terminal of the power supply unit and provided the potential difference between the needle exit and the ground electrode. The needle and the ground electrode were kept in line throughout the electrohydrodynamic atomisation printing experiments.

For film fabrication and templating experiments no ground electrode was used. The hot plate used in these experiments was used as a ground electrode. For electrospinning no ground electrode was used and a pyrex box was used in between the co-axial needle setup and camera to prevent the fibres from getting attracted towards the camera and the light source.

3.3.1.1 Calculation of speed of jetting

The speed of jetting that is investigated in electrospinning experiments with silver particles were calculated as follows.

$$\text{Speed of jetting} = \frac{\text{Flow rate } (m^3\ s^{-1})\ Q}{\text{Area } (m^3)\ A}$$

The area of speed of jetting for the outer needle is calculated from $\frac{\pi}{4}(d_2 - d_1)^2$ where d_2 is the inner diameter of the outer needle and d_1 is the outer diameter of the inner needle. The area of speed of jetting for the inner needle is calculated from $\frac{\pi}{4}(d_3)^2$ where d_3 is the inner diameter of the inner needle.

3.3.2 Syringe Pump

In all electrohydrodynamic experiments carried out in this research, the needle setup was connected to a syringe which in turn connected to a Harvard Apparatus PHD4400 infusion pump using appropriate size silicone rubber tubing. For each new experiment the pump was calibrated for short and long periods of time. The syringe used in all experiments was Hamilton-Microliter Series gastight syringe (HAMILTON Bonaduz AG, Bonaduz, Switzerland). Different capacity syringes were used as required depending on the volume to be processed and the flow rates range.

3.3.3 High speed camera

The frequency of the droplet production in the stable cone-jet mode is very high and the droplet speed after jet break up is in the order of tens of meters per second. Thus, in order to observe the jet break and the droplet motion a high speed camera with an exposure time below 1ms is required. Furthermore a powerful illumination source is also required for capturing high resolution clear images.

In order to observe the jet break up and the droplet motion, SpeedCam MotionBLITZ (Weinberger AG, Dietikon, Switzerland) high speed camera was employed in conjunction with fibre optic light source provided by the same company. The high speed camera consists of a high definition digital camera (High-end CMOS sensor, max. 1,280 × 1,024 pixels, 70 to 4,000 frames / sec, MOCAM-4000 high-speed b/w camera with 5m camera cable), to which a microscopic lens is attached. The lens allows focusing on objects down to a few microns from a distance of approximately 5cm. The camera can be connected to a

computer via the cable and a MotionBLITZ software was used to control the camera.

3.3.4 Droplet size distribution measurements

The droplets produced from the atomisation process were measured using a computer controlled Sympatec Helos (Helium laser optical spectrometer) Modle Vario KF sizing system (Sympatec Ltd., System-Partikel-Technik, Bury, UK). The Sympatec system is based on the diffraction of light occurring when a laser beam impinges on the droplet of the spray. This diffracted light pattern is measured by a set of photodiodes located downstream, from which the size histograms can be obtained.

Before measuring the droplet size from the device, measurements of the light pattern without the spray is generated and has to be taken as reference background. The reference set values should be close to zero for accurate measurements. The lens used for these measurements had a droplet detection capability in the size range 0.5 – 175 μm. The droplet size distribution is generated by the software and the average droplet size was obtained from time-resolved data by calculating the volume-weighted average over 10s. The droplet size distribution experiments were repeated many times in order to check the validity of the data.

3.4 Two dimension printing system

The printing system consists of an X-Y stepper motor driven, motion controlled 2-axis system (**Figure 3.8**). The X and Y tables are mounted directly on one another keeping the 2-axis profile very low. Each stepper motor used in the

device was capable of dividing an entire 360^0 rotation to 4000 equal steps. The stepper drives employed incorporate mini-stepping technology (electrical sub-division of position) and this together with a ball screw pitch of 5 mm, gives a theoretical resolution of 2.5 μm. A datum and an end of travel limit sensor were fitted on each of the tables to trigger the controller when a respective carriage reaches its limit. The 2-axis system is controlled using a programmable motion-controller which communicates directly with a computer.

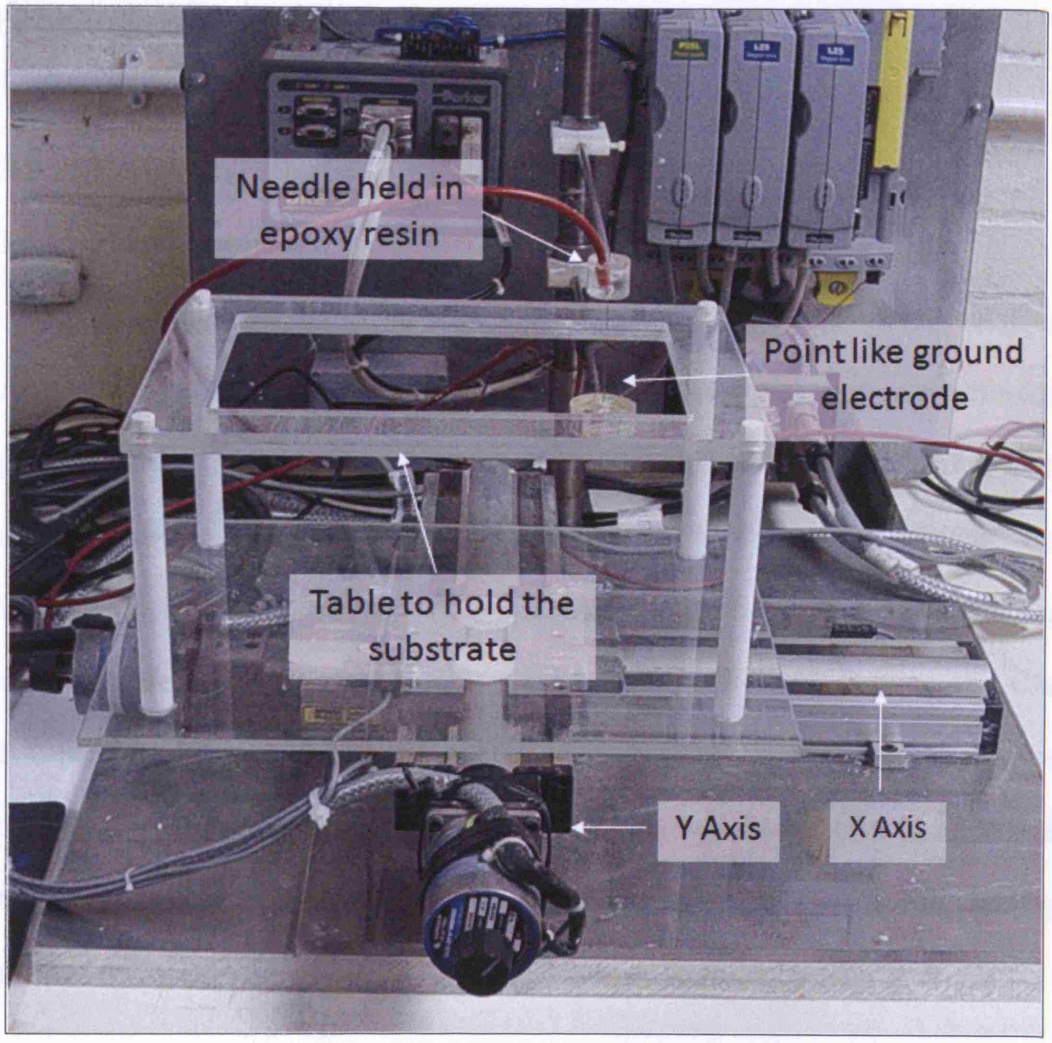

Figure 3.8 2D electrohydrodynamic printing device

A perspex table is mounted firmly on the 2-axis system. The top of the table accommodates a frame for holding firmly an A4 sheet of substrate. The frame is fitted to the base of the table using four PET stilts. Using Motion Planner software, the geometry of the word or any pattern can be created using x and y co-ordinates and downloaded to the 2-axis controller. This allowed the 2-axis system to follow the path of the co-ordinates given, to enable printing. When the 2-axis system was fully set-up, the capillary and ground electrode were fitted firmly in place and kept in line with each other. An A4 sheet was placed in the frame and held firmly between the needle and the ground electrode.

3.5 Result characterisation

3.5.1 Heat treatment

Sintering is an important process to remove the remaining solvent and bond Au particles together to form solid structures. During the experiments the droplets produced from the jet break up were collected on silicon wafers. Thereafter trial-and-error method was used to sinter the samples at different conditions. The following conditions were selected as it produced a crack-free microstructure. The samples were subjected to heating in a muffle furnace in static air up to 400 $^{\circ}$C at 2 $^{\circ}$C per min. Samples were held at 400 $^{\circ}$C for 1 hr before cooling down to ambient temperature at 2 $^{\circ}$C per min. The samples were studied before and after heat treatment using optical microscopy, scanning electron microscopy, energy dispersive X-ray analysis and transmission electron microscopy.

3.5.2 Optical microscopy

The droplets deposited on silicon wafer and different architectures patterned on substrate were first examined using Nikon Microscope ME6000 microscope. This microscope was equipped with an incident illuminating unit (light coming from top of the specimen) with a differential interference contrast option and also equipped with dark field option, which enable us to study the image clearly. A joy-stick which was connected to the table axis of the microscope helps to move the table in x and y directions. This microscope had the facility to alter the magnification lenses and measure dimensions varying from a few μm to few cms. Measurements were carried out by using a special software (Acquis digital imaging) supplied by Synoptics Ltd., Cambridge, UK.

3.5.3 Scanning electron microscopy

The surface analysis of the prepared samples was carried out using Scanning Electron Microscopy (SEM). The samples were mounted on top of a cylindrical steel stub (25 mm x 37.5 mm) supplied by Agar Scientific, Essex, UK). The samples were fixed to these stubs using LEIT adhesive carbon tabs supplied by Agar Scientific. The samples were carbon coated (CED 030 Carbon Evaporator, Balzers Ltd., Liechtenstein) using high purity carbon tread (TAAB Company, Aldermaston, UK). The samples were observed under SEM (JEOL JSM 6100 SEM). Accelerating voltage was varied between 5 – 20 kV and the working distance was varied from 8 – 15mm. The elemental distribution map was plotted using INCA software (INCA Instruments, Oxford, UK).

3.5.4 Transmission electron microscopy

The samples were collected on transmission electron microscopic (TEM) grids (Agar Scientific). The samples were coated with carbon before observing under TEM (JEOL JEM 100CX) with an accelerating voltage of 100 kV. All TEM images were recorded on film and digitally scanned using a commercially available high resolution scanner.

3.5.5 Electrical measurements

The resistance of the deposited track was measured using the well known four-point method. Agilent power supply (E3641A), Agilent digital multi-meter (34410A) and Keithley programmable current amplifier (428) was used for measurements.

Chapter 4

Results

4.1 Electrohydrodynamic atomisation of sphere shaped gold hydrosol

The basic equipment set-up for electrohydrodynamic atomisation consists of a stainless steel needle with an internal diameter of ~200 μm and an external diameter of ~400 μm, held in epoxy resin. The needle was connected to a high voltage power supply which is capable of applying up to 30 kV between the needle and the ground electrode. The inlet of the needle was connected to a syringe pump using a silicone rubber tube and the flow rate of the alcosol to the needle exit was varied between 10^{-11} – 10^{-10} m^3s^{-1}. A ring shaped grounded electrode was kept 15 mm away from the needle exit. A fibre optic light source was used for illumination. A microscope lens in conjunction with a high speed camera was connected to a portable computer, which allowed observation of the medium while undergoing atomisation (**Figure 4.1**).

The gold hydrosol was prepared using the method discussed in the previous chapter and was supplied by the University of Vigo, Spain. The gold hydrosol was used as received. Before subjecting the gold hydrosol for electrohydrodynamic studies, the concentration of the particles and the properties of the solution were measured. The weight percent of the particles was calculated using loss on ignition method. The gold particle concentration was ~0.06% by weight. The properties of

the hydrosol were measured using the methods described in Chapter **3**. All equipment were cleaned and calibrated before the measurements. The properties of the gold hydrosol are given in **Table 4.1**.

Table 4.1 Properties of gold hydrosol

Hydrosol property	**Value**
Density (ρ) / kgm^{-3}	1025
Surface Tension (γ) / mN/m	69
Viscosity (η) / mPa s	1.1
Electrical Conductivity (K) / Sm^{-1}	1.56×10^{-2}

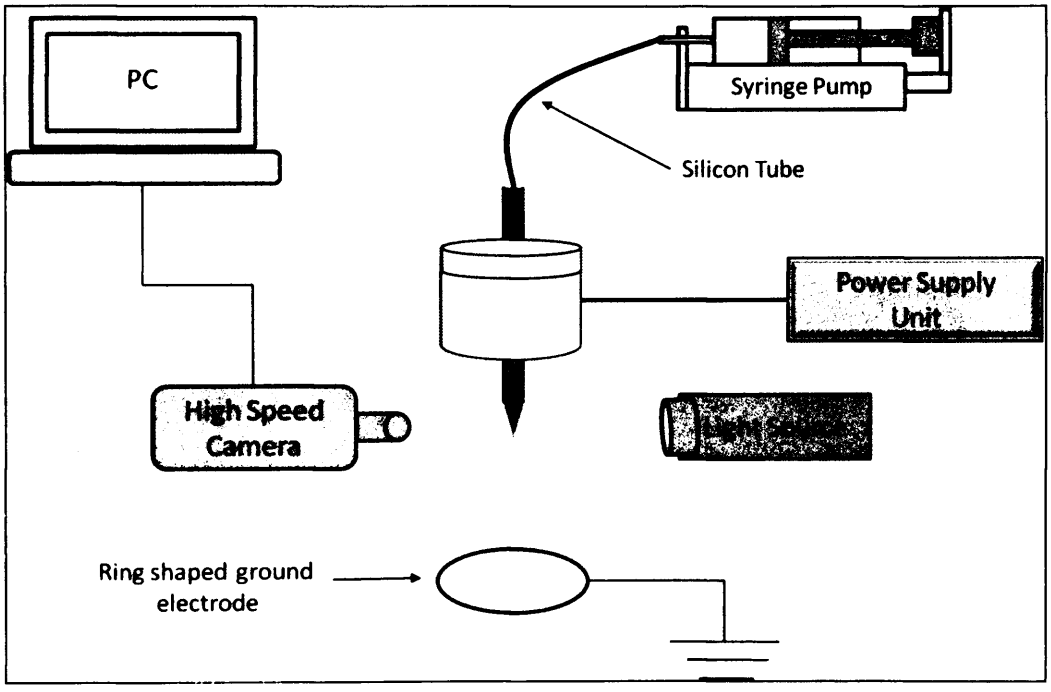

Figure 4.1 Schematic view of the basic electrohydrodynamic equipment set-up

Using the above mentioned equipment set-up, the gold hydrosol was subjected to electrohydrodynamic atomisation. Due to its high surface tension and high electrical conductivity, a stable cone-jet mode was not possible to achieve. **Figure 4.2** shows the instability of the jet while undergoing electrohydrodynamic atomisation captured using a high speed camera. The flow rate was 1 x 10^{-10} m^3s^{-1} and the applied voltage was 4.4 kV.

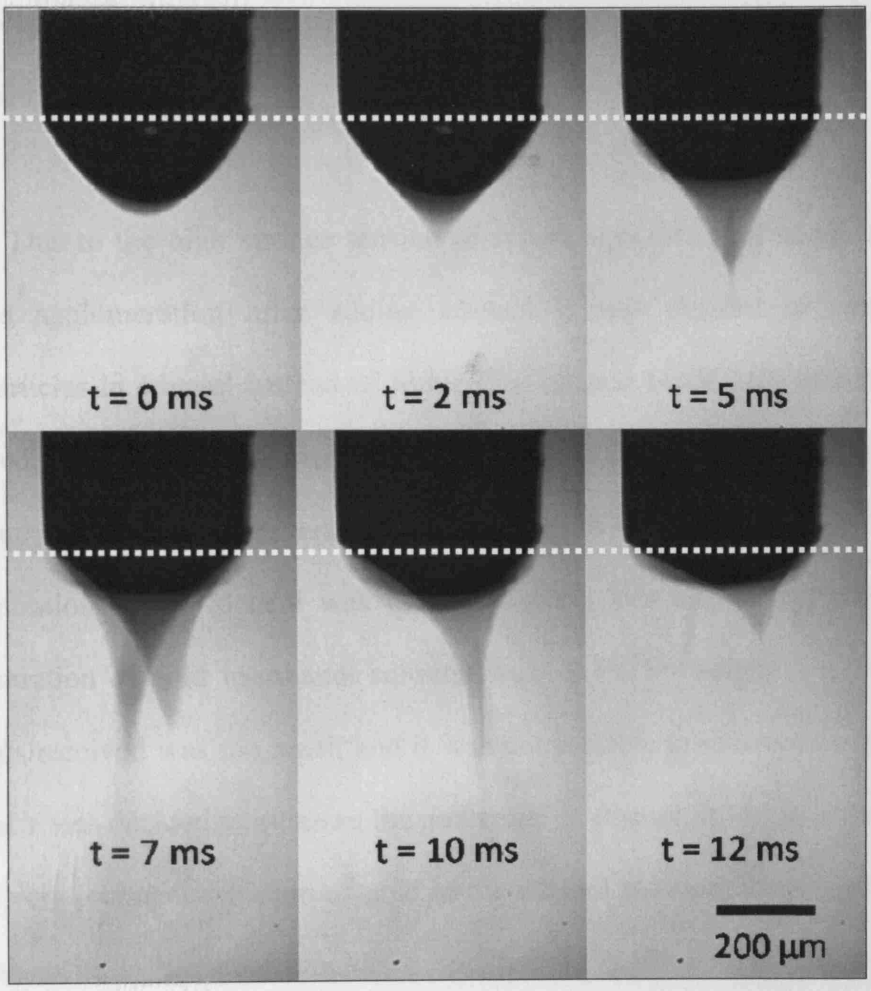

Figure 4.2 Instablity of the jet while undergoing electrohydrodynamic atomisation of the gold hydrosol. Dotted line indicated the exit of the needle

In order to obtain a stable cone-jet, it was decided to evaporate some percentage of solvent (i.e. water) and then later add ethanol to the solution to reduce the surface tension of the solution. The gold hydrosol was kept on a hot-plate and the temperature of the hot-plate was raised to 100 °C and the volume of the hydrosol was reduced systematically by 10 – 50 %. Later the hydrosol was kept at room temperature for 24 hrs and then ethanol was added systematically while the hydrosol was stirred. Addition of ethanol made the ruby-red colour gold hydrosol to change its colour to greyish-blue. This is due to particle agglomeration after addition of ethanol.

Due to the high surface tension of water, high electrical conductivity and particle agglomeration after adding ethanol it was decided to suspend the nanoparticles in ethanol instead of water. The ethanol based gold suspension was prepared using the method discussed in Chapter **3**. The gold alcosol was prepared and supplied by the University of Vigo, Spain and used as received. The concentration of the alcosol was measured using loss on ignition method. The concentration of gold in ethanol solution was ~0.1% by weight. The quantity of alcosols received was too small and it was not possible to measure the properties. Instead it was decided to measure the properties of ethanol. It was assumed that due to the very low concentration of gold in the ethanol solution, the properties of the alcosols to be in the same range of pure ethanol (99.9% purity). The presence of gold particles would increase the electrical conductivity of the solution. **Table 4.2** gives the properties of ethanol which was measured using the methods discussed in Chapter **3**. All measurements were calibrated first before measuring the properties of ethanol.

Table 4.2 Properties of ethanol

Alcosol property	Value
Density (ρ) / kgm^{-3}	790
Surface Tension (γ) / mN/m	23
Viscosity (η) / mPa s	1.3
Electrical Conductivity (K) / Sm^{-1}	3.4×10^{-4}
Relative Permittivity (β)	26

4.2 Electrohydrodynamic atomisation of sphere shaped gold alcosol

4.2.1 Characterisation of cone and jet

The gold alcosol was subjected to electrohydrodynamic atomisation at different flow rates and applied voltages to find out the ability of the alcosol to undergo a stable jetting process. Different modes of atomisation were observed when the voltage was varied from 0 – 5 kV. For classical electrohydrodynamic atomisation to occur, the hydrodynamic time (t_h) must exceed the electrical relaxation time (t_e), and the inequality $\frac{LD^2}{Q} >> \frac{\beta\varepsilon_0}{K}$ must be satisfied [Ganan-Calvo *et al.*, 1997]. L denotes the axial length of the jet, D is the jet diameter, Q is the flow rate, K is the electrical conductivity and β is the relative permittivity. ε_0 is the permittivity constant which is 8.85×10^{-12} Fm^{-1}.

In electrohydrodynamic experiments, the flow rate (Q) and applied voltage were kept constant at 9.1×10^{-11} m^3s^{-1} and 4.6 kV, respectively, as these conditions generated a stable cone-jet (**Figure 4.3**), which is well known to produce a

near-monodisperse stream of fine droplets. D and L measured were ~20 μm and ~200 μm, respectively, giving an electrohydrodynamic time (t_h) of 8.79 x 10^{-4} s. Using the β and K values of ethanol as 26 and 3.4 x 10^{-4} Sm^{-1}, respectively. The electrical relaxation time (t_e) is 6.7 x 10^{-7} s. Thus $t_h >> t_e$ and the condition required for classical EHDA is satisfied. The 0.1 wt. % of gold can only make the K value even higher to satisfy this inequality even more comfortably.

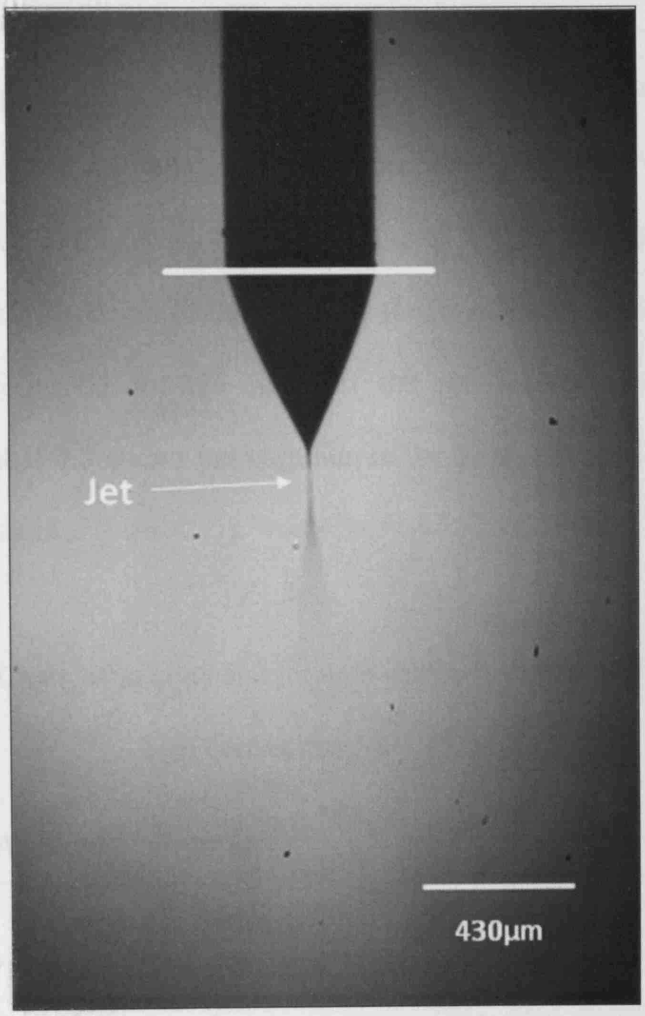

Figure 4.3 Stable cone-jet mode atomisation of gold alcosol. The flow rate is 9.1 x 10^{-11} m^3s^{-1} and applied voltage was 4.6 kV. White line indicates the exit of the needle

4.2.2 Effect of applied voltage

The applied voltage in electrohydrodynamic atomisation plays an important role in the stable cone-jet mode. To find out the effect of applied voltage, in our next set of experiments the flow rate was kept constant at 5 x 10^{-11} m^3s^{-1} the applied voltage was varied from 0 – 5 kV. At 0 kV dripping mode was observed. When the voltage was gradually increased to 2.8 kV micro-dripping mode was observed. Unstable cone-jet modes were observed at 3.5 kV. At 3.8 kV stable cone-jet mode was observed. When the voltage was raised up to 4.6 kV multi jetting mode and further increasing the voltage the jet discharges. **Figure 4.4** shows stable cone-jet mode at different applied voltages. When increasing the applied voltage the shape of the cone as well as the length of the jet changes. When the voltage was increased from 4.2 to 4.6 kV the depth of the cone and the jet diameter got smaller. The cone depth varied from 393 to 295 μm and the jet diameter was reduced from 19 to 14 μm. **Table 4.3** shows the variation in the cone area and the jet diameter in a more detailed form.

Table 4.3 Changes in cone and jet with increasing voltage. The flow rate was kept constant at 5 x 10^{-11} m^3s^{-1}

Applied Voltage (kV)	4.2	4.4	4.6
Cone depth (μm)	393	323	295
Jet diameter (μm)	19	16	14

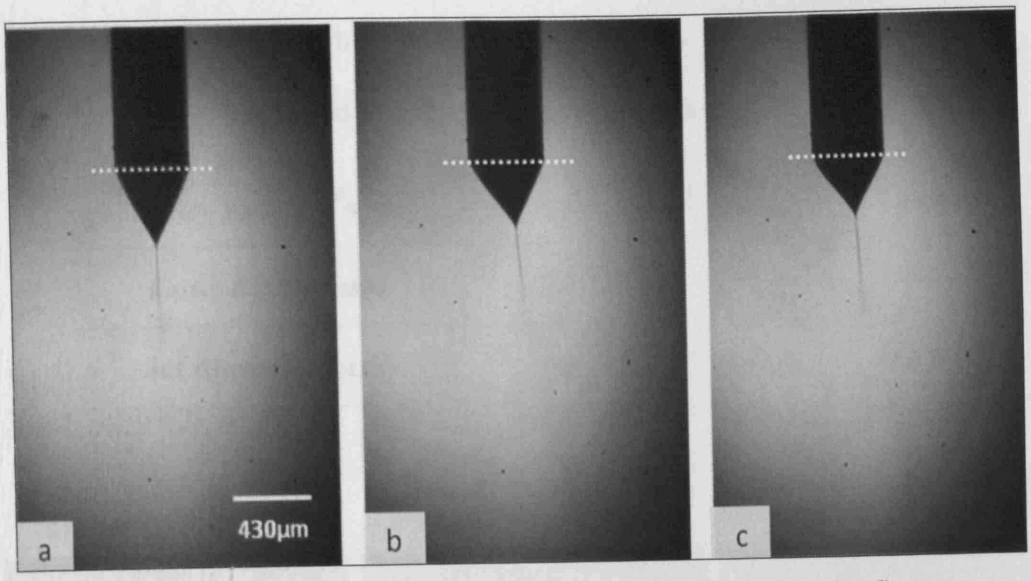

Figure 4.4 Stable cone jet mode of the gold alcosol at the flow rate 5×10^{-11} m^3s^{-1} and applied voltage; a) 4.2 kV, b) 4.4 kV and c) 4.6 kV. Exit of the needle is shown with a dotted line

4.2.3 Effect of flow rate

In order to find out the influence of flow rate in the stable cone-jet mode, the applied voltage was kept constant at 4.6 kV and the flow rate was varied from 2.5 to 9.1 x 10^{-11} m^3s^{-1}. **Figure 4.5** shows stable cone-jet atomisation at different flow rates. With increasing flow rate the cone depth and the jet diameter increased. **Table 4.4** shows a detailed analysis of the cone depth and the diameter of the jets at different flow rates. The cone depth increased from 260 to 524 µm and the jet diameter increased from 11 to 19 µm with the increase of the flow rate.

Table 4.4 Changes in cone and jet with increasing flow rate. The applied voltage was kept constant 4.6 kV

Flow rate (m^3s^{-1})	2.5×10^{-11}	5×10^{-11}	9.1×10^{-11}
Cone depth (µm)	260	295	524
Jet diameter (µm)	11	14	19

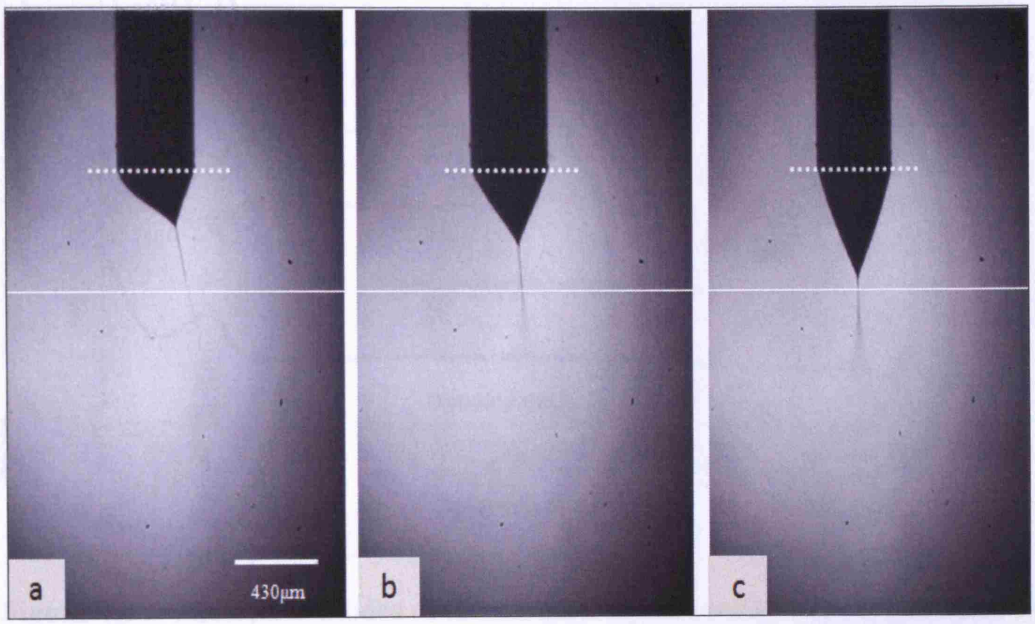

Figure 4.5 Stable cone jet mode of the gold alcosol at applied voltage 4.6 kV and flow rates: a) 2.5×10^{-11} m^3s^{-1}, b) 5×10^{-11} m^3s^{-1} and c) 9.1×10^{-11} m^3s^{-1} respectively. The exit of the needle is shown with a dotted line

4.2.4 Mode selection map

The flow rate of the gold alcosol was varied systematically and the applied voltage was varied from 0 to 5 kV. Various modes of atomisation were observed while gradually increasing the applied voltage. At 0 kV dripping mode and with further increase of the voltage, micro-dripping mode was observed. When the

voltage is increased further unstable cone-jet, stable cone-jet and multi jetting was observed. The different modes of jetting taking place in the parametric space of flow rate and electric field were studied and these results were plotted (**Figure 4.6**). This map can help us to select the region suitable for printing.

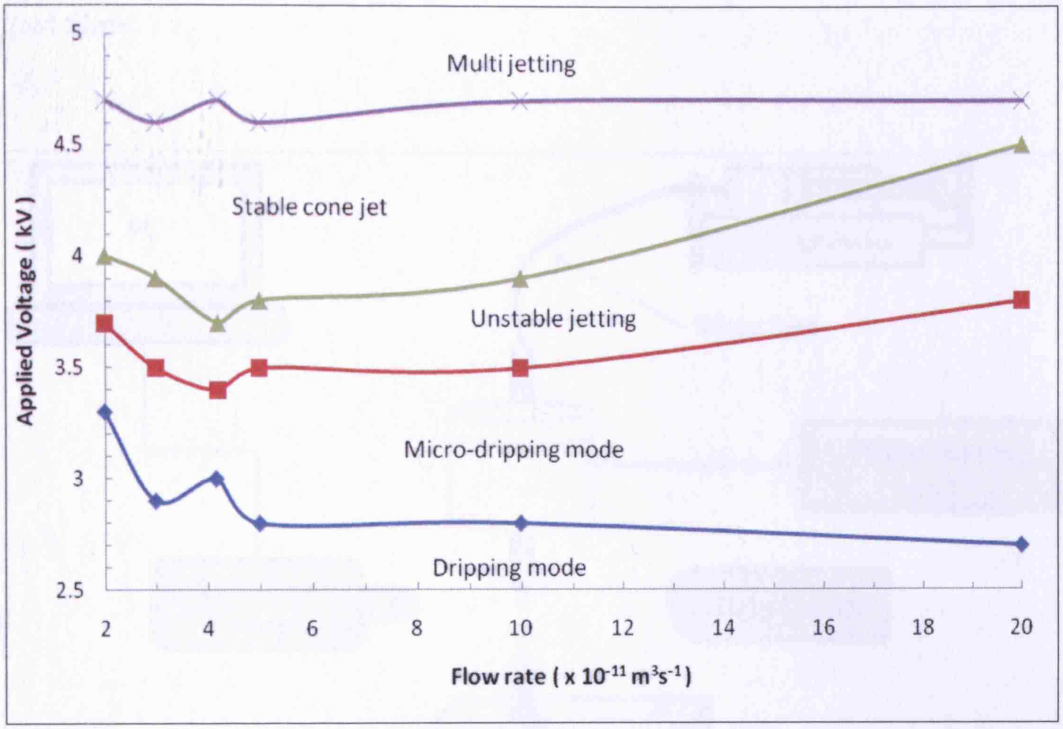

Figure 4.6 Different modes of atomisation observed with varying flow rate and applied voltage when the gold sphere shaped alcosol was subjected to electrohydrodynamic atomisation

4.2.5 Fabrication of nano-structured gold films

The droplets produced by disintegration of the jet were collected on silicon wafers in order to fabricate films. Firstly, spraying was carried out at different times and at different distances from the substrate and the needle exit. The sprayed droplet-relics agglomerated with increasing spray time and formed a large relic. This is mainly due to the high frequency of the droplets generated by the cone-jet

mode atomisation and the slow evaporation of the solvent (i.e. ethanol). Since the frequency of the droplet production can not be varied, it was decided to increase the evaporation rate by heating the substrate. A hot-plate was used and kept underneath the spray surface in order to increase the temperature of the substrate. **Figure 4.7** shows a schematic view of the equipment set-up used for fabrication of gold films.

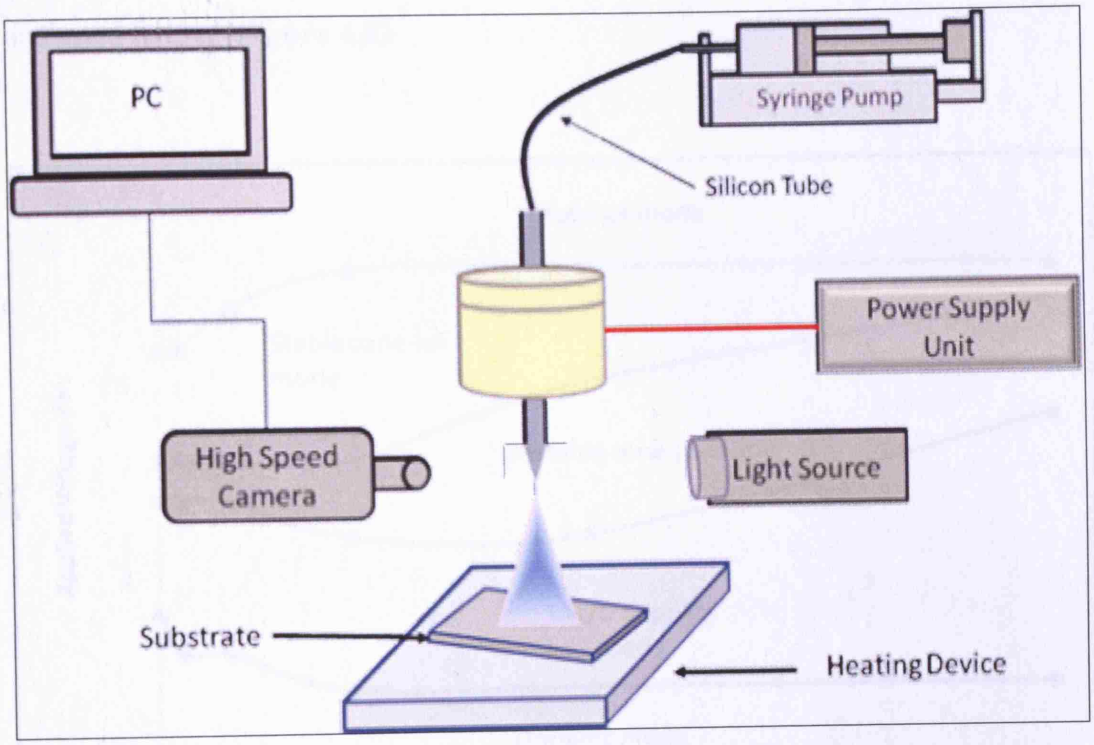

Figure 4.7 Schematic view of the equipment set-up for film fabrication

Different distances and spray times were investigated. With the increasing of the distance between the needle exit and the collection point, more time was necessary to form a dense film. Therefore, a distance of ~3 mm was used to fabricate dense gold films. Secondly, the substrate temperature was varied with increasing spraying time. It was evident that when the substrate temperature was increased more than 50 °C, a stable cone-jet mode was not possible. This is due to

heat transfer from air to the needle exit causing the solvent to evaporate before spraying.

Due to the heating device the electric field changes and in order to find out the new parameters for stable cone-jet mode the voltage and the flow rate was varied from 0 – 5 kV and 1 x 10^{-11} – 2 x 10^{-10} m^3s^{-1} respectively. Various modes were observed such as dripping, micro-dripping, unstable cone-jet, stable cone-jet and multi jetting (**Figure 4.8**).

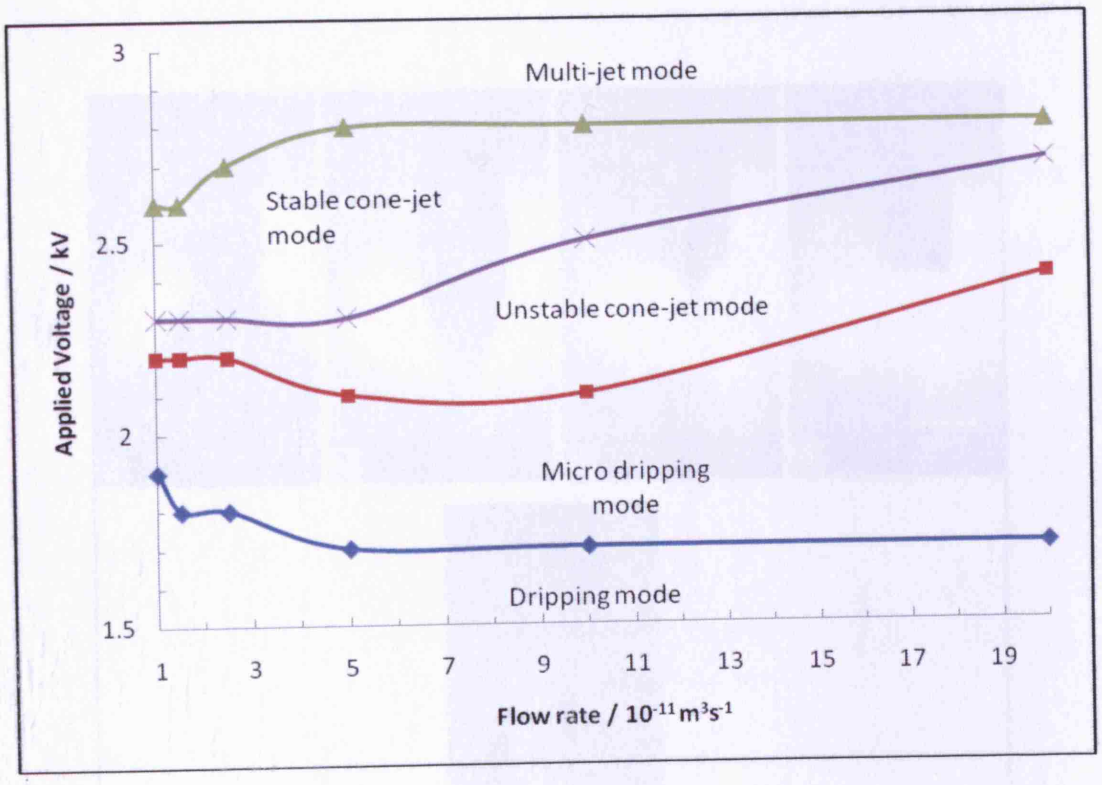

Figure 4.8 Different modes of atomisation observed with varying flow rate and applied voltage when the gold sphere shaped alcosol was subjected to electrohydrodynamic atomisation with a heating device.

Figure 4.9 shows different modes of atomisation that exist at 5 x 10^{-11} m^3s^{-1} at different applied voltages. At zero voltage, dripping mode was observed. When

the voltage gradually increased from zero to 1.8 kV; only micro dripping occurred. At 2.1 kV unstable cone-jetting mode was observed. When the voltage was raised to 2.3 kV stable cone-jet mode occurred and when increased further, at 2.8 kV multi jetting was observed. When the applied voltage was increased further, the jet discharged. A flow rate of 5 x 10^{-11} m^3s^{-1} was used throughout the experiments. This value was selected as the droplet size is directly proportional to the flow rate. However, if the flow rate is too low, stable cone-jet mode jetting was regularly disturbed or the jet was not stable for a sufficient time span to enable film fabrication.

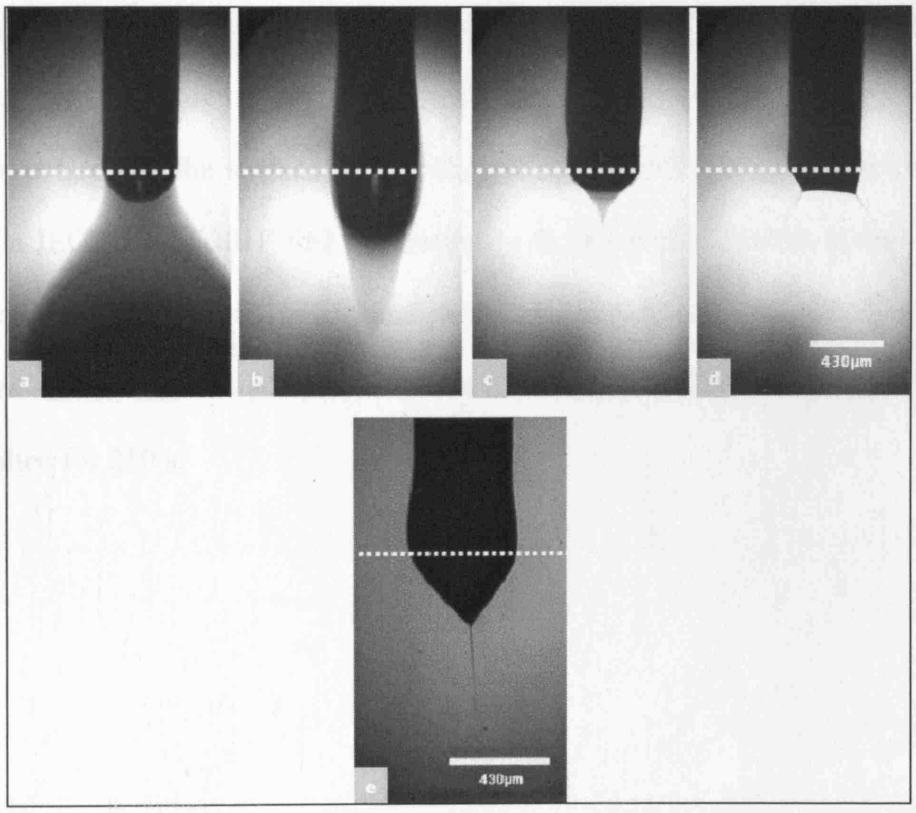

Figure 4.9 Different modes of atomisation at flow rate 5 x 10^{-11} $m^{-3}s^{-1}$ and at different applied voltages, (a) dripping at 0 kV (b) micro-dripping at 1.8 kV (c) unstable cone jet at 2.1 kV (d) multi jet 2.8 kV and (e) stable cone-jet at 2.3 kV

Figure 4.10 shows the classical droplet size distribution of the droplets generated by the jet break-up as detected using the Sympatec system. The droplet size generated was in the range of 0.4 – 2 μm in diameter. The spraying was carried out from 60 – 600 s. After spraying samples were left for drying under room temperature for 24 hrs before sintering in air. Prior to deposition, silicon substrates were cleaned with ethanol and dried under room temperature. The films then underwent heat treatment by ramping the temperature from the ambient temperature to 400 °C at 2 °C min^{-1} and held for 60mins before the films were cooled from 400 °C to ambient temperature at 2 °C min^{-1}.

The sintered samples were coated with carbon before examination by scanning electron microscopy (SEM) and energy dispersive X-ray analysis (EDX). The structure and the surface morphology of the sintered films were investigated using a JEOL JSM-6301F SEM operating in the secondary electron mode with an accelerating voltage of 10 kV and with the working distance up to 15 mm. **Figure 4.11** shows the plan view of the film and the thickness of centre of film deposited for 210 s.

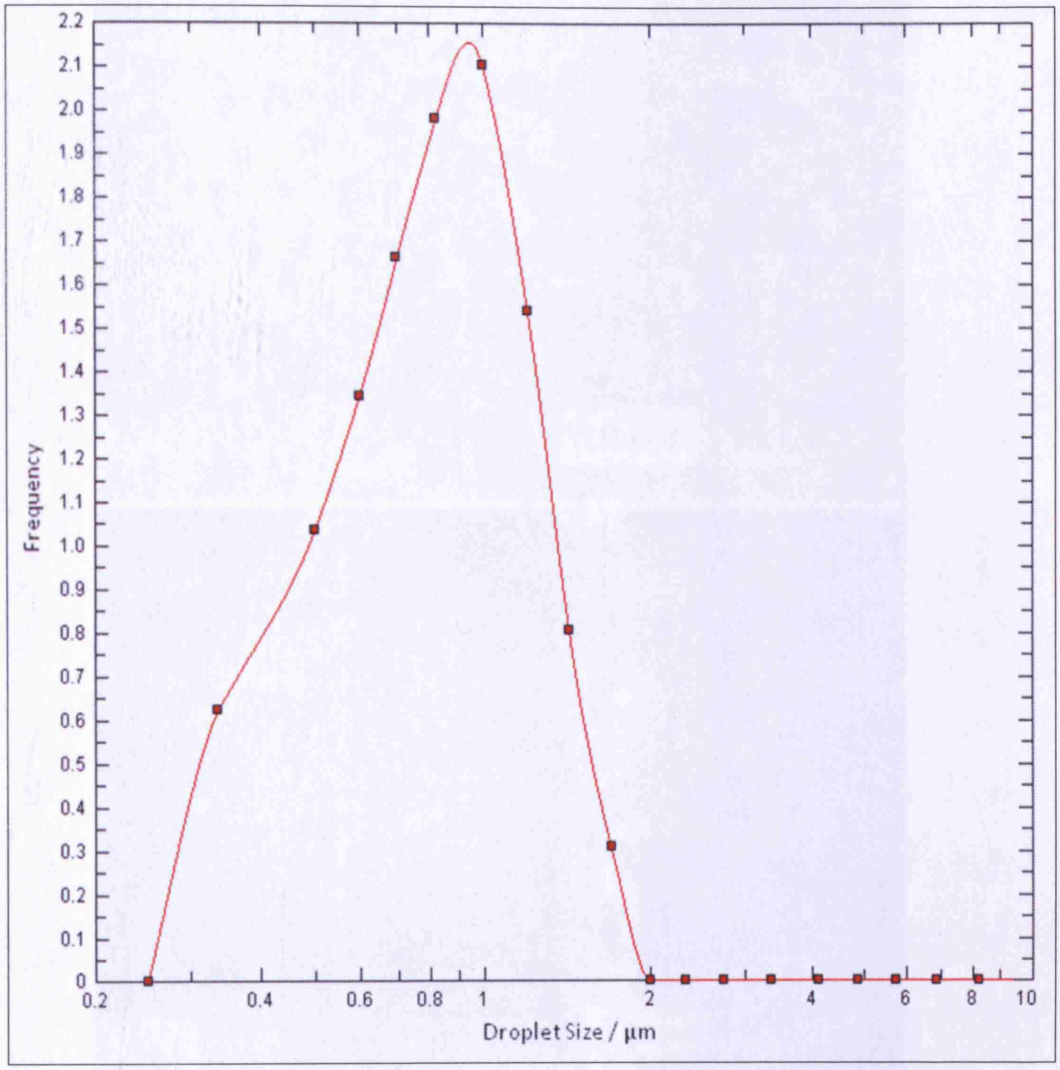

Figure 4.10 Droplet size distribution obtained for stable cone-jet mode electrohydrodynamic atomisation of gold alcosol

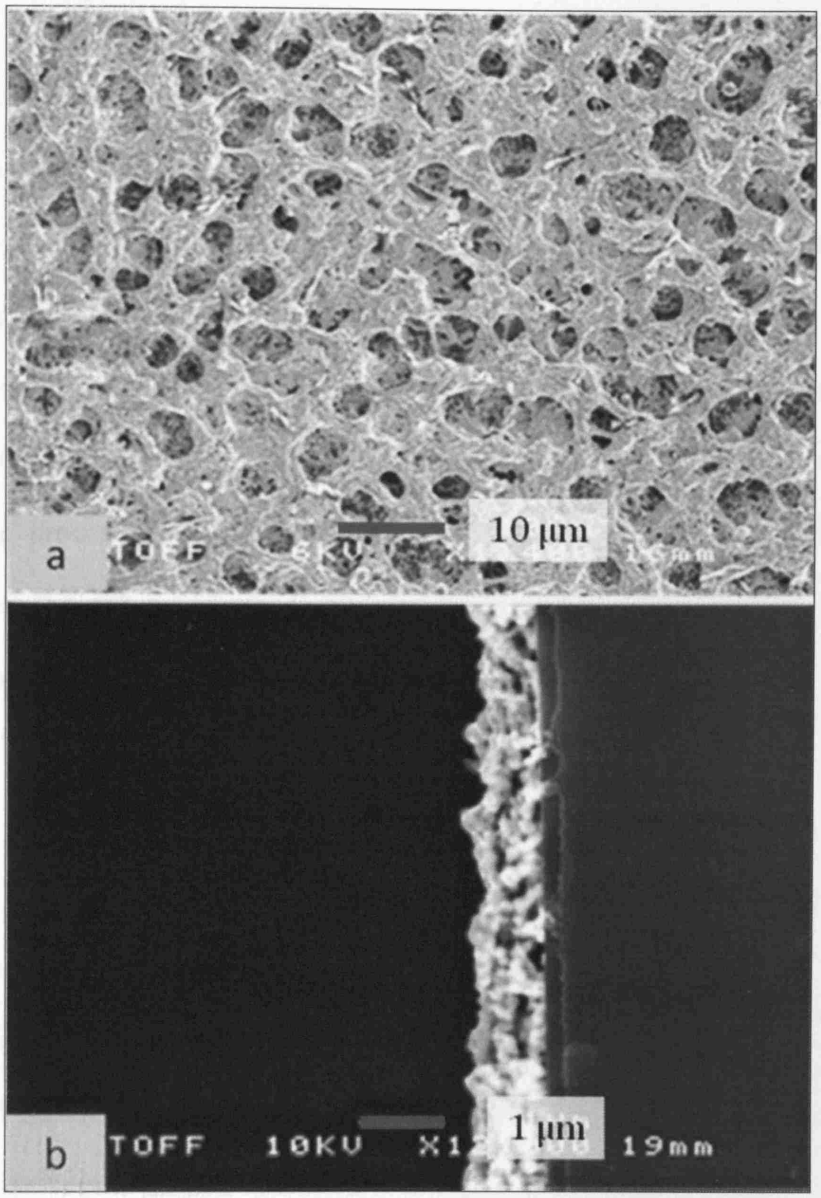

Figure 4.11 Gold film after 210 s of deposition. a) Plan view and b) thickness of centre of film

4.2.6 Electrohydrodynamic atomisation printing

The 2D printing device used for patterning was described in detail in Chapter 3. The electrohydrodynamic atomisation experiments carried out before were used as a guideline for the printing process. The flow rates were varied from the minimum to the maximum where a stable cone-jet could be observed. The voltage was gradually increased and patterning was carried out in the stable cone-jet mode. A point shaped ground electrode was used in order to converge the spray droplets to a particular area. Thereafter trial-and-error approach was used by varying processing parameters such as flow rate, applied voltage and distances between the ground electrode and needle to find out the optimum conditions for patterning.

4.2.6.1 Device configuration

During the printing process, a needle having an inner and outer diameter of ~200 μm and ~400 μm were used. After the 2 axis system was fully set-up, the predefined pattern was downloaded to the printing system. The needle and the ground electrode were aligned with each other. Throughout the printing process, the point shaped ground electrode was kept 4 mm below the silicon wafer. A high voltage power supply, which is capable of applying up to 30 kV, was used to apply the electric field between the needle and the ground electrode. The inlet of the needle was connected to a syringe pump using a silicone rubber tube. **Figure 4.12** shows a schematic diagram of the basic equipment set-up used in printing process.

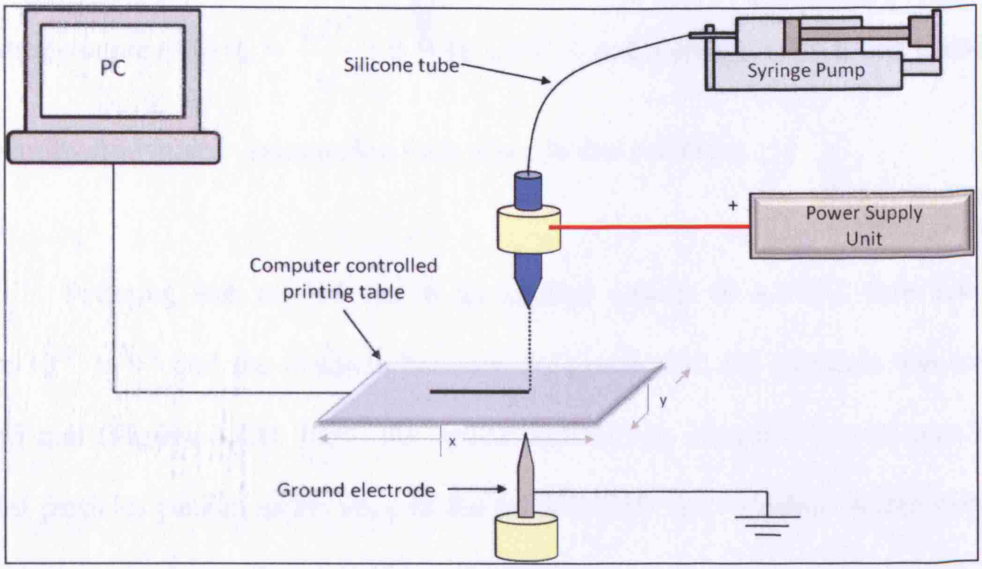

Figure 4.12 Schematic view of the printing process

4.2.6.2 Conditions for printing

Firstly, gold sphere shaped alcosol was used for patterning. Patterning was carried out at an applied voltage of 4.9 kV and a flow rate of 1 x 10^{-10} m^3s^{-1} with the distance between the needle exit and the silicon wafer varying from ~0.25, ~0.5, ~1mm. This patterning experiment suggested the most suitable distance for printing gold sphere shaped alcosol. Since all three alcosols have a very low concentration of metal particles and a similar behaviour under atomisation, it was assumed that all three alcosols would have the similar parameters for printing.

Secondly, patterning was carried out in the stable cone-jet mode at an applied voltage of 4.9 kV and a flow rate of 1 x 10^{-10} m^3s^{-1}. The electrical relaxation time ($t_e = \frac{\beta\varepsilon_0}{K}$) was 6.67 x 10^{-7} s where ε_0 is 8.85 x 10^{-12} Fm^{-1}. The jet diameter (D) and the jet length (L) were ~15 μm and ~250 μm respectively. The

hydrodynamic time ($t_h = \frac{LD^2}{Q}$) is 9.38 x 10^{-3} s, and therefore $t_e << t_h$ and classical electrohydrodynamic atomisation took place in this condition.

Pattering was carried out at an applied voltage of 4.9 kV, flow rate of 5 x 10^{-11} m^3s^{-1} and the distance between the needle and the substrate was set at ~0.5 mm (**Figure 4.13**). From the optical microscopy images it can be seen that most particles packed at the edge of the printed track and a random distribution of particles were observed at the centre of the track.

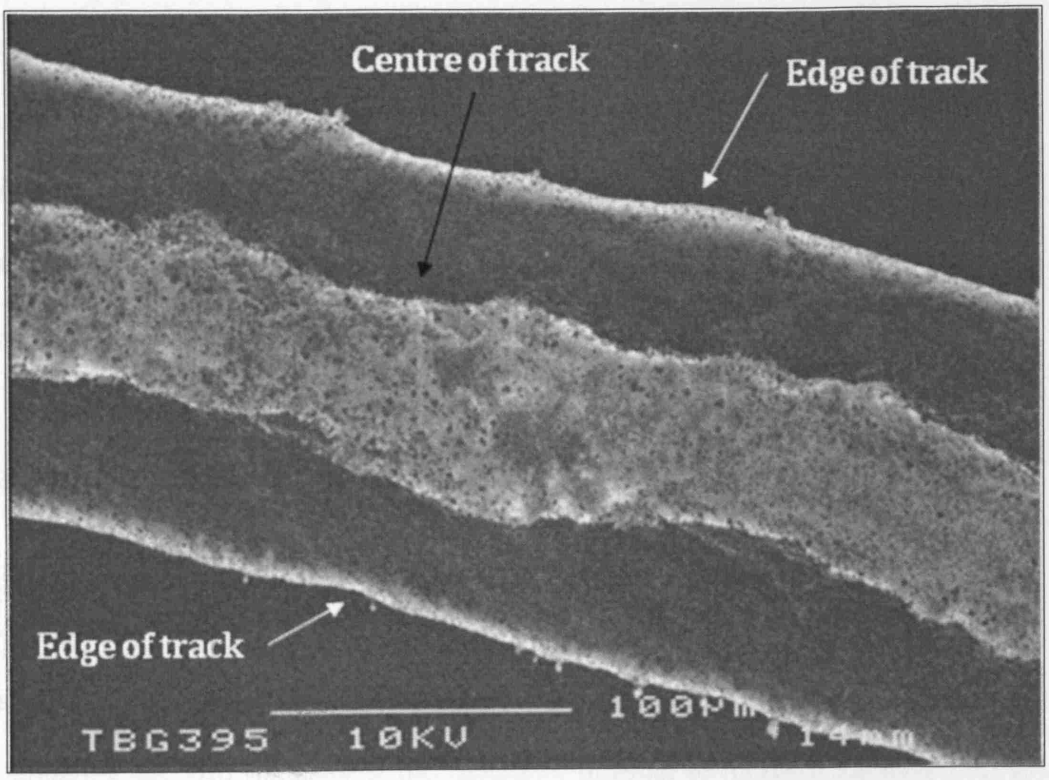

Figure 4.13 Gold track printed at 5 x 10^{-11} m^3s^{-1} flow rate and applied voltage 4.9 kV

4.2.7 Template assisted pattering

Due to rapid solvent evaporation, dense particle packing in the tracks produced by electrohydrodynamic atomisation printing was not possible. In order to achieve dense particle packing and to reduce the track size, templates were used in conjunction with droplets produced by atomisation.

4.2.7.1 Device configuration

The same equipment set-up used in the previous experiments was used. Briefly, a metal capillary was held in epoxy having an internal and external diameters of ~200 and ~400 μm, respectively. A high voltage power supply was connected to the needle and the inlet of the needle was connected to a syringe pump using silicone tube. The high speed camera was focused at the exit of the needle. A hot plate was used to keep the substrate temperature constant throughout the experiments and to evaporate the solvent from the droplets generated from atomisation (**Figure 4.14**).

4.2.7.2 Experimental details

Initially, the template was kept on top of the silicon wafer and the gold alcosol was sprayed for varying times. It was evident from the results that when the spraying time increases, the droplets produced from atomisation agglomerated thus damaging the grid patterns of the template. In order to increase the evaporation of the droplets, the substrate was kept on a hotplate at 50 °C before spraying. Various distances were tried out and it was found that the optimum distance for patterning tracks were ~3 mm away from the silicon wafer. When the distance was increased, more time was needed to produce densely packed tracks containing gold particles.

When the distance was decreased, no stable cone-jet mode was observed. The flow rate was kept at 5 x 10^{-11} m^3s^{-1} and the applied voltage was increased to 2.3 kV to obtain a stable cone-jet. The silicon wafer was placed with the template on top of the hot plate and spraying was carried out up to 240 s.

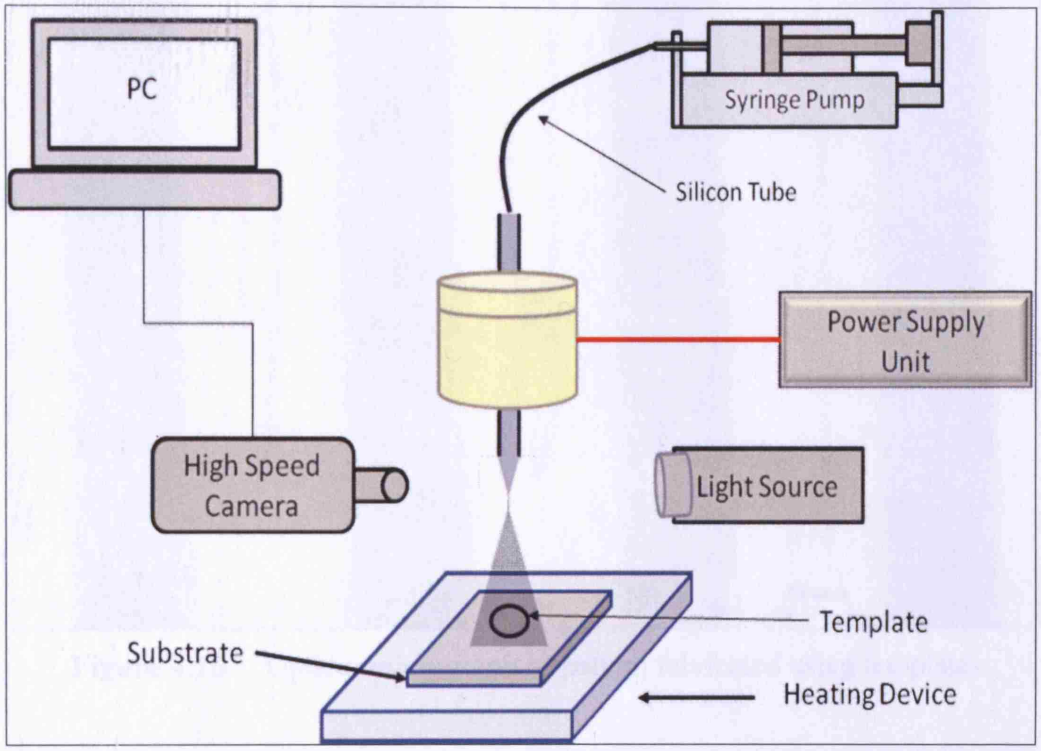

Figure 4.14 Schematic diagram of equipment set-up for templating

Thereafter, the sample was kept in an oven for 1 hr at 90 °C to evaporate any remaining solvent. **Figure 4.15** shows an optical micrograph of the Au tracks fabricated using templates. From the optical micrograph a dense particle arrangement can be observed. Microstructures patterned with the help of templates underwent heat treatment by ramping the temperature from the ambient temperature to 400 °C at 2 °C min^{-1} followed by annealing at 400 °C for a further

1 hr. Finally, the micro-patterns were cooled down from 400 °C to the ambient temperature at 2 °Cmin^{-1}.

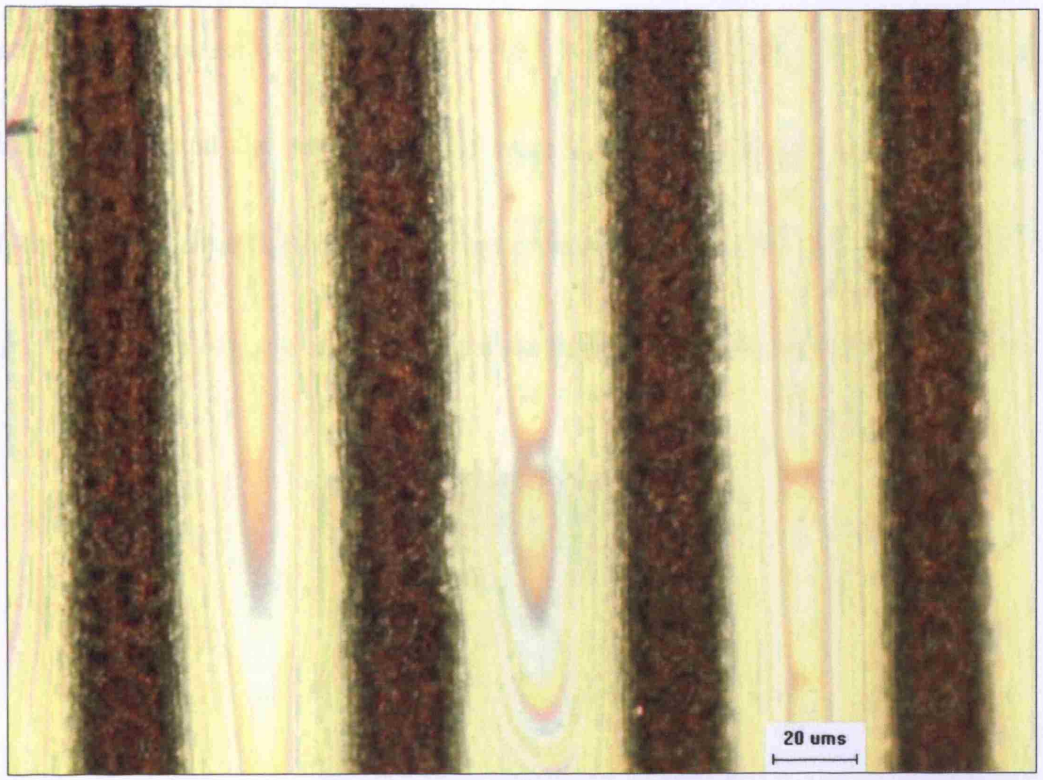

Figure 4.15 Optical micrograph of pattern fabricated using templates

4.3 Electrohydrodynamic atomisation of gold decahedral shaped alcosol

The same equipment set-up that was used in the previous section (**Figure 4.1**) was used for atomising the decahedral shaped gold alcosol. After setting up the equipment, the flow of the alcosol was varied at different flow rates and the voltage was gradually increased from 0 to 5 kV. Different modes of atomisation such as dripping, micro-dripping and cone-jet together with their numerous manifestations were observed from the high speed camera.

4.3.1 Characterisation of cone and jet

A stable cone-jet mode was observed at flow rate (Q) 2 x 10^{-11} m^3s^{-1} and applied voltage of 3.7 kV (**Figure 4.16**). The electrical relaxation time (t_e) for the atomisation process ($\frac{\beta\varepsilon_0}{K}$) was 6.7 x 10^{-7} s where ε_0 is 8.85 x 10^{-12} Fm^{-1}. The jet diameter (D) and the jet length (L) were 8 μm and 150 μm respectively. The hydrodynamic time (t_h) for atomisation process ($\frac{LD^2}{Q}$) is 9 x 10^{-3} s, and therefore $t_e << t_h$ and classical electrohydrodynamic atomisation took place in this condition.

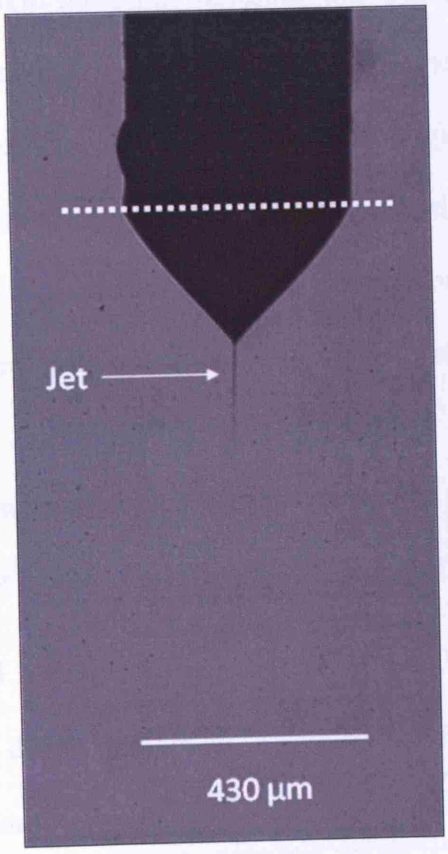

Figure 4.16 A stable cone-jet mode of decahedral shaped alcosol at flow rate 2 x 10^{-11} m^3s^{-1} and applied voltage of 3.7 kV. Dotted line indicates the needle exit

4.3.2 Effect of applied voltage

In order to find out the effect of voltage, the flow rate of the alcosol was changed systematically and the applied voltage was varied from 0 to 5 kV. A stable cone jet mode was observed in the flow rate range of 10^{-11} to 10^{-10} m^3s^{-1} and applied voltage range of 3.6 to 4.3 kV. When the applied voltage was gradually increased from 0 kV, the mode of atomisation changed from dripping to micro-dripping. When the voltage was further increased, spindle and unstable cone-jet mode was observed and thereafter stable cone-jet mode was observed. When the applied voltage was increased further, multi-jetting mode was observed. **Figure 4.17** shows different modes of atomisation at a flow rate of 5 x 10^{-11} m^3s^{-1}. When the voltage was increased from the minimum value for stable cone-jet, the cone depth as well as the diameter of the jet reduced. **Figure 4.18** shows the cone variations with the increasing applied voltage when the alcosol is forced at 2 x 10^{-11} m^3s^{-1}. **Table 4.5** gives more detailed information about the depth of the cone, and the jet diameter variations at flow rate 2 x 10^{-11} m^3s^{-1}.

Table 4.5 The changes of cone and jet of decahedral shaped gold alcosol at a flow rate of 2 x 10^{-11} m^3s^{-1} with different applied voltages

Applied Voltage (kV)	3.7	3.9	4.1
Cone depth (μm)	278	129	104
Jet diameter (μm)	8	6	5

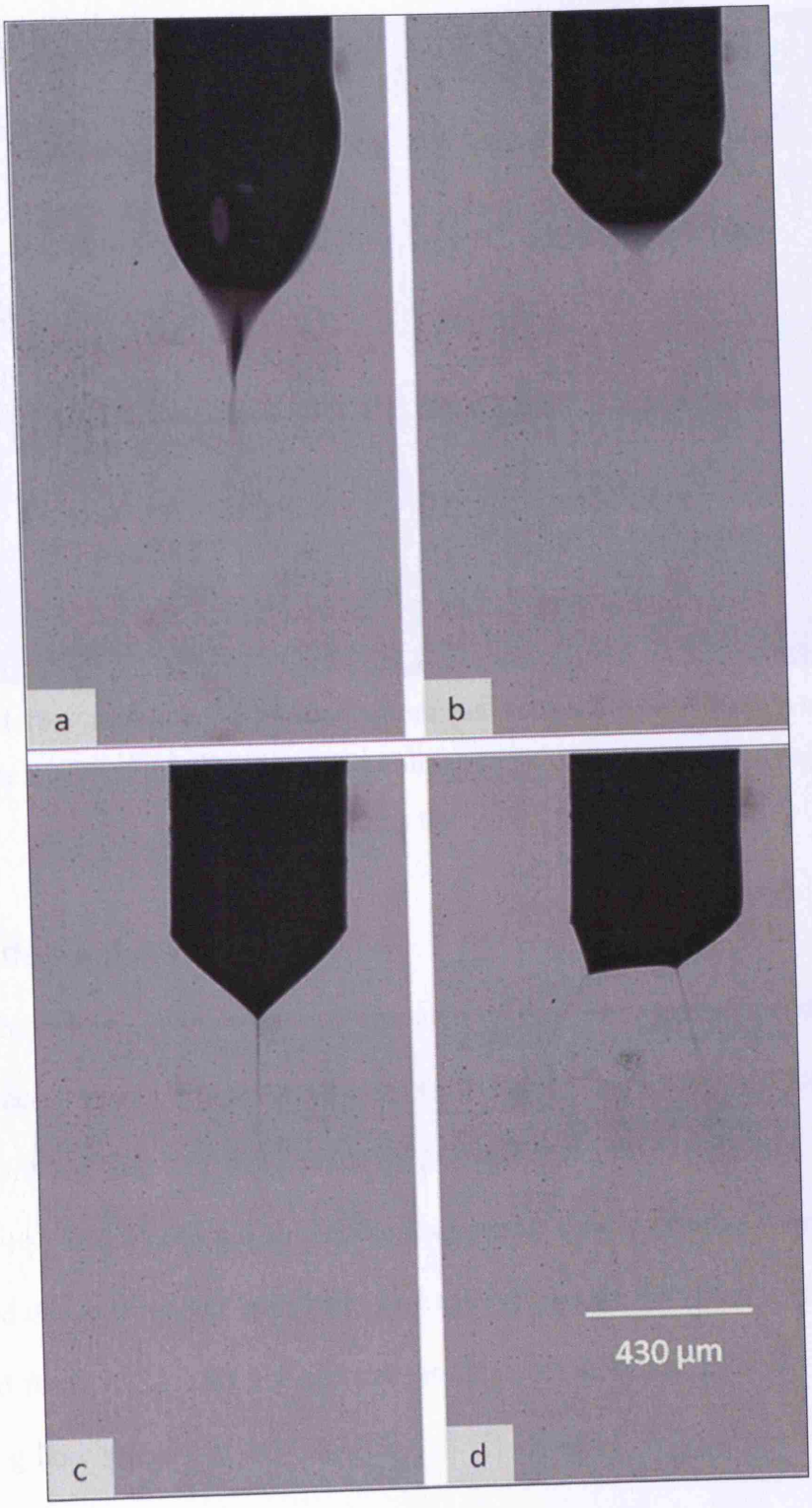

Figure 4.17 Different modes of atomisation observed at 5 x 10^{-11} m^3s^{-1}. a) Spindle mode at 3.4 kV, b) Unstable cone-jet mode at 3.5 kV, c) Stable cone-jet mode at 3.6 kV and d) Multi-jetting mode at 4.3 kV

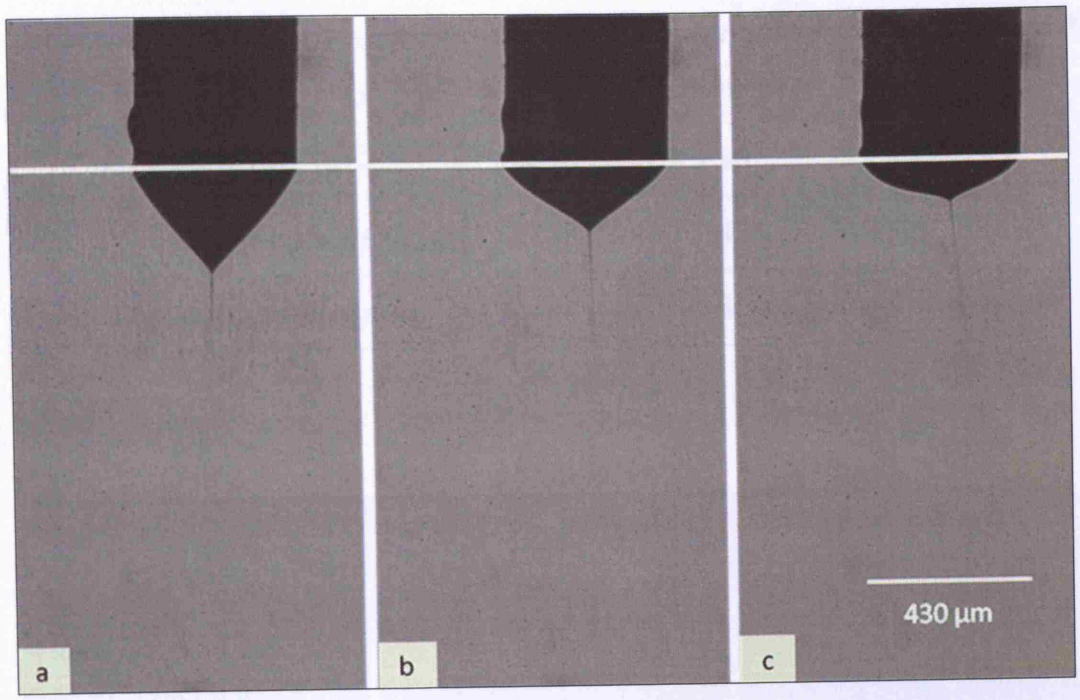

Figure 4.18 Stable cone-jet mode atomisation of decahedral shaped alcosol at flow rate 2 x 10^{-11} m^3s^{-1} and applied voltage a) 3.7 kV, b) 3.9 kV and c) 4.1 kV. White line indicates the exit of the needle

4.3.3 Effect of flow rate

The change in the flow rate can affect the jet and cone significantly in the stable cone-jet mode. **Figure 4.19** shows the stable cone-jet mode obtained at the voltage 3.9 kV and the flow rates of 2 x 10^{-11}, 4 x 10^{-11} and 5 x 10^{-11} m^3s^{-1} respectively. The **Table 4.6** shows the changes in a more detailed form. The cone depth and the jet diameter both increased with increasing flow rate. The cone depth increased from 129 – 180 µm and the jet diameter increased from 6 – 9 µm with increasing flow rate.

Table 4.6 The changes of cone and jet of decahedral shaped alcosol at applied voltage 3.9 kV and at different flow rates

Flow rate (m^3s^{-1})	2×10^{-11}	4×10^{-11}	5×10^{-11}
Cone depth (µm)	129	142	180
Jet diameter (µm)	6	8	9

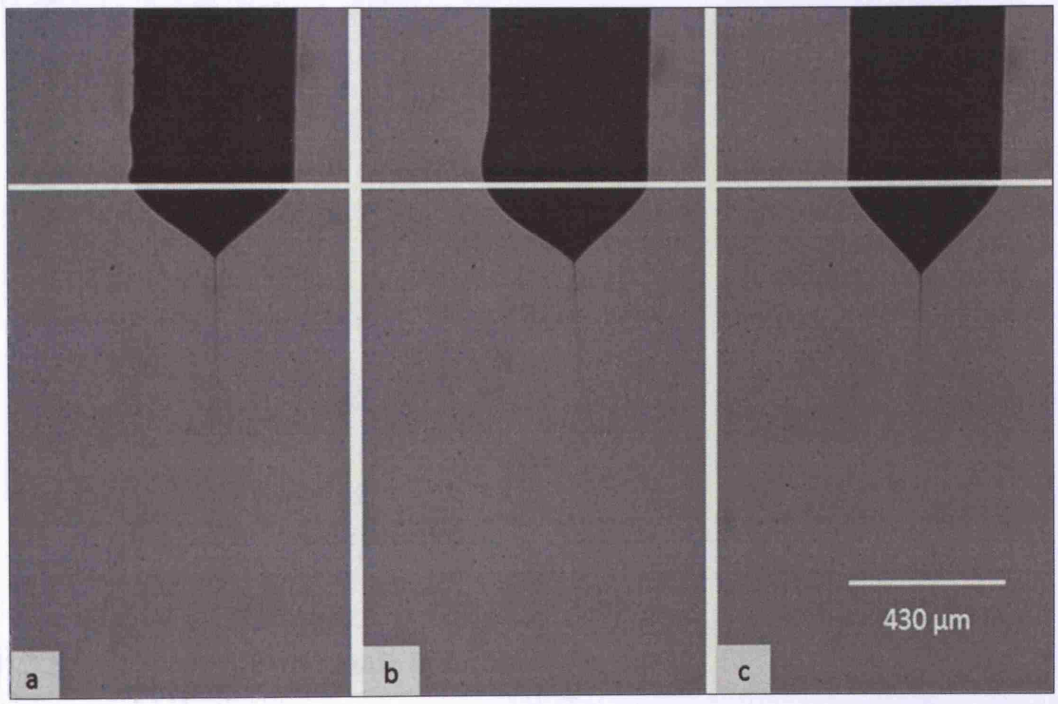

Figure 4.19 Stable cone-jet mode of atomisation of decahedral shaped alcosol at an applied voltage of 3.9 kV and different flow rates. a) 2×10^{-11} m^3s^{-1}, b) 4×10^{-11} m^3s^{-1} and c) 5×10^{-11} m^3s^{-1}

4.3.4 Mode selection map

The flow rate of the decahedral shaped gold alcosol was varied systematically and the applied voltage was varied from 0 – 5 kV. Different modes of atomisation such as dripping, micro-dripping, unstable cone-jet, cone-jet and multi jetting were observed. The different modes of jetting taking place in the

parametric space of flow rate and electric field were studied and these results were plotted (**Figure 4.20**). This map can help us to select the region where the condition meets printing.

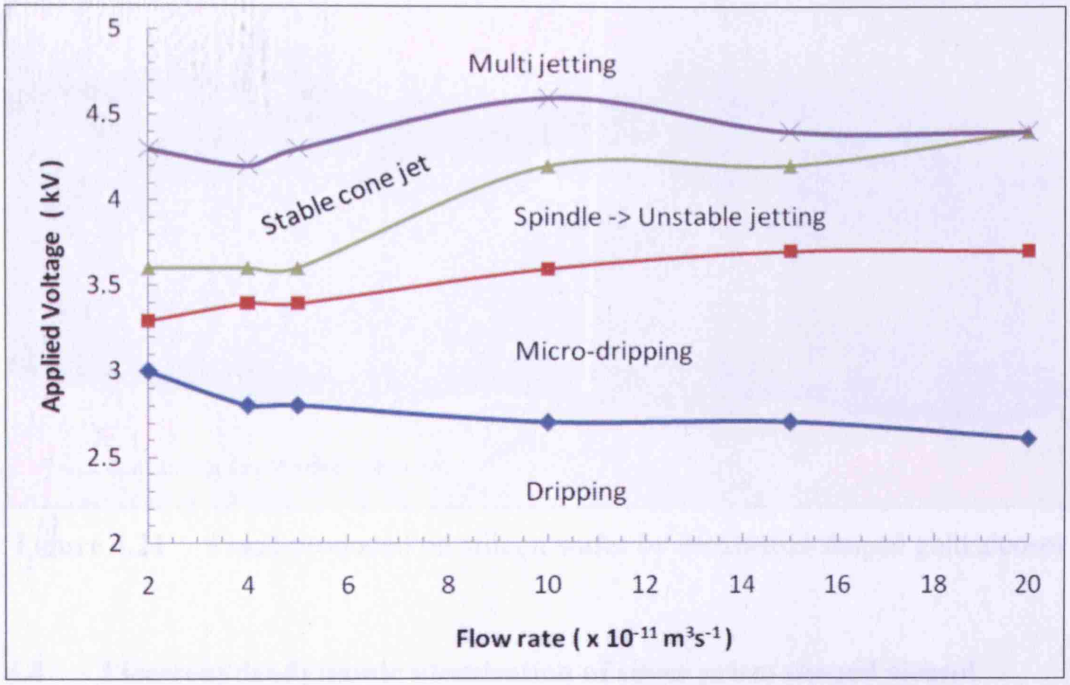

Figure 4.20 Mode selection map for gold decahedral shaped alcosol

4.3.5 Electrohydrodynamic atomisation printing

The printing equipment was set-up and the needle and ground electrode were aligned. The gold decahedral particle shaped gold alcosol was forced through the capillary and was ~0.5 mm away from the substrate. The flow rate was set at 1 x 10^{-10} m^3s^{-1} and the applied voltage of 3.9 kV was used to pattern microstructures onto silicon wafers. **Figure 4.21** shows an optical micrograph of the printed track using the above mentioned conditions.

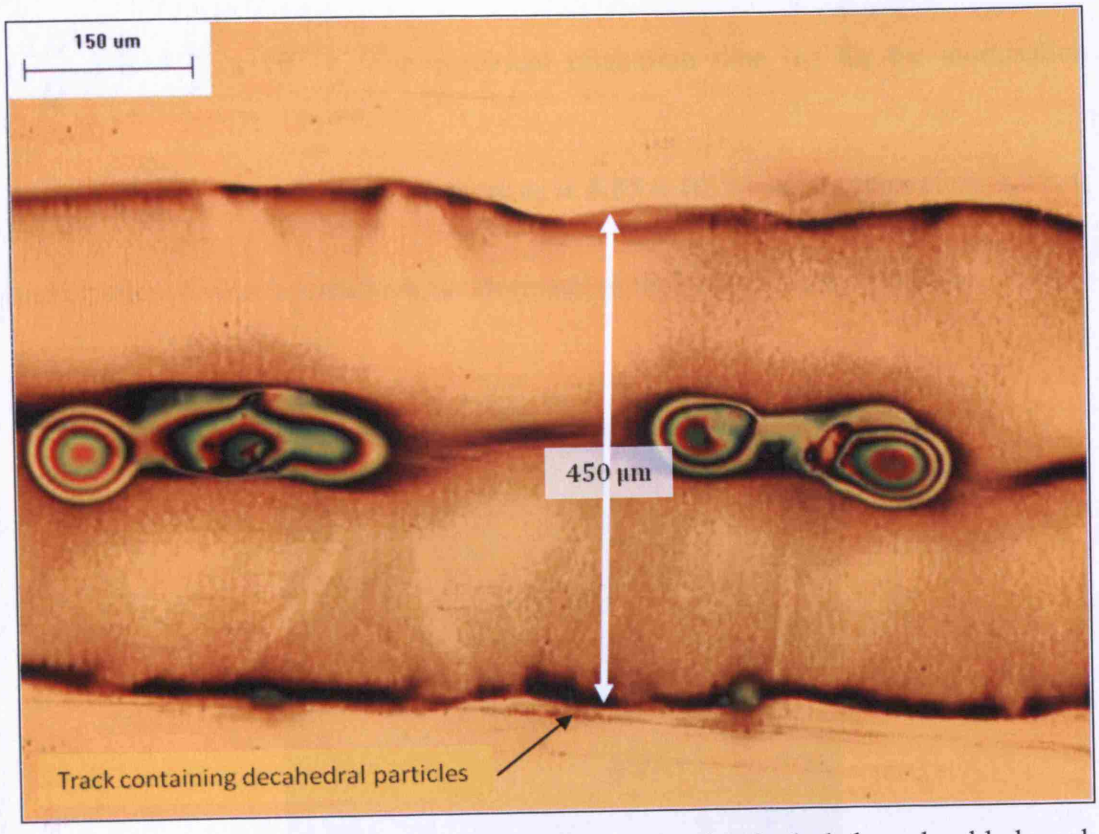

Figure 4.21 Track produced on silicon wafer by decahedral shaped gold alcosol

4.4 Electrohydrodynamic atomisation of silver prism shaped alcosol

The same equipment set-up used before for electrohydrodynamic atomisation of gold was used. Briefly, a metal capillary was connected to a high voltage power supply. The inlet of the capillary was connected to a prefusor pump by silicone tube. A high speed camera was focused at the exit of the capillary. A ring shaped ground electrode was kept 15 mm below the needle exit.

4.4.1 Characterisation of cone and jet

The silver alcosol was subjected to electrohydrodynamic atomisation and a stable cone jet mode was observed at flow rate (Q) 1.5 x 10^{-10} m^3s^{-1} and applied voltage of 3.9 kV (**Figure 4.22**). The jet length (L) was ~175 µm and the jet diameter (D) was ~9 µm. The hydrodynamic time (t_h) for atomisation process

($\frac{LD^2}{Q}$) is 4.73 x 10^{-4} s. The electrical relaxation time (t_e) for the atomisation process ($\frac{\beta\varepsilon_0}{K}$) was 6.7 x 10^{-7} s where ε_0 is 8.85 x 10^{-12} Fm^{-1} and therefore, $t_e << t_h$ and classical electrohydrodynamic atomisation took place in this condition.

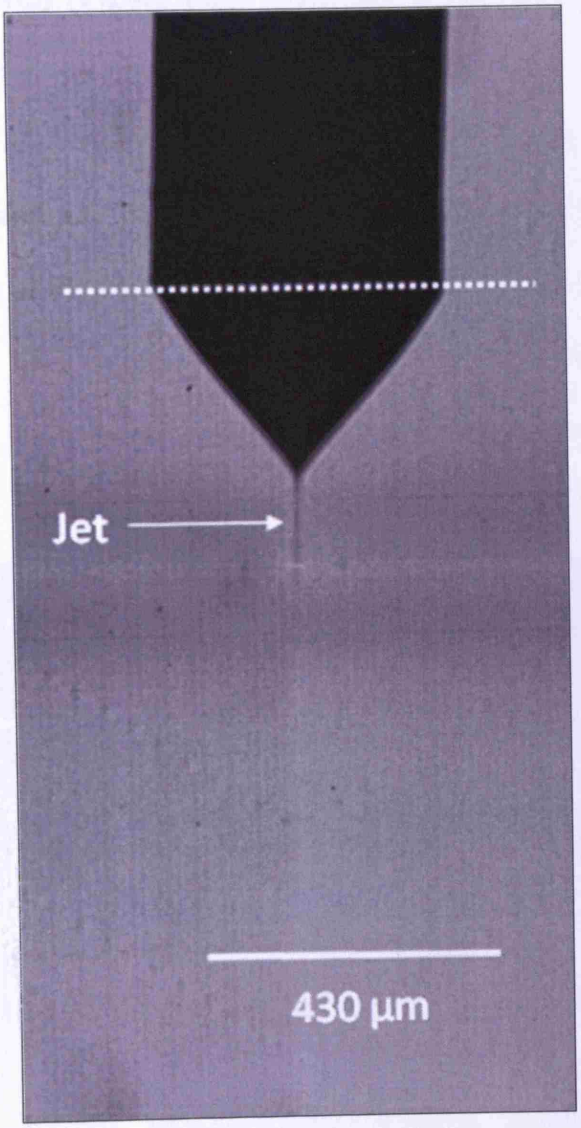

Figure 4.22 A stable cone-jet mode of silver alcosol at flow rate 1.5 x 10^{-10} m^3s^{-1} and applied voltage of 3.9 kV

4.4.2 Effect of applied voltage

The applied voltage in electrohydrodynamic atomization plays an important role. Experiments were carried out to observe the effect of voltage when the silver alcosol is undergoing electrohydrodynamic atomization. A stable cone-jet mode was obtained at the flow rate of 1 x 10^{-10} m^3s^{-1} with applied voltages 3.7 kV, 3.9 kV and 4.1 kV respectively (**Figure 4.23**). Multi jetting was observed when the voltage was increased further. As explained in the previous sections, when increasing the voltage, the shape of the cone as well as the length of the jet changes. When the voltage was increased the depth of the cone as well as the diameter of the jet reduces. The depth of the cone was reduced from 295 to 171 μm. The jet diameter was reduced from 10 – 6 μm. **Table 4.7** shows the changes to the depth of the cone as well as the jet diameter with increasing applied voltage.

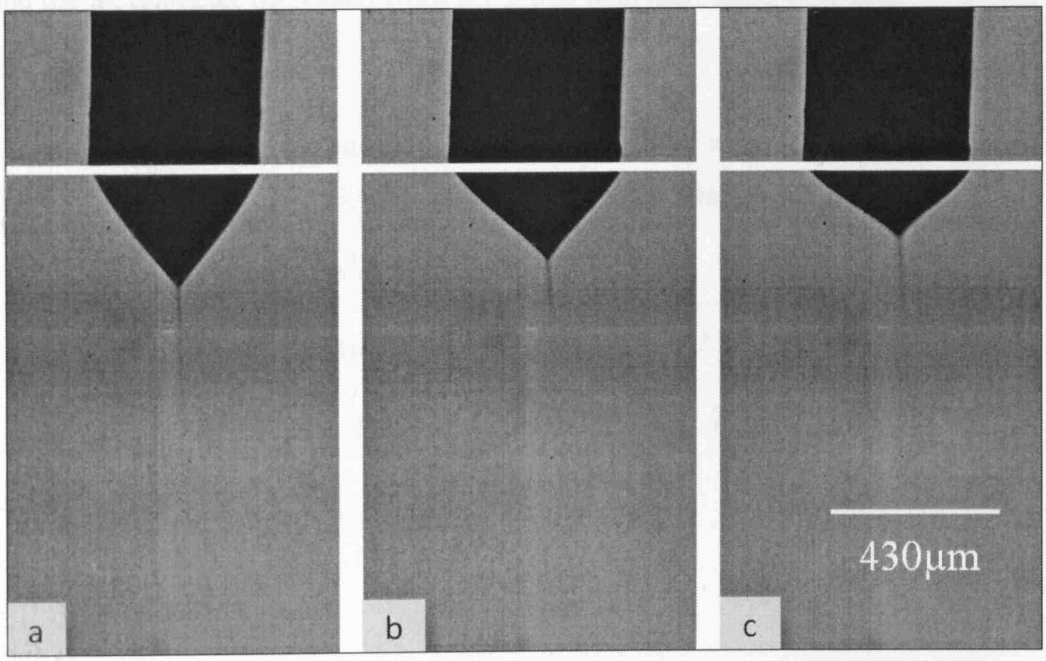

Figure 4.23 Stable cone-jet mode atomisation of silver alcosol at flow rate 1 x 10^{-10} m^3s^{-1} and applied voltage a) 3.7 kV b) 3.9 kV and c) 4.1 kV. White line indicates the exit of the needle

Table 4.7 The changes of cone and jet of silver alcosol at flow rate 1×10^{-10} m^3s^{-1} with different applied voltages

Applied Voltage (kV)	3.7	3.9	4.1
Cone depth (μm)	295	234	171
Jet diameter (μm)	10	8	6

4.4.3 Effect of flow rate

The change in the flow rate can affect the jet and the cone significantly in the stable cone-jet mode. **Figure 4.24** shows the stable cone-jet mode obtained at the voltage 3.9 kV and the flow rate of 5×10^{-11}, 1×10^{-10} and 1.5×10^{-10} m^3s^{-1} respectively. **Table 4.8** shows the changes in the cone depth and the diameter of the jet with increasing flow rate. The cone depth and the jet diameter both increased with increasing flow rate. The cone depth increased from 161 – 292 μm and the jet diameter increased from 6 – 9 μm with increasing flow rate.

Table 4.8 The changes of cone and jet of silver alcosol at applied voltage 3.9 kV and different flow rates

Flow rate (m^3s^{-1})	5×10^{-11}	1×10^{-10}	1.5×10^{-10}
Cone depth (μm)	161	234	292
Jet diameter (μm)	6	8	9

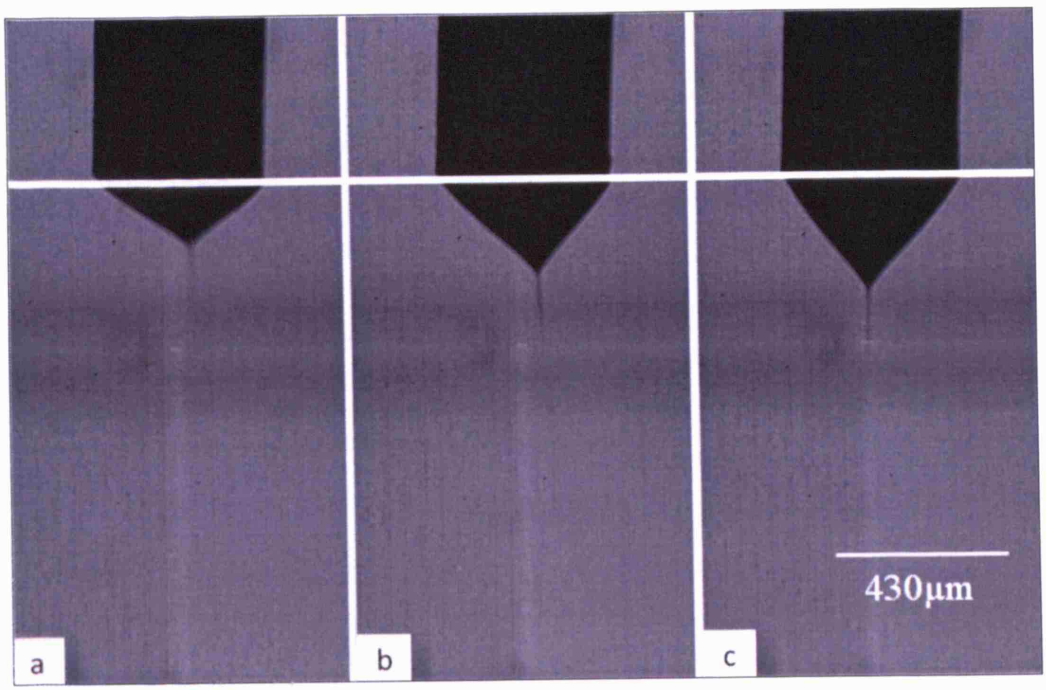

Figure 4.24 Stable cone-jet mode of atomisation of silver alcosol at applied voltage of 3.9 kV and different flow rates. a) 5 x 10^{-11} m^3s^{-1} b) 1 x 10^{-10} m^3s^{-1} and c) 1.5 x 10^{-10} m^3s^{-1}

4.4.4 Mode selection map

The flow rate of the silver alcosol was varied systematically and the applied voltage was varied from 0 to 5 kV. Different modes of atomisation such as dripping, micro-dripping, spindle, unstable cone-jet, cone-jet and multi jetting were observed. The different modes of jetting taking place in the parametric space of flow rate and electric field were studied and these results were plotted (**Figure 4.25**). This map can help us to select the region where the condition reaches printing.

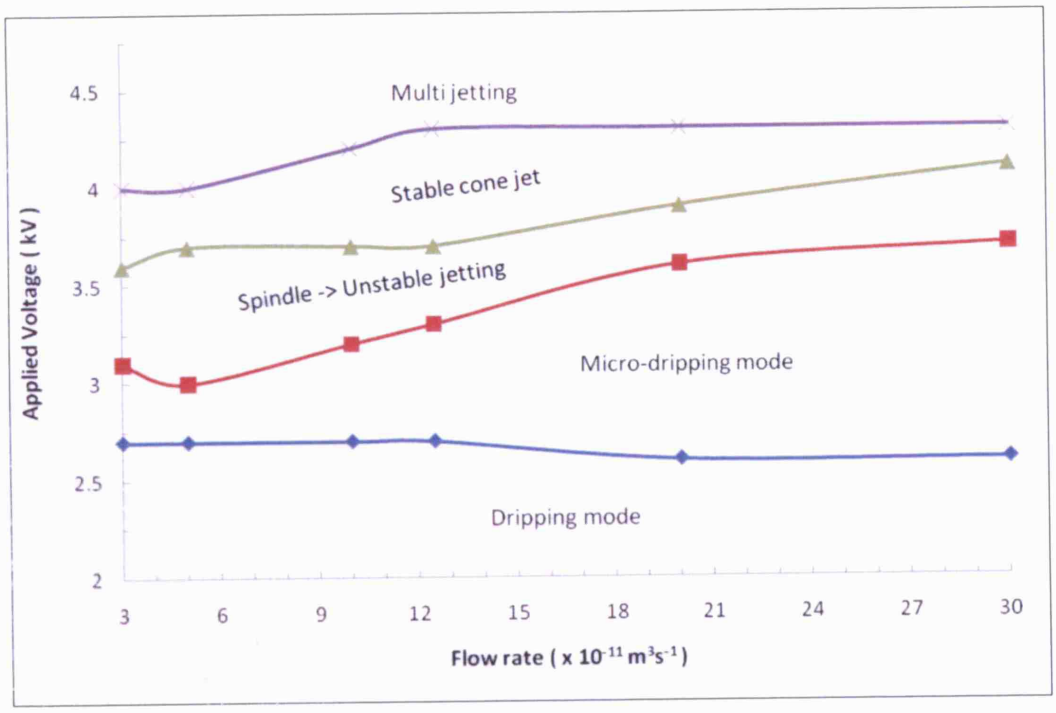

Figure 4.25 Different modes of atomisation observed when the silver alcosol was subjected electrospraying with varying flow rate and applied voltage.

4.4.5 Electrohydrodynamic atomisation printing

The printing equipment was set-up and the needle and ground electrode were aligned. The silver prism shaped alcosol was forced through the capillary and was ~0.5 mm away from the substrate. The flow rate was set at 1 x 10^{-10} m^3s^{-1} and the applied voltage of 3.9 kV was used to pattern microstructures onto silicon wafer. **Figure 4.26** shows an optical micrograph of the printed track using the above named conditions.

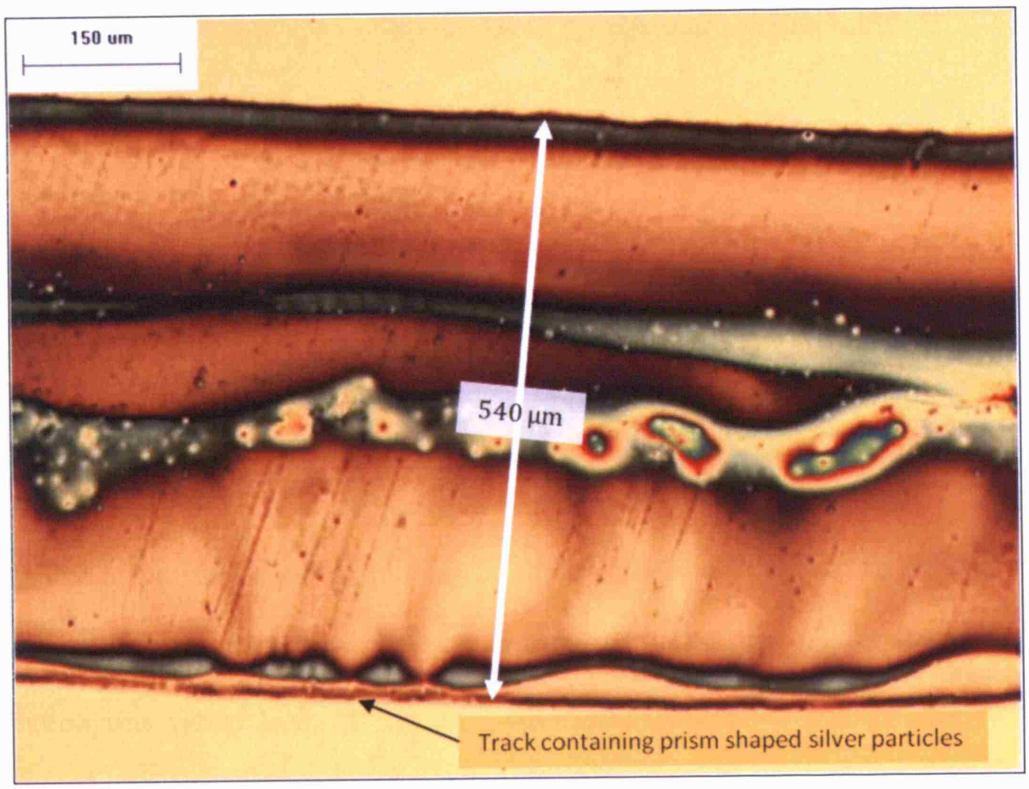

Figure 4.26 Track produced on silicon wafer by silver alcosol

4.5 Encapsulation of metal particles by co-axial jetting

An electrical charged jet of polymer solution was used to encapsulate the gold nanoparticles and silver micron size particles using co-axial dual needle jetting. Initially, both the polymer solution and the silver suspension were atomised using the same equipment setup used in the previous electrohydrodynamic studies, but without a ring shaped ground electrode.

4.5.1 Single needle jetting of polymer mixture

The polymer mixture was prepared and characterised before atomisation as explained in Chapter **3**. The properties of the polymer solution are given in **Table 4.9**.

Table 4.9 Properties of the polymer solution

Property	Value
Density (ρ) / kgm^{-3}	1070
Surface Tension (γ) / mN/m	72
Viscosity (η) / mPa s	2148
Electrical Conductivity (K) / Sm^{-1}	4×10^{-2}

The polymer solution was forced through the needle having an internal and external diameter of 510 and 810 μm respectively. The flow rate of the polymer solution was varied from 10^{-5} to 10^{-14} m^3s^{-1} and the applied voltage was varied from 0 to 10 kV. The polymer solution underwent stable electrospinning in the flow rate regime of 10^{-11} to 10^{-8} m^3s^{-1} and applied voltage between 4.6 and 6.2 kV. **Figure 4.27** shows different jet pictures at various flow rates and applied voltages. By varying the flow rate and applied voltage, fibres having a diameter of ~1 to ~40 μm were produced.

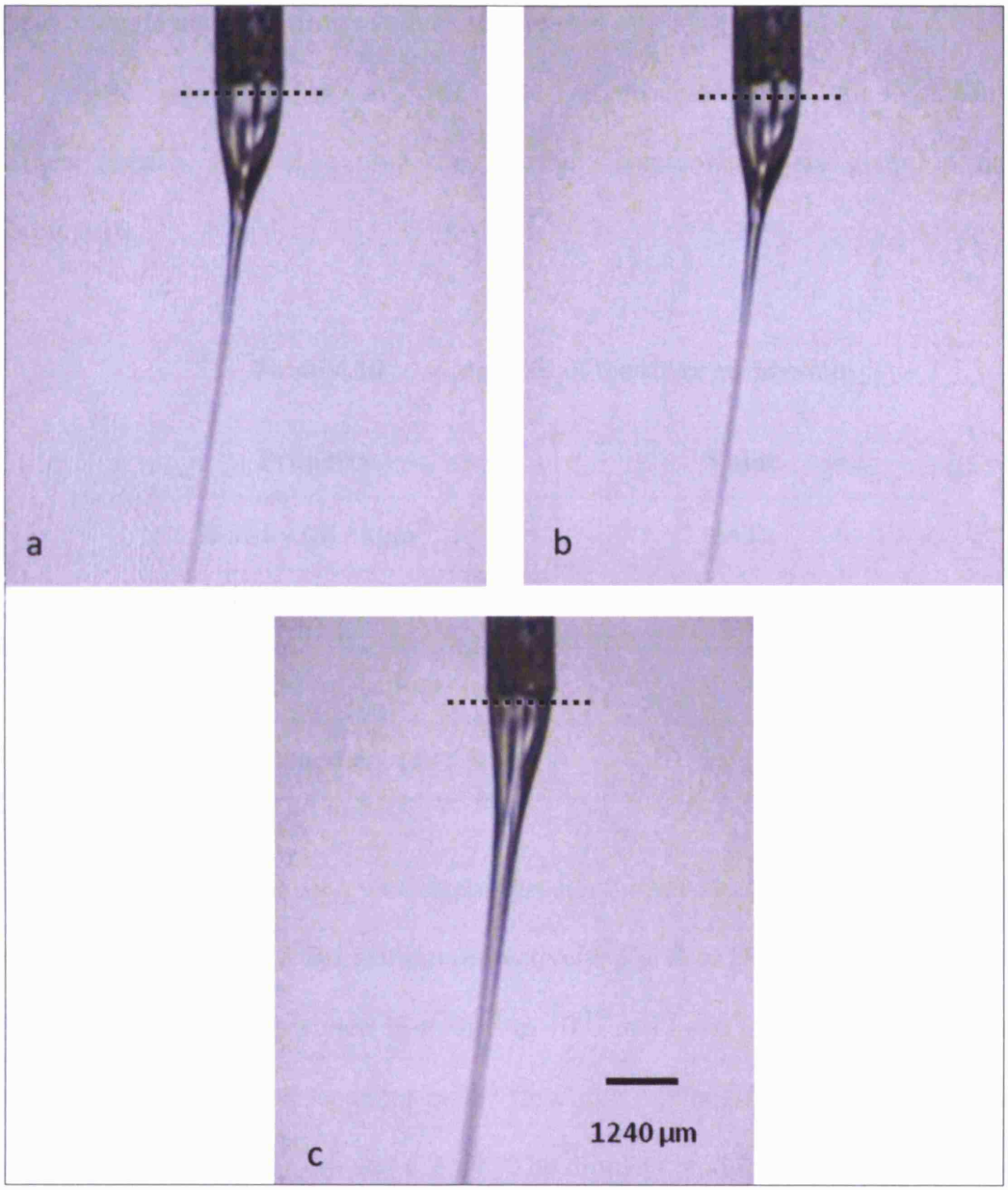

Figure 4.27 Single jetting of the polymer solution at different flow rates.

a) Flow rate was 1 x 10^{-10} m^3s^{-1} and the applied voltage was 4.9 kV;

b) Flow rate was 1 x 10^{-9} m^3s^{-1} and the applied voltage was 4.7 kV;

c) Flow rate was 2 x 10^{-9} m^3s^{-1} and applied voltage was 5.7 kV.

Dotted line indicates needle exit

4.5.2 Single needle jetting of silver suspension

The silver suspension was used as received from the company (Sigma-Aldrich, UK). The properties of the silver solution are given in the **Table 4.10**.

Table 4.10 Properties of the silver suspension

Property	Value
Density (ρ) / kgm^{-3}	1630
Surface Tension (γ) / mN/m	30
Viscosity (η) / mPa s	250 – 500
Electrical Conductivity (K) / Sm^{-1}	4×10^{-8}

The silver suspension was forced through the needle having an internal and external diameter of 510 and 810 μm respectively. The flow rate of the solution and the applied voltage was varied from 10^{-5} to 10^{-14} m^3s^{-1} and 0 – 10 kV. The silver suspension gave a stable cone-jet in the flow rate regime 10^{-11} to 10^{-9} m^3s^{-1} and applied voltage between 4.6 and 6.2 kV. The droplets produced from jet break-up were collected on microscopic slides and observed under optical microscopy. **Figure 4.28** shows the silver suspension subjected to electrohydrodynamic atomisation in the cone-jet mode at different flow rates. **Figure 4.29** shows an optical image of the droplets obtained from the cone-jet mode. The droplet size ranges from few micrometers to ~100 μm in diameter. Whenever the voltage exceeded these limits, the solvent in the silver suspension evaporated literally at the exit. This resulted in agglomeration of silver particles around the needle exit.

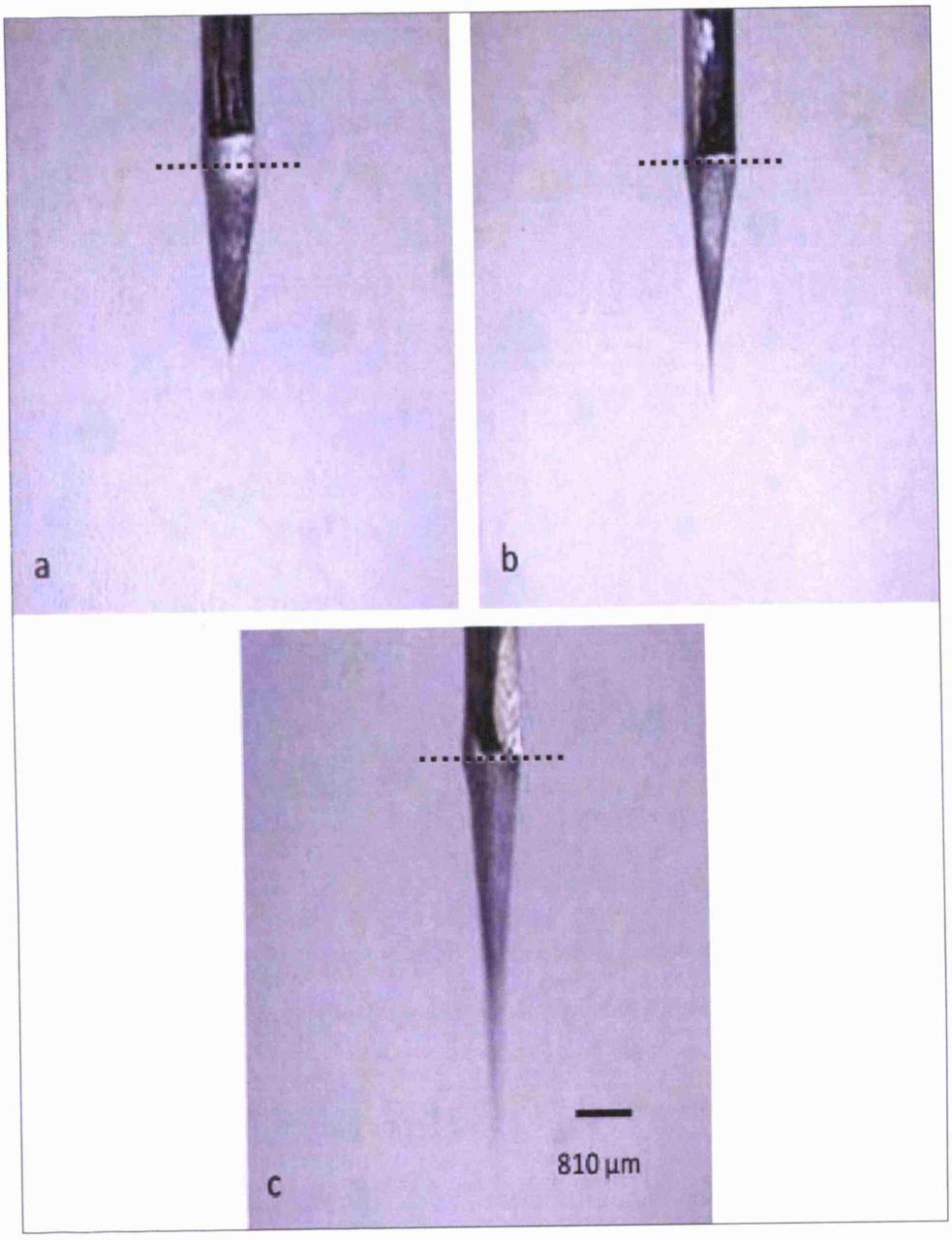

Figure 4.28 Single jetting of the silver suspension at different flow rates. a) Flow rate was 1 x 10^{-10} m^3s^{-1} and the applied voltage is 6.4 kV; b) Flow rate is 1 x 10^{-9} m^3s^{-1} and the applied voltage is 7.9 kV; c) Flow rate is 2 x 10^{-9} m^3s^{-1} and applied voltage is 6.7 kV. Dotted line indicated the needle exit

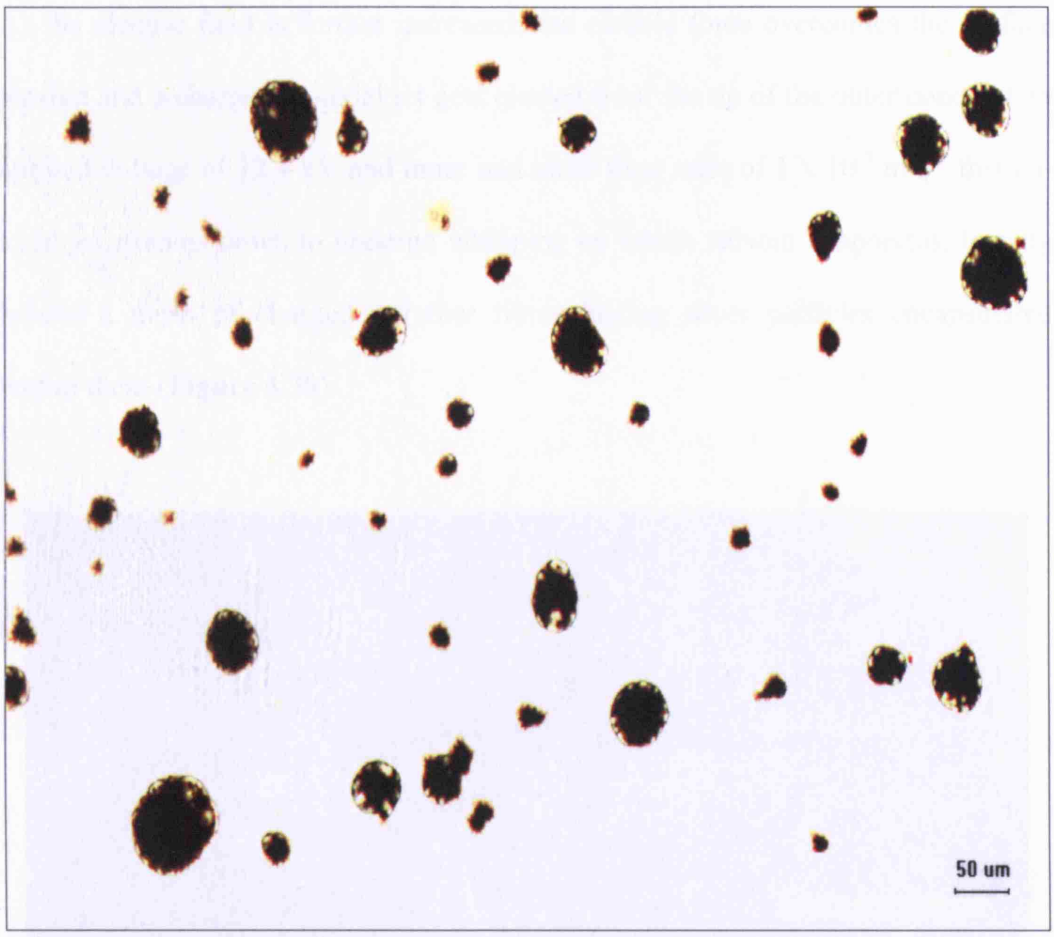

Figure 4.29 Droplet-relics produced from electrohydrodynamic atomisation of silver suspension. Flow rate is $1x10^{-9}$ m^3s^{-1} and the applied voltage is 7.9 kV

4.5.3 Encapsulation of silver particles

After the co-axial needle set-up was configured, the silver suspension was forced through the inner needle and the polymer solution through the outer needle. Firstly, the silver suspension was forced through the inner needle and the applied voltage was increased gradually. Subsequently, polymer solution was pumped through the outer needle and simultaneously the applied voltage was increased in order to maintain the stability of the co-axial jet. With the increase of applied voltage, a cone of polymer solution completely surrounding an inner cone of silver suspension evolved and this co-axial cone obtained was held by its surface tension.

As the electric field is further increased, the electric force overcomes the surface tension and a charged co-axial jet gets ejected from the tip of the outer cone. At an applied voltage of 12.4 kV and inner and outer flow rates of 1 x 10^{-9} m^3s^{-1} this co-axial jet streams down to undergo whipping by which solvent evaporates, leaving behind a mesh of charged polymer fibres having silver particles encapsulated within them (**Figure 4.30**).

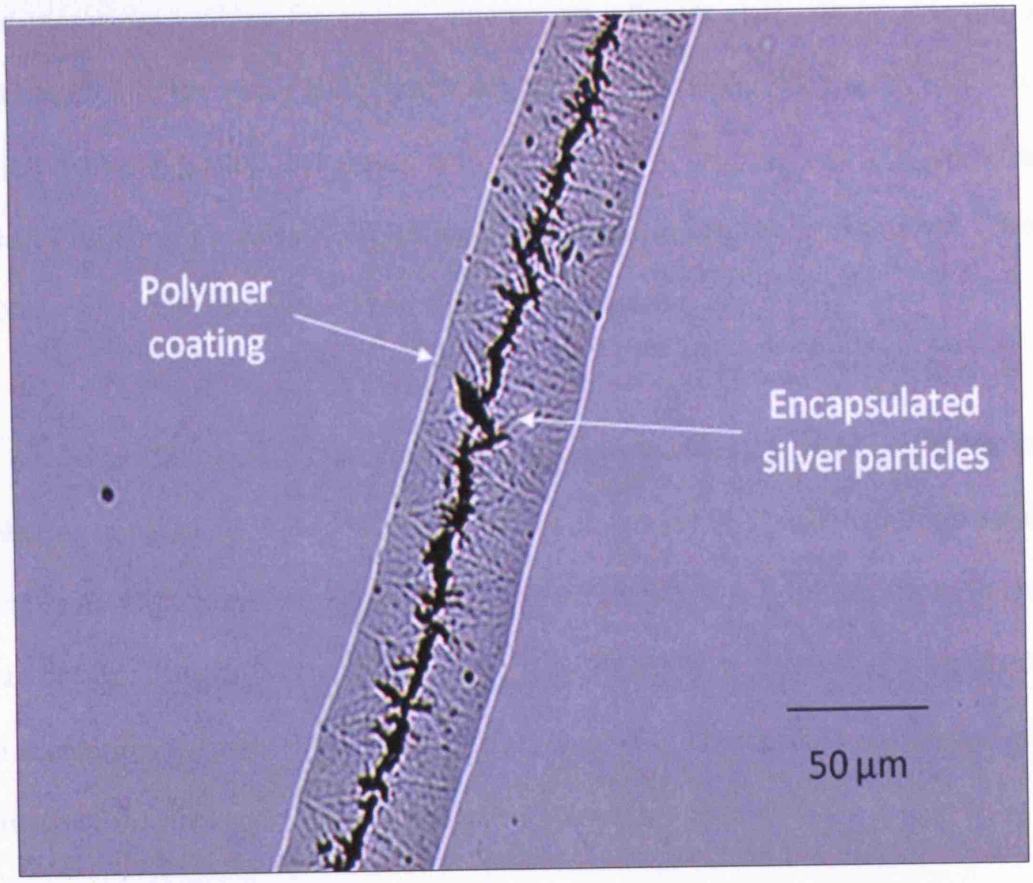

Figure 4.30 Optical micrograph of a fibre produced by co-axial electrospinning

4.5.4 Encapsulation of gold nanoparticles

In order to encapsulate nanoparticles, the gold hydrosol was used together with the polymer mixture. After the co-axial needle set-up was configured, the gold hydrosol was forced through the inner needle and the polymer mixture was forced through the outer needle at different flow rates. The voltage was increased gradually until stable electrospinning was observed. The flow rates and applied voltages were varied and fibres resulting from the spinning process were collected on microscope slides for optical microscopy. **Figure 4.31** shows an optical micrograph of the fibres laying randomly on the glass slide. When compared with other fibre fabrication techniques such as mechanical drawing and melt spinning, electrospinning provides a very simple and versatile approach to generate fibres [Xia *et al.*, 2003] having metal particles encapsulated in fibres.

The fibres resulting from co-axial electrospinning were collected on microscope glass slides and later coated with carbon for SEM analysis. **Figure 4.32** shows an SEM image of the fibres. Due to the particle size gold nanoparticles can not be seen using SEM. Later, the fibres were collected on carbon coated grids for transmission electron microscopy (TEM) analysis. **Figure 4.33** shows a TEM image of the fibre showing gold nanoparticles within the fibre.

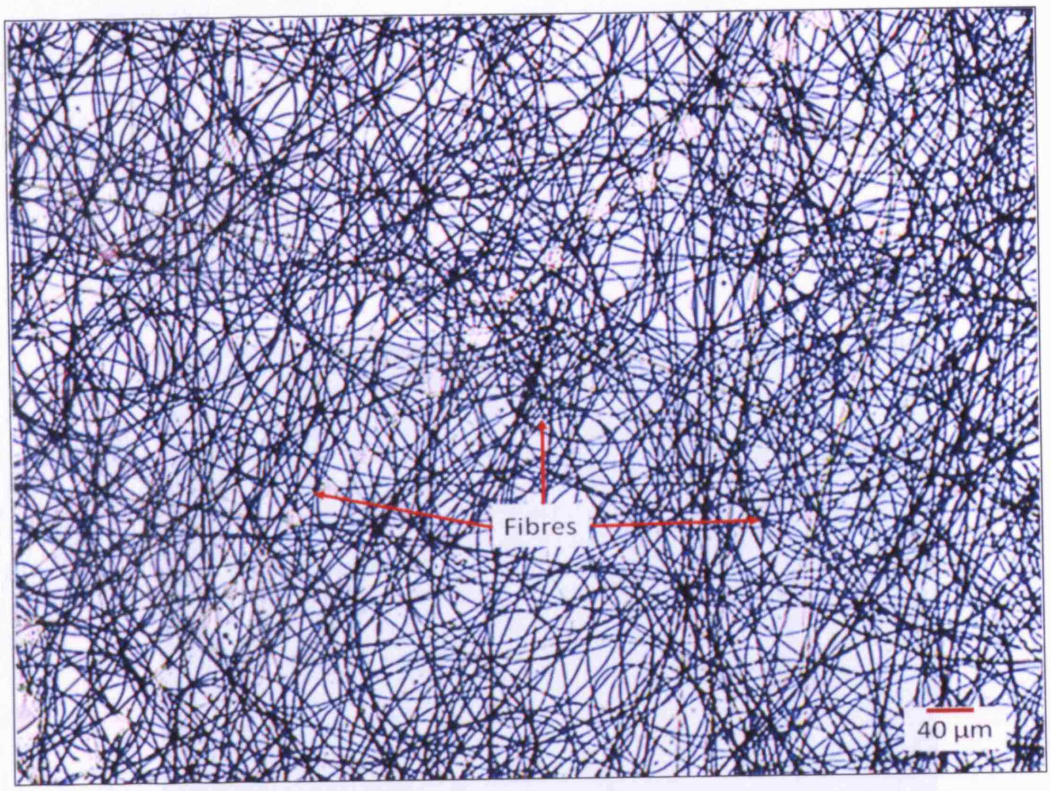

Figure 4.31 Optical micrograph showing fibres containing gold nanoparticles. The flow rate and voltage was 1.83 x 10^{-10} m^3s^{-1} and 7.5 kV

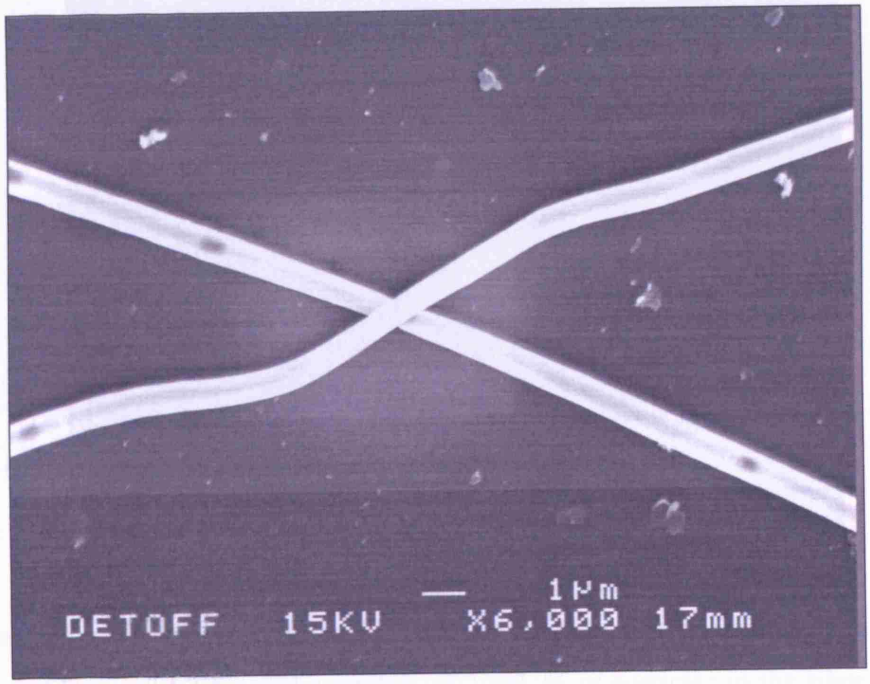

Figure 4.32 SEM micrograph of the gold encapsulated fibres produced by co-axial electrospinning

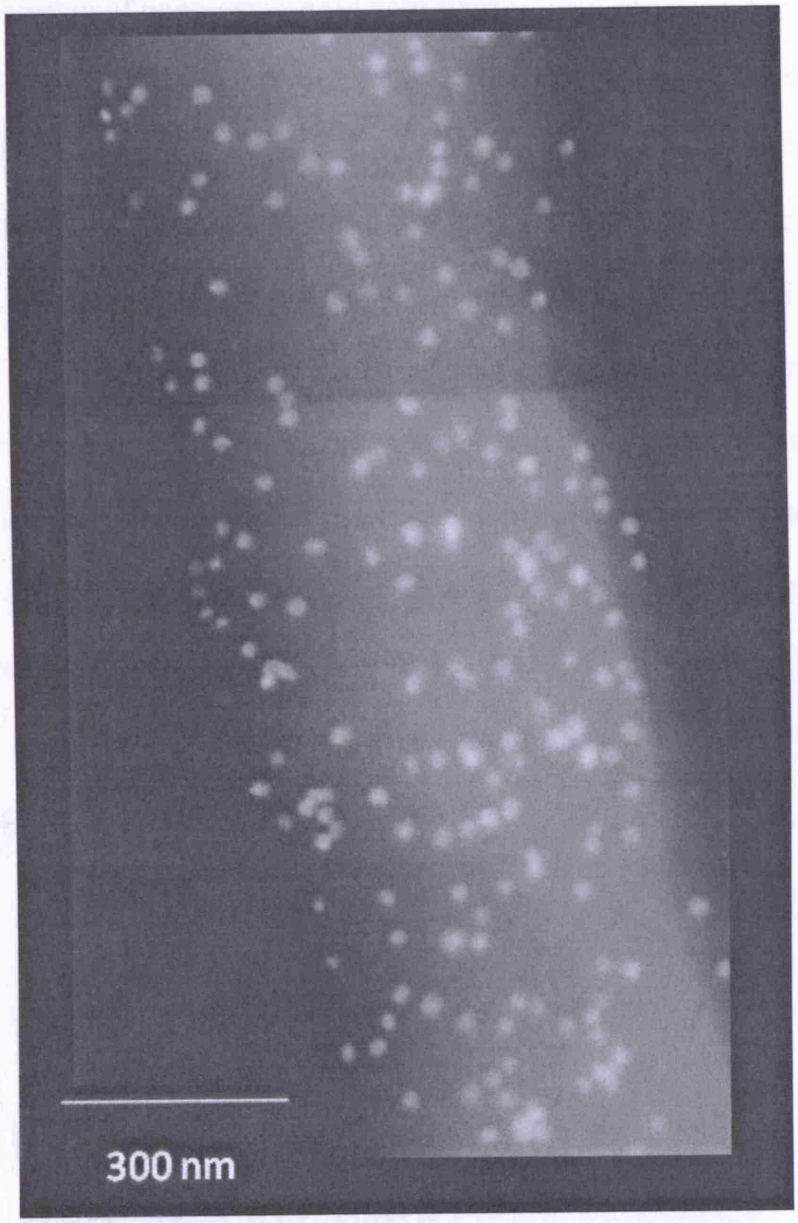

Figure 4.33 TEM image of gold particles within the fibre. White dots represent gold nanoparticles and contains ~0.2 vol. % of particles in the fibre.

Chapter 5

Discussion

5.1 Fabrication of nano-structured gold films

Gold sphere shaped alcosol was subjected to electrohydrodynamic atomisation and the resulting droplets were collected on silicon wafers in order to fabricate gold films. The conditions and operating parameters were explained in detail in Chapter **4**. To find out the optimum sintering temperature, the films were sintered at different temperatures. The sintering temperature was varied from 250 to 600 °C. **Figure 5.1** shows the SEM images of the films sintered at different temperatures. **Figure 5.1b** shows a graded pattern of cracks. This is due to the size segregation effect which occurs during deposition. The larger droplets are found to be in the centre of the film and smaller droplets are found to be at the edge of the film. Thus creating larger aggregates in the centre of the film and size of the aggregates gets smaller towards to edge of the film.

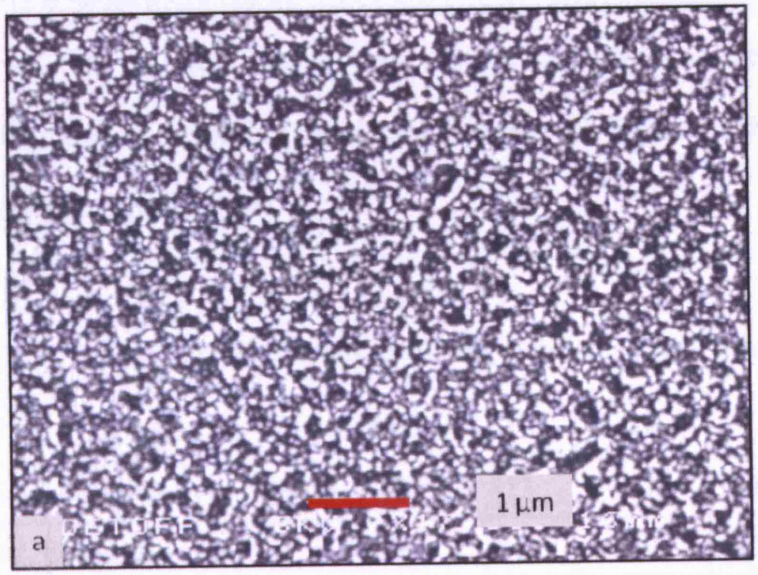

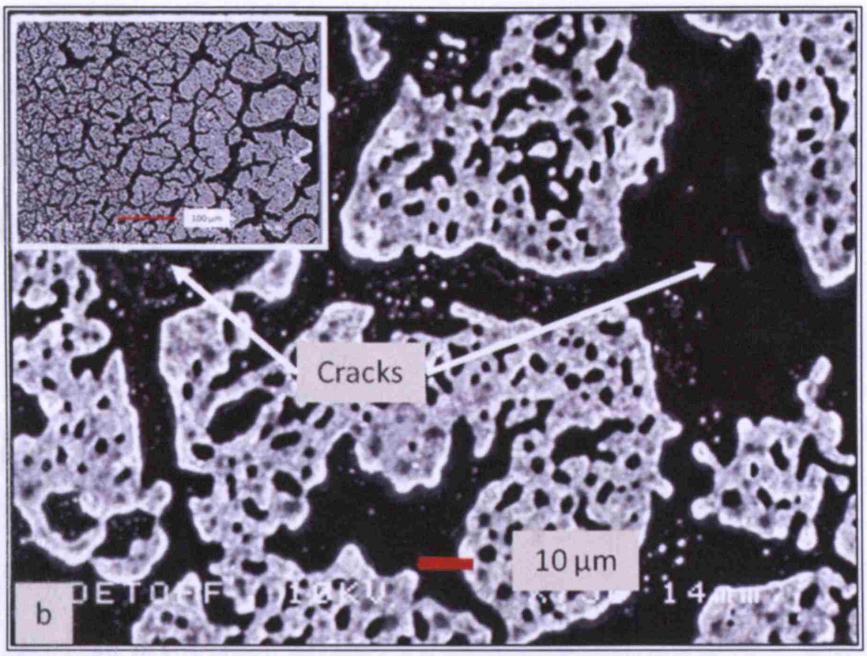

Figure 5.1 Surface of the film at different sintering temperatures. a) 400 °C and b) 500 °C and insert picture shows a low resolution image of the film.

By analysing the films under SEM, it was concluded that 400 °C is the optimum temperature for sintering gold films without cracks. The deposition time was varied from 60 to 600 s. **Figure 5.2** shows the cross section of the centre of the films at different spray times. **Table 5.1** shows the thickness variation of the films at the centre at different spray times. The thickness increased from ~400 to ~2000 nm with increasing deposition time. **Figure 5.3** shows the thickness variation with the increasing time.

Table 5.1 Thickness variation with increasing spray time

Time (s)	60	210	300	450
Average Thickness (nm)	477	813	1211	1830
Std. Deviation (nm)	46	89	69	176

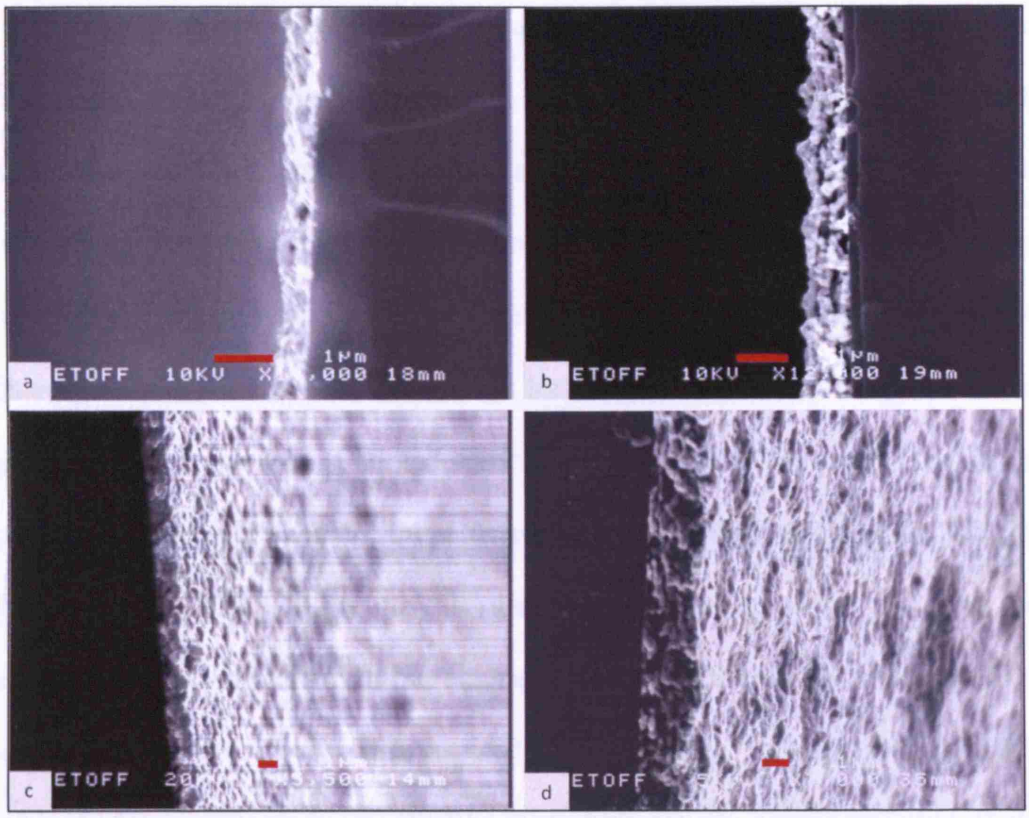

Figure 5.2 Films produced at different spray times, a) 60 s b) 210 s c) 300 s and d) 450 s. Scale bar indicates 1μm

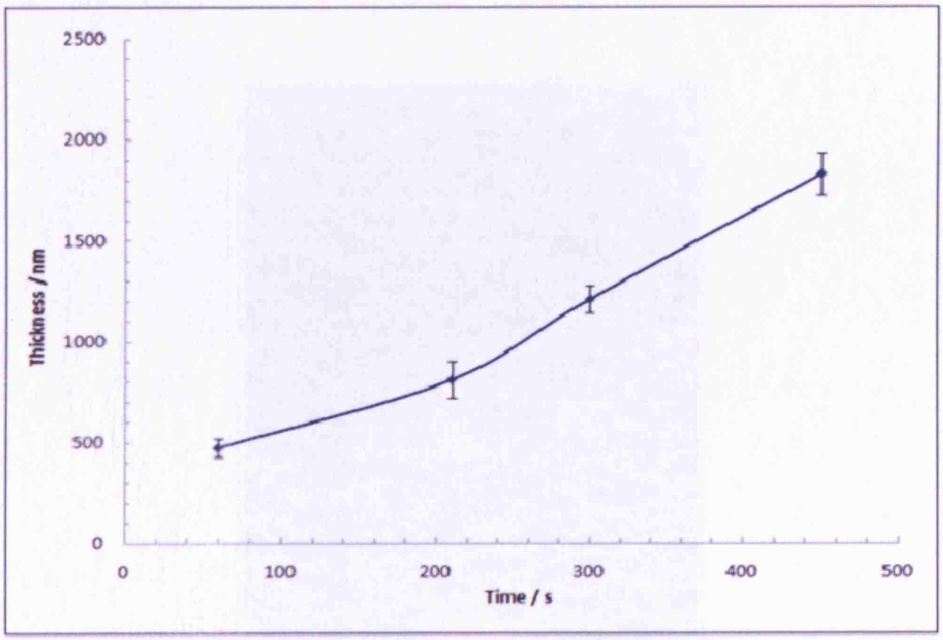

Figure 5.3 Variation of film thickness as a function of increasing deposition time

The films produced at longer spray times are denser and more uniform in thickness as shown in **Figure 5.2c** and **d** when compared with **Figure 5.2a** and **b**. Although the films appear uniform at low magnification level, at higher magnification scanning electron micrographs (**Figure 5.4**) reveals that the films have a morphology which contains several "hillocks" (small gold hills that rise above the film) [Chen *et al.*, 1996]. The formation of hillocks is characteristic of the fabrication route used. Charged particles are attracted to the rough areas in the uneven film; therefore gold nanoparticles may accumulate at one spot and rise above the film. The hillocks increase the surface roughness of the film, and this feature could be very useful in bio-engineering, making it possible to easily attach cells to the surface of the film, as well as for creating "hot spots" for surface enhanced Raman spectroscopy (SERS) measurements. By careful tailoring of the substrate and thus creating small charge concentrated juts to a predetermine pattern on the substrate, formation of hillocks and its distribution can be controlled.

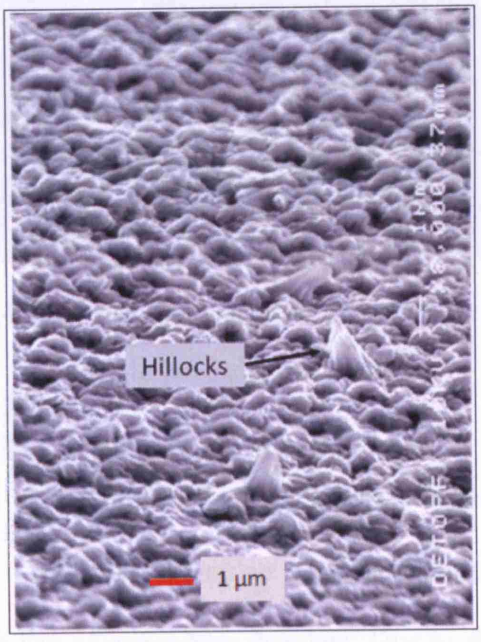

Figure 5.4 Side view of the surface of the film

Figure 5.4 shows the surface of the film examined by SEM. From the tilted view it is evident that the surfaces of the films do not have a smooth surface. With increasing spray time, the formation of hillocks on the surface increases. **Figure 5.5** shows the surface morphology of the films at the centre of the film. The presence of hillocks at the centre is more when compared with the edge of the film. This is due to the "size segregation effect" [Ganan-Calvo *et al.*, 1994].

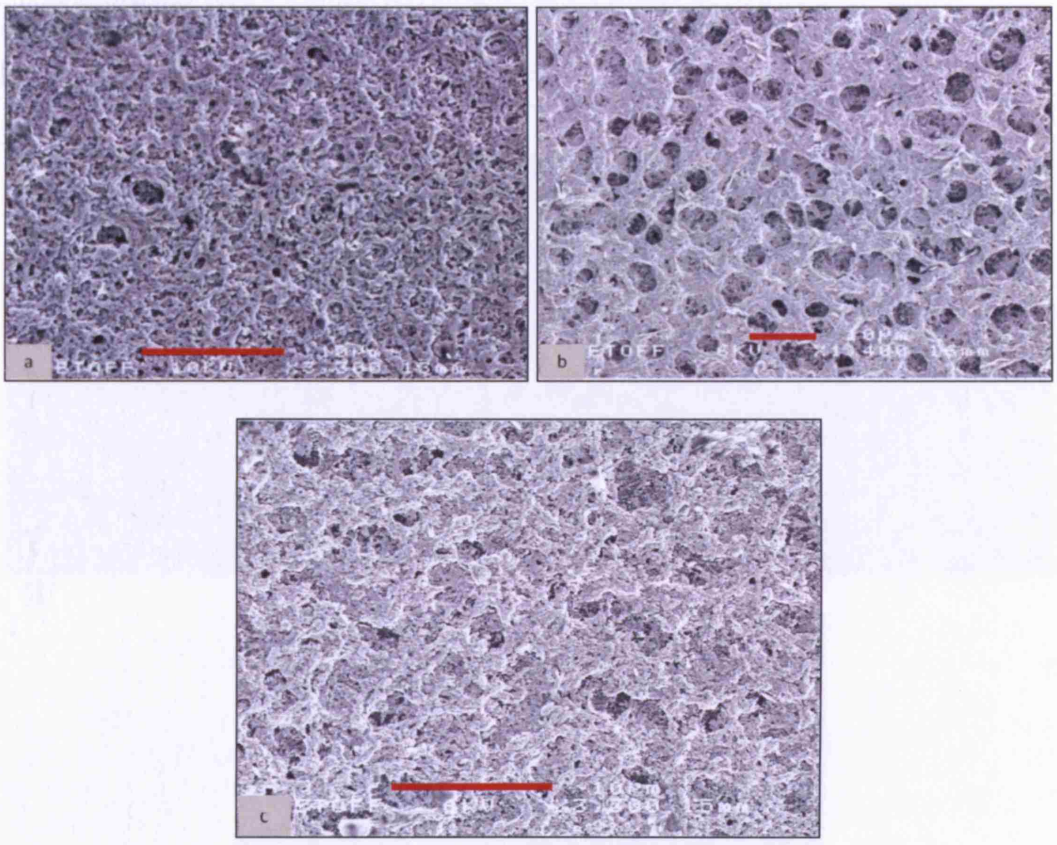

Figure 5.5 Plan view of the centre of the films, a) 60 s b) 210 s and c) 300 s. Scale bar indicates 10 μm

When the alcosol is subjected to electrohydrodynamic atomisation in the cone-jet mode, the jet breaks into a number of primary droplets with a narrow size distribution, and a number of secondary droplets. Due to the electrical interaction

between highly charged droplets a size segregation effect takes place. Hence, smaller droplets will be found at the edge of the spray while large droplets will be found near the centre of the spray [Ganan-Calvo *et al.*, 1994]. **Figure 5.6** shows the edge of the film with increasing spraying time. With less spraying time the edge of the film forms into a porous structure. The bright areas in **Figure 5.6b** and **c** show the top of the hillocks. With increasing spraying time, the porosity of the film at the edge decreases and formation of hillocks increases, due to the increased deposition of particles.

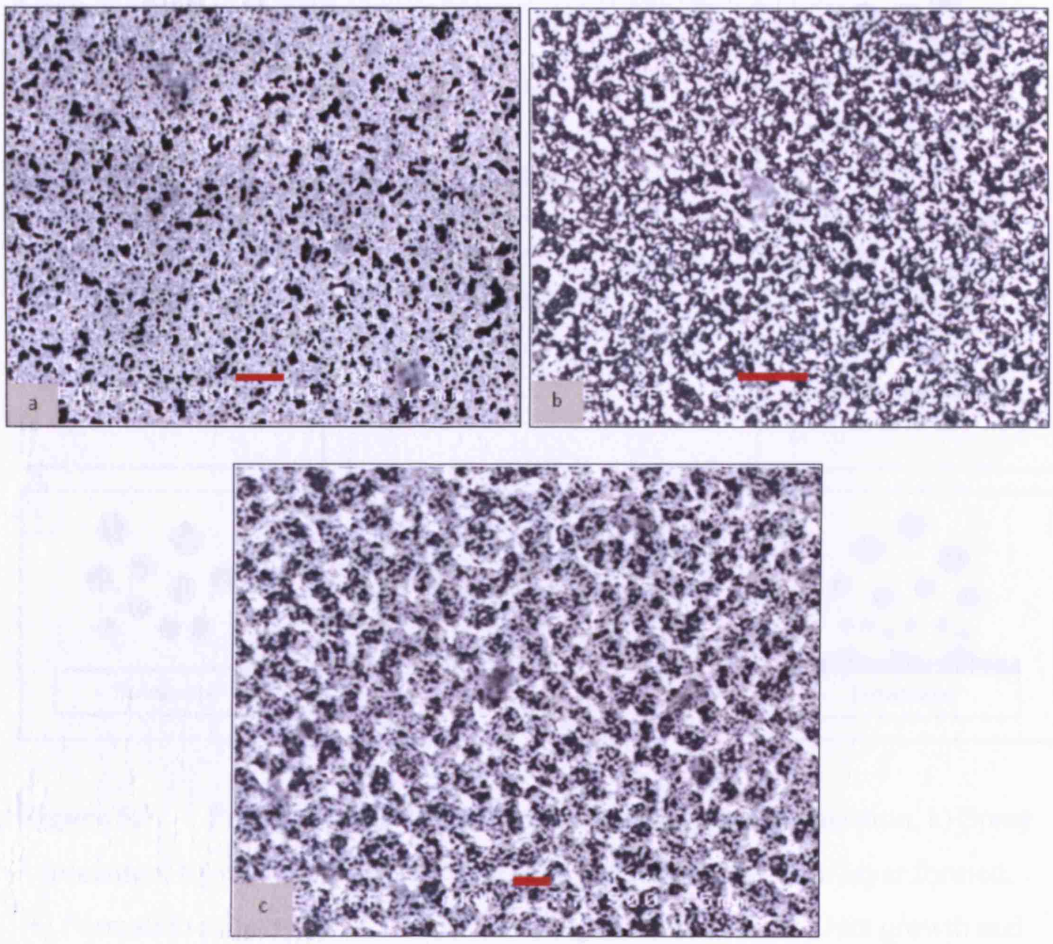

Figure 5.6 Plan view of the edge of the films, a) 60 s b) 210 s and c) 300 s. Scale bar indicates 1μm

Formation of hillocks or juts is a direct result of the atomisation technique used. When the gold alcosol is subjected to electrohydrodynamic atomisation under stable cone-jet mode (**Figure 5.7a**), the resulting charged near-monodisperse droplets get attracted to the substrate by electrostatic forces (**Figure 5.7b** and **c**). The droplets produced from atomisation are still wet when depositing on the substrate. The droplet spreads on the substrate and later discharges (**Figure 5.7c**). The discharge proceeds slowly and a thin film of gold is formed (**Figure 5.7d**).

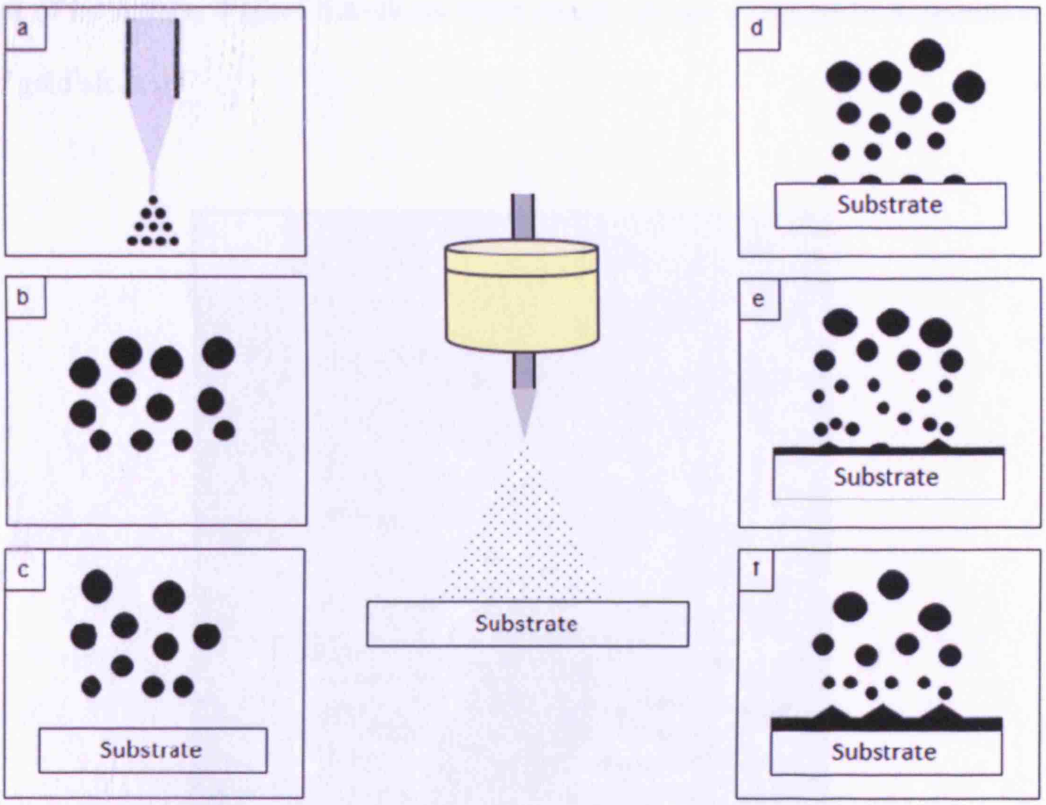

Figure 5.7 Processes involved in electrohydrodynamic atomisation. a) Spray formation, b) and c) Droplet transport and evaporation, d) Thin layer formed, e) Formation of juts and preferential landing of droplets and f) Juts growth and connection

Due to strong electrostatic forces, negative charges are induced on the substrate surface. The distribution of the charge along the substrate surface is not uniform. Induced charges concentrate more at the place where the curvature was greater. Therefore small charge-concentrated juts were formed during deposition. The charged droplets are attracted more strongly to the juts than to the smooth surface, which leads to their preferential landing on the juts (**Figure 5.7e**) [Cheng *et al.*, 1996]. With increasing deposition time the juts become larger and get linked to each other. The final surface of the film contains many juts protruding out of its surface. **Figure 5.8** shows SEM images of juts produced by atomisation of gold alcosol.

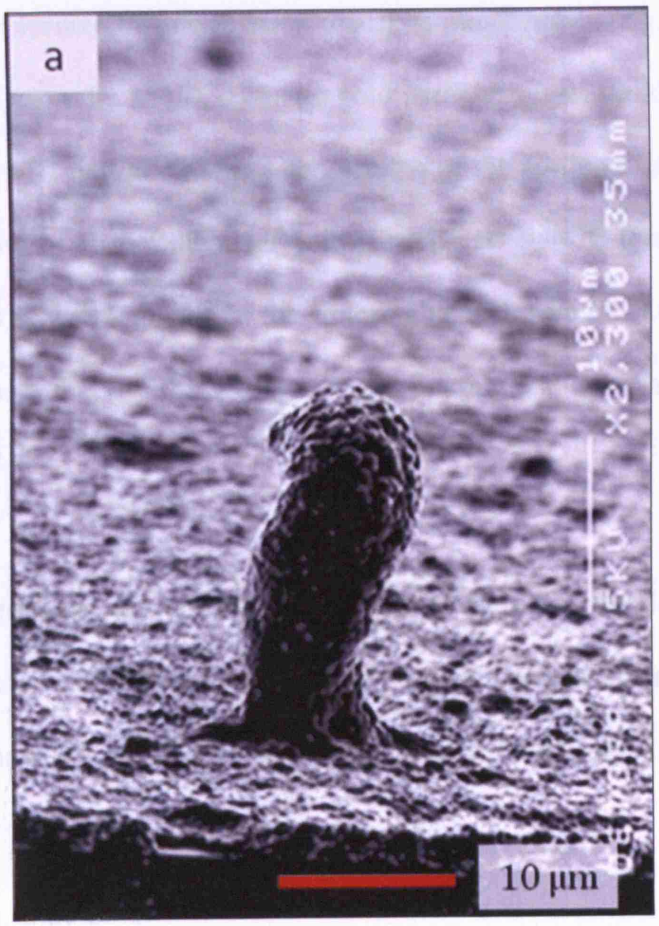

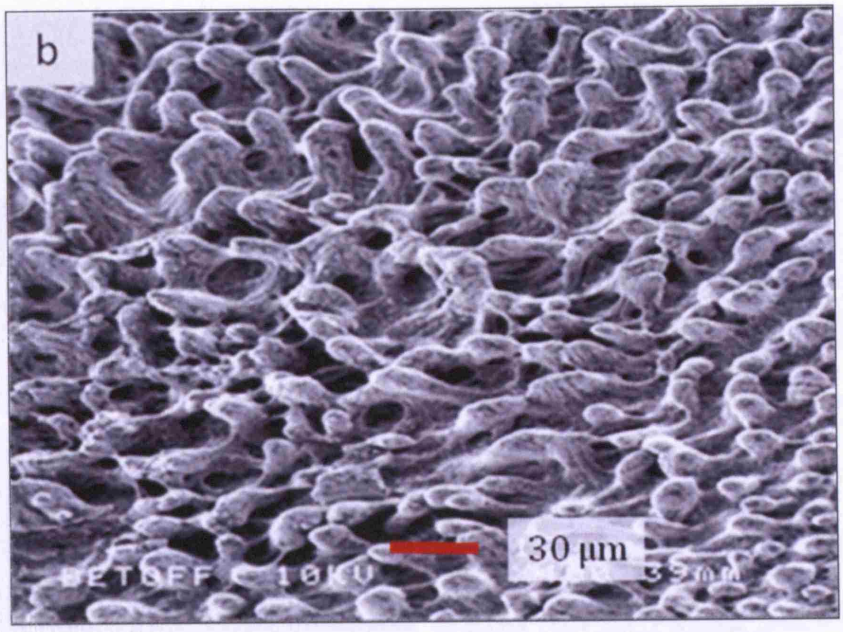

Figure 5.8 Effect of preferential landing of droplets

The microstructures presented in the SEM micrographs (e.g. in **Figure 5.4**) do not clearly discern the 15 nm diameter gold particles present in the alcosol. This is because at 400 °C partial sintering and growth of the particles have taken place. The melting point of 15 nm diameter gold particles is ~950 °C [Shim *et al.*, 2002, Cortie, 2004]. It is well known that the sintering temperature is ~0.6 of the melting temperature. Therefore, at 400 °C appreciable sintering and growth of the particles can be expected.

In comparison to the films obtained using other fabricating methods (**Figure 5.9**), the films obtained using electrohydrodynamic atomisation were more dense. This characteristic might be more beneficial as substrates for Raman spectroscopy and for cell biology.

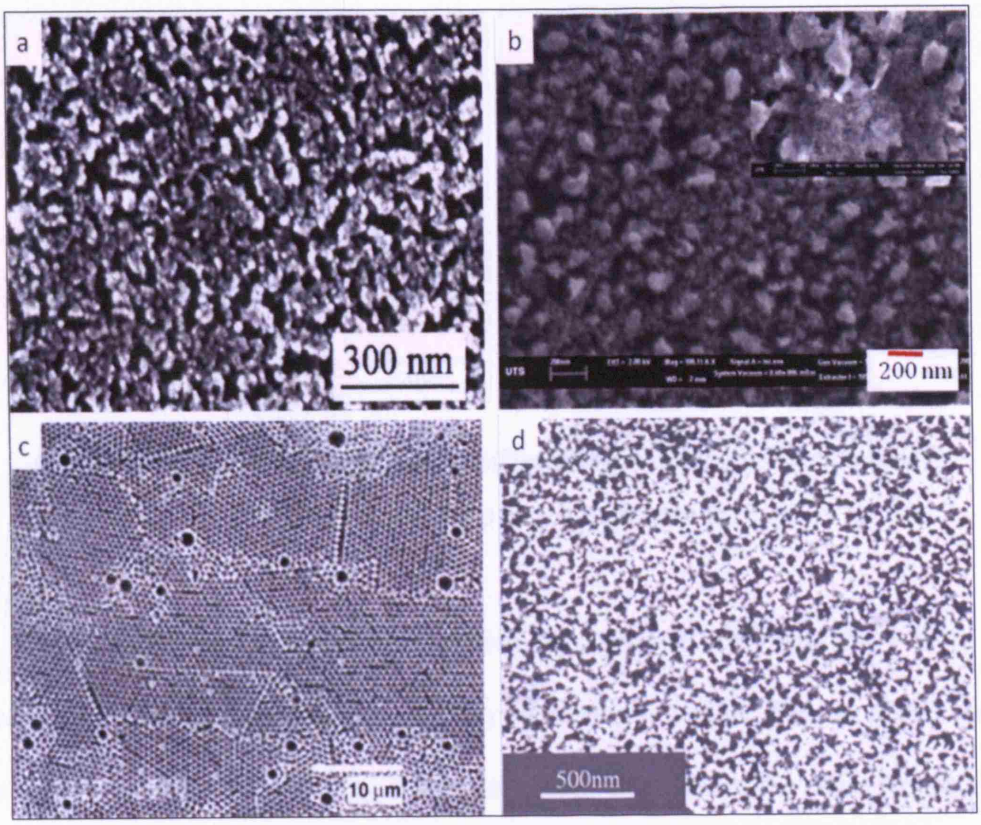

Figure 5.9 Surface of the films fabricated by different methods. a) "Green approach" [Zhao *et. al.*, 2008], b) Sputtering [Maaroof *et.al.*, 2005], c) Colloidal crystal templating [Tessier *et. al.*,2001] and d) Surface vertical deposition Diao *et.al.*, 2003]

5.2 Electrohydrodynamic atomisation printing of gold and silver alcosols

The gold sphere shaped alcosol was atomised under an electric field and the droplets produced from atomisation were used to pattern lines / tracks at different distances (needle exit and the substrate). When the distance between the needle exit and the substrate was less than ~300 µm no stable cone-jet was produced. **Figure 5.10** shows optical microscope images of the tracks printed at off set of ~500 µm and ~1 mm.

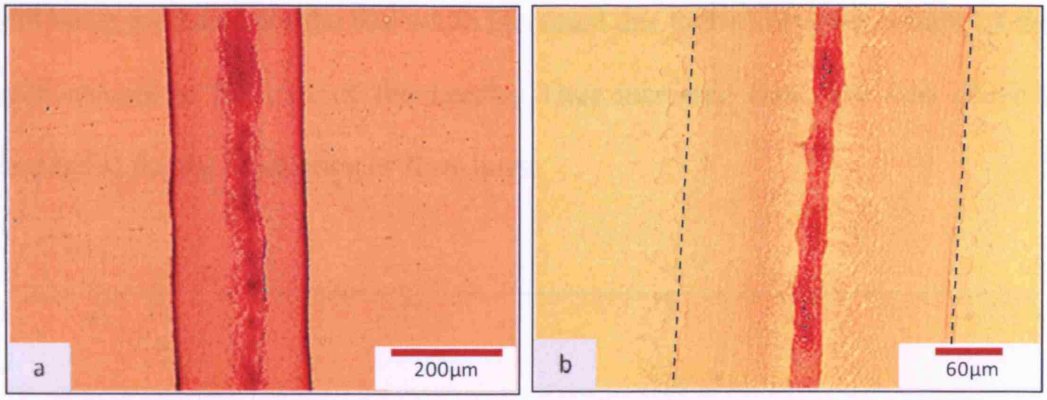

Figure 5.10 Tracks produced at different needle to substrate distances. a) 0.5 mm and b) 1 mm. Dotted lines in *(b)* indicates the edge of the track.

Figure 5.10a shows a track which was printed ~500 µm away from the needle exit where a clear line without any scattering is visible. **Figure 5.10b** shows the track printed at 1 mm away from the needle exit, where the main printed line was not clear due to lot of scattering caused by the satellite droplets produced from atomisation. From this experiment, it suggests that ~500 µm distance between the needle exit and the substrate is the suitable distance for patterning gold / silver alcosols using electrohydrodynamic printing technique.

5.2.1 Sphere shaped gold alcosol printed at different flow rates

Figure 5.11 shows an attempt made to pattern gold tracks at different flow rates. The continuous printing of the lines mainly depend on the flow rate at the exit of the needle. This is evident from the printed results. At lower flow rates (1×10^{-11} m^3s^{-1}) only drops were deposited on the silicon wafer. Hence it did not produce continuous lines. When the flow rate was increased to 5×10^{-11} m^3s^{-1} continuous tracks were visible with a fine line width of ~110 µm being produced. When the flow rate was increased further (1×10^{-10} m^3s^{-1}) continuous lines were

still being produced but the line width increased due to the increased volume of the gold alcosol at the exit of the needle. Thus increased flow rate was deemed unsuitable for the production of finer lines.

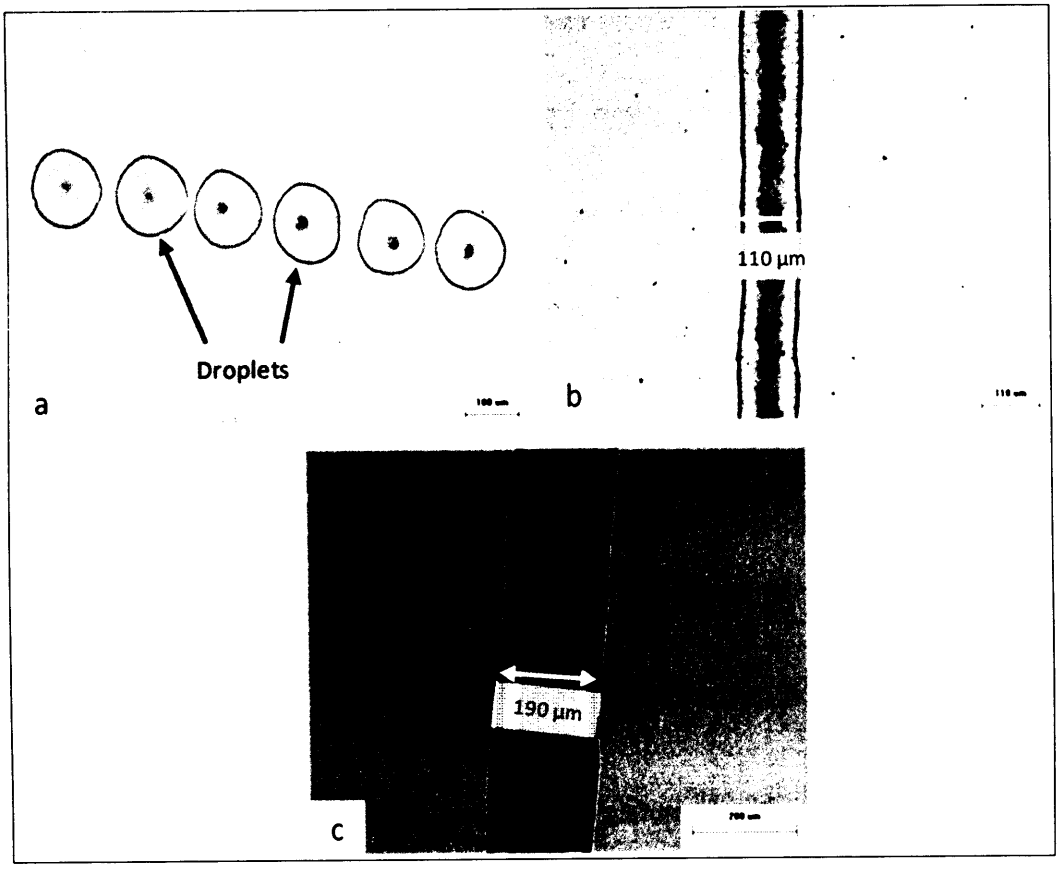

Figure 5.11 Continuous track formation with increasing flow rate.
a) 1 x 10^{-11} m^3s^{-1}, b) 5 x 10^{-11} m^3s^{-1} and c) 1 x 10^{-10} m^3s^{-1}

5.2.2 Decahedral shaped gold alcosol printed at different flow rates

Decahedral shaped gold alcosol was atomised at various flow rates under stable cone-jet mode and was subjected to printing. From the previous experiments with the sphere shaped gold alcosol, it was evident that there exists a minimum flow rate for continuous track printing. From the printing experiments carried out, the minimum flow rate for decahedral shaped alcosol was 5 x 10^{-11} m^3s^{-1}.

Figure 5.12 shows tracks produced at different flow rates. **Figure 5.13** shows a graph showing the track width variation with increasing flow rate.

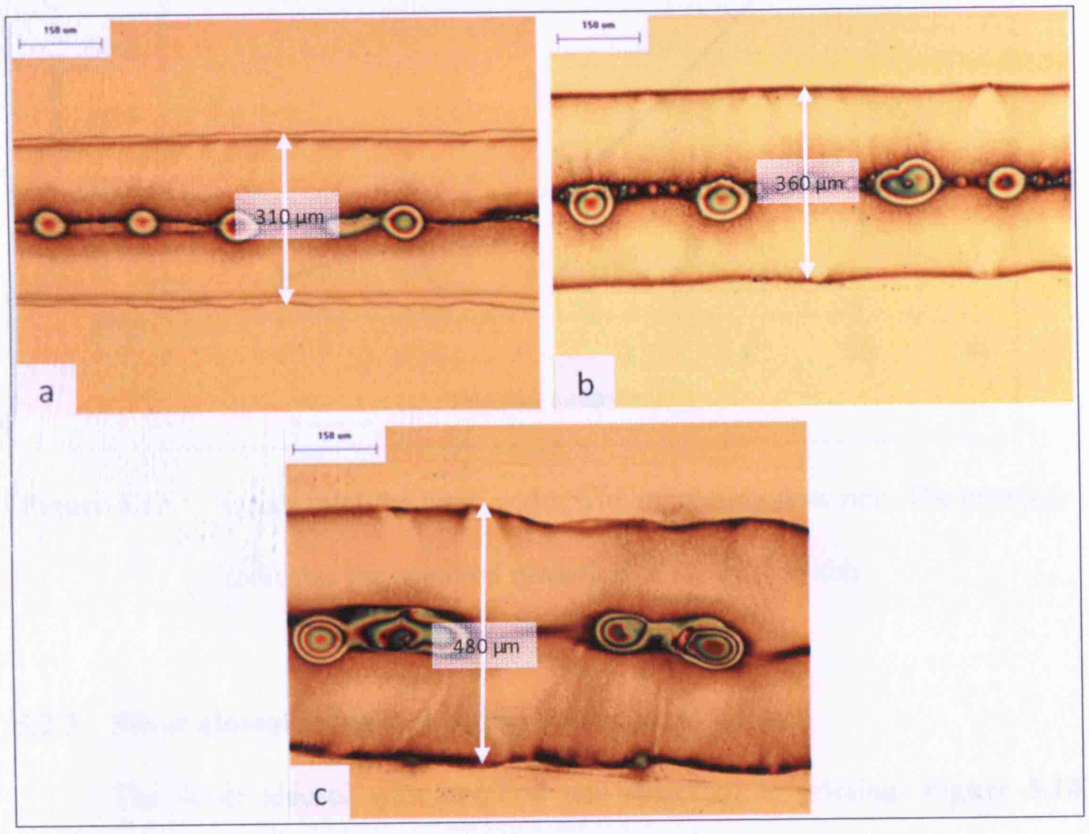

Figure 5.12 Optical micrographs of tracks patterned with increasing flow rate. a) 5×10^{-11} m^3s^{-1}, b) 7.5×10^{-11} m^3s^{-1} and c) 1×10^{-10} m^3s^{-1}

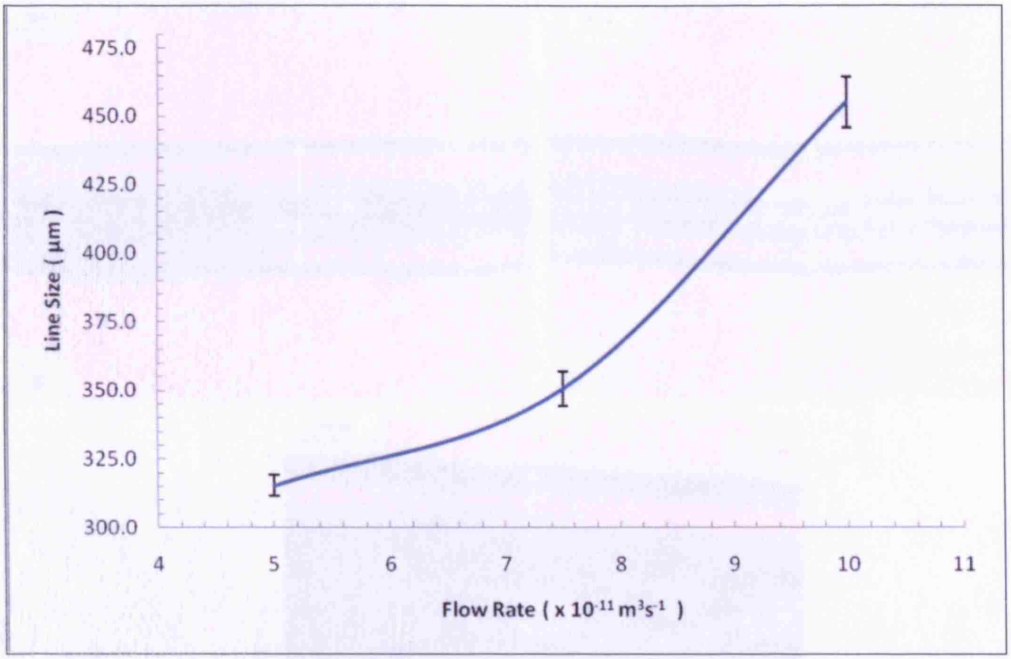

Figure 5.13 Variation of the track width with increasing flow rate. The error bar indicates the standard deviation of the track width.

5.2.3 Silver alcosol printed at different flow rates

The silver alcosol was atomised and subjected to printing. **Figure 5.14** shows optical micrographs of the printed tracks at different flow rates. The minimum flow rate for producing continuous tracks was 5 x 10^{-11} m^3s^{-1}. **Figure 5.15** shows the track width variation with increasing flow rate. As expected, the line size increased with increasing flow rate.

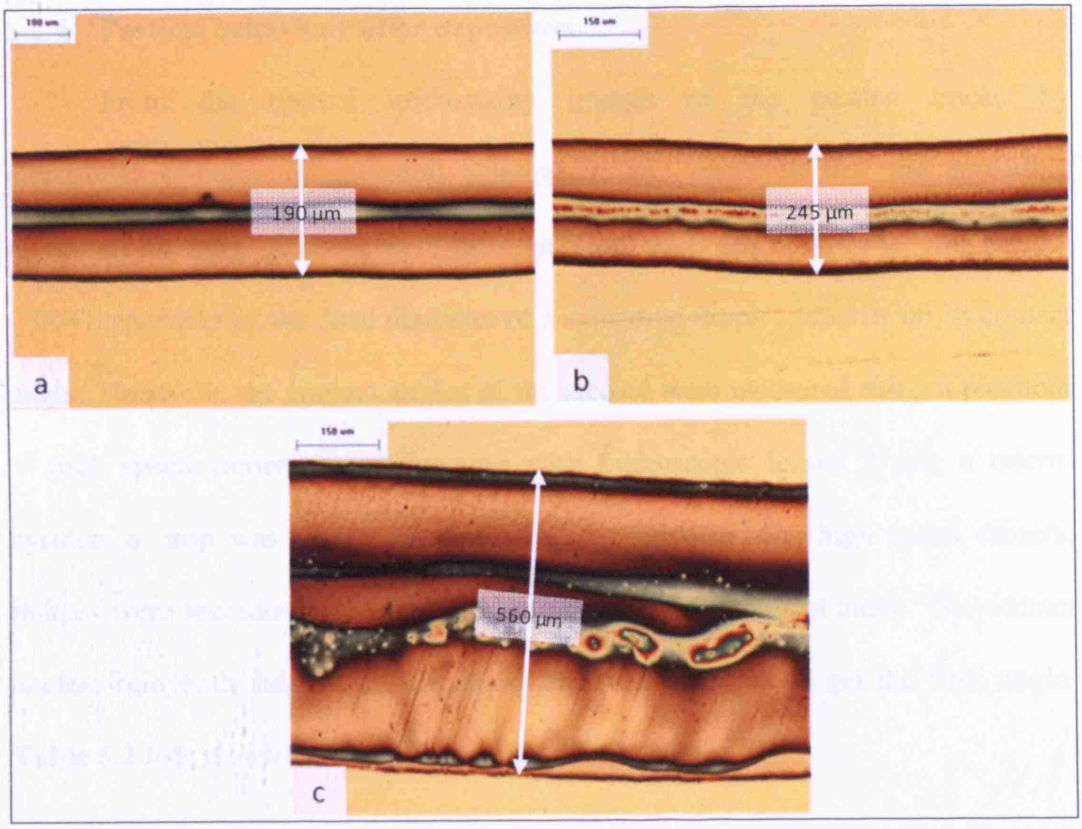

Figure 5.14 Optical micrographs of the tracks patterned with increasing flow rates. a) 5 x 10^{-11} m^3s^{-1}, b) 7.5 x 10^{-11} m^3s^{-1} and c) 1 x 10^{-10} m^3s^{-1}

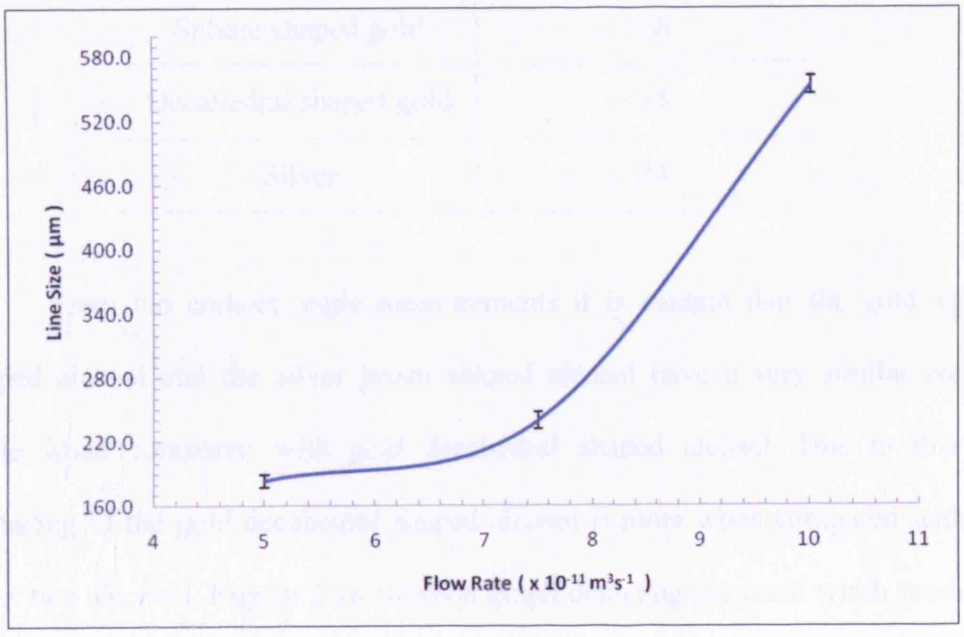

Figure 5.15 Variation of track size with increasing flow rate. The error bar indicates the standard deviation of the track width.

5.2.4 Particle behaviour after deposition

From the optical microscopy images of the printed tracks by electrohydrodynamic atomisation printing, it was observed that the spreading effects of all three alcosols were different from each other. Ikegawa and Azuma (2004) reported that the final diameter of a spreading droplet depends on its contact angle. Therefore, the contact angles of the alcosol were measured using a phantom V high speed camera in conjunction with microscopic lenses. Using a micro-syringe, a drop was placed on a glass slide and using the high speed camera, images were recorded and later used for measuring the contact angle. The contact angles from both sides were measured and then averaged to get the final angle. **Table 5.2** lists the alcosol and its corresponding angle.

Table 5.2 Contact angles of the alcosols on substrate

Alcosol type	Contact angle (°)
Sphere shaped gold	~26
Decahedral shaped gold	~15
Silver	~24

From the contact angle measurements it is evident that the gold sphere shaped alcosol and the silver prism shaped alcosol have a very similar contact angle when compared with gold decahedral shaped alcosol. Due to this the spreading of the gold decahedral shaped alcosol is more when compared with the other two alcosols. **Figure 5.16** shows a graph depicting the track width produced at 5 x 10^{-11} m^3s^{-1} from all three alcosols.

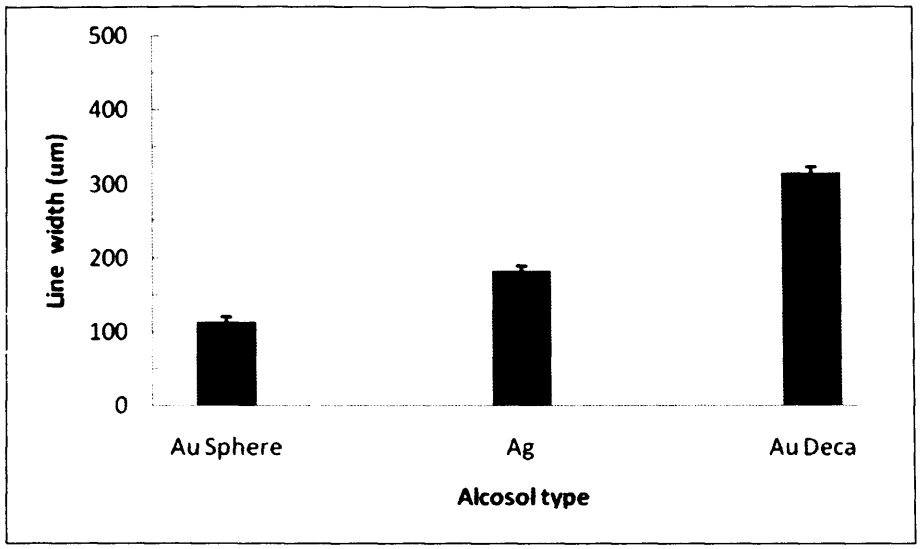

Figure 5.16 Track width variation of alcosols patterned at a flow rate of $5 \times 10^{-11}\ m^3s^{-1}$

Furthermore, in addition to contact angle and the flow rate, the final width of the tracks in all three alcosols will also depend on parameters such as the thickness of the jet produced by the stable cone-jet mode, alcosol properties and the substrate. It is well known that with increasing jet diameter, the droplets produced from atomisation increases in size (droplet diameter) and therefore the track width can also increase. Furthermore, the jet diameter mainly depends on the alcosol properties in addition to applied voltage and flow rate. Since the properties of the all three alcosols are not the same, three different widths can be observed at the same flow rate.

In general with increasing flow rate the track width increases due to more volume of liquid is ejected by the jet. Jayasinghe and co-workers (2002) used electrohydrodynamic atomisation printing technique to pattern alumina onto a substrate. In their experiments, they also reported that with increasing flow rate, the

print track width increases. When compared with their results, the patterns reported in this thesis are around 200 μm smaller and with minimum amount of scattering.

The electrohydrodynamically assisted printed samples were left at room temperature for 24 hrs and the samples were coated with carbon before scanning electron microscopy (SEM). A field emission scanning electron microscope operating in the secondary electron mode with an accelerating voltage of 10 kV and with a working distance up to 15 mm was used in order to study the particle behaviour within the printed track. **Figure 5.17**, **Figure 5.18** and **Figure 5.19** show SEM images of the printed tracks of gold sphere shaped, gold decahedral shaped and silver tracks produced from corresponding alcosols. The SEM images contain a low magnification image of the printed line, the edge of the line and two high magnification images of the centre of the tracks. In all three alcosols, a similar kind of particle behaviour can be observed. Most of the particles can be seen clustering together at the edges of the line and a random distribution of the particles can be seen at the centre of the track.

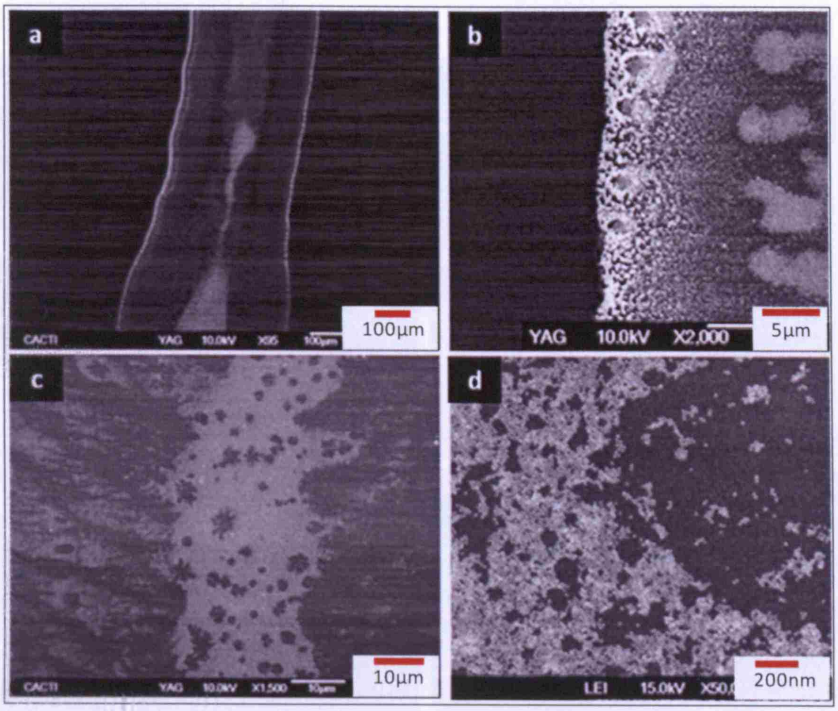

Figure 5.17 SEM micrographs of a track printed using gold sphere shaped alcosol. a) whole track, b) edge of track c) and d) high resolution images of centre of track

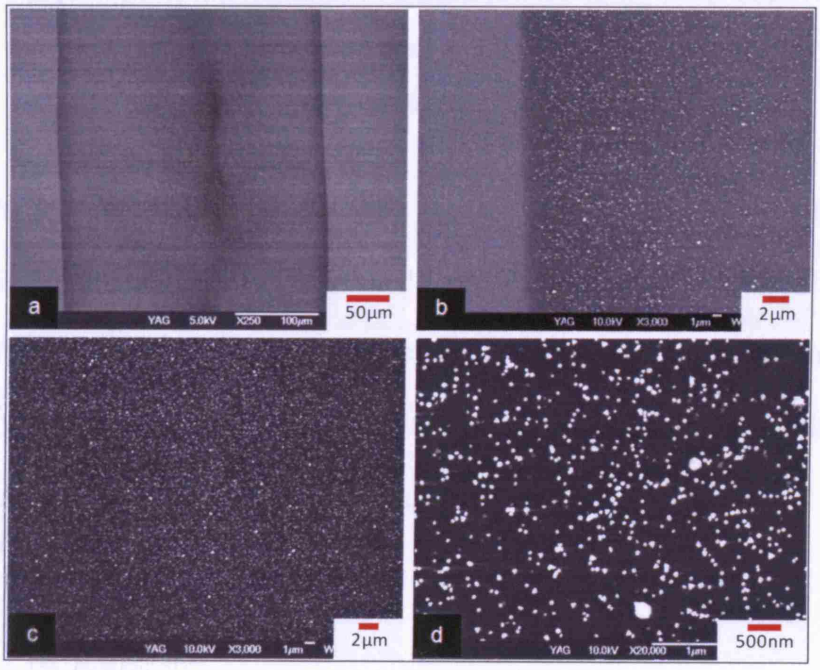

Figure 5.18 SEM micrographs of a track printed using gold decahedral shaped alcosol. a) whole track, b) edge of track c) and d) high resolution images of centre of track

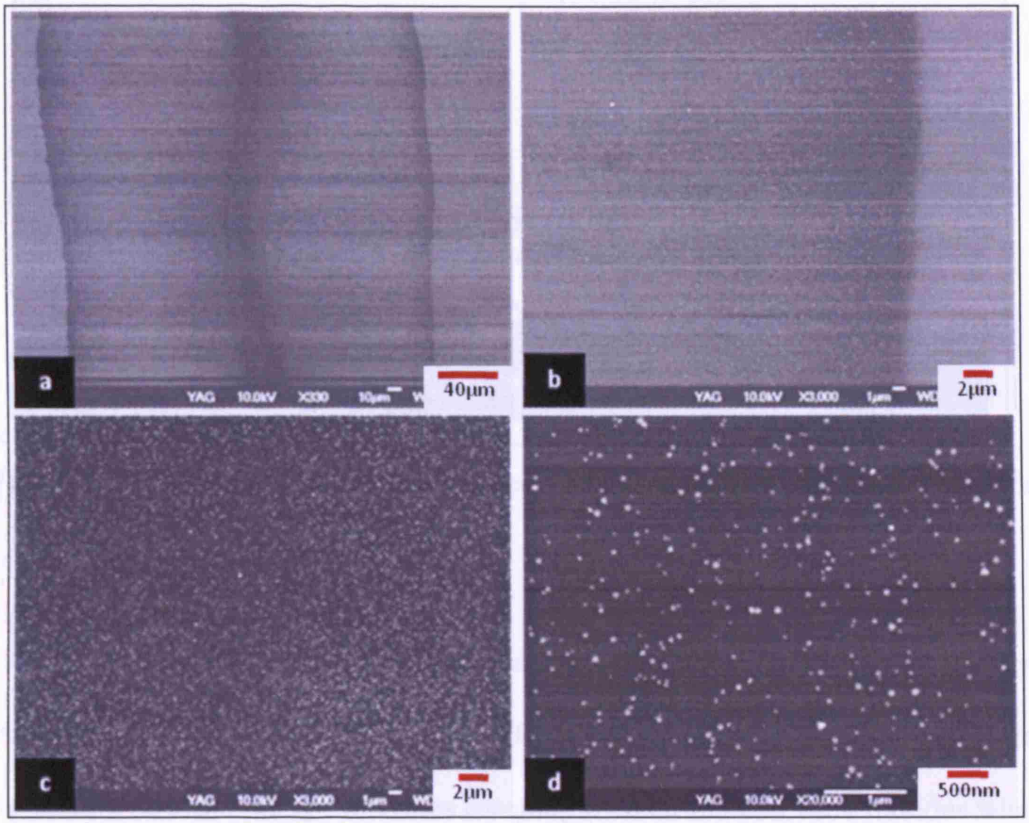

Figure 5.19 SEM micrographs of a track printed using silver prism shaped alcosol. a) whole track, b) edge of track c) and d) high resolution images of centre of track

Particle spreading within the printed line varies due to ultra-rapid evaporation of the solvent in the printed line. The particles suspended in the line can be affected by various forces such as gravity, buoyancy, Brownian motion and Van der Waals interaction (**Figure 5.20**) between either the particles or the particle and the substrate [Sommer and Rozlosnik, 2005].

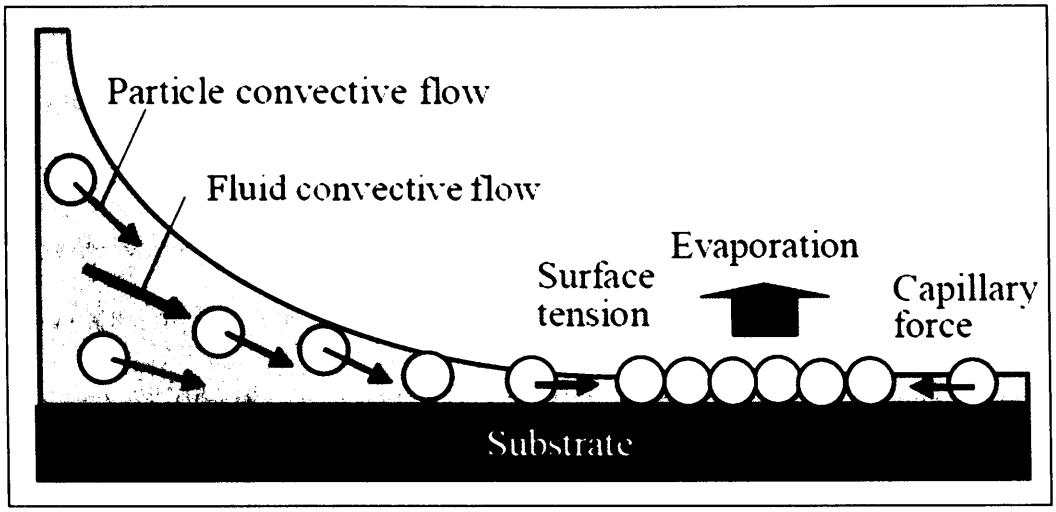

Figure 5.20 Forces acting on the nanoparticles at the edge of the track whilst the solvent evaporates [Nakamura, 2004]

The evaporation flux distribution along the line/track surface is not uniform when the line is patterned on the surface. Edge enhancement arises from the greater probability of evaporating molecules escaping by their random walk motions when leaving from the edge than when leaving from the centre of the droplet [Deegan *et al.*, 2000, Hu and Larson, 2002, Popov, 2005, Park and Moon, 2006]. A random walk initiated at the centre of the drop results in the molecules being reabsorbed so that the final stop is not completed. However, the same random walk initiated from the edge allows the evaporating molecule to escape. This explains why the evaporation rate is larger at the edge. Preferential evaporation at the edge may also result from the capillary suction pressure developed by the aggregated gold / silver nano particles near the contact line [Park and Moon, 2006].

When the contact angle is less than 90^0, the evaporation initially proceeds with an accompanying decrease in the contact angle, but with almost no change in the contact radius. This contact line pinning during a significant part of the

evaporation plays a critical role in drying mediated self assembly from a dilute colloidal droplet on the wetted surface, as demonstrated by Deegan and co-workers (1997). Since the evaporation rate is higher at the edge of the track when compared with the centre of the track, there must be a continuous radial outward flow of the solvent from the centre of the contact area to the contact line of the printed track to compensate for the liquid removed by evaporation. This convective flow and the suspended particles it carries are responsible for the presence of particles at the contact line. The low concentration of the solution as well as forces such as Van der Waals and capillary forces are not strong enough to attract all the particles to the contact line. Furthermore, due to non-uniform solvent evaporation across the line, various random patterns at the centre of the tracks can be observed.

5.3 Template assisted pattering of gold tracks by electrospraying

Due to the low concentration of the metals in the alcosols and its rapid evaporating solvent, electrohydrodynamic printing was not able to produce tracks with dense metal particles within the track. Therefore a template was used in order to reduce the track size and to produce dense tracks. In templating the metal track size mainly depends on the grid size. The needle exit and the template centre were aligned together and then spraying was carried out. After removing the template manually, the samples were characterised using optical microscopy.

From the optical microscopy observations it was revealed that the tracks at the centre of the grids were much more dense when compared with the edge of the template (**Figure 5.21**). This is due to droplet size segregation effect when a liquid is atomised with the help of an electric field [Ganan-Calvo *et al.*, 1994].

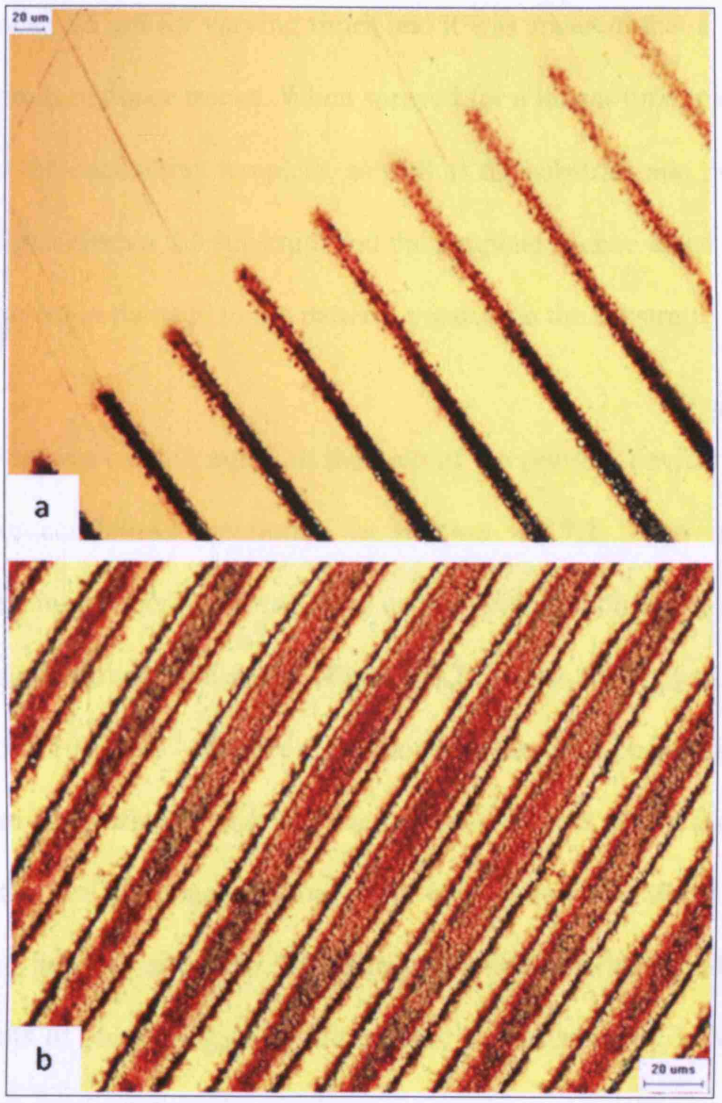

Figure 5.21 Optical micrographs of the sintered tracks produced by templating method. a) Edge of the template and b) Centre of the template.

In order to prevent this happening it was decided to move the sample with the help of the printing device that was used for patterning. The heating device, containing the substrate and the template, was kept on the printing table and moved. It was decided to use the minimum table speed in order to reduce the vibrations that the printer would cause because this would directly affect the stability of the jet. The printing table was moved at 3 mms^{-1} throughout the

template by incrementing 200 μm's when it reaches the end of the template. Spraying was carried out for varying times and it was apparent that a spray time of 240 s would produce dense tracks. When sprayed for a longer time, particles would be attracted to the conductive template, as well as the substrate and this resulted in forming a bridge between the substrate and the template. Hence when removing the template it resulted in damage to the patterns created on the substrate.

Spraying was carried out with the help of the printing device for 240 s and sintered using conditions mentioned in **Section 4.2.7.2**. After sintering, the substrates containing micro-patterns were coated with carbon and were examined using scanning electron microscopy. **Figure 5.22** shows tracks prepared using a flow rate of 5×10^{-11} m^3s^{-1}. **Figure 5.23** shows an elemental analysis of the track produced from templating confirming the presence of gold. From the images it is evident that the particle concentration is not enough for it to sinter and form an interconnected network structure. When the flow rate was increased to 1×10^{-10} m^3s^{-1} few spots of particle agglomeration could be observed by SEM images but still not enough particles to make it a dense pore free structure (**Figure 5.24**).

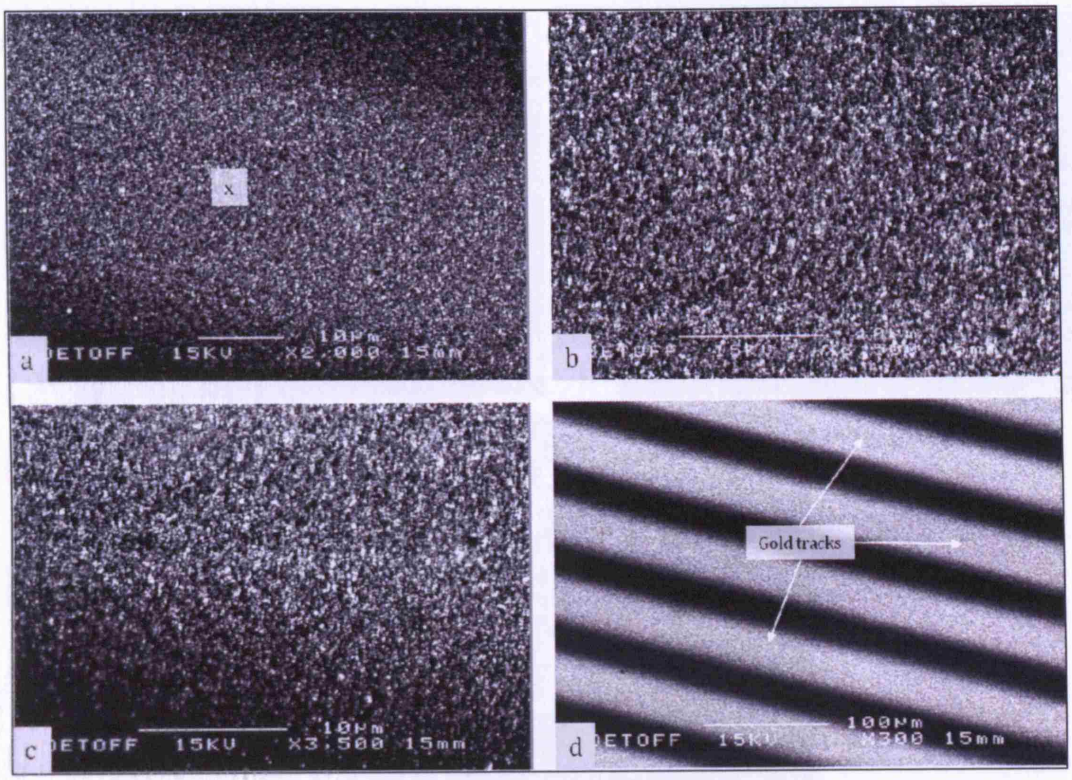

Figure 5.22 SEM images of sintered tracks deposited at a flow rate of 5×10^{-11} m^3s^{-1}. a) Whole track, b) Centre of track and c) Edge of track and d) a low magnification image of the sintered tracks.

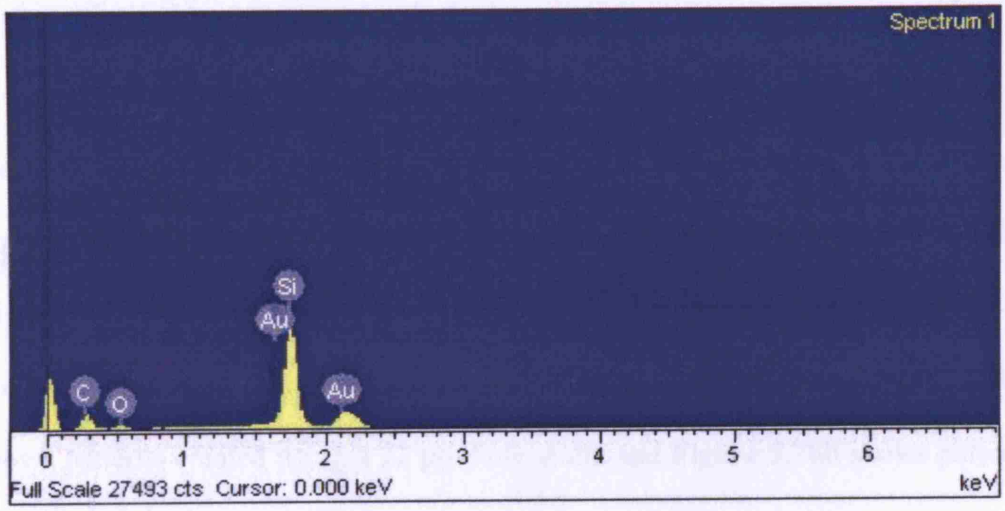

Figure 5.23 Elemental analysis of point "X" in ***Figure 5.22(a)***

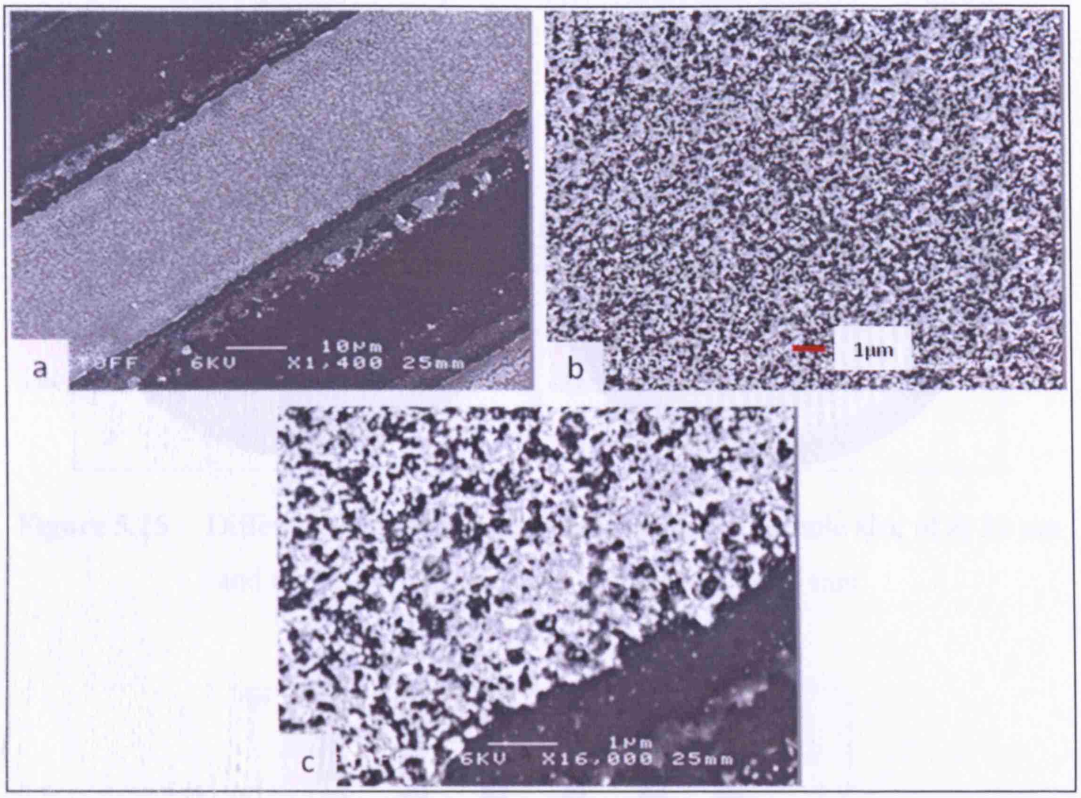

Figure 5.24 SEM images of sintered track deposited using a flow rate of 1×10^{-10} m^3s^{-1}. a) Whole track, b) Centre of track and c) Edge of track

5.3.1 Effect of grid size

As expected, with increasing grid size, the width of the micro-tracks increased. Two different template sizes were used. A template which contains a hole width of 22 µm and a template that contains a hole width of 42 µm were used. **Figure 5.25** shows the different templates used for patterning. **Figure 5.26** shows optical micrographs of the patterns created using two different grids. **Figure 5.26a** shows patterns created using a 22 µm hole width and **Figure 5.26b** shows patterns created using a 42 µm hole width templates.

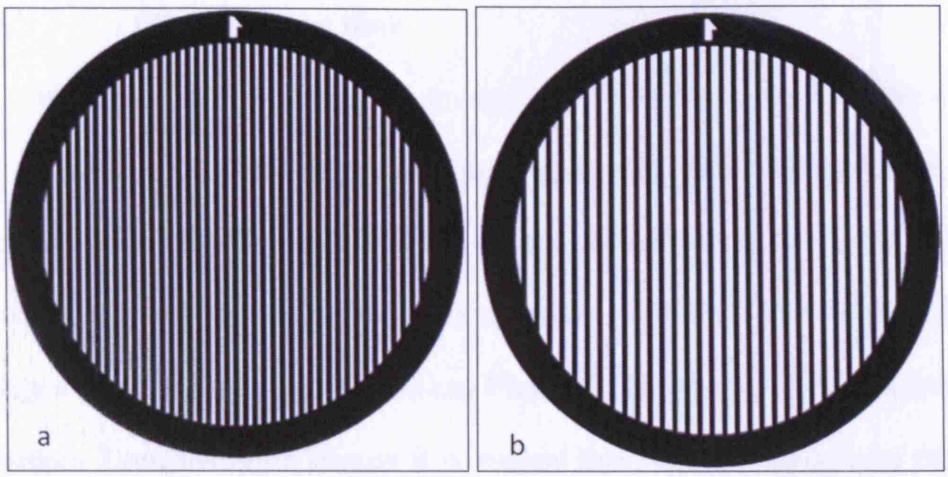

Figure 5.25 Different templates used for patterning with a hole size of a) 22 μm and b) 42 μm. The diameter of the grids was 3 mm

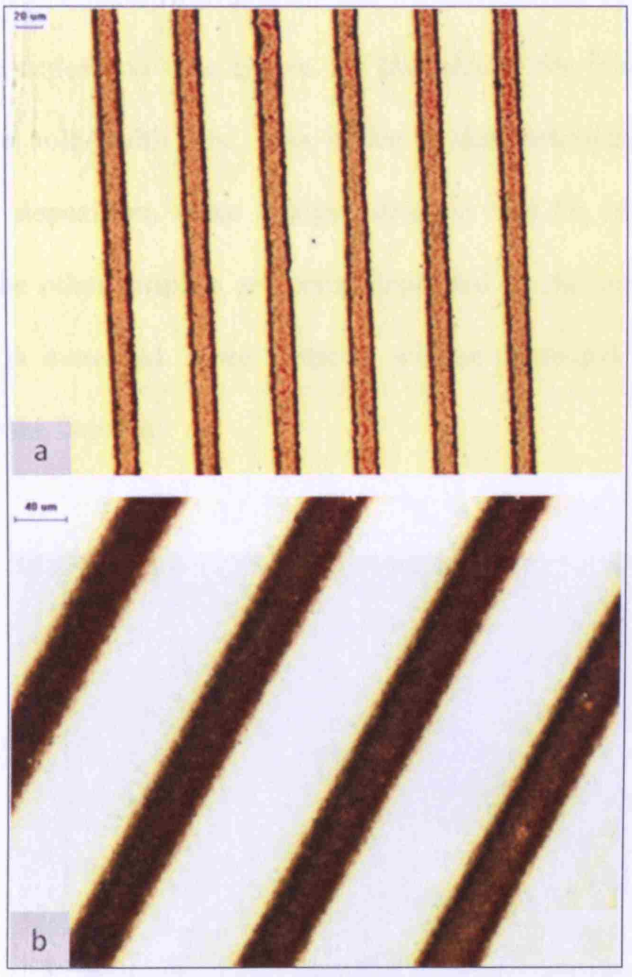

Figure 5.26 Sintered microstructures fabricated using different template sizes. a) 22 μm grid and b) 42 μm grid

5.3.2 Effect of spray time

In order to find out the optimum spray time, the deposition time was varied from 60 – 300 s. Using the mode selection map from Chapter **4** the optimum flow rate selected was 5 x 10^{-11} $m^3s^{-1}$and the voltage selected was 2.3 kV. **Figure 5.27** shows SEM images of the micro-tracks sprayed at different times. **Figure 5.27a** shows a track after 90 s of deposition and **Figure 5.27b** shows a track after 240 s of deposition. From the SEM images it is evident that with less spray time the line width is smaller but a porous structures are visible. With increasing spray time, the porosity within the track reduces and dense assembly of particles can be observed.

When the deposition time is less, the line size of the final track is smaller than the template hole-width size. This is due to the preferential landing of the droplets. During deposition, some charged droplets will be attracted to the Cu template while the other droplets are being deposited on the substrate. When the deposition time is increased, more particles will be deposited on the substrate, hence increasing the line size.

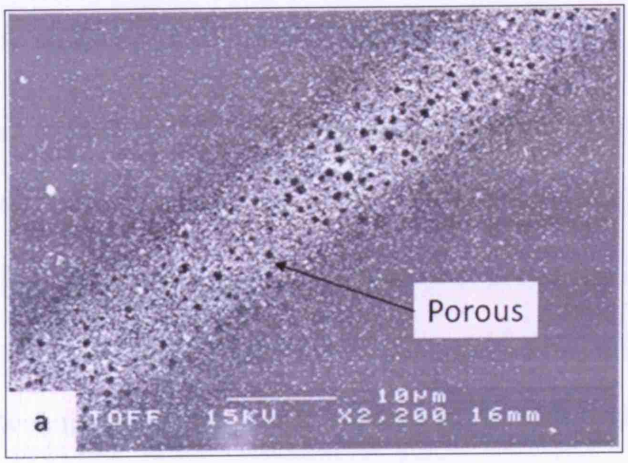

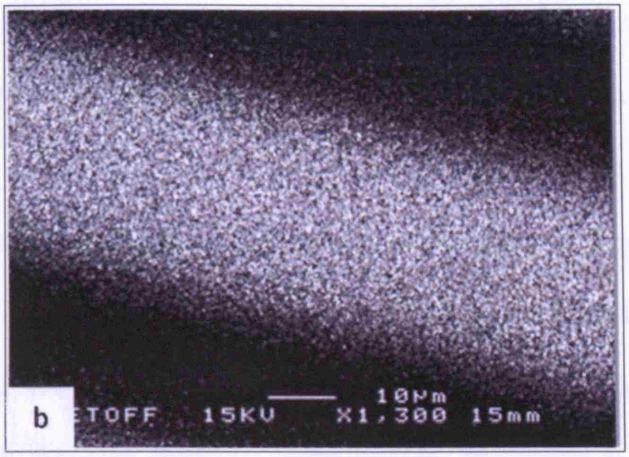

Figure 5.27 SEM images of the tracks deposited using a flow rate of 5×10^{-11} m^3s^{-1}. a) Sprayed for 90 s and b) Sprayed for 240 s

5.3.3 Track profile

In the case of tracks produced by electrohydrodynamic atomisation, due to low concentration of particles and rapid solvent evaporation, some particles will be aggregated to the edge of the track and other particles will be distributed randomly in the centre of the track. In order to overcome non-uniform particle spreading template method can be used get an even distribution of particles along the track. In the case of templating method, spraying can be carried out until the tracks are fully covered with particles and thus avoiding non-uniform particle spreading behaviour.

5.4 Patterning of conducting tracks by electrohydrodynamic printing

Due to low concentration and solvent evaporation, electrohydrodynamic printing and templating method were not suitable for producing dense conducting tracks. In order to produce dense tracks containing gold nanoparticles, a layer-by-layer deposition technique was employed in conjunction with electrohydrodynamic atomisation printing. Patterning was carried out at various number of layers and

with increasing number of layers it was evident that dense uniform tracks could not be achieved due to different solvent evaporation rates along the track.

In order to observe the particle arrangement along the line with increasing solvent evaporation rates it was decided to increase the substrate temperature before patterning. The substrate was kept on top of a heating device and patterning was carried out at different substrate temperatures. The substrate temperature was varied between 30 – 85 °C. The patterning speed was varied from 3 – 9 mms^{-1} in order to find out its effect on the printed line. **Figure 5.28** shows optical micrographs of the printed track deposited at 85 °C with various patterning speeds.

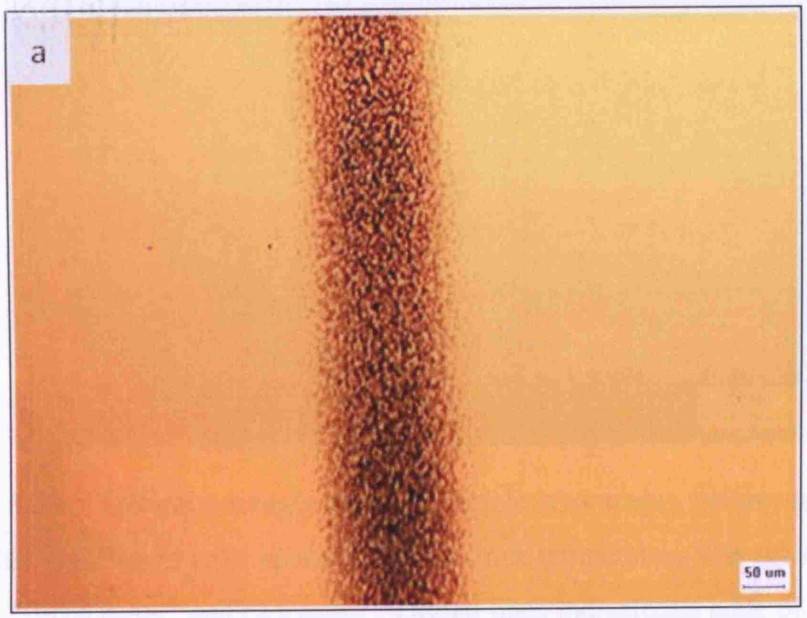

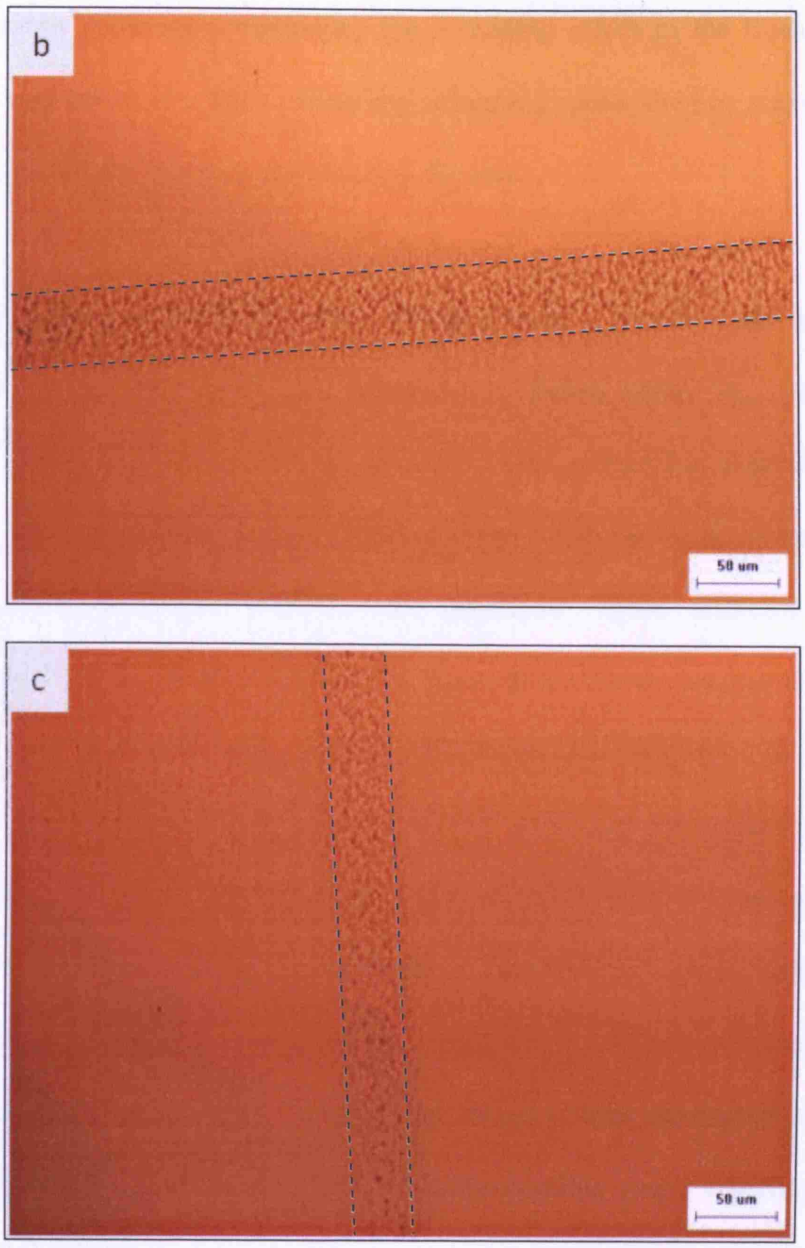

Figure 5.28 Optical micrographs of the single layer tracks (before sintering) deposited at different table speeds. The substrate temperature was set to 85 °C. a) 3 mms^{-1}, b) 6 mms^{-1} and c) 9 mms^{-1}. Dotted lines indicate the edge of the track.

When the substrate temperature was increased to more than 85 °C patterning was not possible due to rapid solvent evaporation from the exit of the needle, hence stable cone-jet mode was not possible to achieve for long durations which was required for patterning. From the optical micrographs, it is evident that

with increasing substrate temperature the spreading effect in the track reduces, hence line size decreases. With increasing patterning speed, the line size decreases due to less amount of droplets patterned on the line.

Although the particle spreading during solvent evaporation can be reduced greatly by increasing the substrate temperature during patterning, due to low concentration of metal particles in the alcosol, it was not possible to produce dense conducting tracks. In order to produce dense tracks containing gold nanoparticles, a layer-by-layer deposition technique was employed. Three different substrate temperatures were selected and patterning was carried out by varying the number of layers from 50 to 150. **Figure 5.29** shows optical micrographs of the tracks (50 layers) produced at a flow rate of 5 x 10^{-11} m^3s^{-1} and an applied voltage of 1.4 kV and a graph depicting the line width variation with increasing substrate temperature. In all experiments the distance between the needle exit and the substrate was ~300 μm. In order to produce more dense tracks the number of layers was increased from 50 to 150. **Figure 5.30** shows optical micrographs of tracks containing different number of layers and corresponding graph depicting the line width variation with increasing number of layers at 85 °C. The line width increased with increasing number of layers due to the chaotic motion of the jet and its digression from the centre line [Lee *et al.*, 2007].

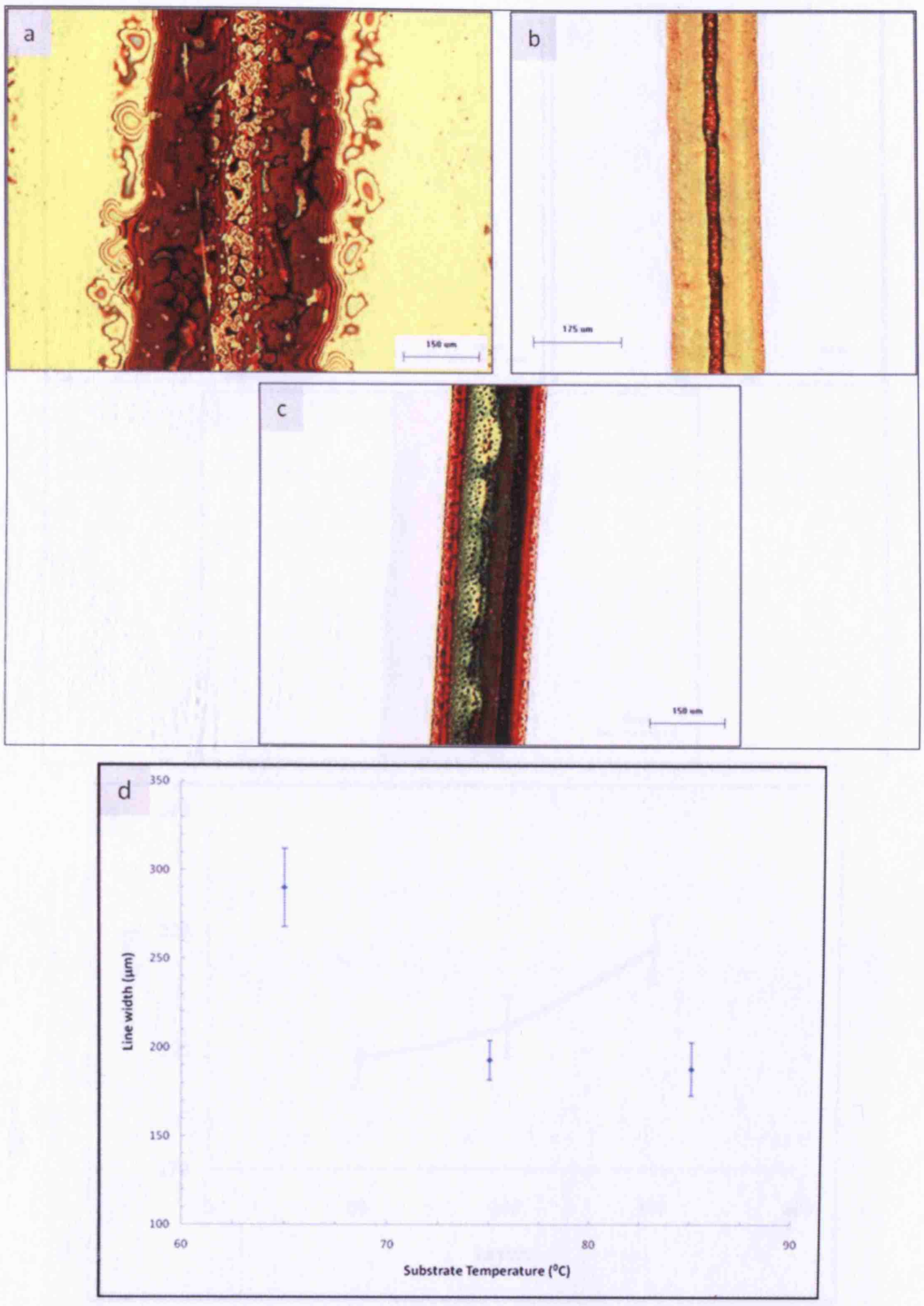

Figure 5.29 Optical micrographs of the patterned tracks (50 layers) at different substrate temperatures. a) 65 °C, b) 75 °C and c) 85 °C and d) a graph depicting the line width variation with increasing temperature. The flow rate was 5 x 10^{-11} m^3s^{-1} and applied voltage was 1.4 kV. The error bars indicates the standard deviation of the track width.

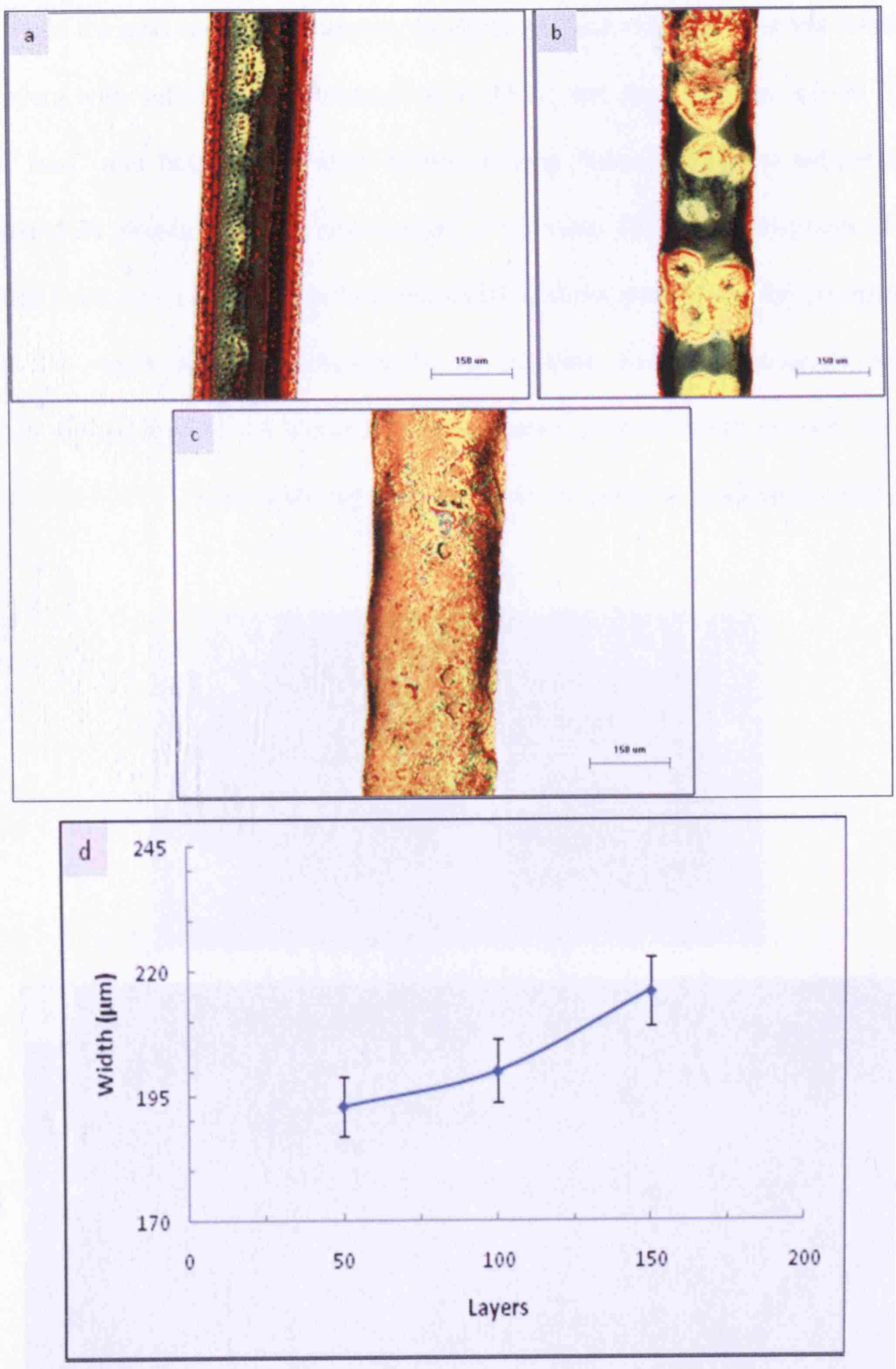

Figure 5.30 Line width variation with increasing number of layers at 85 °C. a) 50, b) 100 c) 150 and d) graph depicting the line width variation with increasing layers. The flow rate was 5 x 10^{-11} m^3s^{-1} and applied voltage was 1.4 kV. The error bars indicate the standard deviation of the width of the line.

In the next set of experiments, tracks were patterned with different numbers of layers with substrate temperature set at 85 °C and later sintered at 400 °C at 2 °C min^{-1} and held for 60 mins before cooling down to ambient temperature. **Figure 5.31** shows a digital photograph, a scanning electron micrograph of the printed track and its corresponding elemental analysis confirming the presence of gold. The microstructures presented in the scanning electron micrograph do not clearly discern the 15 nm diameter gold particles present in the alcosol. This is because at 400 °C partial sintering and growth of the particles have taken place.

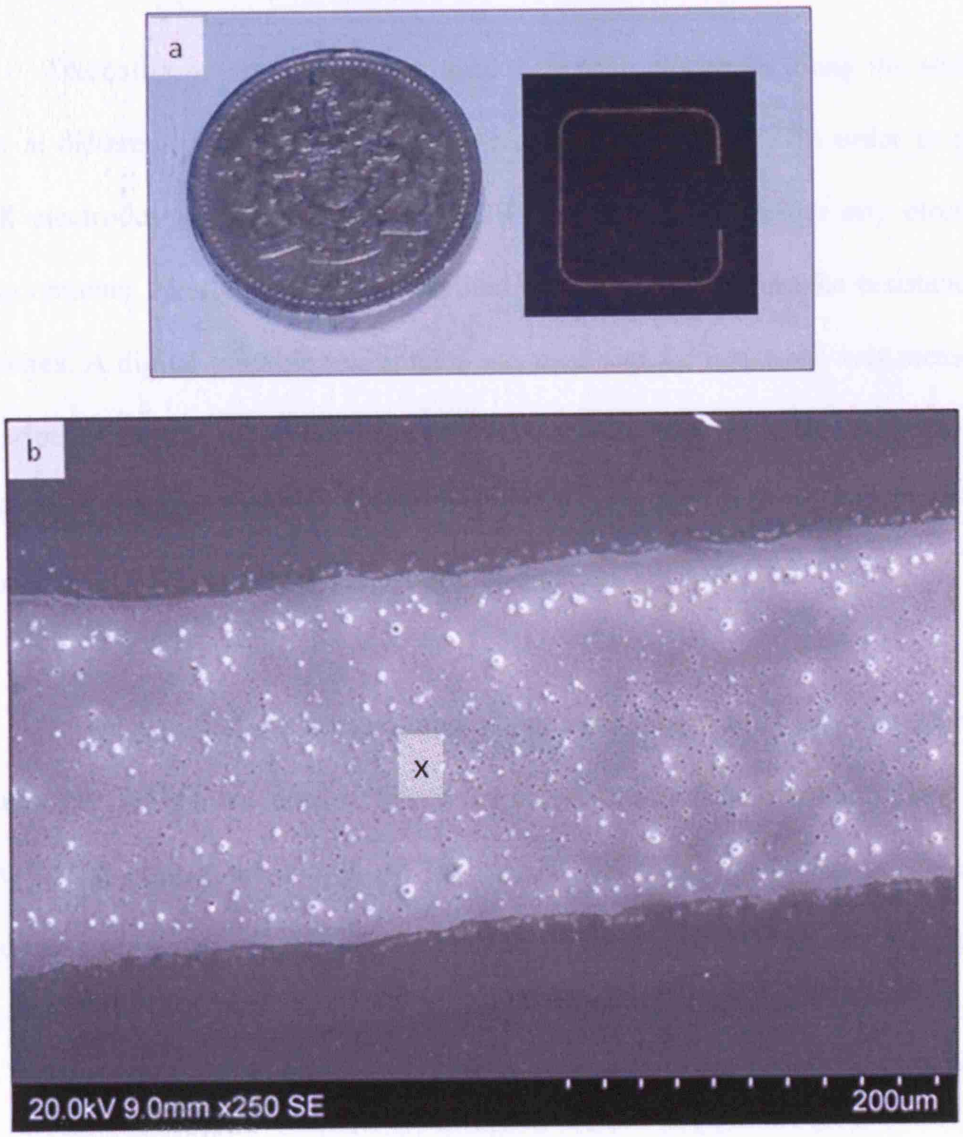

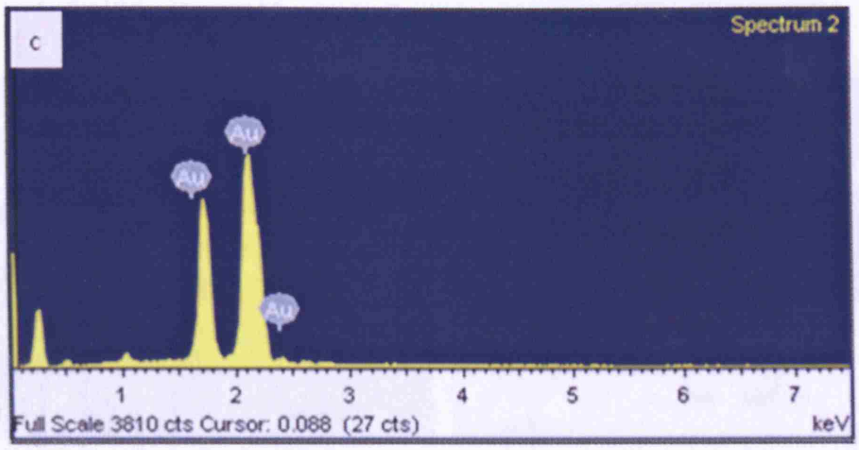

Figure 5.31 a) Digital image of a sintered track, b) Scanning electron micrograph of the printed track and c) Elemental analysis of point 'X' in *(b)*

Thereafter, a silver paste was used to deposit electrodes along the sintered track at different distances. The substrate was heated to 80 °C in order to place small electrodes and then sintered at 120 °C for 10 mins before any electrical measurements. Firstly, a two-point method was used to calculate the resistance of the wires. A digital portable multimeter was used and the resistance was measured at various distances along the track. In order to eliminate the electrode, wire and equipment resistance and to get a very accurate value, four-point method was employed later to measure the resistance of the line.

In order to find out the thickness of the conducting tracks, scanning electron microscopy (SEM) was used to image the cross section of the tracks. **Figure 5.32** show SEM images of the cross section of the tracks produced at different conditions and a graph depicting the thickness variation with increasing number of layers.

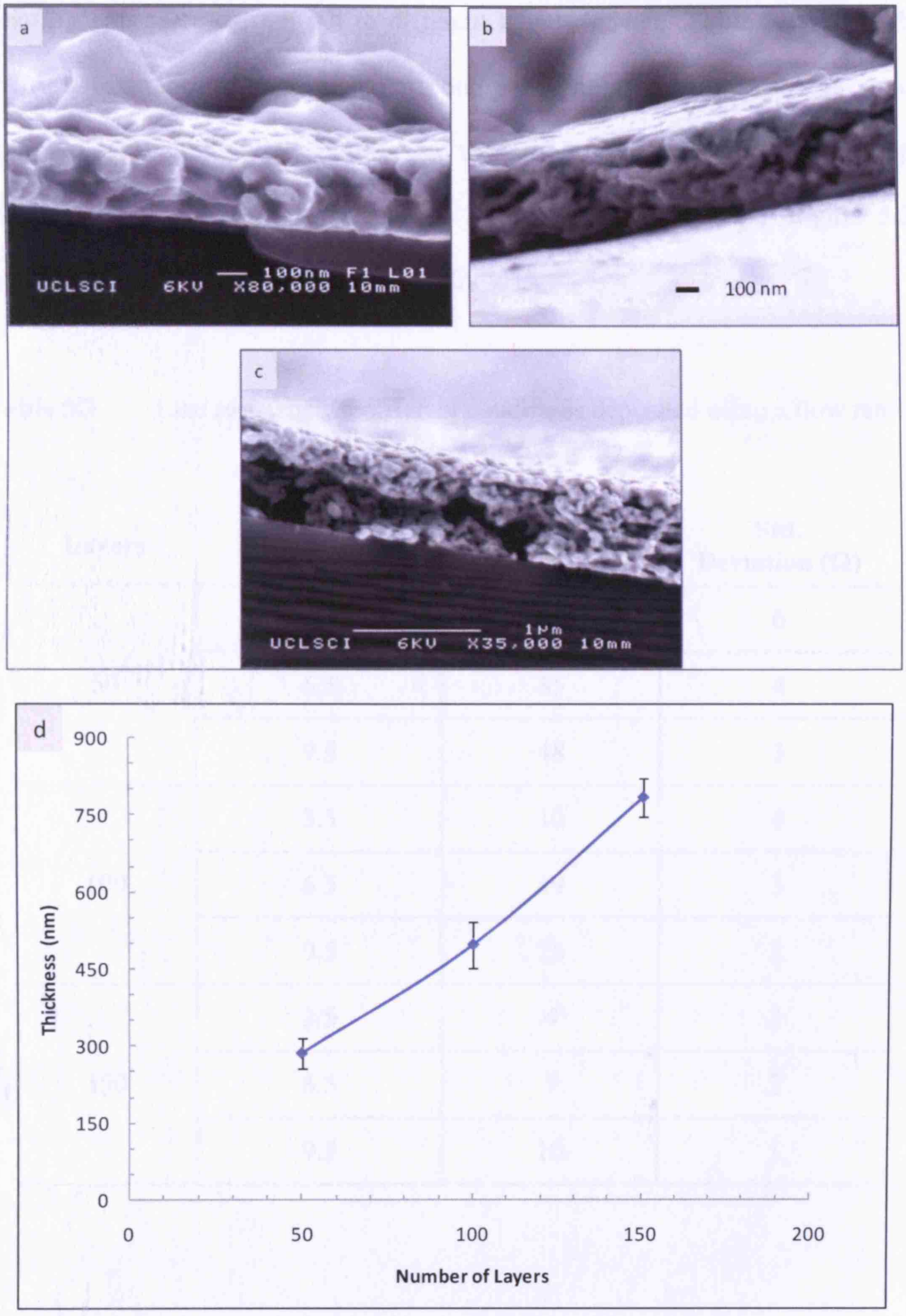

Figure 5.32 Thickness of the tracks with increasing number of deposition layers. a) 50, b) 100, c) 150 and d) graph depicting the thickness variation with increasing deposition layers. Error bars indicates the standard deviation of the thickness of the track

The number of layers were varied from 50 to 150 and electrical measurements were carried out to different lengths of line. **Table 5.3** shows the electrical resistance at each different condition. The applied voltage was varied from 0 to 15 V and the voltage drop and the current were recorded. The *I-V* graph was later plotted and the resistance was calculated from the graph. **Figure 5.33** shows the line resistance at different conditions.

Table 5.3 Line resistance at different conditions deposited using a flow rate of 5×10^{-11} m^3s^{-1}

Layers	Length (mm)	Resistance (Ω)	Std. Deviation (Ω)
50	3.5	20	6
	6.5	35	4
	9.5	48	3
100	3.5	10	4
	6.5	19	3
	9.5	25	2
150	3.5	4	2
	6.5	7	2
	9.5	10	1

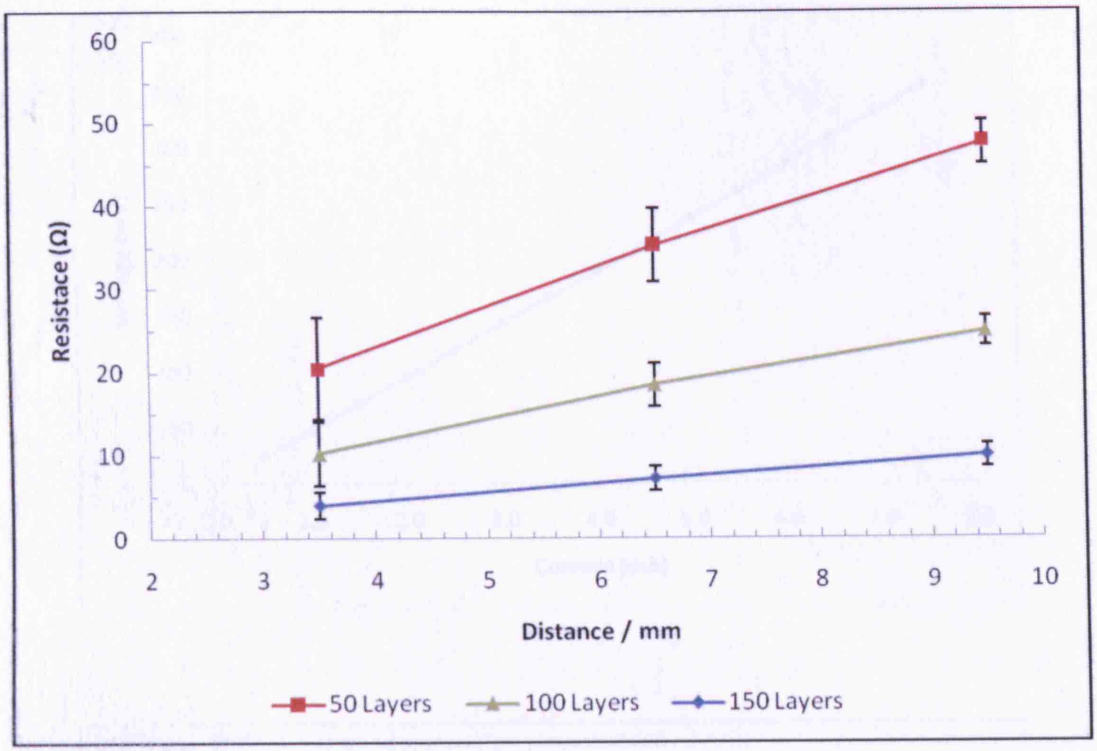

Figure 5.33 Line resistance with increasing number of layers and length deposited using a flow rate of 5 x 10^{-11} m^3s^{-1}

Figure 5.34 shows *I-V* characteristics of the tracks with increasing number of layers and they all showed a linear Ohmic behaviour. The electrical resistivity (ρ) of the produced tracks were calculated by the formula $\rho = {}^{RA}/_{L}$, where *R* is the electrical resistance of the line, *L* is the length of line and A is the cross sectional area of the line. From the SEM images of the cross section of the track revealed that the sintered track is very similar to a rectangular shape. The atomic forced microscope studies carried out by Lee and co-workers (2006) reported that tracks printed on the substrate to be very similar to a rectangular shape. Therefore, to calculate the cross section area ($A = w \times t$) where *w* is the width of the track and *t* is the thickness of the track was used.

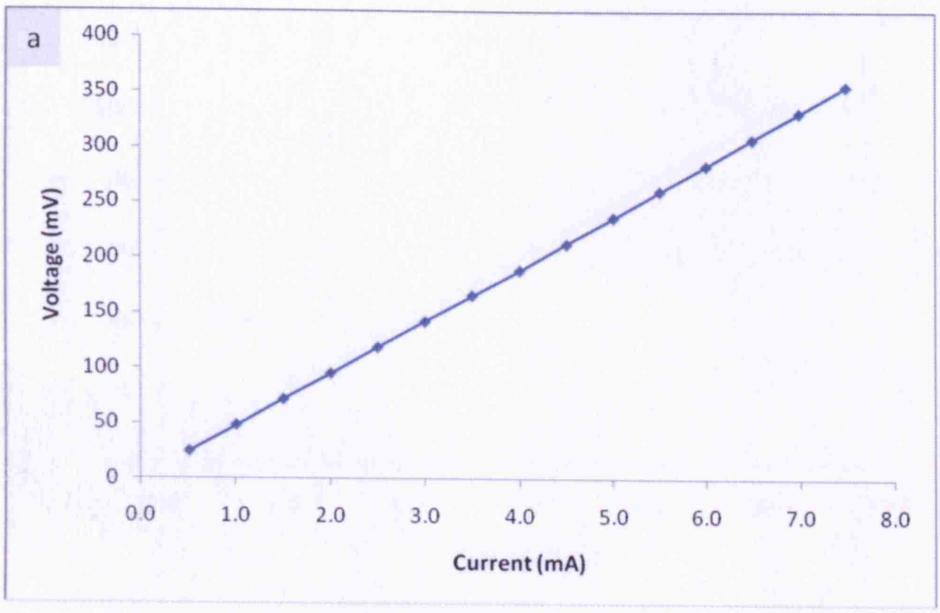
a
Voltage (mV)
400
350
300
250
200
150
100
50
0
0.0
1.0
2.0
3.0
4.0
5.0
6.0
7.0
8.0
Current (mA)

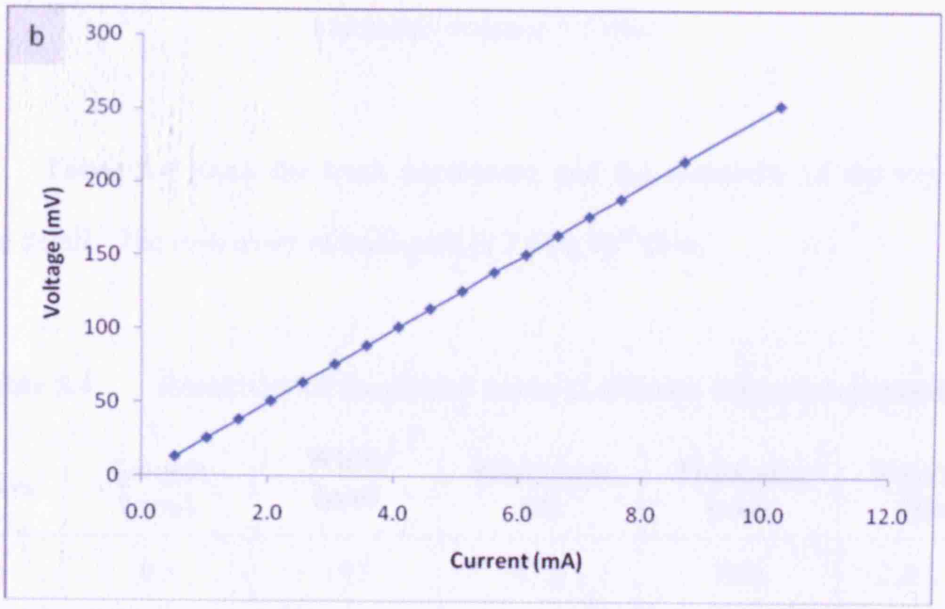
b
Voltage (mV)
300
250
200
150
100
50
0
0.0
2.0
4.0
6.0
8.0
10.0
12.0
Current (mA)

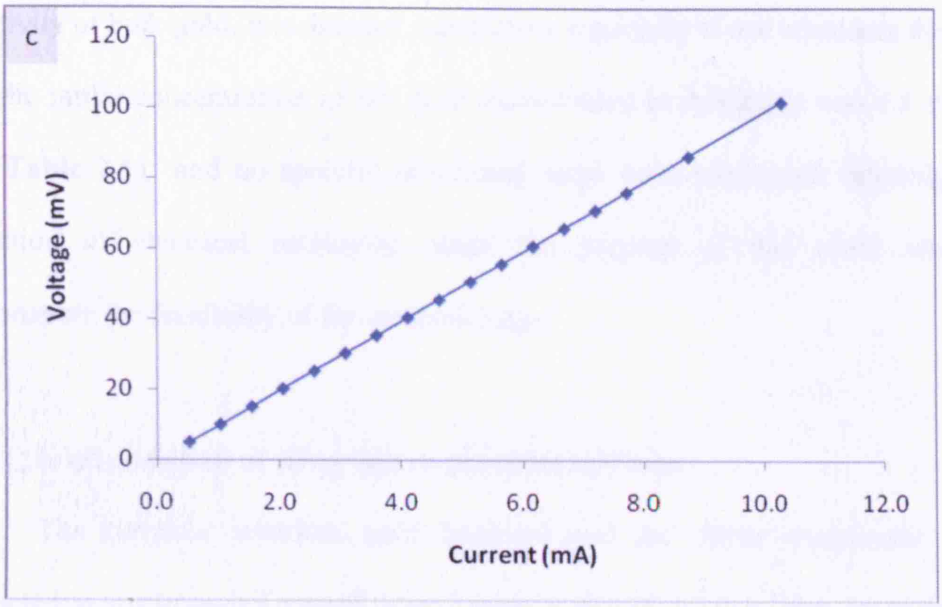

Figure 5.34 *I-V* graphs of tracks. a) 50 layers, b) 100 layers and c) 150 layers. Measured distance 9.5 mm

Table 5.4 gives the track parameters and the resistivity of the tracks in more detail. The resistivity of bulk gold is 2.44 x 10^{-8} Ω m.

Table 5.4 Resistivity of the printed tracks at different deposition parameters

Layers	Length (mm)	Width (μm)	Resistance (Ω)	Thickness (nm)	Resistivity (Ωm)
50	9.5	193	47.6	286	2.8 x 10^{-7}
100	9.5	200	24.8	497	2.6 x 10^{-7}
150	9.5	216	9.9	784	1.8 x 10^{-7}

The electrical resistivity of the printed tracks using layer-by-layer approach was in the range of 1.8 x 10^{-7} – 2.8 x 10^{-7} Ωm. The resistivity of the track changes with increasing number of layers due to more particles being deposited on the track and thus making it more conducting. Although this value is higher than the

resistivity of bulk gold, it is deemed satisfactory especially if one considers the fact that the initial concentration of the gold alcosol used in this study was 0.1 wt. % (see **Table 2.1**) and no specific processing steps were performed targeting the reduction of electrical resistivity, since the purpose of this study was to demonstrate the feasibility of the methodology.

5.4 Encapsulation of silver micro-particles in fibres

The polymer solution, gold hydrosol and the silver suspension were subjected to electrohydrodynamic atomisation as described in the previous chapter. The gold hydrosol was not able to be atomised under stable cone-jet mode due to its surface tension (69 mN/m) and its high electrical conductivity (1.56×10^{-2} Sm^{-1}). The silver suspension had a much lower surface tension (30 mN/m) compared to the polymer solution (72 mN/m) and this helps to make it jet and atomize compared with the polymer, which electrospins, as in classical electrohydrodynamic atomization overcoming the surface tension with electrical forces is essential. The electrospinning of the polymer is helped by its high viscosity, which is significantly higher than that of the silver suspension. The electrical conductivity of the silver suspension is low as it contained organic solvents and a thermoplastic binder and in suspension the silver particles are not in contact with each other.

In the next set of investigations, the polymer solution and silver suspension were subjected to the process of co-axial jetting simultaneously. In these experiments the silver suspension was always pumped through the inner needle and the polymer through the outer needle. With the increase of applied voltage, a cone

of polymer solution completely surrounding an inner cone of silver suspension evolved and this co-axial cone obtained was held by its surface tension. As the electric field was further increased the electric force overcomes the surface tension and a charged co-axial jet was ejected from the tip of the outer cone. At an applied voltage of 12.4 kV and inner and outer flow rates of 1 x 10^{-10} m^3s^{-1}, this co-axial jet (**Figure 5.35**) streams down to undergo whipping by which the solvent evaporates leaving behind a mesh of charged polymer fibres having silver particles encapsulated within them. **Figure 5.36a** shows a typical fibre with a uniform diameter of ~30 μm along its length. Agglomerates of silver particles were seen to spread along the fibre length and elemental line scan analysis (**Figure 5.36b**) proved the presence of Ag encapsulated within the polymer coating.

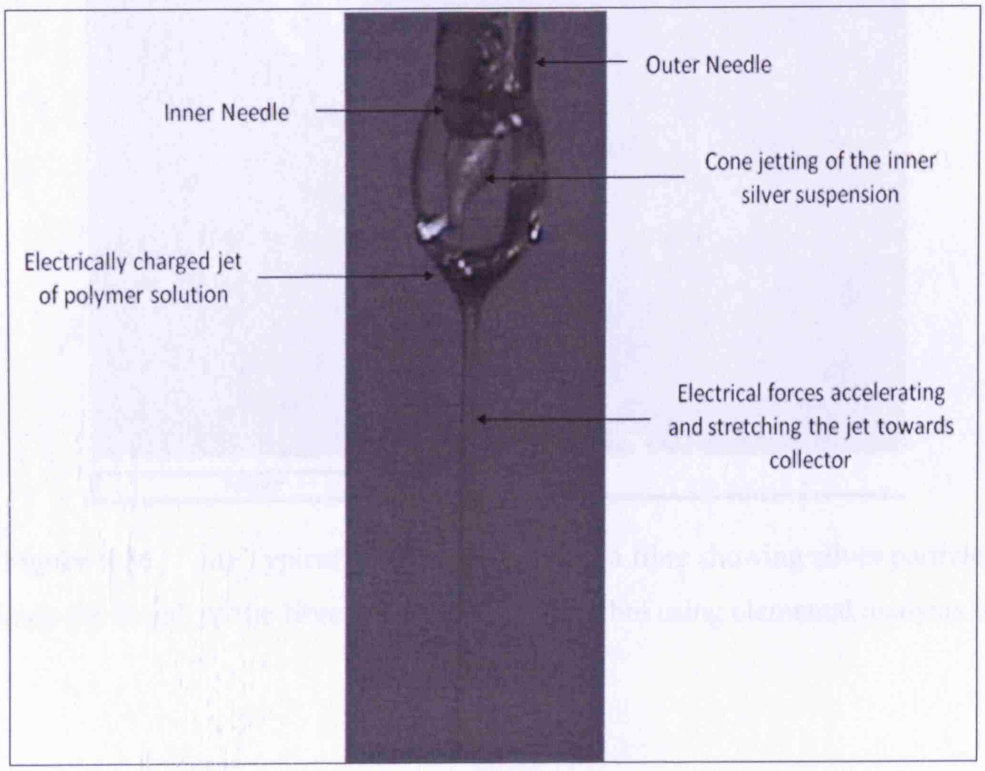

Figure 5.35 Co-axial jetting of silver suspension and polymer solution. The flow rate of inner and outer needles was 1 x 10^{-10} m^3s^{-1} and applied voltage was 12.4 kV

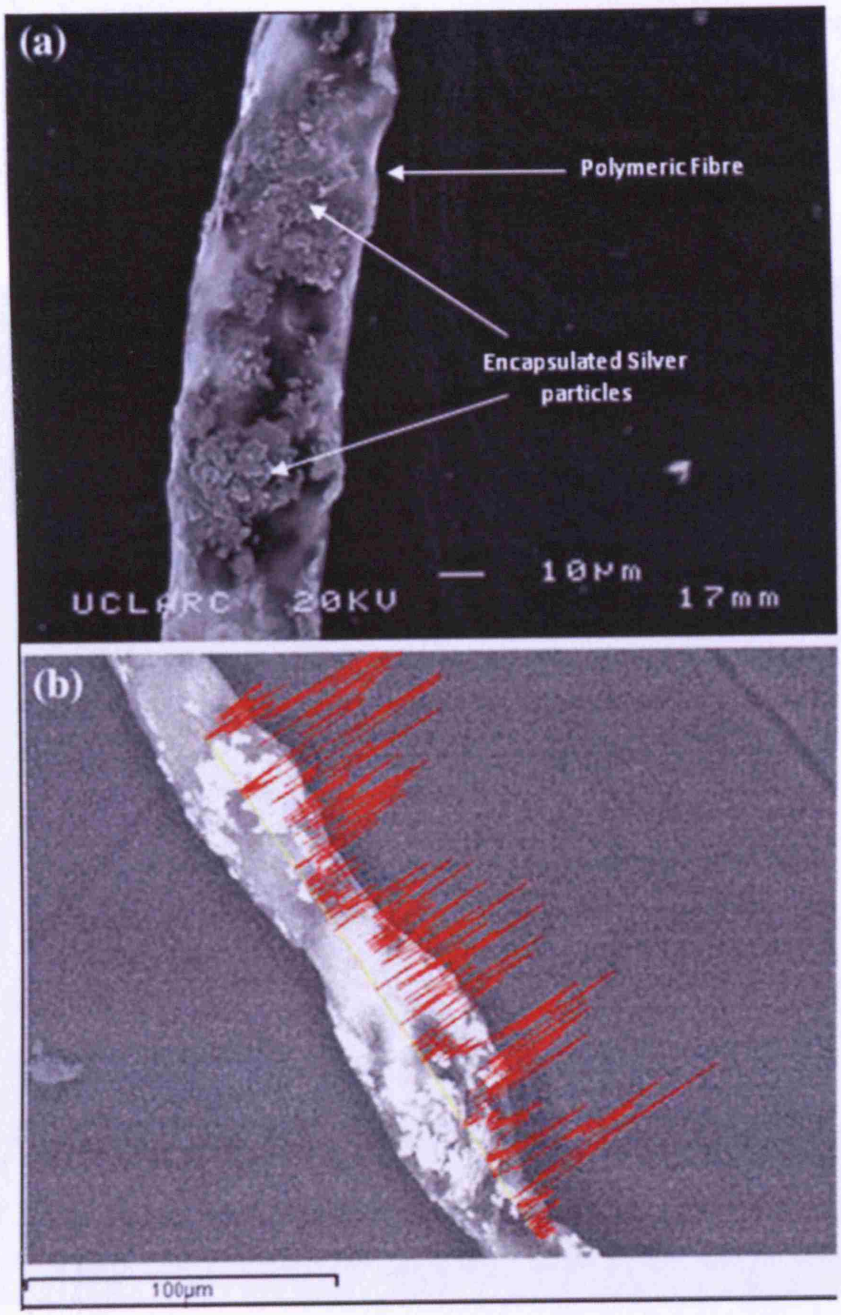

Figure 5.36 (a) Typical SEM micrograph of a fibre showing silver particles along the length of the fibre. (b) Line scan of a fibre using elemental analysis for silver

Figure 5.37 shows a SEM of fibre mesh collected on glass slide. Closer examination of the fibres revealed that it contains few beads. Experiments carried

out by Fong and co-workers (1999) reported that, this unexpected phenomenon is caused by solution viscosity, surface tension and net charge density induced by the electrospinning process are the main factors in the formation of beads during the formation of electrospun fibres.

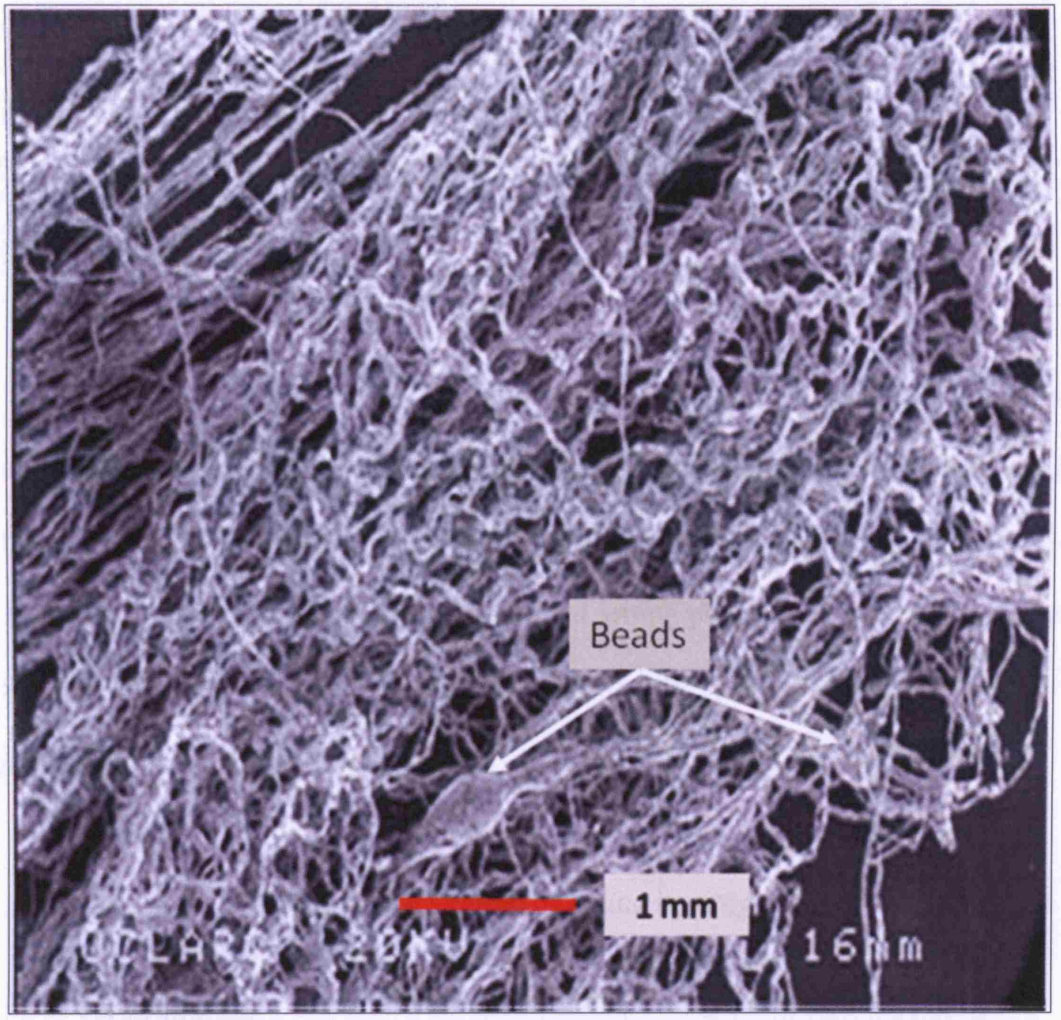

Figure 5.37 Typical fibre mesh collected on the glass slides. Both inner and outer needle flow rate was 1 x 10^{-9} m^3s^{-1}. The applied voltage was 12.4 kV

In a subsequent set of experiments, both the polymer solution and the silver suspension were pumped together in the inner and outer needles respectively at various flow rates. In these investigations, the outer flow rate was set to a constant

value 1 x 10^{-9} m^3s^{-1} and the inner flow rate was varied in regimes of 1 x 10^{-9} m^3s^{-1} to 1 x 10^{-12} m^3s^{-1} (**Table 5.5**).

Table 5.5 Different inner and outer needle flow rates used for encapsulation

Combination	Outer flow rate (m^3s^{-1})	Inner flow rate (m^3s^{-1})
A	1 x 10^{-9}	1 x 10^{-9}
B	1 x 10^{-9}	1 x 10^{-10}
C	1 x 10^{-9}	1 x 10^{-11}
D	1 x 10^{-9}	1 x 10^{-12}

The corresponding speed of jetting for various flow rates was calculated by dividing the flow rates by the relevant cross-section area of the inner and outer needles as explained in **Section 3.1.1**. The applied voltage was varied from 10.9 – 11.6 kV. From each combination the co-axial jetting process was recorded and the samples collected were analysed. **Table 5.6** gives the speed of the inner and outer jets.

Table 5.6 Speed of jetting investigated

Combination	Outer needle speed of jetting / mms^{-1}	Inner needle speed of jetting / mms^{-1}
A	2.5	20
B	2.5	2
C	2.5	0.2
D	2.5	0.02

The fibres generated from electrospinning at various flow rates detailed above (**Table 5.5**) were collected on microscopic glass slides and later coated with gold for SEM analysis. Overall, arrangements of the silver particles in the encapsulated samples prepared were dependent on the speed of jetting in the inner needle. **Figure 5.38** show the co-axial jetting observed from combination A, B, C and D detailed in **Table 5.5**. **Figure 5.39** show the corresponding structure of the encapsulation observed. For combination A, the inner speed of jetting was much higher than all other combinations and the fibres collected showed densely packed silver particles across and along the fibre, apart from a few regions, surrounded by a very thin layer of polymer **Figure 5.38a** and **Figure 5.39a**.

As the speed of jetting in the inner needle was decreased by four orders of magnitude, the pattern of the silver particle assemblies encapsulated in polymer changed. In **Figure 5.39b** the particles are present as separate globular regions along the length of the fibre. In **Figure 5.39c** and **d** the silver particles seem to sit along an inner strand of polymer, but at the lowest jetting speed in the inner needle, the silver particles are in distinctive agglomerates, which are spaced well apart along the length fibre (**Figure 5.39d**).

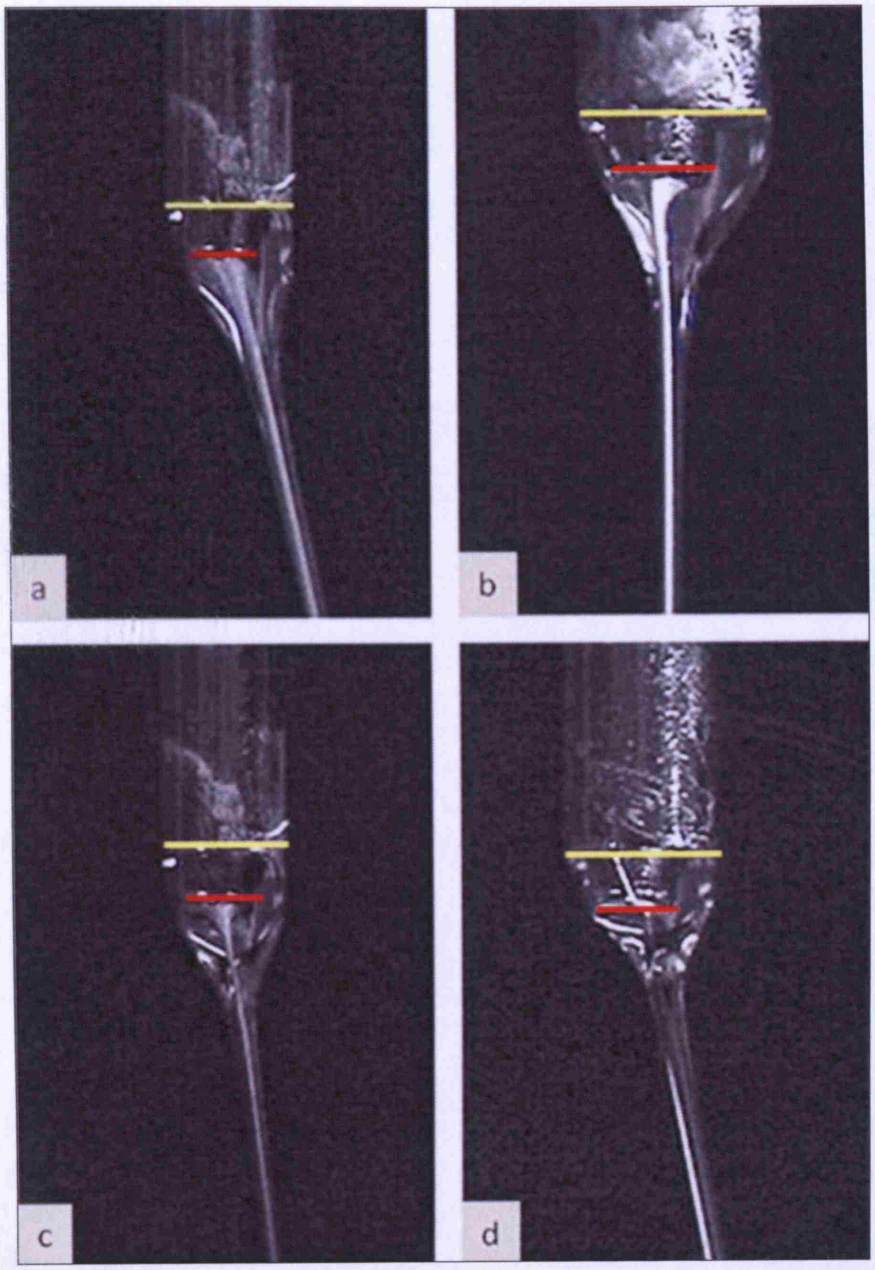

Figure 5.38 Co-axial jetting of polymer solution on outer needle and silver suspension on the inner needle undergoing various speed of jetting as shown in ***Table 5.6***. Yellow line indicate the exit of the outer needle and red line indicate the exit of the inner needle

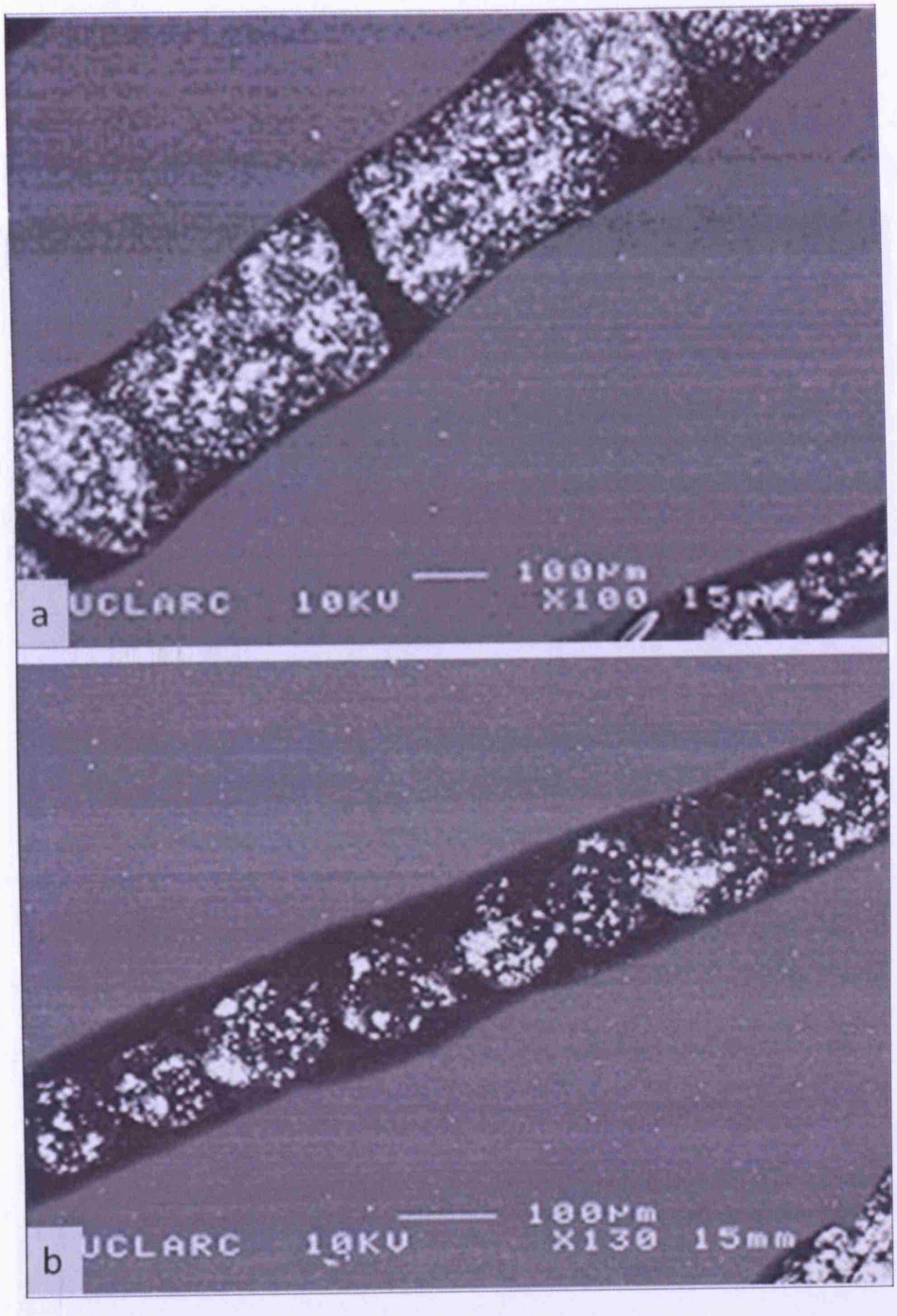
a
UCLARC 10KV 100μm X100 15mm
b
UCLARC 10KV 100μm X130 15mm

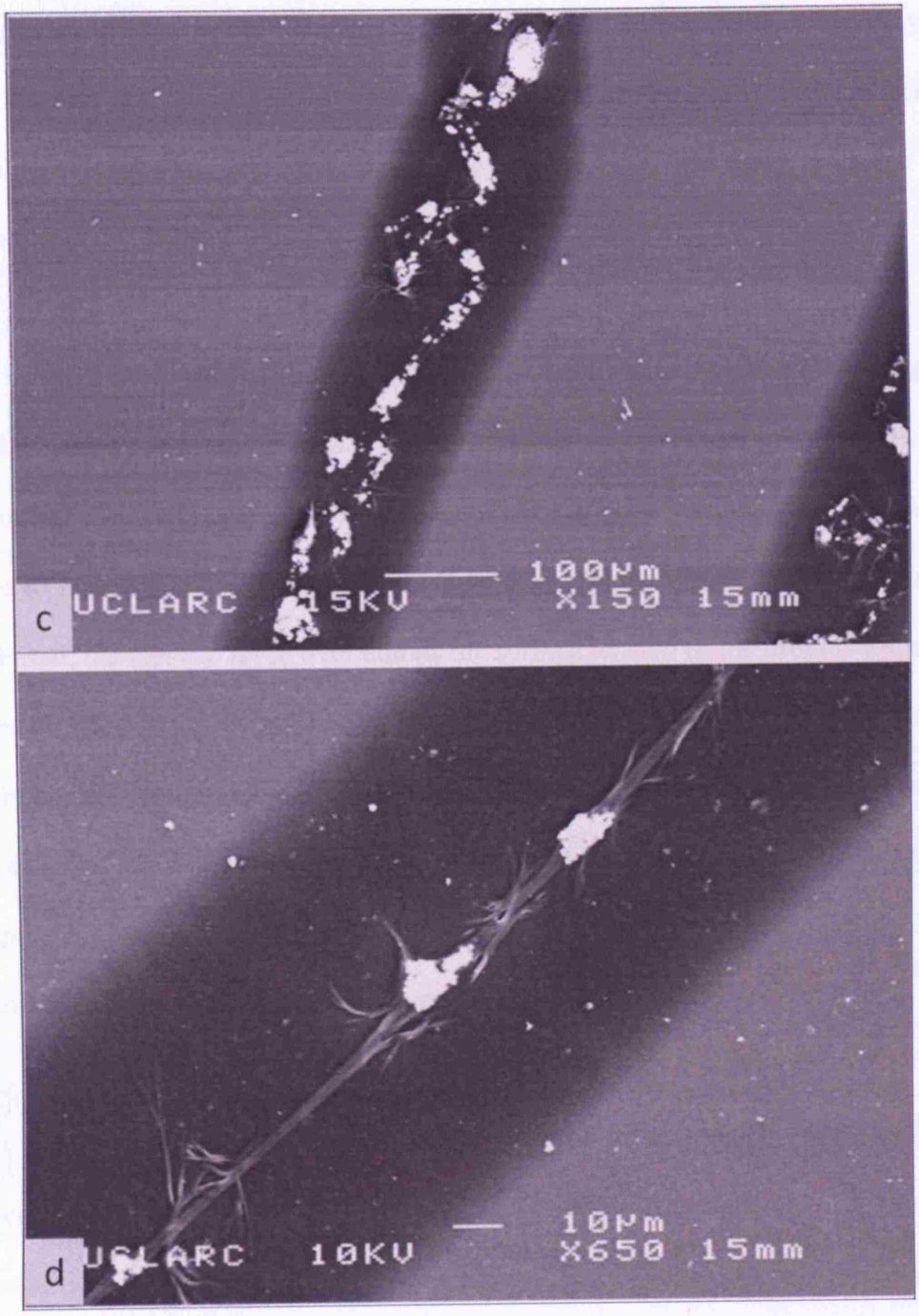

Figure 5.39 Fibres collected from various speeds of jetting (***Table 5.6***) showing encapsulated silver in the middle. The morphology of the encapsulated silver was a direct replica of their corresponding speed of jetting on the inner needle

5.5 Encapsulation of gold sphere shaped nanoparticles in fibres

The polymer mixture and the gold hydrosol was used in outer and inner needles respectively and subjected to electrospinning. **Figure 5.40** show an image captured from the camera before subjecting to electrospinning. The polymer solution and the gold hydrosol were subjected to the process of co-axial jetting simultaneously. The flow rate of the polymer solution and gold hydrosol was varied from $1 \times 10^{-8} - 1 \times 10^{-11}$ m^3s^{-1}.

First, the gold hydrosol was forced into the inner needle and the applied voltage was increased gradually. Subsequently, polymer solution was forced through the outer needle and simultaneously the applied voltage was increased in order to maintain the stability of the co-axial jet. As the electric field is gradually increased, the electric force over comes the surface tension of the droplet at the exit of the needle and a charged co-axial jet was ejected from the tip of the outer cone. At an applied voltage of 7.8 kV and inner and outer flow rates of 5×10^{-11} m^3s^{-1}, this co-axial jet (**Figure 5.41**) streams down to undergo whipping by which solvent evaporates leaving behind a mesh of charged polymer fibres, having gold nanoparticles encapsulated within them.

Figure 5.42 shows TEM images of the fibres which were collected 20 cm below the needle exit. From the TEM images it is apparent that the gold nanoparticles disperse in a random order and is due to turbulent flow encountered in the jetting operation which causes intense mixing in the cone [Shtern and Barrero, 1995, Barrero *et al.*, 1998]. The mixing of the gold alcosol and the polymeric medium has helped the turbulent flow and the dispersion of the gold

nanoparticles in the product. By careful tailoring of the gold concentration and the processing parameters, it should be possible to reach the percolation threshold in the composite and this will pave the way for preparing polymeric sheaths with pre-designed electrical conductivity / insulation.

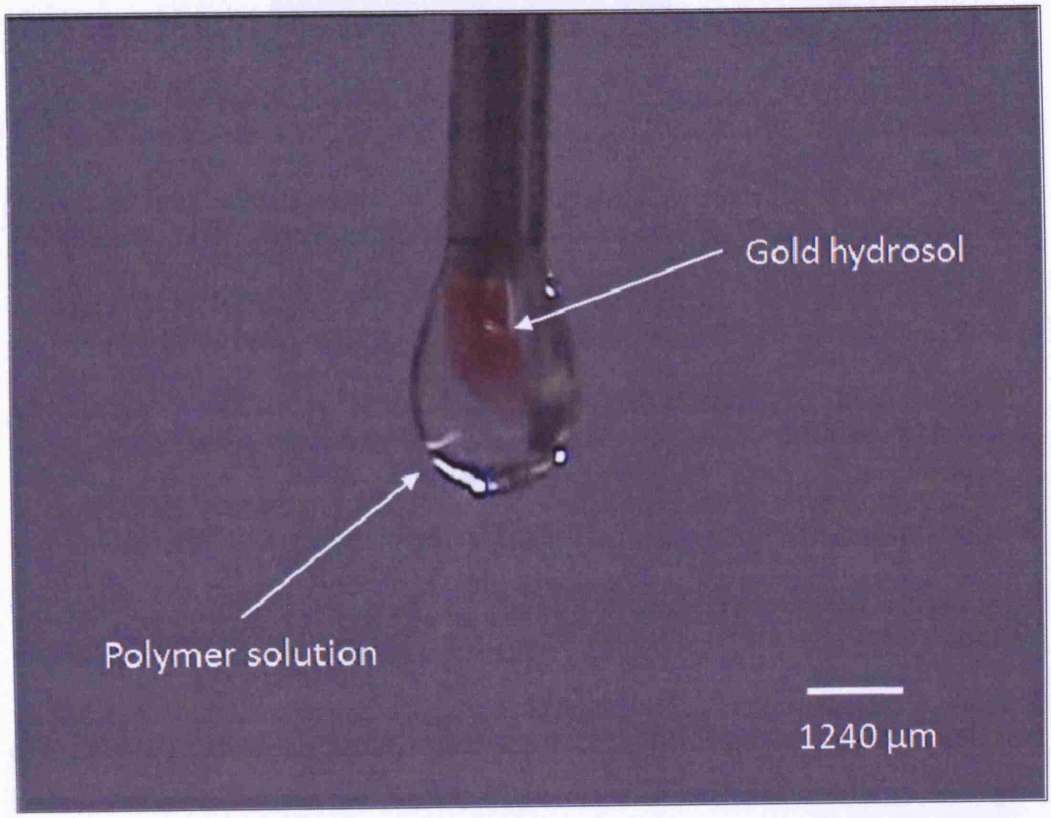

Figure 5.40 The polymer mixture and the gold hydrosol before subjecting to electrospinning

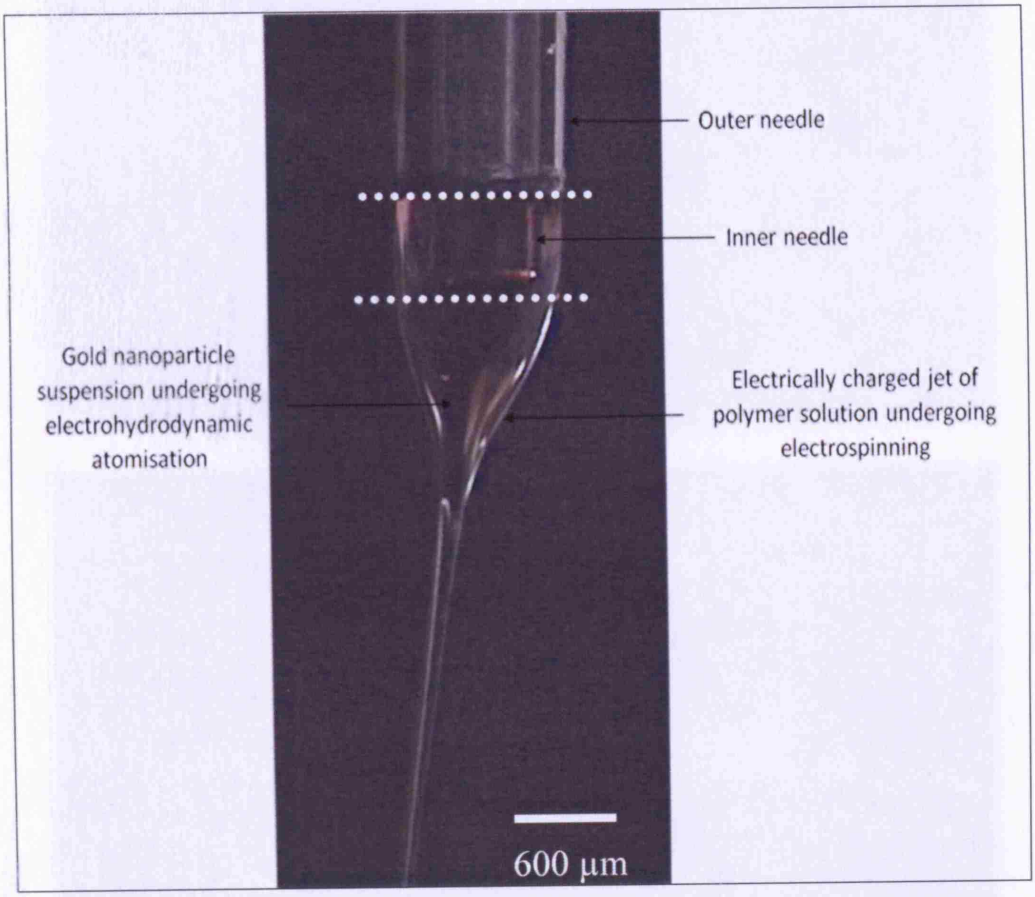

Figure 5.41 Co-axial jet produced by electrospinning. Dotted lines indicate the outer and inner needle exit

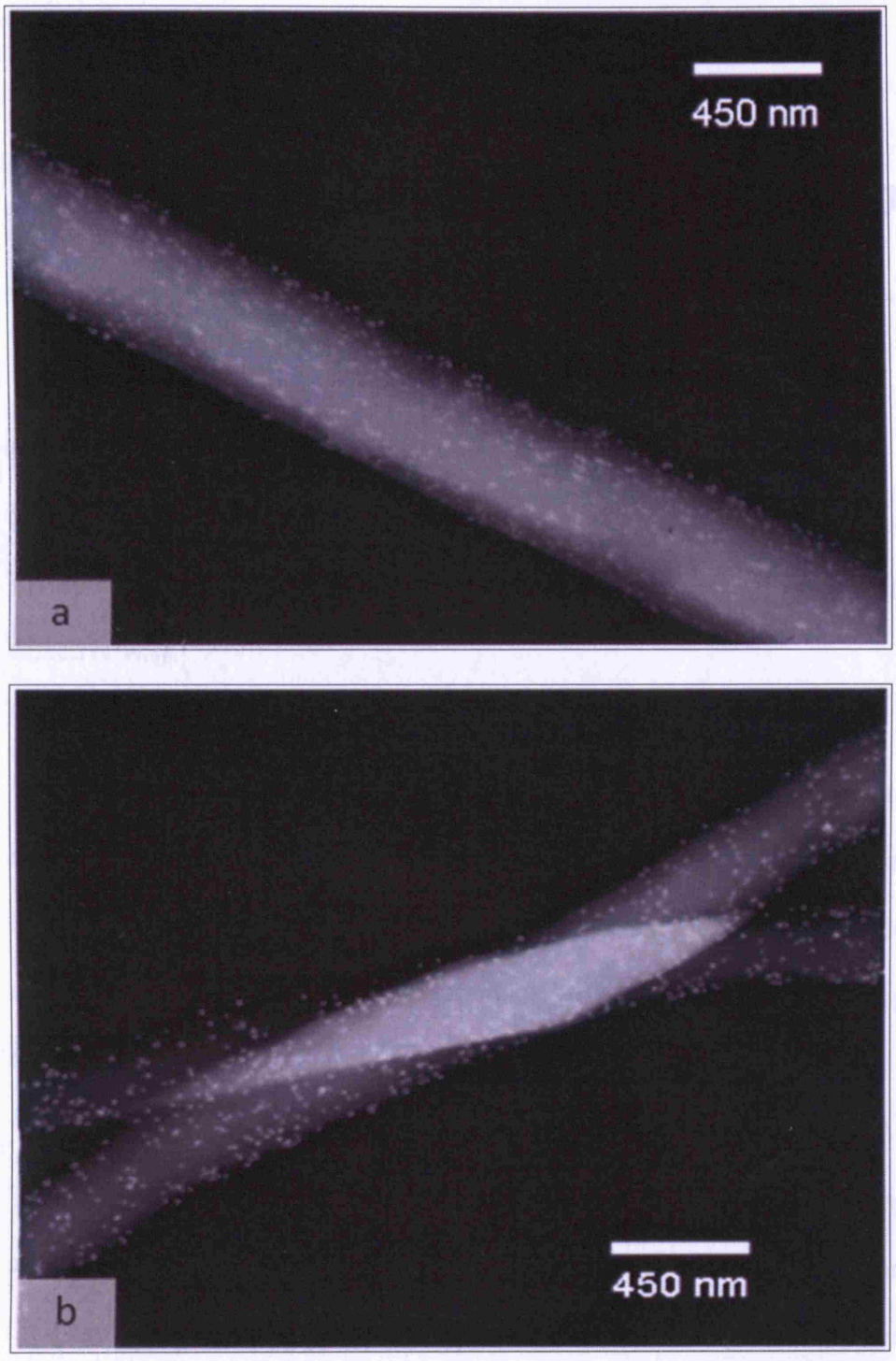

Figure 5.42 Gold particles encapsulated fibres produced from electrospinning. White dots along the polymer indicated gold nanoparticles

Chapter 6

Conclusions & Future work

6.1 Conclusions

The conclusions of this research are as follows:

- Electrohydrodynamic atomisation can be used to process solutions containing metallic particles to fabricate various microstructures in a simple and cost effective way.

- Water based gold solution can not be electrically atomised using a straight edge needle to achieve a stable cone-jet mode due to its high surface tension and high electrical conductivity. Therefore metal nanoparticles were suspended in ethanol to achieve a stable cone-jet mode to produce a near-monodisperse stream of droplets.

- The gold and silver alsocols were subjected to electrohydrodynamic atomisation in the stable cone-jet mode and its effects were studied by varying the parameters such as applied voltage and alcosol flow rate. In all cases the cone depth and the jet diameter decreases with increasing applied voltage.

- Mode selection maps (flow rate vs applied voltage) for all alcosols were plotted which gave a basic indication for film fabrication and printing.

- Gold films were fabricated using the sphere shaped gold alcosol. With increasing deposition time, the film thickness increases as expected. Gold films with a thickness ranging from ~500 nm to micrometer scale can be easily fabricated using electrohydrodynamic atomisation.

- Due to the "size segregation effect" the centre of the films was much denser when compared with the edge of the film. Due to the highly charged droplets and the size segregation effect, formation of hillocks can be observed on the surface of the films. With increasing spraying time formation of hillocks increases due to more droplets being deposited.

- 2D electrohydrodynamic atomisation print-patterning is a convenient and a powerful deposition technique which enables the fabrication of high resolution microstructures utilizing nanometer sized particle suspensions. The distance between the needle and substrate is a key parameter in electrohydrodynamic atomisation printing. From the initial experiments carried out, the optimum distance was found to be ~0.5 mm for all alcosols.

- The finest line width possible to produce from electrohydrodynamic atomisation was ~110 μm. Due to the solvent evaporation and the low concentration of the alcosol used, after deposition a small percentage of particles were agglomerated at the edge of the printed line, and the remaining particles aggregated randomly at the centre of the track.

- Due to the low concentration of metal particles and rapid solvent evaporation, conductive tracks were not possible to produce directly from electrohydrodynamic atomisation printing. In order to produce conductive tracks, a layer-by-layer deposition technique was used in conjunction with electrohydrodynamic atomisation printing.

- The resistivity of the printed tracks using the layer-by-layer deposition technique varied between $1.8 \times 10^{-7} - 2.8 \times 10^{-7}$ Ω m. This is an interesting result considering the gold concentration used in ink-jet printing was about 200 – 300 times higher than what is reported in this thesis.

- With the use of co-axial capillaries and electrospinning process metal particles were encapsulated in polymer sheaths. By changing the inner jetting speed, different patterns containing metal particles could be produced within the fibre.

6.2 Future work

Based on the research conducted and the outcome produced in this thesis, the following recommendations are made for future work.

- In order to get much finer metal films, the concentration of the solution should be increased, the physical properties should be altered to produce nanosized droplets by electrohydrodynamic atomisation and to decrease the deposition time. In order to find out the solvent effect on the film produced, solvents with a range of boiling points (eg. 45 °C – 150 °C) need to be investigated.

- Jet behaviour during electrohydrodynamic atomisation printing process should be further investigated in order to accurately control the patterned result. In order to capture the jet images a small high speed camera with microscopic lenses should be attached near to the printing head (needle). The changes of the cone and the jet before printing, during printing and after printing should be carefully compared.

- Small structures can not be accurately printed on substrates due to vibrations that occur from the printing device. The printing table should be modified and the printer head should be isolated from the printing device so that it will decrease the vibrations which results in a better quality track.

- A careful study should be carried out with increasing particle loading to find out the concentration where all the particles agglomerate to form a dense metal track. Furthermore, the solvent should be also varied to observe changes in the patterned track.

- The metal solutions physical properties should be altered in order to get nano-sized droplets before subjecting to electrohydrodynamic atomisation printing, thus resulting in finer tracks.

- In order to produce conductive metal tracks, the concentration of the solution should be increased and to get a fine track, the substrate should be modified to a hydrophobic surface. A literature review should be carried out on different ways of coating the substrate to find out the best method to coat the substrate.

- The effect of flow rate, applied voltage and the needle size should be carried out and modelled. From this research, the effect of flow rate on the printing resolution was found out. A systematic investigation should be carried out on the printing resolution as a function of flow rate and applied voltage. The influence of the capillary diameter and its effects should be also carefully investigated.

- A detailed study should be carried out by varying the deposition time and the flow rate in template assisted patterning to find out the effects on the track width and the porosity of the track.

- Layer-by-layer deposition technique should be further explored. The chaotic motion of the jet should be carefully controlled in order to pattern fine structures.

- The 2-axis printing device should be extended to 3-axes. The 3-axis printing device could be employed to fabricate 3D metal structures by electrohydrodynamic atomisation printing. By using a higher metal concentration, 3D printing device can be used to fabricate sophisticated circuit boards for future devices.

- In order to produce dense metal particles inside a fibre by electrospinning, the metal particle concentration should be increased and the particles should be suspended in a medium where it is immiscible with the polymer solution. Electrospinning of these two immiscible solutions should be carried out and by

carefully altering the flow rates and applied voltages, different microstructures along the fibre could be produced.

- Microbubbles are very important vehicles in medical diagnostics, as significant therapeutic agents, and this market is only just being explored. In the medical ultrasound imaging, for example, microbubbles are used as contrast agents on account of their ability to scatter ultrasound nonlinearly and as a drug deliver agent. One important method of stabilising microbubbles and enhancing their non-linear behaviour is, to reinforce them with particulates and gold nanoparticles are an ideal source for this. Co-axial electrohydrodynamic atomisation technique together with gold hydrosol should be employed to facilitate microbubbling for therapeutic and medical diagnostics applications.

REFERENCES

ALLEN, C. G., DORR, J. C., KHANDEKAR, A. A., BEACH, J. D., SCHICK, I. C., SCHICK, E. J., COLLINS, R. T. & KUECH, T. F. (2007) Microcontact printing of indium metal using salt solution "ink". *Thin Solid Films,* 515, 6812-6816.

ALLEN, M. L., ARONNIEMI, M., MATTILA, T., ALASTALO, A., OJANPERA, K., SUHONEN, M. & SEPPA, H. (2008) Electrical sintering of nanoparticle structures. *Nanotechnology,* 19, 175201.

ATKINSON, A., DOORBAR, J., HUDD, A., SEGAL, D. L. & WHITE, P. J. (1997) Continuous ink-jet printing using sol-gel "ceramic" inks. *Journal of Sol-Gel Science and Technology,* 8, 1093-1097.

BALASUBRAMANIAN, K., JAYASINGHE, S.N., EDIRISINGHE, M.J. (2006) Coaxial electrohydrodynamic atomization of ceramic suspensions. *International Journal of Applied Ceramic Technology*, 3, 55-60.

BARRERO, A., GANAN-CALVO, A. M., DAVILA, J., PALACIO, A. & GOMEZ-GONZALEZ, E. (1998) Low and high Reynolds number flows inside Taylor cones. *Physical Review E,* 58, 7309-7314.

BAUMGARTEN, P. K. (1971) Electrostatic spinning of acrylic microfibers. *Journal of Colloid and Interface Science,* 36, 71-79.

BESRA, L. AND LIU, M. (2006) A review on fundamentals and applications of electrophoretic deposition (EPD). *Progress in Materials Science*, 52, 1-61.

BIERI, N. R., CHUNG, J., HAFERL, S. E., POULIKAKOS, D. & GRIGOROPOULOS, C. P. (2003) Microstructuring by printing and laser curing of nanoparticle solutions. *Applied Physics Letters,* 82, 3529-3531.

BIERI, N. R., CHUNG, J., POULIKAKOS, D. & GRIGOROPOULOS, C. P. (2004) Manufacturing of nanoscale thickness gold lines by laser curing of a

discretely deposited nanoparticle suspension. *Superlattices and Microstructures,* 35, 437-444.

CARSON, R. S. & HENDRICK, C. D. (1965) Natural Pulsations in Electrical Spraying of Liquids. *Aiaa Journal,* 3, 1072-1075.

CHAO, D., PATEL, A., BARWICZ, T., SMITH, H. I. & MENON, R. (2005) Immersion zone-plate-array lithography. *Journal of Vacuum Science & Technology B,* 23, 2657-2661.

CHEN, A. H., WANG, H. Q. & LI, X. Y. (2005) One-step process to fabricate Ag-polypyrrole coaxial nanocables. *Chemical Communications,* 1863-1864.

CHEN, C. H., KELDER, E. M., VANDERPUT, P. & SCHOONMAN, J. (1996) Morphology control of thin LiCoO2 films fabricated using the electrostatic spray deposition (ESD) technique. *Journal of Materials Chemistry,* 6, 765-771.

CHOI, T. Y., POULIKAKOS, D. & GRIGOROPOULOS, C. P. (2004) Fountain-pen-based laser microstructuring with gold nanoparticle inks. *Applied Physics Letters,* 85, 13-15.

CHUNG, J., BIERI, N. R., KO, S., GRIGOROPOULOS, C. P. & POULIKAKOS, D. (2004) In-tandem deposition and sintering of printed gold nanoparticle inks induced by continuous Gaussian laser irradiation. *Applied Physics a-Materials Science & Processing,* 79, 1259-1261.

CLOUPEAU, M. & PRUNETFOCH, B. (1989) Electrostatic Spraying of Liquids in Cone-Jet Mode. *Journal of Electrostatics,* 22, 135-159.

CLOUPEAU, M. & PRUNETFOCH, B. (1990) Electrostatic Spraying of Liquids - Main Functioning Modes. *Journal of Electrostatics,* 25, 165-184.

CLOUPEAU, M. & PRUNETFOCH, B. (1994) Electrohydrodynamic Spraying Functioning Modes - a Critical-Review. *Journal of Aerosol Science,* 25, 1021-1036.

CLOUPEAU, M. (1994) Recipes for Use of Ehd Spraying in Cone-Jet Mode and Notes on Corona Discharge Effects. *Journal of Aerosol Science,* 25, 1143-1157.

CORBIERRE, M. K., CAMERON, N. S., SUTTON, M., MOCHRIE, S. G. J., LURIO, L. B., RUHM, A. & LENNOX, R. B. (2001) Polymer-stabilized gold nanoparticles and their incorporation into polymer matrices. *Journal of the American Chemical Society,* 123, 10411-10412.

CORTIE, M. B. (2004) The weird world of nanoscale gold. *Gold Bulletin,* 37, 12-19.

DANIEL, M. C. & ASTRUC, D. (2004) Gold nanoparticles: Assembly, supramolecular chemistry, quantum-size-related properties, and applications toward biology, catalysis, and nanotechnology. *Chemical Reviews,* 104, 293-346.

DEARDEN, A. L., SMITH, P. J., SHIN, D. Y., REIS, N., DERBY, B. & O'BRIEN, P. (2005) A low Curing temperature silver ink for use in ink-jet printing and subsequent production of conductive tracks. *Macromolecular Rapid Communications,* 26, 315-318.

DEEGAN, R. D., BAKAJIN, O., DUPONT, T. F., HUBER, G., NAGEL, S. R. & WITTEN, T. A. (1997) Capillary flow as the cause of ring stains from dried liquid drops. *Nature,* 389, 827-829.

DEEGAN, R. D., BAKAJIN, O., DUPONT, T. F., HUBER, G., NAGEL, S. R. & WITTEN, T. A. (2000) Contact line deposits in an evaporating drop. *Physical Review E,* 62, 756-765.

DELAMARCHE, E., VICHICONTI, J., HALL, S. A., GEISSLER, M., GRAHAM, W., MICHEL, B. & NUNES, R. (2003) Electroless deposition of Cu on glass and patterning with microcontact printing. *Langmuir,* 19, 6567-6569.

DELAMORA, J. F. & LOSCERTALES, I. G. (1994) The Current Emitted by Highly Conducting Taylor Cones. *Journal of Fluid Mechanics,* 260, 155-184.

DELAMORA, J. F. (1992) The Effect of Charge Emission from Electrified Liquid Cones. *Journal of Fluid Mechanics,* 243, 561-574.

DEMERS, L. M., PARK, S. J., TATON, T. A., LI, Z. & MIRKIN, C. A. (2001) Orthogonal assembly of nanoparticle building blocks on dip-pen nanolithographically generated templates of DNA. *Angewandte Chemie-International Edition,* 40, 3071-3073.

DEMIR, M. M., YILGOR, I., YILGOR, E. & ERMAN, B. (2002) Electrospinning of polyurethane fibers. *Polymer,* 43, 3303-3309.

DIAO, J. J., QIU, F. S., CHEN, G. D. & REEVES, M. E. (2003) Surface vertical deposition for gold nanoparticle film. *Journal of Physics D-Applied Physics,* 36, L25-L27.

DOSHI, J. & RENEKER, D. H. (1995) Electrospinning process and applications of electrospun fibers. *Journal of Electrostatics,* 35, 151-160.

DROZIN, V. G. (1955) The electrical dispersion of liquids as aerosols. *Journal of Colloidal Science,* 10, 158-164.

ENUSTUN, B. V. & TURKEVICH, J. (1963) Coagulation of Colloidal Gold. *Journal of the American Chemical Society,* 85, 3317-3328.

FENG, J. J. (2002) The stretching of an electrified non-Newtonian jet: A model for electrospinning. *Physics of Fluids,* 14, 3912-3926.

FENG, J. J. (2003) Stretching of a straight electrically charged viscoelastic jet. *Journal of Non-Newtonian Fluid Mechanics,* 116, 55-70.

FENN, J. B., MANN, M., MENG, C. K., WONG, S. F. & WHITEHOUSE, C. M. (1989) Electrospray Ionization for Mass-Spectrometry of Large Biomolecules. *Science,* 246, 64-71.

FONG, H., CHUN, I. & RENEKER, D. H. (1999) Beaded nanofibers formed during electrospinning. *Polymer,* 40, 4585-4592.

FRIDRIKH, S. V., YU, J. H., BRENNER, M. P. & RUTLEDGE, G. C. (2003) Controlling the fiber diameter during electrospinning. *Physical Review Letters,* 90, 144502.

FU, L., LIU, X. G., ZHANG, Y., DRAVID, V. P. & MIRKIN, C. A. (2003) Nanopatterning of "hard" magnetic nanostructures via dip-pen nanolithography and a sol-based ink. *Nano Letters,* 3, 757-760.

GANAN-CALVO, A. M. (1995) The role of the viscosity in the EHD spraying of liquids in cone-jet mode. *Electrostatics 1995.*

GANAN-CALVO, A. M. (1997) Cone-jet analytical extension of Taylor's electrostatic solution and the asymptotic universal scaling laws in electrospraying. *Physical Review Letters,* 79, 217-220.

GANAN-CALVO, A. M. (1999) The electrohydrodynamic atomization of liquids today. *Journal of Aerosol Science,* 30, S547-S548.

GANAN-CALVO, A. M. (2004) On the general scaling theory for electrospraying. *Journal of Fluid Mechanics,* 507, 203-212.

GANAN-CALVO, A. M., DAVILA, J. & BARRERO, A. (1997) Current and droplet size in the electrospraying of liquids. Scaling laws. *Journal of Aerosol Science,* 28, 249-275.

GANAN-CALVO, A. M., LASHERAS, J. C., DAVILA, J. & BARRERO, A. (1994) The Electrostatic Spray Emitted from an Electrified Conical Meniscus. *Journal of Aerosol Science,* 25, 1121-1142.

GEISSLER, M., WOLF, H., STUTZ, R., DELAMARCHE, E., GRUMMT, U. W., MICHEL, B. & BIETSCH, A. (2003) Fabrication of Metal Nanowires Using Microcontact Printing. *Langmuir,* 19, 6301-6311.

GEORGE, M. A. & GLAUNSINGER, W. S. (1994) The Electrical and Structural-Properties of Gold-Films and Mercury-Covered Gold-Films. *Thin Solid Films,* 245, 215-224.

GOMEZ-ROMERO, P. (2001) Hybrid Organic-Inorganic Materials - In Search of Synergic Activity. *Advanced Materials,* 13, 163-174.

GRACE, J. M. & MARIJNISSEN, J. C. M. (1994) A Review of Liquid Atomization by Electrical Means. *Journal of Aerosol Science,* 25, 1005-1019.

GRAF, C., VOSSEN, D. L. J., IMHOF, A. & VAN BLAADEREN, A. (2003) A general method to coat colloidal particles with silica. *Langmuir,* 19, 6693-6700.

GRIGOREV, A. I. & SHIRYAEVA, S. O. (1994) The Theoretical Consideration of Physical Regularities of Electrostatic Dispersion of Liquids as Aerosols. *Journal of Aerosol Science,* 25, 1079-1091.

GUO, H. C., NAU, D., RADKE, A., ZHANG, X. P., STODOLKA, J., YANG, X. L., TIKHODEEV, S. G., GIPPIUS, N. A. & GIESSEN, H. (2005) Large-area metallic photonic crystal fabrication with interference lithography and dry etching. *Applied Physics B-Lasers and Optics,* 81, 271-275.

HAAHEIM, J., EBY, R., NELSON, M., FRAGALA, J., ROSNER, B., ZHANG, H. & ATHAS, G. (2005) Dip Pen Nanolithography (DPN): process and instrument performance with NanoInk's NSCRIPTOR system. *Ultramicroscopy,* 103, 117-132.

HAIQING LIU & HSIEH, Y. (2002) Ultrafine fibrous cellulose membranes from electrospinning of cellulose acetate. *Journal of Polymer Science Part B: Polymer Physics,* 40, 2119-2129.

HANARP, P., KALL, M. & SUTHERLAND, D. S. (2003) Optical properties of short range ordered arrays of nanometer gold disks prepared by colloidal lithography. *Journal of Physical Chemistry B,* 107, 5768-5772.

HARTMAN, R. P. A., BORRA, J. P., BRUNNER, D. J., MARIJNISSEN, J. C. M. & SCARLETT, B. (1999a) The evolution of electrohydrodynamic sprays produced in the cone-jet mode, a physical model. *Journal of Electrostatics,* 47, 143-170.

HARTMAN, R. P. A., BRUNNER, D. J., CAMELOT, D. M. A., MARIJNISSEN, J. C. M. & SCARLETT, B. (1999b) Electrohydrodynamic atomization in the cone-jet mode physical modeling of the liquid cone and jet. *Journal of Aerosol Science,* 30, 823-849.

HARTMAN, R. P. A., BRUNNER, D. J., CAMELOT, D. M. A., MARIJNISSEN, J. C. M. & SCARLETT, B. (2000) Jet break-up in electrohydrodynamic atomization in the cone-jet mode. *Journal of Aerosol Science,* 31, 65-95.

HAYATI, I., BAILEY, A. & TADROS, T. F. (1987a) Investigations into the Mechanism of Electrohydrodynamic Spraying of Liquids .2. Mechanism of Stable Jet Formation and Electrical Forces Acting on a Liquid Cone. *Journal of Colloid and Interface Science,* 117, 222-230.

HAYATI, I., BAILEY, A. I. & TADROS, T. F. (1986) Mechanism of Stable Jet Formation in Electrohydrodynamic Atomization. *Nature,* 319, 41-43.

HAYATI, I., BAILEY, A. I. & TADROS, T. F. (1987b) Investigations into the Mechanisms of Electrohydrodynamic Spraying of Liquids .1. Effect of Electric-Field and the Environment on Pendant Drops and Factors Affecting the Formation of Stable Jets and Atomization. *Journal of Colloid and Interface Science,* 117, 205-221.

HEBNER, T. R., WU, C. C., MARCY, D., LU, M. H. & STURM, J. C. (1998) Ink-jet printing of doped polymers for organic light emitting devices. *Applied Physics Letters,* 72, 519-521.

HEINZL, J. & HERTZ, C. H. (1985) Ink-Jet Printing. *Advances in Imaging and Electron Physics,* 65, 91-171.

HICKMAN, J. J., OFER, D., LAIBINIS, P. E., WHITESIDES, G. M. & WRIGHTON, M. S. (1991) Molecular Self-Assembly of 2-Terminal, Voltammetric Microsensors with Internal References. *Science,* 252, 688-691.

HIGUERA, F. J. (2003) Flow rate and electric current emitted by a Taylor cone. *Journal of Fluid Mechanics,* 484, 303-327.

HOGAN, J. J. & HENDRICK, C. D. (1965) Investigation of Charge-to-Mass Ratio of Electrically Sprayed Liquid Particles. *Aiaa Journal,* 3, 296-301.

HU, H. & LARSON, R. G. (2002) Evaporation of a sessile droplet on a substrate. *Journal of Physical Chemistry B,* 106, 1334-1344.

HU, J. T., ODOM, T. W. & LIEBER, C. M. (1999) Chemistry and physics in one dimension: Synthesis and properties of nanowires and nanotubes. *Accounts of Chemical Research,* 32, 435-445.

HU, J., LI, W., CHEN, J., ZHANG, X. & ZHAO, X. (2008) Novel plating solution for electroless deposition of gold film onto glass surface. *Surface and Coatings Technology,* In Press, Corrected Proof.

HUANG, S. M., FU, Q., AN, L. & LIU, J. (2004) Growth of aligned SWNT arrays from water-soluble molecular clusters for nanotube device fabrication. *Physical Chemistry Chemical Physics,* 6, 1077-1079.

HUANG, Z. M., ZHANG, Y. Z., KOTAKI, M. & RAMAKRISHNA, S. (2003) A review on polymer nanofibers by electrospinning and their applications in nanocomposites. *Composites Science and Technology,* 63, 2223-2253.

HULL, P. J., HUTCHISON, J. L., SALATA, O. V. & DOBSON, P. J. (1997) Synthesis of nanometer-scale silver crystallites via a room-temperature electrostatic spraying process. *Advanced Materials,* 9, 413-417.

IKEGAWA, M. & AZUMA, H. (2004) Droplet behaviors on substrates in thin-film formation using ink-jet printing. *Jsme International Journal Series B-Fluids and Thermal Engineering,* 47, 490-496.

IWATA, F., NAGAMI, S., SUMIYA, Y. AND SASAKI, A. (2007) Nanometre-scale deposition of colloidal Au particles using electrophoresis in a nanopipette probe, *Nanotechnology,* 18, 105301.

JAWOREK, A. & KRUPA, A. (1996) Generation and characteristics of the precession mode of EHD spraying. *Journal of Aerosol Science,* 27, 75-82.

JAWOREK, A. & KRUPA, A. (1999) Classification of the modes of EHD spraying. *Journal of Aerosol Science,* 30, 873-893.

JAYASINGHE, S. N. & EDIRISINGHE, M. J. (2002) Effect of viscosity on the size of relics produced by electrostatic atomization. *Journal of Aerosol Science,* 33, 1379-1388.

JAYASINGHE, S. N. & EDIRISINGHE, M. J. (2004) Electrostatic atomisation of a ceramic suspension. *Journal of the European Ceramic Society,* 24, 2203-2213.

JAYASINGHE, S. N., EDIRISINGHE, M. J. & DE WILDE, T. (2002) A novel ceramic printing technique based on electrostatic atomization of a suspension. *Materials Research Innovations,* 6, 92-95.

JONES, A. R. & THONG, K. C. (1971) Production of Charged Monodisperse Fuel Droplets by Electrical Dispersion. *Journal of Physics D-Applied Physics,* 4, 1159-1166.

KAMAT, P. V. (2002) Photophysical, Photochemical and Photocatalytic Aspects of Metal Nanoparticles. *J. Phys. Chem. B,* 106, 7729-7744.

KAMYSHNY, A., BEN-MOSHE, M., AVIEZER, S. & MAGDASSI, S. (2005) Ink-jet printing of metallic nanoparticles and microemulsions. *Macromolecular Rapid Communications,* 26, 281-288.

KESSICK, R., FENN, J. & TEPPER, G. (2004) The use of AC potentials in electrospraying and electrospinning processes. *Polymer,* 45, 2981-2984.

KIM, D., JEONG, S., PARK, B. K. & MOON, J. (2006) Direct writing of silver conductive patterns: Improvement of film morphology and conductance by controlling solvent compositions. *Applied Physics Letters,* 89, 264101.

KIM, M. C. & LEE, S. Y. (2004) Change of atomization performance with selection of nozzle materials in electrohydrodynamic spraying. *Atomization and Sprays,* 14, 175-190.

KIM, S. J. & MCKEAN, D. E. (1998) Aqueous TiO2 suspension preparation and novel application of ink-jet printing technique for ceramics patterning. *Journal of Materials Science Letters,* 17, 141-144.

KLEBE, R. J. (1988) Cytoscribing - a Method for Micropositioning Cells and the Construction of Two-Dimensional and 3-Dimensional Synthetic Tissues. *Experimental Cell Research,* 179, 362-373.

KUHN, L. & MYERS, R. A. (1979) Ink-Jet Printing. *Scientific American,* 240, 162-178.

LARRONDO, L. & MANLEY, R. S. J. (1981a) Electrostatic Fiber Spinning from Polymer Melts .1. Experimental-Observations on Fiber Formation and Properties. *Journal of Polymer Science Part B-Polymer Physics,* 19, 909-920.

LARRONDO, L. & MANLEY, R. S. J. (1981b) Electrostatic Fiber Spinning from Polymer Melts .2. Examination of the Flow Field in an Electrically Driven Jet. *Journal of Polymer Science Part B-Polymer Physics,* 19, 921-932.

LARRONDO, L. & MANLEY, R. S. J. (1981c) Electrostatic Fiber Spinning from Polymer Melts .3. Electrostatic Deformation of a Pendant Drop of Polymer Melt. *Journal of Polymer Science Part B-Polymer Physics,* 19, 933-940.

LEE, D. Y., HWANG, E. S., YU, T. U., KIM, Y. J. & HWANG, J. (2006) Structuring of micro line conductor using electro-hydrodynamic printing of a silver nanoparticle suspension. *Applied Physics a-Materials Science & Processing,* 82, 671-674.

LEE, D. Y., SHIN, Y. S., PARK, S. E., YU, T. U. & HWANG, J. (2007) Electrohydrodynamic printing of silver nanoparticles by using a focused nanocolloid jet. *Applied Physics Letters,* 90, 081905.

LEE, H. H., CHOU, K. S. & HUANG, K. C. (2005) Inkjet printing of nanosized silver colloids. *Nanotechnology,* 16, 2436-2441.

LEE, J., SUNDAR, V. C., HEINE, J. R., BAWENDI, M. G. & JENSEN, K. F. (2000) Full color emission from II-VI semiconductor quantum dot-polymer composites. *Advanced Materials,* 12, 1102-1105.

LI, D. & XIA, Y. N. (2004) Electrospinning of nanofibers: Reinventing the wheel? *Advanced Materials,* 16, 1151-1170.

LI, D., MCCANN, J. T., GRATT, M. & XIA, Y. (2004a) Photocatalytic deposition of gold nanoparticles on electrospun nanofibers of titania. *Chemical Physics Letters,* 394, 387-391.

LI, D., WANG, Y. L. & XIA, Y. N. (2004b) Electrospinning nanofibers as uniaxially aligned arrays and layer-by-layer stacked films. *Advanced Materials,* 16, 361-366.

LI, M. T., WANG, J. A., ZHUANG, L. & CHOU, S. Y. (2000) Fabrication of circular optical structures with a 20 nm minimum feature size using nanoimprint lithography. *Applied Physics Letters,* 76, 673-675.

LI, Y., MAYNOR, B. W. & LIU, J. (2001) Electrochemical AFM "dip-pen" nanolithography. *Journal of the American Chemical Society,* 123, 2105-2106.

LITBORN, E., EMMER, A. & ROERAADE, J. (1999) Chip-based nanovials for tryptic digest and capillary electrophoresis. *Analytica Chimica Acta,* 401, 11-19.

LIZ-MARZAN, L. M. (2004) Nanometals: Formation and color. *Materials Today,* 7, 26-31.

LOSCERTALES, I. G., BARRERO, A., GUERRERO, I., CORTIJO, R., MARQUEZ, M. & GANAN-CALVO, A. M. (2002) Micro/nano encapsutation via electrified coaxial liquid jets. *Science,* 295, 1695-1698.

MAAROOF, A. I., CORTIE, M. B. & SMITH, G. B. (2005) Optical properties of mesoporous gold films. *Journal of Optics A: Pure and Applied Optics*, 303-309.

MAHONEY, J. F., YAHIKU, A. Y., DALEY, H. L., MOORE, R. D. & PEREL, J. (1969) Electrohydrodynamic Ion Source. *Journal of Applied Physics,* 40, 5101-5106.

MAYER, A. B. R. (1998) Formation of noble metal nanoparticles within a polymeric matrix: nanoparticle features and overall morphologies. *Materials Science and Engineering: C,* 6, 155-166.

MAYNOR, B. W., FILOCAMO, S. F., GRINSTAFF, M. W. & LIU, J. (2002) Direct-writing of polymer nanostructures: Poly(thiophene) nanowires on semiconducting and insulating surfaces. *Journal of the American Chemical Society,* 124, 522-523.

MCCANN, J. T., LI, D. & XIA, Y. N. (2005) Electrospinning of nanofibers with core-sheath, hollow, or porous structures. *Journal of Materials Chemistry,* 15, 735-738.

MEESTERS, G. M. H., VERCOULEN, P. H. W., MARIJNISSEN, J. C. M. & SCARLETT, B. (1992) Generation of Micron-Sized Droplets from the Taylor Cone. *Journal of Aerosol Science,* 23, 37-49.

MICHELSON, D. (1990) Electrostatic Atomization. *Bristol and New York; Adam Hilger Press.*

MUTOH, M., KAIEDA, S. & KAMIMURA, K. (1979) Convergence and Disintegration of Liquid Jets Induced by an Electrostatic-Field. *Journal of Applied Physics,* 50, 3174-3179.

NAGORNYI, V. S. & BEZRUKOV, V. I. (1980) Droplet emission in an electrostatic field. *Magn Gidrodin USSR,* 16, 111.

NAKAMURA, H. (2004) Colloidal Crystals -Self-Assembly of Monodispersed Colloidal Particles. *R&D Review of Toyota CRDL,* 39, 33-39.

NISHINO, Y. & IKAI, K. (2006) Internal friction study of microplasticity in polycrystalline gold thin films. *Materials Science and Engineering a-Structural Materials Properties Microstructure and Processing,* 442, 347-351.

NOYMER, P. D. & GAREL, M. (2000) Stability and atomization characteristics of electrohydrodynamic jets in the cone-jet and multi-jet modes. *Journal of Aerosol Science,* 31, 1165-1172.

NUR, H. M., SONG, J. H., EVANS, J. R. G. & EDIRISINGHE, M. J. (2002) Ink-jet printing of gold conductive tracks. *Journal of Materials Science-Materials in Electronics,* 13, 213-219.

OGATA, N., VAN TASSEL, J. AND RANDALL, C. A. (2001) Electrode formation by electrophoretic deposition of nanopowders, *Materials Letters, 49, 7-14.*

ONNERFJORD, P., NILSSON, J., WALLMAN, L., LAURELL, T. & MARKO-VARGA, G. (1998) Picoliter sample preparation in MALDI-TOF MS using a micromachined silicon flow-through dispenser. *Analytical Chemistry,* 70, 4755-4760.

PARK, B. K., KIM, D., JEONG, S., MOON, J. & KIM, J. S. (2007) Direct writing of copper conductive patterns by ink-jet printing. *Thin Solid Films,* 515, 7706-7711.

PARK, J. & MOON, J. (2006) Control of colloidal particle deposit patterns within picoliter droplets ejected by ink-jet printing. *Langmuir,* 22, 3506-3513.

PAWLOWSKI, K. J., BELVIN, H. L., RANEY, D. L., SU, J., HARRISON, J. S. & SIOCHI, E. J. (2003) Electrospinning of a micro-air vehicle wing skin. *Polymer,* 44, 1309-1314.

PERELAER, J., DE GANS, B. J. & SCHUBERT, U. S. (2006) Ink-jet printing and microwave sintering of conductive silver tracks. *Advanced Materials,* 18, 2101-2104.

PINER, R. D., ZHU, J., XU, F., HONG, S. H. & MIRKIN, C. A. (1999) "Dip-pen" nanolithography. *Science,* 283, 661-663.

POPOV, Y. O. (2005) Evaporative deposition patterns: Spatial dimensions of the deposit. *Physical Review E,* 71, 036313.

POPOVIC, N., NENADOVIC, T., BOGDANOV, Z., MILIC, M. & PETROVIC, R. (1990) Low-Temperature Diffusion Effects on Microstructural Changes in Thick Gold-Films on Silicon. *Thin Solid Films,* 193, 453-462.

QUIST, A. P., PAVLOVIC, E. & OSCARSSON, S. (2005) Recent advances in microcontact printing. *Analytical and Bioanalytical Chemistry,* 381, 591-600.

RAYLEIGH, L. (1878) On The Instability Of Jets. *Proc. London Math. Soc.,* s1-10, 4-13.

RAYLEIGH, L. (1879a) On the Capillary Phenomena of Jets. *Proceedings of the Royal Society of London,* 29, 71-97.

RAYLEIGH, L. (1879b) On the stability of jets. *Proc. London Math. Soc.,* 10, 4.

RAYLEIGH, L. (1882) On the equilibrium of liquid conducting masses charged with electricity. *Philosophical Magazine,* 14, 184.

RENEKER, D. H. & CHUN, I. (1996) Nanometre diameter fibres of polymer, produced by electrospinning. *Nanotechnology,* 7, 216-223.

RENEKER, D. H., YARIN, A. L., FONG, H. & KOOMBHONGSE, S. (2000) Bending instability of electrically charged liquid jets of polymer solutions in electrospinning. *Journal of Applied Physics,* 87, 4531-4547.

REYNTJENS, S. & PUERS, R. (2001) A review of focused ion beam applications in microsystem technology. *Journal of Micromechanics and Microengineering,* 11, 287-300.

RODRÍGUEZ-GONZÁLEZ, B., PASTORIZA-SANTOS, I., LIZ-MARZÁN, L.M. (2006) Bending Contours in Silver Nanoprisms. *Journal of Physical Chemistry B,* 110, 11796-11799.

ROGERS, J. A., PAUL, K. E. & WHITESIDES, G. M. (1998) Quantifying distortions in soft lithography. *Journal of Vacuum Science & Technology B,* 16, 88-97.

ROSELL-LLOMPART, J. & DELAMORA, J. F. (1994) Generation of Monodisperse Droplets 0.3 to 4 um in Diameter from Electrified Cone-Jets of Highly Conducting and Viscous-Liquids. *Journal of Aerosol Science,* 25, 1093-1119.

SÁNCHEZ-IGLESIAS, A., PASTORIZA-SANTOS, I. , PÉREZ-JUSTE, J., RODRÍGUEZ-GONZÁLEZ, B., GARCÍA DE ABAJO, F.J., LIZ-MARZÁN, L.M. (2006) Synthesis and Optical Properties of Gold Nanodecahedra with Size Control. *Advance Materials*, 18, 2529-2534.

SHIM, J. H., LEE, B. J. & CHO, Y. W. (2002) Thermal stability of unsupported gold nanoparticle: a molecular dynamics study. *Surface Science,* 512, 262-268.

SHIN, Y. M., HOHMAN, M. M., BRENNER, M. P. & RUTLEDGE, G. C. (2001) Electrospinning: A whipping fluid jet generates submicron polymer fibers. *Applied Physics Letters,* 78, 1149-1151.

SHIRYAEVA, S. O. & GRIGOREV, A. I. (1995) The Semiphenomenological Classification of the Modes of Electrostatic Dispersion of Liquids. *Journal of Electrostatics,* 34, 51-59.

SHTERN, V. & BARRERO, A. (1995) Bifurcation of Swirl in Liquid Cones. *Journal of Fluid Mechanics,* 300, 169-205.

SMITH, D. P. H. (1986) The Electrohydrodynamic Atomization of Liquids. *Ieee Transactions on Industry Applications,* 22, 527-535.

SOMMER, A. P. & ROZLOSNIK, N. (2005) Formation of crystalline ring patterns on extremely hydrophobic supersmooth substrates: Extension of ring formation paradigms. *Crystal Growth & Design,* 5, 551-557.

STOKES, N., MCDONAGH, A. M. & CORTIE, M. B. (2007) Preparation of nanoscale gold structures by nanolithography. *Gold Bulletin,* 40, 310-320.

SUBRAMANIAN, V., WOLF, E. AND KAMAT, P.V (2001) Semiconductor-Metal Composite Nanostructures. To What Extent Do Metal Nanoparticles Improve the Photocatalytic Activity of TiO_2 Films?. *Journal of Physical Chemistry B,* 105, 11439 -11446.

SUNG, K. & LEE, C. S. (2004) Factors influencing liquid breakup in electrohydrodynamic atomization. *Journal of Applied Physics,* 96, 3956-3961.

SZCZECH, J. B., MEGARIDIS, C. M., GAMOTA, D. R. & ZHANG, J. (2002) Fine-line conductor manufacturing using drop-on-demand PZT printing technology. *Ieee Transactions on Electronics Packaging Manufacturing,* 25, 26-33.

TANG, K. Q. & GOMEZ, A. (1996) Monodisperse electrosprays of low electric conductivity liquids in the cone-jet mode. *Journal of Colloid and Interface Science,* 184, 500-511.

TAY, B. Y., EVANS, J. R. G. & EDIRISINGHE, M. J. (2003) Solid freeform fabrication of ceramics. *International Materials Reviews,* 48, 341-370.

TAYLOR, G. (1964) Disintegration of Water Drops in Electric Field. *Proceedings of the Royal Society of London Series a-Mathematical and Physical Sciences,* 280, 383-397.

TAYLOR, G. (1969) Electrically Driven Jets. *Proceedings of the Royal Society of London Series a-Mathematical and Physical Sciences,* 313, 453-475.

TENG, K. F. & VEST, R. W. (1987) Liquid Ink Jet Printing with Mod Inks for Hybrid Microcircuits. *Ieee Transactions on Components Hybrids and Manufacturing Technology,* 10, 545-549.

TENG, K. F. & VEST, R. W. (1988) Metallization of Solar-Cells with Ink Jet Printing and Silver Metallo-Organic Inks. *Ieee Transactions on Components Hybrids and Manufacturing Technology,* 11, 291-297.

TERANISHI, T., KIYOKAWA, I. & MIYAKE, M. (1998) Synthesis of monodisperse gold nanoparticles using linear polymers as protective agents. *Advanced Materials,* 10, 596-599.

TESSIER, P., VELEV, O. D., KALAMBUR, A. T., LENHOFF, A. M., RABOLT, J. F. & KALER, E. W. (2001) Structured metallic films for optical and spectroscopic applications via colloidal crystal templating. *Advanced Materials,* 13, 396-400.

UENO, K., MIZEIKIS, V., JUODKAZIS, S., SASAKI, K. & MISAWA, H. (2005) Optical properties of nanoengineered gold blocks. *Optics Letters,* 30, 2158-2160.

VAN TASSEL, J. AND RANDALL, C. A. (2004) Potential for integration of electrophoretic deposition into electronic device manufacture; demonstrations using silver/palladium, *Journal of Materials Science, 39,* 867-879.

VARGUEZ, P., AVILES, F. & OLIVA, A. I. (2008) Mechanical properties of gold nanometric films onto a polymeric substrate. *Surface and Coatings Technology,* 202, 1556-1563.

VONNEGUT, B., NEUBAUER, R. L., GELLER, M. & MAYNARD, K. (1952) production of monodisperse liquid particles by electrical atomization. (project cirrus). Occasional report no. 36. Seventh occasional report. Multiple-stage dilution of aerosols by use of aspirators. (project cirrus). Occasional report no. 37. Eighth occasional report.

WANG, D. Z., JAYASINGHE, S. N. & EDIRISINGHE, M. J. (2005) High resolution print-patterning of a nano-suspension. *Journal of Nanoparticle Research,* 7, 301-306.

WATANABE, H., MATSUYAMA, T. & YAMAMOTO, H. (2003) Experimental study on electrostatic atomization of highly viscous liquids. *Journal of Electrostatics,* 57, 183-197.

WATT, F., BETTIOL, A., VAN KAN, A., TEO, J. & BREESE, B. H. (2005) ION BEAM LITHOGRAPHY AND NANOFABRICATION: A REVIEW. *International Journal of Nanoscience,* 4, 269-286.

WHITESIDES, G. M., OSTUNI, E., TAKAYAMA, S., JIANG, X. Y. & INGBER, D. E. (2001) Soft lithography in biology and biochemistry. *Annual Review of Biomedical Engineering,* 3, 335-373.

WILBUR, J. L., KUMAR, A., BIEBUYCK, H. A., KIM, E. & WHITESIDES, G. M. (1996) Microcontact printing of self-assembled monolayers: Applications in microfabrication. *Nanotechnology,* 7, 452-457.

WILLNER, I. & WILLNER, B. (2001) Molecular and biomolecular optoelectronics. *Pure and Applied Chemistry,* 73, 535-542.

WOLFE, D. B., LOVE, J. C., PAUL, K. E., CHABINYC, M. L. & WHITESIDES, G. M. (2002) Fabrication of palladium-based microelectronic devices by microcontact printing. *Applied Physics Letters,* 80, 2222-2224.

WU, B., HO, A., MOLDOVAN, N. & ESPINOSA, H. D. (2007) Direct deposition and assembly of gold colloidal particles using a nanofountain probe. *Langmuir,* 23, 9120-9123.

XIA, Y. N. & WHITESIDES, G. M. (1995) Use of Controlled Reactive Spreading of Liquid Alkanethiol on the Surface of Gold to Modify the Size of Features Produced by Microcontact Printing. *Journal of the American Chemical Society,* 117, 3274-3275.

XIA, Y. N. & WHITESIDES, G. M. (1998) Soft lithography. *Annual Review of Materials Science,* 28, 153-184.

XIA, Y. N., MRKSICH, M., KIM, E. & WHITESIDES, G. M. (1995) Microcontact Printing of Octadecylsiloxane on the Surface of Silicon Dioxide and Its Application in Microfabrication. *Journal of the American Chemical Society,* 117, 9576-9577.

XIA, Y. N., YANG, P. D., SUN, Y. G., WU, Y. Y., MAYERS, B., GATES, B., YIN, Y. D., KIM, F. & YAN, Y. Q. (2003) One-dimensional nanostructures: Synthesis, characterization, and applications. *Advanced Materials,* 15, 353-389.

XU, J., DRELICH, J. & NADGORNY, E. M. (2004) Laser-Based Patterning of Gold Nanoparticles into Microstructures. *Langmuir,* 20, 1021-1025.

YARIN, A. L., KOOMBHONGSE, S. & RENEKER, D. H. (2001) Taylor cone and jetting from liquid droplets in electrospinning of nanofibers. *Journal of Applied Physics,* 90, 4836-4846.

ZELENY, J. (1914) The Electrical Discharge from Liquid Points, and a Hydrostatic Method of Measuring the Electric Intensity at Their Surfaces. *Physical Review,* 3, 69-91.

ZELENY, J. (1915) On the conditions of instability of electrified drops with applications to the electrical discharge from liquid points. *Proceedings of the Cambridge Philosophical Society,* 18, 17-24.

ZELENY, J. (1917) Instability of Electrified Liquid Surfaces. *Physical Review,* 10, 1-6.

ZELENY, J. (1935) the role of surface instability in electrical discharges from drops of alcohol and water in air at atmospheric pressure. *Journal of Franklyn Institute,* 219, 659-671.

ZHANG, H., CHUNG, S. W. & MIRKIN, C. A. (2003) Fabrication of sub-50-nm solid-state nanostructures on the basis of dip-pen nanolithography. *Nano Letters,* 3, 43-45.

ZHANG, R. W., ZHANG, D., MAO, H., SONG, W. L., GAO, G. & LIU, F. Q. (2006) Preparation and characterization of Ag/AgO nanoshells on carboxylated polystyrene latex particles. *Journal of Materials Research,* 21, 349-354.

ZHAO, W., XU, J. J., SHI, C. G. & CHEN, H. Y. (2006) Fabrication, characterization and application of gold nano-structured film. *Electrochemistry Communications,* 8, 773-778.

ZONG, X., KIM, K., FANG, D., RAN, S., HSIAO, B. S. & CHU, B. (2002) Structure and process relationship of electrospun bioabsorbable nanofiber membranes. *Polymer,* 43, 4403-4412.